Exploration of properties and phases of correlated bosons in optical potentials

by

Sunayana Dutta
Roll No. 146121028

A thesis submitted
in Partial Fulfillment of the Requirement
for the Degree of
DOCTOR OF PHILOSOPHY IN PHYSICS.

Supervisor
Prof. Saurabh Basu

Department of Physics
Indian Institute of Technology Guwahati
Assam 781039, India.

November 2019

Exploration of properties and phases of correlated bosons in optical potentials

by

Sunayana Dutta
Roll No. 146121028

A thesis submitted
in Partial Fulfillment of the Requirement
for the Degree of
DOCTOR OF PHILOSOPHY IN PHYSICS.

Supervisor
Prof. Saurabh Basu

Department of Physics
Indian Institute of Technology Guwahati
Assam 781039, India.

November 2019

DECLARATION

The work in this thesis entitled "*Exploration of properties and phases of correlated bosons in optical potentials*" has been carried out by me under the supervision of Prof. Saurabh Basu, Department of Physics, Indian Institute of Technology Guwahati. No part of this thesis has been submitted elsewhere for award of any other degree or qualification. The research work has been carried out during the period from July, 2014 to June, 2019.

In keeping with general practice of reporting scientific observations, due acknowledgments have been made wherever the work described is based on the findings of other investigations.

Sunayana Dutta,
Roll no. 146121028,
Department of Physics, IIT Guwahati,
Guwahati-781039, Assam, India.
DATE: .....

CERTIFICATE

It is certified that the work contained in the thesis entitled "*Exploration of properties and phases of correlated bosons in optical potentials*" by Ms. Sunayana Dutta (Roll No 146121028), a student of the Department of Physics, IIT Guwahati was carried out under my supervision and has not been submitted elsewhere for the award of any degree.

Prof. Saurabh Basu,
Department of Physics, IIT Guwahati,
Guwahati-781039, Assam, India.
DATE: .....

DISCLAIMER

The bibliography included in this thesis is, by no means complete but contains the ones which are consulted thoroughly by me. I apologize for inadvertently missing out some of the research papers, review articles and other scientific documents pertaining to the focus of this thesis which should also have been cited. For illustration purpose some of the figures in this thesis are taken from other sources and have been properly cited.

Dedicated to my beloved parents

and

grandparents ...

ACKNOWLEDGMENTS

First and foremost, I would like to express my sincere gratitude towards my Ph.D. supervisor, Prof. Saurabh Basu for giving me the opportunity to join in his research group. His constant guidance, knowledge and intelligent ideas have helped me to complete my thesis work successfully well in time. Despite his own busy official schedule, he gave me time for discussion throughout all these years. Finally, it has been a pleasure for me to work under his guidance.

My sincere gratitude also goes to our collaborators, Dr. Axel U. J. Lode and Dr. Marios C. Tsatsos for all their engaging discussions and immense support regarding my research work. Their useful suggestions and insightful comments have also helped me improve my understanding of the field. Their words of encouragement have played a great part in motivating me to work harder.

I would like to express my gratitude towards my Doctoral Committee Members, Prof. Girish Sampath Setlur, Prof. Tarak Nath Dey, Dr. Tapan Mishra and Prof. N Selvaraju for their valuable inputs and feedbacks from time to time, which helped in further improving the quality of my research work.

I am grateful to Dr. Pankaj Kumar Mishra for his engaging discussions and immense support regarding my work. My special thanks also goes to Dr. Kanhaiya Pandey for his helpful discussions.

I am also thankful to the current and the former Heads of the department of Physics, Prof. Subhradip Ghosh, Prof. P. Poulose and Prof. Saurabh Basu, for providing all the resources needed for my research, and also all other faculty members of the department, the technical stuff and office members for helping me whenever I needed. Without their support, it would not have been possible to conduct this research. I thank to all the technical assistants of the department of physics, especially Mr. Basab Bijoy Purkayastha, for his assistance in various ways during my research tenure.

I would like to thank my seniors: Dr. Apurba Barman, Dr. Debashish Das, Dr. Ravi Kumar Patta and Dr. Deepanjali Goswami for their support and cooperation. My special thanks goes to Dr. Priyadarshini Kapri for her assistance and emotional support in several ways. I would like to thank my groupmembers: Shilpi, Priyanka and Sayan for the stimulating discussions and for creating a great working environment. I would also like to thank all my 2014 batchmates, seniors and juniors in the department for their company and help in any direct or indirect ways.

I would like to thank all the inspiring people who have motivated me in one way or another in my life. I am thankful to my friends: Neeraj, Monika, Jyoti, Indu, Joy, Ranjan for their constant moral support throughout my journey. I would also like to thank all my teachers, who have inspired me in any direct and indirect ways throughout my life, which has led me towards pursuing Physics as a career.

Moreover, I would like to thank my college friend Papuli Chaliha for her special support that she had given me in innumerable ways.

My special thanks also goes to my best friend Dr. Mousmita Sarma, for being my greatest emotional support and for always being there for me throughout my roller coaster journey.

Last, but not the least, I would like to express heartfelt gratitude to my family for their role in my life. My parents, who sacrificed their own dreams to give us a comfortable life, raised me with great patience and taught me to love and trust unconditionally, have always been a source of inspiration to me. Their discipline and values have molded me to the person that I am today. Their patience and perseverance has been a constant source of inspiration throughout my life. Their unconditional love, support and faith in me are the most precious gifts that I cherish. I am thankful to my sister, Ainu for always being my support and offering me a helping hand whenever I needed. I am grateful to all of them for their unconditional love, support and faith in me which have always been the driving force in everything that I have done in my life.

List of Publications and Conferences Attended

Journal Publications

1. Apurba Barman, **Sunayana Dutta**, Ayan Khan, and Saurabh Basu, "Understanding the Bose glass phase via a percolation scenario", *Eur. Phys. J. B*, **86**, 308 (2013).

2. **Sunayana Dutta**, Apurba Barman, Anat Siddharth, Ayan Khan, and Saurabh Basu, "Tunneling dynamics of correlated bosons in a double well potential", *Eur. Phys. J. B*, **88**, 139 (2015).

3. **Sunayana Dutta**, Pankaj Kumar Mishra, Budhaditya Chatterjee, and Saurabh Basu, "Dynamics of interacting bosons in a double well potential", *Europhysics Letters*, **124**, 30002 (2018).

4. **Sunayana Dutta**, Marios C Tsatsos, Saurabh Basu, and Axel U J Lode, "Management of the Correlations of Ultracold Bosons in Triple Wells" *New J. Phys.*, **20**, 053044 (2019).

5. SK Noor Nabi, **Sunayana Dutta**, and Saurabh Basu, "Ultracold gases in presence of time-dependent synthetic gauge field" *Eur. Phys. J. B*, **93**, 3 (2020).

Book Chapter(s)

1. "Exploring Many-Body Physics with Bose-Einstein Condensates", *High Performance Computing in Science and Engineering'18, pp: 89-110, Springer, Cham (2019)*,
   O. E. Alon, V. S. Bagnato, R. Beinke, S. Basu, L. S. Cederbaum, B. Chakrabarti, B. Chatterjee, R. Chitra, F. S. Diorico, **S. Dutta**, L. Exl, A. Gammal, S. K. Haldar, S.

Klaiman, C. Lévêque, R. Lin, N. J. Mauser, P Molignini, L Papariello, R. Roy, K. Sakmann, A. I. Streltsov, G. D. Telles, M. C. Tsatsos, R. Wu, A. U. J. Lode.

Conference Procedings

1. **Sunayana Dutta** and Saurabh Basu, "Condensate characteristics of bosons in a tilted optical lattice", *Journal of Physics: Conference Series*, **759**, 012036 (2016).

2. **Sunayana Dutta**, Budhaditya Chatterjee, Pankaj Kumar Mishra, Axel U. J. Lode, Marios C. Tsatsos, and Saurabh Basu, "Tunneling Dynamics of interacting bosons in a quantum seesaw potential", *Journal of Physics: Conference Series*, **1290**, 012030 (2019).

Conferences/Schools attended

1. **XXVII IUPAP Conference on Computational Physics (CCP-2015)**, Indian Institute Of Technology Guwahati, Assam, India, (2015).

2. Attended **SERB** school on the topic "*Frontiers in Quantum Optics*" organized by *department of Physics, Indian Institute Of Technology Guwahati, Assam, India (2017)*.

3. **PRL conference on Condensed Matter Physics**, Physical Research Laboratory, Gujarat, India, (2018).

4. **Recent Trends in Cold and Ultracold Matter**, Indian Institute Of Technology Guwahati, Assam, India, (2018).

5. **XXX IUPAP Conference on Computational Physics (CCP-2018)**, University of California, Davis, USA (2018).

Abstract

In the thesis, we investigate various intriguing properties and phases of interacting bosons in different optical potentials. Our primary focus is to explore the tunneling dynamics and ground state properties of correlated bosons and how these exotic quantum features can be manipulated via tuning the fundamental properties of the system, such as, interactions, depth and geometry of the trapping potential etc. The thesis is divided mainly into two parts depending on the methodologies, namely, the Bose-Hubbard model (BHM) and the Multiconfigurational time-dependent Hartree approach for bosons (MCTDHB) employed to tackle various interesting quantum features. First, with BHM we study the quantum dynamics of correlated bosons in a double well potential. We capture interesting distinctive features for tunneling dynamics in presence of both attractive and repulsive interactions for weak and strong coupling regimes and also explore the sensitivity of the dynamics on different initial configurations in which the system is prepared. Hence, the role of an external driving on the tunneling dynamics of interacting bosons confined in a double-well potential, such as, emergence or suppression of chaotic dynamics in presence of such driving is thoroughly investigated. Further, we analyze the effect of time-dependent synthetic magnetic fields on the quantum phase transition, that is, the Mott-insulating (MI) to the superfluid (SF) phase transition. In the second part of thesis with MCTDHB, first we simulate an experimental scenario where as if the 'charged' bosons are placed in a constant electric field, thereby inducing a tilt in the optical potential and subsequently we analyze the ground state properties, such as, fragmentation and condensation of bosons in such a tilted triple well potential. Here we obtain how the interplay of the interaction strength and the tilt parameter can be used to manipulate correlations and fragmentation of these many-boson systems. We also investigate the dynamics of interacting bosons confined in a temporally driven tilted double well potential that imitates a quantum seesaw and how it can be exploited to control the tunneling dynamics of these interacting bosons. Furthermore, we simulate a

system of few bosons confined in a two-dimensional single harmonic trap in presence of a synthetic gauge field and investigate the many-body dynamics of such a system. Finally, the importance of the second formalism that has been employed to deal with various topics, namely, MCTDHB formalism for a tilted triple well corresponding to both contact and long range interaction potential as a prototype example is presented in the thesis.

List of Figures

CONTENTS

CHAPTER 1

INTRODUCTION

1.1 Bose-Einstein condensation: Developments so far

The successful experimental realization of Bose-Einstein condensation (BEC) in 1995 in a series of astounding experiments on vapors of Rubidium [1] and Sodium [2] have provided a powerful paradigm to study a variety of exotic quantum many-body phenomena [3–6] in macroscopic systems [7–9], thereby, emerging it into an exciting research endeavour for the atomic physics and the condensed matter physics community alike. The Bose-Einstein condensation (BEC) was basically a theoretical concept, proposed by Albert Einstein in 1925, on the basis of a paper that investigated the statistical distribution of photons [10] by the Indian physicist Satyendra Nath Bose. Bose discovered that the thermal energy distribution of photons is very different to that of Maxwell-Boltzmann approach, while the former is solely based on the postulates of quantum theory and indistinguishability of particles. Einstein realized that as a consequence of this, at sufficiently low temperatures, a system of noninteracting particles could occupy the lowest energy state of the system. Thus, at absolute zero temperature, all the particles would "condense" into this state of lowest energy and hence could behave as a matter wave by sharing the same single-particle state. This paved the idea of Bose-Einstein condensation. Henceforth, the particles that obey the distribution function discovered by Bose and Einstein are termed as bosons.

Albeit Einstein's original predication was for a gas of noninteracting bosons, soon

after the discovery of superfluidity in liquid helium (^{4}He) in 1938 [11, 12], Fritz London proposed that despite the presence of strong interatomic interactions in ^{4}He, the phenomena may have been an exposition of something similar to Bose-Einstein condensation. In 1941, Landau developed the first self-consistent theory of superfluidity with regard to the elementary excitations spectrum of the fluid. The first microscopic theory of interacting Bose gases was developed by Bogoliubov in 1947. Thereafter, extensive theoretical work had been developed in regard to better understand the relationship between Bose-Einstein condensation and superfluidity, after Landau and Lifshitz [1951], Penrose and Onsager in 1956 had proposed the concept of off-diagonal long range order of the Bose gas. At that time, it was believed that interactions present in the superfluids would modify the physics of Bose-Einstein condensation. Certainly is the case. Later on, many theoretical works and advanced experiments reveal that the fractional condensate present in superfluid liquid ^{4}He is only 7% even at absolute zero temperature [13–15].

The Bose-Einstein condensate and the condensation process itself were predicted to have many unusual features and for many years experts around the globe have tried to produce it in the laboratories. The novel laser and magnetic based cooling techniques were developed in 1970s; where the experimentalists could cool down the dilute atomic gases to extremely low temperatures [16–18]. The two main criteria of this process were to produce an extremely good vacuum and evaporative cooling. In the beginning, the spin-polarized hydrogen, because of its light mass was the main candidate for realizing Bose-Einstein condensation. Over a period of time, it is observed that alkali atoms are also well suitable for these laser based techniques as their optical transitions can be achieved by available laser and because they have a favourable internal energy-level structure for them to be cooled down to very low temperatures. After trapping, the temperature further can be lowered by evaporative cooling. With these phenomenal progresses in the cooling techniques, Carl Wieman and Eric Cornell very first envisioned a route to Bose-Einstein condensate in a dilute gas of Rubidium (Rb) atoms [1, 19]. Sodium (Na) atoms were the second in line soon after by Wolfgang Ketterle [2]. The occurrence of Bose-Einstein condensation in vapours of ^{7}Li were also reported in [20]. Later, also in other different atomic species, such as, spin-polarized hydrogen [21], metastable ^{4}He [22] and ^{41}K [23], signatures of Bose-Einstein condensation were observed. After six years from the first experimental realization of Bose-Einstein condensation, Wieman, Cornell and Ketterle were awarded with the 2001 Nobel Prize in Physics “for the achievements of Bose-Einstein condensation in dilute gases of alkali atoms, and for early fundamental

studies of the properties of the condensate" [24].

The cooling of atoms is achieved via various novel techniques, for example, laser cooling technique [16–18, 25], magnetic based cooling technique [26] and so on as mentioned earlier. In the case of laser cooling technique, basically an incident photon from the laser beam is absorbed by the atom and hence an impulse is experienced by it, thereby resulting an excitation of the atom. The atom will recoil in the opposite direction of the incident photon when it emits the absorbed photon. As the emission of photon is a random process, it may transfer zero momentum during the process. In case of red detuning, where the frequency of the laser is lower than that of atomic transitions, a photon absorption is only possible as the atom approaches the laser field, thereby the induced Doppler shift compensates for the detuning. This leads to the loss of kinetic energy of the atoms and hence results in lower the temperature of the gas. This method is also known as "optical molasses" [16]. There is an availability of other sophisticated methods for this cooling technique, such as, Sisyphus cooling [18, 27]. The atoms also can be cooled as well as trapped by the most widely used magneto-optical trap [18]. The key idea of this device is to employ spatially varying magnetic field, that induces a position dependent Zeeman-splitting. This results into an exertion of position dependent force by the laser beams and rendering a total force towards the center of the trap. Usually the trapping potential is considered to be harmonic in nature and this results into an inhomogeneous system. The method of "forced evaporative cooling" is used to further lower the temperature. We will not go further into cooling techniques for which substantial volume of literature exists already. The complete discussions on various cooling techniques can be found in Ref. [27].

The first signature of Bose-Einstein condensation was emerged from the time of flight measurements [28]. Here by switching off the confining trap, the atoms were allowed to expand and then image was processed with optical methods. The sharp peak observed in the velocity distribution below a critical temperature provided a clear evidence for Bose-Einstein condensation [Fig.(1.1) from Ref. [28]]. After 1995, two major developments expedited the growth in the field of ultracold atoms. Firstly, the possibility of tuning the interaction strength between the particles by Feshbach resonances [29, 30] and thereby providing to explore the Bose-Einstein condensates spanned from weakly to strongly coupled regime. The second one was the progress in developing and shaping different sort of trap geometries. Although many of the preliminary experiments were performed with single well traps, the developments in sophisticated trapping techniques allowed one to

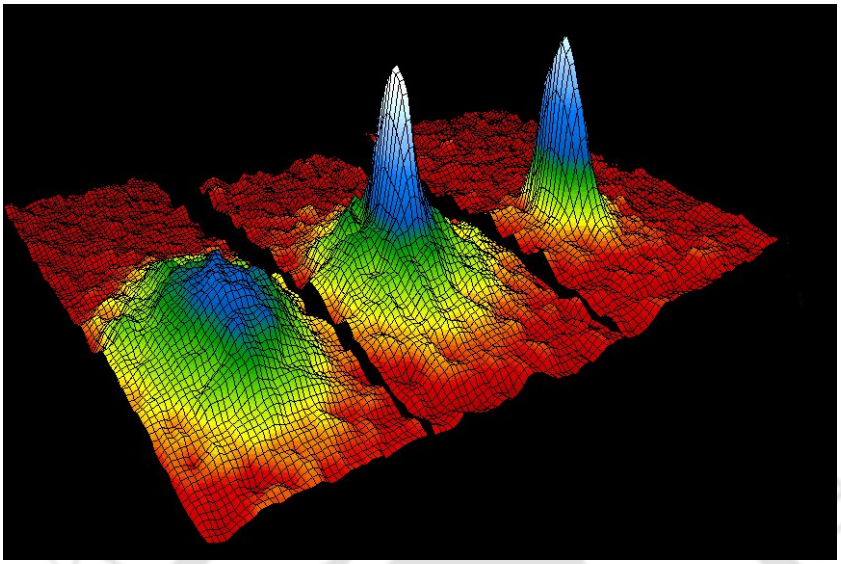

Figure 1.1: The velocity distribution of Rb atoms in the experiment of BEC by Anderson *et al*. in 1995. The left image represents a gas at a temperature just above the condensation; central image represents the appearance of the condensate and right image corresponds to further evaporation of the gas, that results into nearly pure condensate. The colour distribution defines the number of atoms at each velocity; red being the fewest and white being the most.

shape almost to any arbitrary traps. Particularly, traps with numerous potential minima became very popular in this domain. In recent times, multi-well traps [31] and quasi-two and one-dimensional Bose Einstein condensates are commonly used in experiments. One of the most prominent features of trapped ultracold Bose gases is that they are inhomogeneous in nature and this allows access to a wide range of physical phenomena, such as, interference of matter waves, Josephson-like effects, tunneling dynamics and strongly correlated bosons which were not attainable with previous experiments on superfluid ^{4}He. Most importantly, with these novel techniques Bose-Einstein condensation emerges not only in momentum space, but also in coordinate space, providing a direct experimental investigation of the condensate viable and extending new opportunities for interesting studies.

1.1.1 Noninteracting bosonic gas

Since a noninteracting bosonic gas is in a fully condensed state at absolute zero temperature $T = 0$, all N bosons can be described by a 'giant' single boson wave function. Thus the many-body wave function can be expressed in terms of all these identical single-particle

wave functions, $\phi(\mathbf{r})$ as,

$$\Psi(\mathbf{r}_1, \mathbf{r}_2, \mathbf{r}_3, ..., \mathbf{r}_N) = \prod_{i=1}^{N} \phi(\mathbf{r}_i) \tag{1.1}$$

In terms of order parameter $\psi(\mathbf{r})$, a Bose-Einstein condensate can be determined as [13],

$$\psi(\mathbf{r}) = \sqrt{N}\phi(\mathbf{r}) \tag{1.2}$$

which is simply a normalized wave function of the single particle state $\phi(\mathbf{r})$ in which the condensation takes place. Here the particle density is obtained as $n(\mathbf{r}) = |\psi(\mathbf{r})|^2$.

For a system of bosons where the many-body state is considered as a superposition of states with different particle numbers N and a well defined macroscopic phase, the order parameter can be defined as expectation of the single-particle field operator, $\hat{\Psi}(\mathbf{r})$ that annihilates a boson at position $\mathbf{r}$ [32–35],

$$\psi(\mathbf{r}) = \left\langle \hat{\Psi}(\mathbf{r}) \right\rangle \tag{1.3}$$

However, for a state with the occupancy assuming an integer value $\left\langle \hat{\Psi}(\mathbf{r}) \right\rangle = 0$.

1.1.2 Interacting ultracold bosonic gas

The interaction between the atoms in a dilute ultracold gas of bosons is dominated by elastic binary collisions and therefore can be treated in the frame of scattering theory. However real interatomic scattering potential, $V_{sc}(\mathbf{r})$ ($\mathbf{r}$ being the interparticle spacing) is really complicated and can be calculated in an ab initio calculation only for a hydrogen atom.

1.1.2.1 Weakly coupled bosonic gas

Let us consider a gas of N weakly interacting ultracold bosons confined in an external potential, V_{ext}. The many-boson Hamiltonian of these interacting bosons in second quantized notation is given by,

$$\begin{aligned} \hat{H} = & \int d\mathbf{r}\, \hat{\Psi}^{\dagger}(\mathbf{r}) \left(-\frac{\hbar^2}{2m}\nabla^2 + V_{ext}(\mathbf{r}) \right) \hat{\Psi}(\mathbf{r}) + \\ & \frac{1}{2} \int d\mathbf{r}\, d\mathbf{r}'\, \hat{\Psi}^{\dagger}(\mathbf{r}) \hat{\Psi}^{\dagger}(\mathbf{r}')\, V_{sc}(\mathbf{r}-\mathbf{r}')\, \hat{\Psi}(\mathbf{r}) \hat{\Psi}(\mathbf{r}') \end{aligned} \tag{1.4}$$

here $\hat{\Psi}^{\dagger}(\mathbf{r})$ [$\hat{\Psi}(\mathbf{r})$] is the bosonic creation [annihilation] field operator which creates [annihilates] a boson at the position $\mathbf{r}$. For s-wave scattering, the interactomic potential can be replaced with an effective contact interaction as,

$$V_{sc}(\mathbf{r}') = \frac{4\pi\hbar^2 a_s}{m}\delta(\mathbf{r}') = g\delta(\mathbf{r}') \tag{1.5}$$

m is the mass of the bosons, a_s is the s-wave scattering length and $g = \frac{4\pi\hbar a_s}{m}$ is the coupling constant. Here the interaction is determined by the scattering length, a_s [36]. Therefore in terms of Eq.(1.5), the second term of Eq.(1.4) reduces to

$$\frac{4\pi\hbar^2 a_s}{m}\int d(\mathbf{r})\hat{\Psi}^{\dagger}(\mathbf{r})\hat{\Psi}^{\dagger}(\mathbf{r})\hat{\Psi}(\mathbf{r})\hat{\Psi}(\mathbf{r}) \tag{1.6}$$

In the case a dilute gas, the diluteness of the gas is characterized by the ratio of the scattering length, a_s and the interparticle spacing $\mathbf{r}$. A parameter can be defined by using this ratio as na_s^3, where n is the boson density (it is typically $< 10^{-3}$). This dilute gas can be described by a mean field approximation, which was first developed by Bogoliubov in 1947 [37]. Here the Bose-Einstein condensate can be described by an order parameter as in Eq.(1.2) for dilute gas. Under spontaneously broken gauge symmetry, the bosonic field operator, $\hat{\Psi}(\mathbf{r},t)$ can be replaced by its expectation value as $\hat{\Psi}(\mathbf{r},t) = \langle\hat{\Psi}(\mathbf{r},t)\rangle$; here it is a complex function and fluctuation around the mean value is $\delta\hat{\Psi}(\mathbf{r},t)$. Therefore

$$\hat{\Psi}(\mathbf{r},t) = \langle\hat{\Psi}(\mathbf{r},t)\rangle + \delta\hat{\Psi}(\mathbf{r},t) \tag{1.7}$$

By neglecting the fluctuations, one obtains the celebrated non-linear Gross-Pitaevskii equation [38, 39] as,

$$i\hbar\frac{\partial}{\partial t}\Psi(\mathbf{r},t) = \left(-\frac{\hbar^2\nabla^2}{2m} + V_{ext}(\mathbf{r}) + g|\Psi(\mathbf{r},t)|^2\right)\Psi(\mathbf{r},t) \tag{1.8}$$

The many boson wave function in this weakly interacting domain is still determined by the identical one body wave functions, such as the non-interacting regime described via Eq.(1.1). However in this weakly interacting regime, bosons do not condense into the ground state of the single-particle Hamiltonian, instead condense into a state that is determined by Eq.(1.8). Thus Gross Pitaevskii equation is very much essential to describe various properties of the condensate, for example, interference between condensates [7], vortices [40] and so on.

Further Bogoliubov theory is a better method which is beyond the mean field description owing to the inclusion of fluctuations, $\delta\hat{\Psi}(\mathbf{r},t)$ present in the weakly coupled

($na_s^3 << 1$) bosons in the dilute gas. These fluctuations render depletion of the condensed state and this depletion is of the order of $(na_s^3)^{1/2}$, which is typically very small (about 1% in experiments). In Bogoliubov theory, many boson ground state is formulated as an optimized product of the identical, symmetric two particle functions $\phi(\mathbf{r}_i, \mathbf{r}_j, t)$ [32]. In this approach, the two particle correlations are taken into account in such a way that the configurations in which the ith and jth particle are together in coordinate space, are suppressed.

1.1.2.2 Strongly correlated bosonic gas

In the weak coupling regime, the interaction energy, ϵ_{int} is small compared to the kinetic energy ϵ_{kin} per particle and the ratio between these energies is obtained as [41],

$$\frac{\epsilon_{int}}{\epsilon_{kin}} = \frac{gnm}{\hbar^2 n^{2/3}} \approx 4\pi n^{1/3} a_s \tag{1.9}$$

Generally, the interparticle spacing, $n^{-1/3}$ is much larger than the scattering length, a_s in Bose-Einstein condensate. Here n denotes boson density. Hence, the ratio, $\frac{\epsilon_{int}}{\epsilon_{kin}}$ is usually very low (of the order of 0.002) and thus the condensate can be well defined by a macroscopic wave function with small quantum depletion.

For strong coupling regime, the interaction energy per particle shall be of the same order or larger than the kinetic energy. One way to obtain this regime is either by increasing the number density or the scattering length by tuning via a Feshbach resonance [as clear from Eq.(1.9)]. The experimental realization of this feature in Rb has been reported recently where scattering length is increased by several orders of magnitude and a phenomenon of collapse and followed by explosion of the condensate have been reported there [42, 43]. However, there is a problem in this approach that is the severe decrease in life time of the condensate due to three-body losses [44] and it is enhanced with the increase in the density and the scattering length.

There is a completely different approach that exists in which bosons are loaded into a three-dimensional optical lattice and then the condensate is split into larger than 100,000 lattice sites with an average occupancy of $1-2$ atoms per lattice site [45]. Here the atoms can move from one site to its neighbour by tunneling and thus the tunneling energy imitates the role of kinetic energy and the atoms are characterized by their effective masses. The effective mass becomes exponentially large with the increase in the lattice depth and this results into rise in kinetic energy. This eventually leads to increase in

the ratio, $\frac{\epsilon_{int}}{\epsilon_{kin}}$ without having to tune the density or the scattering length. For prominent interaction energy, the system can only be described by the strongly coupled regime. This ratio is also important to observe a quantum phase transition from a superfluid to a Mott insulating state [46, 47].

1.2 Optical lattice potentials

The challenges in the understanding of a crystal lattice is as follows. Presence of Coulomb interactions among the electrons, the inevitable coupling of the electrons to the crystal lattice vibrations and disorder, impurities etc present in the crystal are the few causes behind the complexity of the real crystals. Thus it is really difficult to incorporate all these effects simultaneously and solve reliably such a complicated many-body system to a precision. To overcome this difficulty, Jacksh *et al*. [47] and Greiner *et al*. [48] have developed an alternative way, where strongly interacting systems can be studied with ultracold atomic gases by loading them into optical lattices. The typical lattice spacing of an optical lattice is about 1000 times larger than that of a real crystal. Optical lattices render a simplified way of experimental realization of various models of condensed matter theory. Thus by using one quantum system to study another, optical lattices enact Richard Feynman's pioneering idea of 'quantum simulation'. Theorists can check the validity of their models by using the results obtained from optical lattices, such as, investigating the phase diagram or time evolution of a physical phenomenon etc. Moreover, many factors, such as interatomic interaction strengths, brand structure, composition of spin and disorder levels can be easily controlled in optical lattice, which are otherwise impossible in real crystals.

Optical lattices are periodic potentials formed by superposition of two coherent counter propagating laser beams. This results into a standing wave with a periodic pattern of dark (minima) and bright bands (maxima). This periodic array of maxima and minima are separated by a distance that is of the order of the wavelength of incident laser beams which are typically of the order of few thousand Å, the lattice parameter in a crystal has values lowered by three orders of magnitude. Thus the optical lattice provides a hugely magnified view that facilitates understanding of the many-body phenomena better. With additional laser beams focused in a region from different directions, two- and three-dimensional optical lattices can also be fabricated.

Due to light-matter interactions, an electric dipole moment is induced in the ultracold

atoms thereby resulting into modification of their energy levels via AC Stark effect. Depending on the intensity of the incident laser beam, the ultracold atoms are either pulled towards the bright (hills) or the dark bands (valleys) and thereby creating a spatially dependent optical lattice potential. From several aspects, the ultracold atoms in optical lattices have resemblance with electrons in real crystals. However, in addition to already discussed facts, the optical lattices have many other advantages over the real crystal, such as, a defect and impurity free environment offered by these potentials. Also the easy controllability of the lattice properties by tuning the laser parameters enhances the advantage in dealing with them and understand the physical principles of the phenomena involved for example, the interaction between the ultracold atoms can be tuned by employing a magnetic field via Feshbach resonance. By changing the laser intensity, the depth of optical lattice can be controlled, by tuning the polarization of the laser beam, the orientation of the lattice can be changed, and finally by changing the laser configuration, different lattice geometries, such as, square, triangular, kagome and honeycomb can be realized. The bosonic atoms are much easier to work with in comparison to the fermions, as due to Pauli's as exclusion principle it is difficult to cool degenerate fermions owing to degeneracy pressure which is present even at absolute zero, $T = 0$.

Usually, whether a specific isotope of an atom is bosonic or fermionic in nature is decided by the number of constituents of the isotope, that is, protons, electrons and neutrons. When this number is even with an integer nuclear spin, the atom in question is a boson. Whereas if this number is odd along with a half-integer nuclear spin, the resulting atom is a fermion.

Generally, in experiments, Bose-Einstein condensate is first created and then gradually by ramping up the laser beams, the periodic lattice potentials are formed. Thus eventually the atoms reorder itself to adapt with the new environment. Nowadays, with many different species, such as, in case of bosons; Rubidium-87, Sodium-23, Potassium-40 and Cesium-133; and for fermions; Potassium-40, Lithium-6 and Strontium-87, optical lattice experiments are being carried out. In 1990 first batch of optical lattices came into the picture when the laser-cooling techniques were on the verge of it's development, as it increases the efficiency of optical cooling. It became popular with the creation of the first Bose-Einstein condensates. This way it was possible to investigate various quantum many-body phenomena, such as, superfluid-Mott insulator phase transition, Josephson junctions with optical lattice potentials. Let us briefly discuss the physics behind optical

lattices.

1.2.1 Dipole potentials

Let us discuss the physics of interaction between the atoms and the laser beam. Now the ultracold atom is illuminated with an electric field **E**, oscillating with a frequency ω, corresponding to the standing wave produced by the counter propagating laser beams of the form,

$$\mathbf{E}(\mathbf{r},t) = E(\mathbf{r})\, e^{-iwt}\hat{\mathbf{e}} \tag{1.10}$$

here $E(\mathbf{r})$ is the spatial part of the complex amplitude of the electric field that oscillates at a frequency ω. $\hat{\mathbf{e}}$ denotes the unit vector along the direction of polarization. This electric field induces an atomic dipole moment, oscillating with the same frequency ω and can be expressed as,

$$\mathbf{P}(\mathbf{r},t) = P(\mathbf{r})\, e^{-iwt}\hat{\mathbf{e}} \tag{1.11}$$

The complex amplitude, $P(\mathbf{r})$ of the dipole oscillator can be written in terms of $E(\mathbf{r})$ as,

$$P(\mathbf{r}) = \alpha(\omega)\, E(\mathbf{r}) \tag{1.12}$$

here $\alpha(\omega)$ is the complex polarizability and is a function of the laser frequency ω. $E(\mathbf{r})$ is the complex amplitude of the oscillating electric field of the laser beams. The resulting dipole potential due to the interaction between the induced dipole moment and the laser field is given as

$$V_{dp}(\mathbf{r}) = -\frac{1}{2}\langle \mathbf{P}(\mathbf{r},t).\mathbf{E}(\mathbf{r},t)\rangle = -\frac{1}{2\epsilon_0 c}\Re(\alpha)\, I(\mathbf{r}) \tag{1.13}$$

the angular bracket corresponds to the time averaging of the oscillatory term. The laser field intensity $I(\mathbf{r})$ is denoted as,

$$I(\mathbf{r}) = \frac{1}{2\epsilon_0 c}|E(\mathbf{r})|^2 \tag{1.14}$$

Thus in presence of the laser beam, the potential energy experienced by the atoms is proportional to the intensity of the beam and the real part of the polarizability. For a periodic intensity, I, there is an array of minima or maxima, rendering an environment that is equivalent to a lattice potential for the atoms. However spontaneous scattering

is proportional to the imaginary part of the polarizability. The scattering rate for the absorption of photons by the dipole is given as,

$$\Gamma_{sc}(\mathbf{r}) = -\frac{1}{\hbar\epsilon_0 c}\Im(\alpha)\, I(\mathbf{r}) \tag{1.15}$$

To confine the atoms in the optical lattice, the induced dipole potential, $V_{dp}(\mathbf{r})$ and the scattering rate, $\Gamma_{sc}(\mathbf{r})$ play pivotal roles.

Usually the polarizability, $\alpha(\omega)$ is a complex function of the driving frequency and also dependent on the electronic structure of the atoms and hence it requires a quantum explanation. Whereas, if the oscillating frequency, ω is far from the transition frequency of the atoms ω_0, it can be calculated with Lorentz's model of a classical damped oscillator [49]. The effective potential and the scattering rate assume the following forms,

$$V_{dp}(\mathbf{r}) = -\frac{3\pi c^2}{2\omega_0^3}\left[\frac{\Gamma}{\delta}\right] I(\mathbf{r}) \tag{1.16}$$

$$\Gamma_{sc}(\mathbf{r}) = \frac{3\pi c^2}{2\hbar\omega_0^3}\left[\frac{\Gamma}{\delta}\right]^2 I(\mathbf{r}) \tag{1.17}$$

here $\delta = \omega - \omega_0$ defines the detuning parameter corresponding to the atomic resonance, ω_0 denotes the resonance frequency of the classical oscillator model and Γ represents the on resonance damping rate. As a consequence of Eq.(1.16) and Eq.(1.17), the following are the important observations that can be drawn:

(i) The sign of optical dipole potential is dependent on the detuning parameter, δ of the laser beam. If $\delta > 0$; *blue detuning*, the potential is positive and the atoms are attracted towards the maximum intensity resulting into a repulsive potential. When $\delta < 0$; *red detuning*, the potential is negative and the atoms are localized in the minimum intensity region, thereby creating an attractive potential for the atoms.

(ii) The detuning for an optical dipole potential is dependent on the power of the laser beam and the maximum inelastic rate. So it is possible to create larger potential depths by minimizing the detuning of the laser beam, as dipole potential scales as $\sim \frac{I}{\delta}$. Whereas the inelastic scattering rate scales as $\sim \frac{I}{\delta^2}$. The scattering rate in terms of the detuning and the trap depth is given as,

$$\hbar\Gamma_{sc}(\mathbf{r}) = \frac{\Gamma}{\delta} V_{dp}(\mathbf{r}) \tag{1.18}$$

Thus, in order to minimize the scattering rate and achieve a reasonable potential depth, the intensity and the laser detuning should be as large as possible only constrained by the range of laser power.

The atomic polarizability can be calculated by a semi-classical model (detailed derivation can be found in [49]). Consider the atoms as a two level quantum system with ground state $|g\rangle$ and first excited state $|e\rangle$ separated by the energy $\hbar\omega_0$. In the case of very large detuning ($\Gamma_{sc} << \Gamma$), the damping rate is determined by the dipole matrix element denoted by,

$$\Gamma(\mathbf{r}) = \frac{\omega_0^3}{3\pi\epsilon_0\hbar c^3}\left|\langle e|\hat{\mu}|g\rangle\right|^2 \tag{1.19}$$

here $\hat{\mu} = -e\hat{\mathbf{r}}$ is the dipole operator. This approach is valid for small values of the detuning, $\delta << \omega_0$. As the intensity of laser field becomes very high, the excited state gets heavily populated and the validity of the classical treatment fails [49].

1.2.2 AC Stark effect

As the neutral atoms do not have an electric dipole moment, the interactions between the atoms and the electric field of the incident laser beams induces a dipole moment by means of AC stark effect [49, 50]. Basically AC stark effect is the phenomenon of splitting (shifting) of energy levels of atoms due to the presence of an external electric field and it is analogous to Zeemann effect. Let us consider a two level atom with ground state, $|g\rangle$ and excited state, $|e\rangle$ and illuminated with a far-detuned laser beam. The energy shift due to the interaction for non-degenerate states is given by,

$$\Delta\epsilon = \sum_{i\neq j}\frac{\left|\langle g|H_{int}|e\rangle\right|^2}{\epsilon_i - \epsilon_j}. \tag{1.20}$$

The interaction between the atom and the laser beam is described by the Hamiltonian, $H_{int} = -\hat{\mu}.\mathbf{E}$ ($\hat{\mu} = -e\mathbf{r}$ is electric dipole operator). $\mathbf{E}$ is laser field and ϵ_i are the energies of the atoms in presence of the laser field. For the unperturbed ground state, $|g\rangle$, the ground state energy is the sum of the internal energy of the atom and the energy of the laser field. As the atom absorbs a photon from the electric field, the total energy becomes,

$$\epsilon_j = n\hbar\omega_0 + (n-1)\hbar\omega = \hbar\delta_{ij} + n\hbar\omega \tag{1.21}$$

here $\delta_{ij} = \omega - \omega_0$ is the detuning parameter. Hence for a two level system, the energy shift due to atom-laser interaction is finally expressed as,

$$\delta\epsilon = \pm\frac{3\pi c^2}{2\omega_0^3}\frac{\Gamma}{\delta}I \tag{1.22}$$

The ± sign correspond to the ground and the excited sates respectively. This shift in energy is called as AC stark effect and is directly proportional to the intensity of the laser beam. Thus a spatially dependent laser beam can be used to create distinct intensity profile, that serves as a periodic array of potential wells in which atoms can be trapped in its ground state at a very low temperature. Similarly, perturbation theory can be expanded to multi-level systems, the detailed discussion can be found in [49].

1.2.3 Different geometries of optical lattices

Now we are going to discuss how a variety of lattice geometries for the trapping optical potential can be created by using different configurations of the laser beams and this provides a very powerful paradigm to simulate various condensed matter systems. By interfering two counter propagating laser beams, a periodic potential profile can be achieved. Different types of optical lattices can be created by employing various frequencies and orientations for each pair of the laser beams in one, two, or three dimensions. As an example, let us consider two counter-propagating laser beams with frequency, ω_L and wavelengths $\lambda_{1,2}$ corresponding to the wavevectors $k_{1,2}$. For linearly polarized beams, the resultant electric field in the x-direction can be expressed as,

$$\mathbf{E}(x) = E_0 \left[\hat{\mathbf{e}}_1 \, e^{i(k_1 x - \omega_L t)} + \hat{\mathbf{e}}_2 \, e^{-i(k_2 x - \omega_L t)}\right] \tag{1.23}$$

here $\hat{\mathbf{e}}_1$ and $\hat{\mathbf{e}}_2$ define the polarization vectors of the two laser beams. E_0 is the electric field amplitude. The field intensity, I can be evaluated as,

$$\begin{aligned} I \propto |E|^2 &= E_0^2 \left[\hat{\mathbf{e}}_1 \, e^{i(k_1 x - \omega_L t)} + \hat{\mathbf{e}}_2 \, e^{-i(k_2 x - \omega_L t)}\right] \left[\hat{\mathbf{e}}_1 \, e^{i(k_1 x - \omega_L t)} + \hat{\mathbf{e}}_2 \, e^{-i(k_2 x - \omega_L t)}\right]^* \\ &= 2E_0^2 \left[1 + \hat{\mathbf{e}}_1 . \hat{\mathbf{e}}_2 \cos(k_1 + k_2)x\right] \end{aligned} \tag{1.24}$$

Hence, the lattice potential, $V_{op} \propto I$ is effectively experienced by the confined atoms. The last term in Eq.(1.24) defines the interference between the two beams and when the polarization of the two beams become orthogonal, this term diminishes. Thus the time-averaged potential in the case of linearly polarized beams with same frequency, ω and wave vector, k is obtained as,

$$V_{op}(x) \propto E_0^2 \left[1 + 2\cos(2kx)\right] \tag{1.25}$$

Similarly, in higher dimensions, a periodic potential can be formed by interfering additional pairs of laser beams from different directions. Like for two sets of orthogonal

counter-propagating laser beams, the optical lattice potential assume the form,

$$V_{op}(x,y) \quad \propto \quad E_0^2\,[\cos^2(kx)+\cos^2(ky)+2\hat{\mathbf{e}}_1.\hat{\mathbf{e}}_2\,\cos\phi\,\cos(kx)\,\cos(ky)] \qquad (1.26)$$

here ϕ is the temporal variation of phase between the two sets of beams. $\hat{\mathbf{e}}_1$ and $\hat{\mathbf{e}}_2$ denote the polarization of the beams along x and y directions respectively. The interference term in Eq.(1.26) can be ignored by considering orthogonal polarization vectors and choosing slightly different wavelengths for the standing wave. Thus, by superimposing two or three mutually perpendicular standing waves from two sets of counter propagation laser beams with orthogonal polarizations, optical lattices in two and three dimensions respectively can be created. In the case of non-orthogonal polarization vectors with same laser frequencies, the beams interfere and leads to a variation the optical potential geometry depending on the relative phase of the beams, such as, a checker board kind of pattern. Again a simple square lattice can formed by by choosing orthogonal polarizations between the standing waves. Here the interference term destroys and this results into a potential which simply a summation of two superimposed 1D lattice potentials. Finally, a variety of optical lattices can be achieved by tuning the orientation and signs of the detuning parameter of the laser beams [51].

1.2.4 Atomic interactions via Feshbach Resonance

Interaction among the atoms is very pivotal in order to determine the many-body physics. Originally in solid state physics, the interaction between two particles is considered to be short ranged that arises from van der Waals force and can be described with Lenneard-Jones potential of the form, $U(r) = 4\epsilon\left[\left(\frac{\sigma}{r}\right)^{12} - \left(\frac{\sigma}{r}\right)^{6}\right]$, where ϵ is the depth of the well and σ denotes the distance at which the interparticle potential between the particles become zero or van der Waals radius and r is the distance between any two particles. For ultracold systems, at sufficiently low temperatures, the interaction between the cold atomic gases are short ranged and can be defined by s-wave scattering length a_s. In terms of short-range pseudo-potential, the two-body interaction can be expressed as,

$$U(r-r') \quad \approx \quad \frac{4\pi\hbar^2 a_s}{2M_r}\delta(r-r') \qquad (1.27)$$

M_r is the reduced mass and with the help of Feshbach resonance, the two-body scattering length, a_s can be tuned [52].

Now let us briefly discuss about the physical origin of Feshbach resonance. Feshbach resonance is the essential tool to tune interparticle interaction between the atoms in

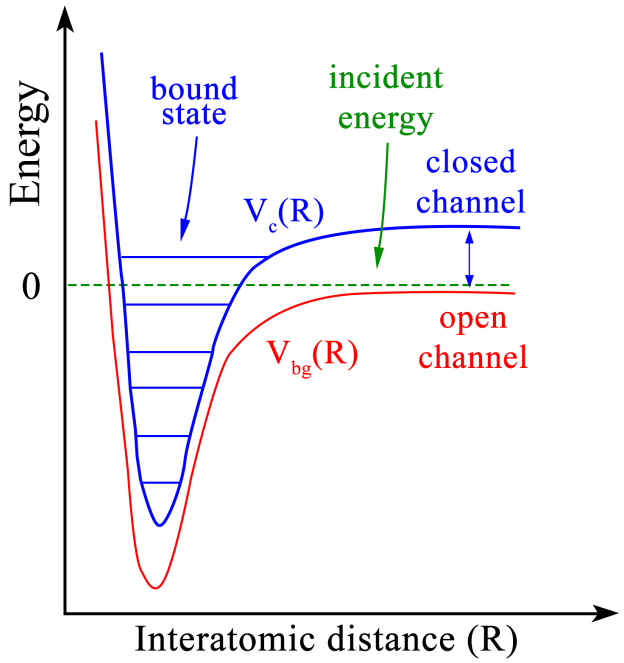

Figure 1.2: The two channel model for a Feshbach resonance is depicted. At very first atoms are prepared in the open channel that corresponds to the potential, $V_{bg}(R)$, subject to a collision at low incident energy. The phenomenon of collision occurs when the open channel is resonantly coupled to the closed channel, $V_c(R)$. A scattering resonance takes place when a bound state of the closed channel has an energy that approaches to zero. The closed channel's position can be manipulated with respect to the open one by tuning the magnetic field B.

ultracold gases. As shown in Fig.(1.2) (from reference [52]), the two molecular potential curves $V_{bg}(R)$ and $V_c(R)$ are considered here. In the case of large internuclear distance R, the two free atoms of the ultracold gas is asymptotically connected by the background potential, $V_{bg}(R)$. While for two-particle collision, with small energy E, $V_{bg}(R)$ denotes the energetically open channel, referred as, the *entrance channel*, while the other potential $V_c(R)$ favours the bound molecular states near the threshold of the open channel and hence is known as the *closed channel*. For two-particle collision, a Feshbach resonance appears when the bound molecular state in the closed channel energetically approaches the scattering state in the open channel [as shown in Fig.(1.2) from reference [52]]. In this situation, even weak coupling can render strong mixing between the two channels. Here the energy difference can be tuned via changing the magnetic field when the corresponding magnetic moment are different, thereby resulting into a magnetically tuned Feshbach resonance. This magnetically tuned method is the general way for achieving resonant coupling and has enormous applications [53]. For this magnetically tuned

Feshbach resonance, the s-wave scattering length a_s can be expressed in terms magnetic field B as,

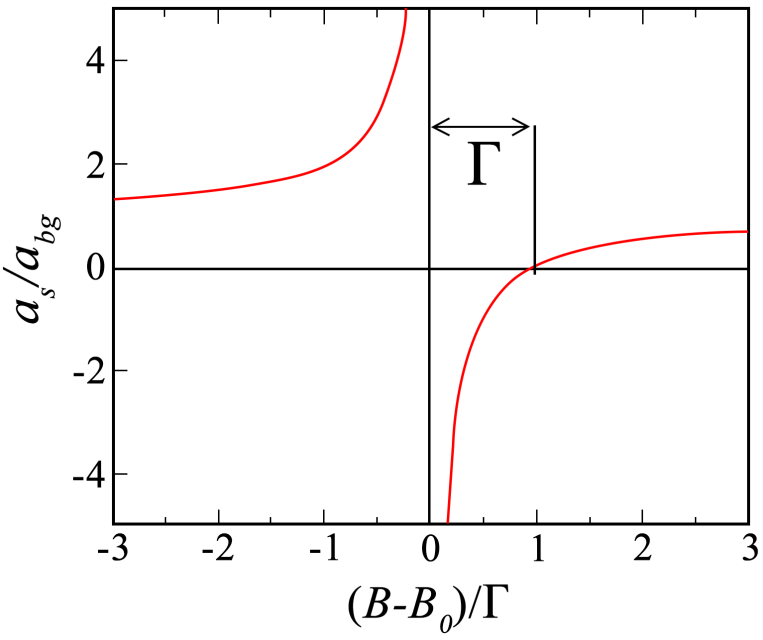

Figure 1.3: The behaviour of scattering length, a_s/a_{bg} as a function of magnetic field, B in a magnetically tuned Feshbach resonance is depicted in this diagram.

$$a_s(B) = a_{bg}\left(1-\frac{\Gamma}{B-B_0}\right) \tag{1.28}$$

here a_{bg} denotes to the background scattering length corresponding to the interaction potential of the open channel, $V_{bg}(R)$ and represents the off-resonant value. The parameter B_0 represents the resonance position where the scattering length diverges ($a \to \infty$) and the parameter Γ defines the resonance width [53]. Fig.(1.3) depicts a schematic plot for resonance expression Eq.(1.28). Notably, both a_{bg} and a_s can either be negative or positive, that means both attractive and repulsive interactions can be realized successfully. In an alternative way, a Feshbach resonance can also be achieved by tuning optically that renders to optical Feshbach resonances which is similar to the magnetically tuned one. Thus, the optical resonances are very promising in cases where magnetically tunable resonances are not available.

1.3 Theoretical methods for ultracold bosonic gas

The governing equation of ultracold, dilute, atomic gases of Bose-Einstein condensate is the interacting many-body Schrödinger equation. However, it is difficult to solve this equation even for a few number of bosons and hence approximations are very essential.

One of the most popular approximative method is the Gross-Pitaevskii theory, developed by Eugene P. Gross [38] and Lev P. Pitaevskii [39], independently in 1961 which made the study of the inhomogeneous, interacting condensates possible. The ansatz for many-body wave function in this approximation can be expressed as,

$$|\Psi(t)\rangle \quad = \quad |N;t\rangle. \tag{1.29}$$

Here the many-boson ansatz is estimated as a single time-dependent permanent in which all the N bosons occupy the only available state (orbital). Hence, coefficients $C_{\vec{n}}(t)$ are not used to determine the ansatz Eq.(1.29), as only a single permanent is in use. Following the approximation of consideration of only a single state, that is, the only available quantum state, is fully condensed at all times introduces a limitation in this theory. Though conceptually a condensate implies the fully condensed state, there are existence of other varieties of condensates, such as, fragmented condensates etc, where two or more available single-particle quantum states are populated by a large number of particles. Thus the phenomenon of fragmentation, which is otherwise important, cannot be described by Gross-Pitaevskii theory. Also the usage of one single-particle state (orbital) to describe a condensate prevents this theory from explaining correlations which intrinsically carry the signatures of multi-orbitals.

Another renown theoretical approximation to describe the trapped ultracold bosons is the Bose-Hubbard model [54, 55] derived by Gersch and Knollmann; which is a bosonic counterpart of the original model that was introduced by J. Hubbard in 1963 [56] that describes interacting electrons in lattices. Unlike Gross-Pitaevskii theory, here description of a fragmented condensate is possible with the Bose-Hubbard model, which assumes presence of a lattice (an optical lattice) very similar to a crystal lattice and the ultracold atoms are loaded in it. The bosons are allowed to move by means of a hopping energy from one lattice site to its nearest neighbour and in the same site, they interact via onsite Hubbard potential. Despite the simplicity of this model, it is capable of capturing various exotic quantum phenomena, such as, the strongly correlated Mott insulator and its quantum phase transition to a superfluid phase. It is a discrete lattice

model and thus very different from Gross-Pitaevskii approximation. The detailed of this theory is discussed in **Chapter 2**.

The existence of a substantial volume of literature on Bose-Einstein condensates, both from theoretical and experimental perspectives, are largely dependent on these two models. However, the detailed physics involved in a quantum many-body system is known to a limited extent, or at best known approximately.

1.4 Simulation techniques for ultracold bosonic gas

In recent years, an essentially exact, numerically efficient, multi-orbital and, many-body method has been developed which is known as the *multi-configurational time-dependent Hartree approach, MCTDH* [57–59]. The bosonic version of this method, developed very recently, is coined as the *multi-configurational time-dependent Hartree method for bosons, MCTDHB* [60–63]. Here we go beyond the methods discussed in the previous section; Gross-Pitaevskii and BHM and employ the optimized single-boson basis states determined by MCTDHB. The MCTDHB method variationally optimizes the basis state and the expansion coefficients in the basis state [60, 61] and hence its solutions do not assume any predetermined symmetry or shape of the described many-body state. There is no restriction of the number of orbitals, geometry, dimensionality, and interparticle interactions for the time-dependent many-boson problem in this formalism. This method is simply a systematic generalization of the (one-orbital) Gross-Pitaevskii mean-field theory. An open source version of the MCTDHB algorithm is implemented in the MCTDH-X software package, employed to simulate various problems in **Chapter 4**. The detail theory of this technique is discussed in the next chapter (**Chapter 2**).

There exists an another simulation technique termed as *Dynamical Mean-Field Theory, DMFT* and has vast applicability for the investigation of correlated many-body quantum systems in a lattice. The bosonic version of this technique is coined as *bosonic dynamical mean field theory, B-DMFT* that renders an inclusive, thermodynamically consistent approximation scheme for the investigation of correlated bosonic system in lattice [64]. In the limit of high spatial dimensions or coordination number of the lattice, the B-DMFT becomes exact in nature. The normal and condensed bosons are treated on equal weightage in this technique and hence it incorporates the effects originated by dynamic coupling. This technique regenerates all the previously explored limits in the parameter space, such as, Beliaev-Popov and Hartree-Fock-Bogoliubov

approximations and is simply the generalization of the already established mean-field theories of interacting bosons. The self consistency equations of this technique are the equations that corresponds to a bosonic single-impurity coupled to two reservoirs of bosons that are in the condensed and in the normal state respectively.

1.5 Intriguing features of ultracold bosons

The tunneling phenomenon gathered immense attention since the beginning of quantum theory due to dearth of classical correlative. The quantum tunneling transpires in every potential through classically allowed and also forbidden regions. In a potential, generally, a classically penetrable (energetically favoured) region is separated by a barrier from a classically impenetrable (energetically forbidden) region. However a quantum particle can easily cross the barrier and tunnel through the forbidden region even in absence of the sufficient energy, as its position is determined by a probability distribution which has non-zero value in the classically forbidden region. To get a clearer picture of the

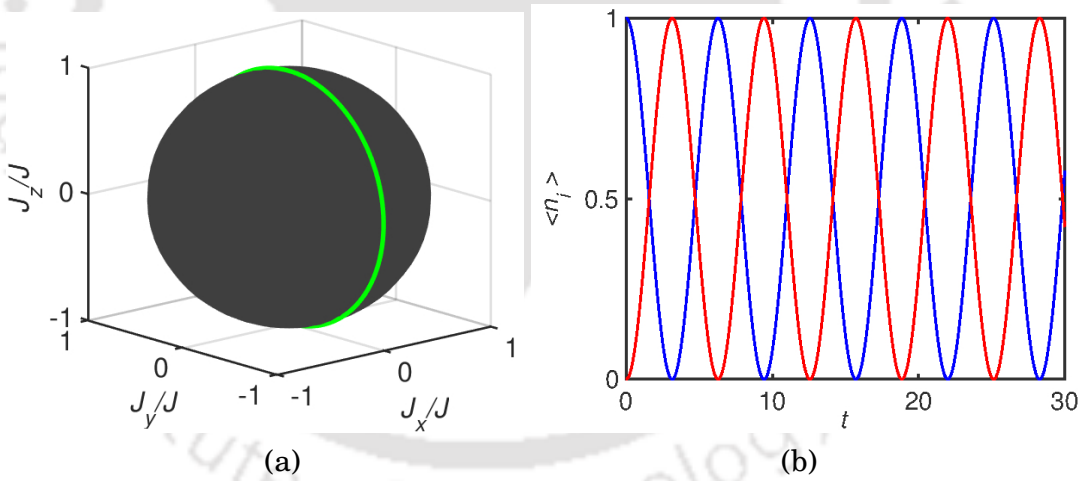

Figure 1.4: Tunneling dynamics of a system of bosons in a double well potential for noninteracting case. (a) shows the dynamics of the Bloch vectors, that is, J_x, J_y and J_z on the surface of a Bloch sphere of unit radius. (b) shows the dynamics of occupation densities, $< n_i >$ as a function of time.

above discussion, let us consider a system of bosons in a double well potential. The tunneling dynamics can also be studied by employing the Bloch vectors, that is, the component of angular momentum, J_i. For noninteracting case, that is, the *Rabi Regime*, the usual Rabi oscillations are observed. From Fig.1.4(a), it is observed that in *Rabi Regime*, the Bloch vector passes through the poles of the Bloch sphere. It may be noted

that the poles denote maximum population difference between the wells, because the z-component of the Bloch vectors, J_z values corresponding to the poles are $J_z = \pm 1$. Here J_z corresponds to the population imbalance between the two wells [details can be found in Eqs.(2.30) of **Chapter 2**]. Fig.1.4(b), included for comparison, shows the dynamics of the the expectation values of the occupation densities of the two wells. The occupation density oscillates between zero and unity as time progresses and will continue for larger time intervals. Thus during the course of motion, the particles execute a back and forth motion between the wells and hence signal tunneling independently between the wells. This independent tunneling for noninteracting regime is also known as Rabi oscillations.

Another intriguing feature of ultracold bosons is the quantum phase transition from superfluid (SF) to Mott insulating phase (MI) at zero temperature driven by the interplay between tunneling and on-site interaction between the bosons [47]. Fig.(1.5) shows phase

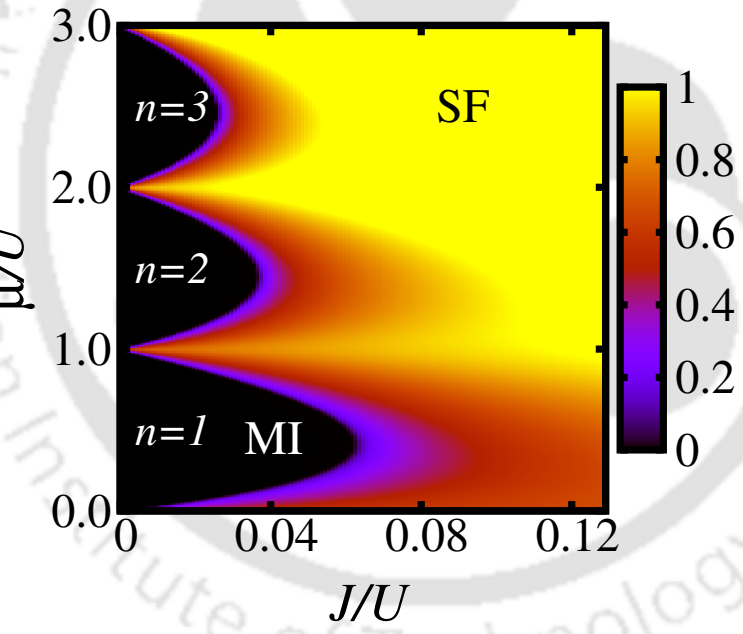

Figure 1.5: Phase diagram of the Mott-insulator to superfluid phase transition of ultracold bosons in optical lattices.

diagram of SF to MI phase transition of a systems bosons, generated by employing Bose-Hubbard model. Usually, the ground state of many boson system can be in two states. First is the superfluid state in which bosons are completely delocalized over the whole lattice due to overlapping of the wavefuntions of the system. Second one is the Mott-insulating state in which the number of bosons per lattice site, n is fixed and the system is completely localized. The driving source for this phase transition is the ratio of

tunneling energy, J and onsite interaction, U and this ratio, J/U can be manipulated via lattice depth and hence in experiments the transition can be realized by tuning the laser intensity [47]. Therefore, the most favourable phase of the system is determined by the values of J/U and the chemical potential, μ/U, that fixes the the total number bosons. For small values of J/U which corresponds to deep lattice depths, the bosons are in a Mott-insulating state with a constant number of bosons per site, n as clear from Fig.(1.5). However, for high J/U values, that is, for shallow lattice depths, the system remains in superfluid phase [Fig.(1.5)], with fixed, n.

1.6 Motivation and Overview of the Thesis

The possibility of tunneling of particles through a classically impenetrable barrier is a famous quantum mechanics problem [65–67]. The inclusion of interaction between the particles may help or hinder the tunneling phenomena. Thus the time resolved tunneling probability may demonstrate interesting effects pertaining to the roles of the interaction parameters and the initial configuration of the particles. The confinement of a system of few correlated bosons in a double well trap is a paradigmatic model to study these effects. A range of fundamental quantum phenomena corresponding to the tunneling dynamics of the particles, such as, suppression of the tunneling probabilities, and thereby trapping them in one of the wells etc, can be studied in this model. Occurrence of such trapping phenomena are experimentally realized with a Bose-Einstein condensate as reported in [68, 69]. In recent times, these studies involving a few bosons have turned out to be more relevant after the successful experimental realization of 'boson sampling' [67, 70]; where a small number of bosons were involved for experimental demonstration to achieve remarkable control of multiphoton interferences in large interferometers. The dynamics of Fock states for a two-site Bose-Hubbard model (BHM) (without the density exchange term) with a few bosons has been investigated and the time evolution of tunneling probabilities are computed in [71, 72]. However, there exist, among other things, lack of a detailed analysis of quantum dynamics in strong and weak coupling regimes and the sensitivity of the time evolved state to a variety of initial conditions.

Also the ultracold atoms in a periodically shaken optical lattice, that is, periodically driven systems, have garnered immense attention following the exhibition of exotic behaviour of periodically driven systems, such as, the display of the transition from integrability to chaotic features in certain limits [73, 74], and dynamical Anderson

localization [73, 75], dynamical stabilization both in classical and quantum mechanics, coherent control of phase transition from superfluid to Mott insulator [76], and parameter-controlled adiabatic transformation of a static Bose-Einstein condensate (BEC) into a dynamical Floquet condensate [77] etc. The experimental realization of these driven systems lead to induce many-body localization [78, 79] and other intriguing quantum phenomena.

Nowadays direct imaging of quantum many-body correlations is possible, such as, detection of one-, two-, and even many-body correlation have already been reported [80–82] due to the impressive degree of experimental controllability of the ultracold atoms in optical lattices. To understand such many-body physics of interacting ultracold atoms, it is important to first approach and analyze their (few-body) building blocks [83–86]. While some of these many-body aspects have been already analyzed [87, 88], a scheme to control the emergent correlations still needs to be approached.

In recent times, successful creation of artificial gauge fields in continuum [89] and in lattice [90, 91] pioneered, as well as have elevated the way for the study of the physics of charged particles with neutral atoms. These developments lead to the experimental investigation of various rich quantum phenomena, such as, topological properties [92–94], quantum Hall states [95], Hofstadter's fractal energy spectrum [90, 91], and supersolid like states in non-Abelian fields [96, 97]. The above list is of course not exhaustive.

Motivated by the findings discussed above, in this thesis we investigate various interesting features regarding the properties of the ground state and time evolution of interacting bosons in a variety of optical potentials. In the following, we report a more detailed plan of the thesis by including a brief description of the several problems that have been addressed in the form of different chapters of the thesis. The thesis is divided into two parts depending mainly on the methodologies used therein. In this thesis, we have employed two different formalisms to study properties and phase diagrams of interacting bosons in an optical potential. They are, namely, the familiar *Bose-Hubbard Model, BHM*, which is a discrete lattice model that incorporates the interparticle interaction to be solely of the density-density type. The equation of motion can be solved exactly in the Fock basis rendering the tunneling dynamics, whereas the phase properties are usually computed using standard site decoupling mean field theory. Second, a *multi-configurational time-dependent Hartree approach for bosons, MCTDHB* is employed, which is a continuum simulation approach to tackle static and dynamic properties, such as, fragmentation and condensation of particles in presence of contact and non-contact

interactions. There are a total of six chapters in this thesis. We move forward with a brief description on the content of each one of the chapters as in the following.

Chapter 2 deals with a brief discussion of the formalism of Bose-Hubbard model (BHM) and a detailed elaboration of the multi-configurational time-dependent Hartree approach for bosons (MCTDHB). A two-site Bose-Hubbard model (BHM) is a simplest candidate to investigate various phases and the dynamics of the correlated bosonic atoms in a double-well potential or a bosonic junction, such as, triple well. In this thesis, we have considered a few variants of the Bose-Hubbard model. We also discuss in detail on the multi-configurational time-dependent Hartree approach for bosons (MCTDHB) (implemented via the MCTDH-X software package).

In **Chapter 3**, we have employed variants of Bose-Hubbard model (BHM) to study the tunneling dynamics and various phases of the correlated bosons under three different situations, namely, the tunneling dynamics of bosons in a double well potential, a periodically driven system and a time-dependent synthetic gauge field. We devide them into three sections and present them in the following.

In Sec. 3.1, we investigate the quantum dynamics of a few bosons in a double well potential using Bose-Hubbard model. In particular, we study the dependencies of tunneling probabilities in presence of strong and weak on-site interaction potentials, and in addition, we have considered the effect of nearest neighbour density-density interaction term therein. The tunneling probabilities of the bosons show distinctive features including sensitivity of the dynamics to a variety of initial conditions, such that the final configuration of the system crucially depends on the initial state of the system in which it is prepared. We also include a brief discussion on the effects of admixture of initial states on the tunneling probabilities. Finally, we have extended the above scenario to a triple well potential. We briefly report on the results corresponding to the triple well case where the dynamics, unlike the double well, show very little sensitivity to initial conditions.

Next in Sec. 3.2, we include the effect of an external time-dependent driving on the tunneling dynamics of interacting bosons confined in a double well potential [74]. Here we consider a system of bosons interacting via a harmonically driven interaction potential. In particular we have considered the case of harmonic driving, wherein, at large values of the amplitude and the phase of the periodic driving, there is onset of chaotic features in the tunneling dynamics. We explore distinct routes to this chaotic dynamics by independently tuning the amplitude and the phase of the driving potential.

Further, we superpose a chirped signal on the periodic driving and investigate whether it aids or hinders the emergence and proliferation of chaos. It is observed that, in fact, a chirp modulation restores order in the tunneling dynamics of the system.

In the Sec. 3.3, we explore a system of interacting bosons in presence of a time dependent synthetic gauge field using a mean-field approach. In particular, we explore the time-dependence of the form t^{α} , where we have considered three distinct values of α, namely, $\alpha = 0.5, 1, 2$. Here we compute the phase diagram demonstrating a superfluid-Mott insulator phase transition of bosons in presence of the gauge field and hence make comments on the stabilization of the Mott insulating lobes in the phase diagram. We further study the effect of time-dependent gauge fields on the energy spectrum of the system.

In **Chapter 4**, we employ our second formalism and study the phases and dynamics of correlated bosons via MCTDHB approach again under three different scenarios as elaborated in the following.

In Sec. 4.1, we simulate an experimental scenario where as if the 'charged' bosons are placed in a constant electric field, thereby inducing a tilt in the system and investigate the ground state properties of such a system in a tilted triple-well potential. Inclusion of the tilt certainly broadens the number of control parameters and enriches the emergent phenomena. Here the many-body state is characterized by the eigenvalues of the reduced one-body density matrix (RDM). To get a spatially resolved picture of the emergent correlations, we also compute the Glauber correlation functions from RDM. We investigate the interplay between the interparticle interaction and the tilt of the trapping potential, and how it can be employed to manipulate correlations and the phenomenon of fragmentation using RDM.

Hence in Sec. 4.2, we investigate the tunneling dynamics of interacting bosons confined in a temporally driven tilted double well potential that imitates a quantum seesaw. Here the quantum seesaw is modeled by considering a driven double-well potential with a driving protocol of temporally varying tilt of harmonic nature with a constant frequency. This study establishes the fact that by tuning the temporal evolution of the quantum seesaw, a precise control on the temporal evolution of the occupation density in the natural orbitals of the system can be achieved. Finally, we also demonstrate from the dynamics of the population imbalance between the wells that how one can manipulate the noise present in the system. As the harmonic modulation of the seesaw potential is achievable experimentally, our simulations can be realized in laboratories dealing with

cold atomic gases.

Finally, in Sec. 4.3, we simulate a scenario where a system of few bosons confined in a two-dimensional harmonic trap is subjected to a synthetic gauge field. Here we investigate the effect of the gauge field on the temporal evolution of the natural occupations as well as the natural orbitals of the system, that is, by evaluating the eigenvalues and eigenvectors of one-body reduced density matrices, RDM.

In **Chapter 5**, we undertake a discussion which emphasized on the the importance of the Multiconfigurational time-dependent Hartree approach for bosons, MCTDHB, as how the optimized basis state that involves in MCTDHB is more accurate in certain situations. Finally, possible implementation of the long range interaction between the bosons, which in true sense can not be achieved in a BHM, has been discussed to explore various ground state properties.

Finally, in **Chapter 6**, we conclude by stating the key results of the thesis where we provide a summary of the major findings of the research work carried out. We also briefly discuss the outline on the scope of future studies based on this research work.

CHAPTER 2

FORMALISMS USED IN THE STUDY

This chapter presents an overview of the two formalisms that have been employed to address the problem of solving the time-dependent Schrödinger equation for a system of many bosons in various environments, namely, Bose-Hubbard model, *BHM* and multiconfigurational time-dependent Hartree approach for bosons, *MCTDHB*. For completeness, we are also going to briefly introduce some basic theoretical concepts used in these two formalisms.

2.1 Second Quantization

Now we are going to briefly discuss the formalism of second quantized notations and the Fock state representation of a state with N bosons. The spin-statistics theorem renders that the wave function $\Psi(\mathbf{r}_1,...,\mathbf{r}_N)$ corresponding to a system of N-bosons is a fully symmetrized N-particle state, that is, [98, 99]

$$\Psi(...,\mathbf{r}_i,...,\mathbf{r}_j,...) = +\Psi(...,\mathbf{r}_j,...,\mathbf{r}_i,...) \tag{2.1}$$

The above state can be obtained by employing a Fock basis state (number basis) of the N-particle Hilbert space $\mathscr{H}^{(N)}$ corresponding to the the wave function Ψ in the second quantized notations. The Fock basis takes into account of the above mentioned symmetrization principle and also the commutation relations for identical bosons as discussed in the following.

A Fock basis state for a complete orthonormal set of single-particle states (orbitals) $\{\phi_i\}$; where $i = 1,...,\infty$, is expressed as,

$$|n_1, n_2, ..\rangle = \prod_i \left[\frac{1}{n_i!}\left(\hat{a}_i^\dagger\right)^{n_i}\right]|0\rangle \tag{2.2}$$

here $\{n_i\}$ are integers and denote the occupation numbers of the individual states and $|0\rangle$ defines the vacuum state where no particle is present. $\hat{a}_i^\dagger[\hat{a}_i]$ corresponds to the creation [annihilation] operator that creates [annihilates] a boson in the state ϕ_i. The application of these operators on a Fock basis state imply,

$$\begin{aligned}\hat{a}_i|n_1,...,n_i,...\rangle &= \sqrt{n_i}\,|n_1,...,n_i-1,...\rangle \\ \hat{a}_i^\dagger|n_1,...,n_i,...\rangle &= \sqrt{n_i+1}\,|n_1,...,n_i+1,...\rangle\end{aligned} \tag{2.3}$$

where the number operator, n_i for any single-particle state, ϕ_i is given as,

$$\hat{n}_i = \hat{a}_i^\dagger \hat{a}_i \tag{2.4}$$

The occupation numbers of the states in terms of total number of particle, N for a system of constant number of bosons read as,

$$N = \sum_i n_i \tag{2.5}$$

The creation [annihilation] operators obey the usual bosonic commutation relations,

$$\left[\hat{a}_i, \hat{a}_j\right] = 0; \qquad \left[\hat{a}_i^\dagger, \hat{a}_j^\dagger\right] = 0; \qquad \left[\hat{a}_i, \hat{a}_j^\dagger\right] = \delta_{ij} \tag{2.6}$$

The bosonic field operator, $\hat{\Psi}(\mathbf{r},t)$ that creates [annihilates] a boson in the state $|\mathbf{r}\rangle$ in terms of creation [annihilation] operators of bosons of Eq.(2.3) is denoted by,

$$\begin{aligned}\hat{\Psi}^\dagger(\mathbf{r},t) &= \sum_i \hat{a}_i^\dagger(t)\,\phi_i^*(\mathbf{r},t) \\ \hat{\Psi}(\mathbf{r},t) &= \sum_i \hat{a}_i(t)\,\phi_i(\mathbf{r},t)\end{aligned} \tag{2.7}$$

here the creation [annihilation] operators alongwith the single-boson states are in general time-dependent and the single-boson states, $\phi_i(\mathbf{r},t)$ are orthonormal at all times, that is,

$$\langle\phi_i|\phi_j\rangle = \delta_{ij} \quad \forall\ t \tag{2.8}$$

Further $\hat{a}_i^\dagger$ $[\hat{a}_i]$ in terms of these field operators can be written as,

$$\hat{a}_i^\dagger = \int \phi_i(\mathbf{r},t)\,\hat{\Psi}^\dagger(\mathbf{r},t)\,d\mathbf{r}, \qquad \hat{a}_i = \int \phi_i^*(\mathbf{r},t)\,\hat{\Psi}(\mathbf{r},t)\,d\mathbf{r} \tag{2.9}$$

The field operators, $\hat{\Psi}(\mathbf{r})$, satisfy the usual bosonic commutation relations, that is,

$$\left[\hat{\Psi}(\mathbf{r}),\hat{\Psi}(\mathbf{r}')\right] = 0; \qquad \left[\hat{\Psi}^{\dagger}(\mathbf{r}),\hat{\Psi}^{\dagger}(\mathbf{r}')\right] = 0; \qquad \left[\hat{\Psi}(\mathbf{r}),\hat{\Psi}^{\dagger}(\mathbf{r}')\right] = \delta(\mathbf{r}-\mathbf{r}') \quad (2.10)$$

Thus the density operator in terms of field operators is expressed as,

$$\hat{\rho}(\mathbf{r}) = \hat{\Psi}^{\dagger}(\mathbf{r})\hat{\Psi}(\mathbf{r}) \quad (2.11)$$

with the number operator of bosons satisfying,

$$\hat{N} = \int \hat{\rho}(\mathbf{r})\, d\mathbf{r} \quad (2.12)$$

2.2 Bose-Hubbard Model (BHM)

The bosons in optical lattices are in general correlated. Hubbard models which are very widely used can be successfully employed to describe intriguing quantum phenomena displayed by these strongly correlated systems, such as, the phase transition from a superfluid (SF) to a Mott-Insulator (MI) phase etc. In this quantum phase transition, the SF phase is described by a non-zero SF order parameter and finite compressibility. Although, in this framework several approximations are necessary, namely, the exclusion of inter-site interactions and tunneling to distant neighbours (lattice sites) followed by the limitation to the lowest available single-particle band etc. In the following, the bosonic version of the Hubbard model, that is, Bose-Hubbard model will be discussed briefly.

For interacting bosons confined in an optical lattice potential, the scattering of bosons can be described by a delta function shaped pseudo-potential such as,

$$V_{int}(\mathbf{r}) = \frac{4\pi\hbar^2 a_s}{2m_r}\,\delta(\mathbf{r}) \quad (2.13)$$

here a_s is the s-wave scattering length and m_r is the reduced mass of the scattered bosons. This approximation signifies that the bosons can interact only when they are at the same site. Thus for an interacting bosonic gas, the Bose-Hubbard Hamiltonian (BHH) in the second quantization is expressed as,

$$\begin{aligned}\hat{H}_{BHH} &= \int d^3\mathbf{r}\ \hat{\Psi}^{\dagger}(\mathbf{r})\left(\frac{\hat{\mathbf{P}}^2}{2m} + V_0(\mathbf{r}) + V_T(\mathbf{r})\right)\hat{\Psi}(\mathbf{r}) \\ &\quad + \frac{1}{2}\,\frac{4\pi a_s\hbar^2}{m}\int d^3\mathbf{r}\ \hat{\Psi}^{\dagger}(\mathbf{r})\hat{\Psi}^{\dagger}(\mathbf{r})\hat{\Psi}(\mathbf{r})\hat{\Psi}(\mathbf{r}) \end{aligned} \quad (2.14)$$

Here $\hat{\Psi}^{\dagger}(\mathbf{r})$ [$\hat{\Psi}(\mathbf{r})$] are the bosonic field operators that create [annihilate] bosons at the positions $\mathbf{r}$. Here the bosons are held together by a trapping potential V_T along with an optical potential, that later being considered as a periodic potential of the form $V_0(\mathbf{r}) = \sum_i V_{i0} \sin kr_i$, thereby confining them into individual lattice sites.

To describe a boson which is trapped in a specific lattice site, Wannier functions are very useful parameters. For a specific lattice site i, the Wannier functions are defined as,

$$w^{\alpha}(\mathbf{r}-\mathbf{r}_i) = \frac{1}{\sqrt{N}} \sum_q e^{-i\mathbf{q}.\mathbf{r}_i} \phi^{\alpha}_{\mathbf{q}}(\mathbf{r}) \tag{2.15}$$

here $\mathbf{r}_i$ corresponds to the center of the respective lattice sites and N is the total number of sites along a particular direction. α denotes the band indices for the complete set, that is, $\alpha = (\alpha_x, \alpha_y, \alpha_z)$, termed as orbital. q denotes the momenta. Here the sign of the Bloch functions, $\phi(\mathbf{r})$ is considered in such a way that these are positive at $q = 0$ for even bands and have positive slope at $q = 0$ for odd bands, leads to the localization of Wannier functions at a specific lattice site. These functions form a complete orthonormal set and that leads to the following transformation,

$$\phi^{\alpha}_q(\mathbf{r}) = \frac{1}{\sqrt{N}} \sum_i e^{i\mathbf{q}.\mathbf{r}_i} w^{\alpha}(\mathbf{r}-\mathbf{r}_i) \tag{2.16}$$

Now the bosonic field operators, $\hat{\Psi}(\mathbf{r})$ can be expanded in site localized basis of Wannier functions in the ground state as [100],

$$\hat{\Psi}(\mathbf{r}) = \sum_i w(\mathbf{r}-\mathbf{r}_i)\hat{a}_i \tag{2.17}$$

where the operator $\hat{a}_i$ annihilates a boson on site i and $w(\mathbf{r}-\mathbf{r}_i)$ represents the Wannier functions which are linear combinations of Bloch waves and are localized at a certain lattice site $\mathbf{r}_i$ for the lowest band (orbital), $\alpha = (0,0,0)$.

Thus by considering only the lowest available band, Eq.(2.14) reduces to [46, 47],

$$\hat{H}_{BHH} = -J \sum_{\langle i,j \rangle} \hat{a}^{\dagger}_i \hat{a}_j + \frac{U}{2} \sum_i \hat{n}_i(\hat{n}_i - 1) + \sum_i (\epsilon_i - \mu)\hat{n}_i \tag{2.18}$$

The angular bracket corresponds to the fact that i and j are nearest neighbouring sites, $a^{\dagger}_i$ [a_i] creates [annihilates] a boson on site i and $\hat{n}_i = \hat{a}^{\dagger}_i \hat{a}_i$ is the local number density operator for bosons and μ controls the number of bosons in the system.

Here the first term is the kinetic energy that describes the strength of the hopping, J, between the neighbouring sites and can be expressed as,

$$J = -\int d^3\mathbf{r}\, w^*(\mathbf{r}-\mathbf{r}_i) \left[-\frac{\hbar^2}{2m}\nabla^2 + V_0(\mathbf{r}) \right] w(\mathbf{r}-\mathbf{r}_i) \tag{2.19}$$

The second term determines the onsite interaction energy between the bosons at a site i with a strength U and is given as,

$$U = \frac{4\pi a_s \hbar^2}{m} \int d^3\mathbf{r}\, |w(\mathbf{r})|^4 \tag{2.20}$$

In the last term, chemical potential energy, μ tunes the number of particles of the system and ϵ_i is the random onsite energy that can be used to model disorder via,

$$\epsilon_i = \int d\mathbf{r}\, V_T(\mathbf{r}_i)\, |w(\mathbf{r}-\mathbf{r}_i)|^2 \tag{2.21}$$

For the limit of validation of single band approximation, where $V_0 \gg E_r$ with E_r as the recoil energy, the hopping parameter J can be obtained as, [41]

$$J = \frac{4}{\sqrt{\pi}} E_r \left(\frac{V_0}{E_r}\right)^{\frac{3}{4}} e^{-2\sqrt{\frac{V_o}{E_r}}} \tag{2.22}$$

and the onsite interaction parameter, U in terms of V_0 and E_r can be expressed as,

$$U = \frac{8}{\sqrt{\pi}} E_r\, k\, a_s \left(\frac{V_0}{E_r}\right)^{\frac{3}{4}} \tag{2.23}$$

here k being the wave vector of the laser field.

This establishes the connection between the ultracold atoms in optical lattices and the BHM. This connection eventually leads to the experimental realization of the signature of SF-MI quantum phase transition by Greiner *et al.* in 2002 in a gaseous vapor of ultracold Rb atoms that was confined in a three dimensional optical lattice [48]. This follows the realization of SF-MI phase transition in 1D [101] and 2D later on [102]. Henceforth, the theoretical studies of cold atomic gases have vastly expanded.

In recent times, experiments with ultracold Chromium atoms, Cr [103] reveal that an extension to the BHM is experimentally relevant. Cr atom has a large dipole moment which leads to long range dipolar interactions unlike alkali atoms that have been mostly used in optical lattice experiments. Thus Cr atom is an ideal candidate to explore the phase diagram of the BHM with long range interactions, known as the extended Bose Hubbard model (EBHM). Inclusion of an inter-site potential term, $V\sum_{\langle ij\rangle} n_i n_j$ in the Hamiltonian in Eq.(2.18) corresponds to the interaction between nearest neighbours in the BHM. This term is known as the density-density interaction between particles at different sites. A substantial volume of literatures exist that analyze the possibility of different exotic phenomena using the EBHM [104, 105].

To study BHM, the methods that are being opted have enclosed a variety of approaches, such as, exact diagonalization (ED) [106, 107], mean field theory [108–113], Quantum Monte Carlo techniques [114, 115] etc.

In the subsequent subsections, we are going to briefly discuss about the methods that are employed to solve various problems of this thesis. First, we are going to discuss the simplest candidate to solve BHM exactly, namely the exact dynamics which is an exact analysis of the dynamics of bosons. However this method is restricted to smaller systems as the size of the Hilbert space becomes enormously large with increase in the system size.

Further to explore the ground state properties of the BHM mean field technique (MFT) is employed where MFT can minimize the complexity of the problem via site decoupling scheme. This method based on the decoupling of the hopping term in the Hamiltonian is able to capture the physics behind SF-MI phase transition. Sheshadri *et al*. [108] first proposed this method to explore a homogeneous system. Later on, it was extended to the inhomogeneous systems [113, 116]. This method is similar to Gutzwiller method that was first introduced to solve Hubbard model for fermions and later extended to bosons [47, 110].

Also the Bogoliubov approximation is one of these decoupling scheme where interaction term in the Hamiltonian is decoupled, whereas this approach is unable to explain the SF-MI phase transition. However it is very useful for explaining the condensate properties in the weak interaction regime.

It is important to note that we have only used the following methods in this thesis to solve the BHM that are simple yet efficient. However, for completeness, a brief note on a few other methods are mentioned above.

2.2.1 Exact Dynamics

Here we briefly discuss about the exact dynamics that have been employed to explore the dynamical evolution of the Fock space for the Bose Hubbard model (BHM) with a few bosons. In a two-mode BHM, in order to obtain the tunneling dynamics, the state vector of the system is expanded in the Fock bases for a fixed number of bosons, N confined in a double well potential and is given as [117],

$$|\Psi(t)\rangle = \sum_{l=0}^{N} \frac{c_l(t)}{\sqrt{l!(N-l)!}} \hat{a}_1^{\dagger l} \hat{a}_2^{\dagger N-l} |0\rangle \tag{2.24}$$

here out of N bosons $(N-l)$ are in the right well and l are in the left. $c_l(t)$s are the complex coefficients. To obtain the dynamics, the following equations of motion (EOM) are needed to be solved,

$$i\hbar\frac{d|\Psi(t)\rangle}{dt} = \hat{H}_{BHH}|\Psi(t)\rangle \tag{2.25}$$

where $\hat{H}_{BHH}$ is the BH Hamiltonian (BHH) for a system of N interacting bosons occupying the weakly coupled low lying energy states of a symmetric double well potential and is given as,

$$\hat{H}_{BHH} = -J\left(\hat{a}_1^\dagger\hat{a}_2+\hat{a}_2^\dagger\hat{a}_1\right)+\frac{U}{2}\left(\hat{a}_1^{\dagger 2}\hat{a}_1^2+\hat{a}_2^{\dagger 2}\hat{a}_2^2\right) \tag{2.26}$$

The EOM in terms of the the coefficients $c_l(t)$ is expressed as,

$$i\frac{dc_l(t)}{dt} = -k_l c_{l+1}-k_{l-1}c_{l-1}+a_l c_l \tag{2.27}$$

here $k_l = J\sqrt{(l+1)(N-l)}$ and $a_l = \frac{U}{2}\left[l^2+(N-l)^2-N\right]$.

For example, in a system of two bosons ($N=2$), the Eq.(2.27) reduces to,

$$i\frac{d}{dt}\begin{pmatrix} c_0 \\ c_1 \\ c_2 \end{pmatrix} = \begin{pmatrix} U & -\sqrt{2}J & 0 \\ -\sqrt{2}J & 0 & -\sqrt{2}J \\ 0 & -\sqrt{2}J & U \end{pmatrix}\begin{pmatrix} c_0 \\ c_1 \\ c_2 \end{pmatrix} \tag{2.28}$$

Hence the dynamics can be obtained by solving these coupled EOMs. However as mentioned earlier, performing the exact calculation for larger number of particles is cumbersome and computationally demanding, thus we keep our discussion to a smaller number of bosons ($N\sim 20$) with this method.

2.2.2 Dynamics using EQMs for SU(2) generators

In Schwinger representation, the SU(2) generators, that is, the angular momentum operators, can be introduced in the following way,

$$\left(\hat{L}_k\right)_{ij} = \frac{\hbar}{2}\left(\sigma_k\right)_{ij}\hat{a}_i^\dagger\hat{a}_j \tag{2.29}$$

here $\{(\sigma_k\}$ are Pauli spin matrices. The components of angular momentum operators are finally expressed as,

$$\begin{aligned}\hat{L}_x &= \frac{1}{2}(\hat{a}_1^\dagger\hat{a}_2+\hat{a}_2^\dagger\hat{a}_1)\\ \hat{L}_y &= \frac{1}{2i}(\hat{a}_1^\dagger\hat{a}_2-\hat{a}_2^\dagger\hat{a}_1)\\ \hat{L}_z &= \frac{1}{2}(\hat{a}_1^\dagger\hat{a}_1-\hat{a}_2^\dagger\hat{a}_2)\end{aligned} \tag{2.30}$$

These operators, $\hat{L}_i$ obey the usual commutation relations, $[\hat{L}_i, \hat{L}_j] = i\hat{L}_k$ ($\hbar = 1$). With these SU(2) generators the usual two-site (double well) BHH can be written as,

$$\hat{H} = \frac{\epsilon}{2}(\hat{a}_1^\dagger \hat{a}_2 + \hat{a}_2^\dagger \hat{a}_1) + \frac{\gamma}{2}(\hat{a}_1^\dagger \hat{a}_1 - \hat{a}_2^\dagger \hat{a}_2) - \frac{c}{4}(\hat{a}_1^\dagger \hat{a}_1 - \hat{a}_2^\dagger \hat{a}_2)^2 \tag{2.31}$$

here ϵ is the coupling between the modes (i.e. hopping parameter and $\epsilon < 0$ here), γ is the energy difference between the quantum states and c is the onsite interaction term, reduces to the following form,

$$\hat{H} = \epsilon \hat{L}_x + \gamma \hat{L}_z - c\hat{L}_z^2 \tag{2.32}$$

The z-component, that is $\hat{L}_z$ denotes the difference in population density between the two wells.

The analogy between Eqs.(2.31) and (2.32) can be made clearer with the help of an eigenstate, $|\chi_n\rangle$ which denotes n particles in the first well with $(N-n)$ in the second. The operators L_x, L_y and L_z are defined by their action on $|\chi_n\rangle$ which are stated here for the sake of completeness as,

$$\begin{aligned}
L_x^2|\chi_n\rangle &= \frac{1}{4}[\sqrt{(n+1)(n+2)(N-n)(N-n-1)}|\chi_{n+2}\rangle \\
&\quad +(n(N-n+1)+(n+1)(N-n))|\chi_n\rangle \\
&\quad +\sqrt{n(n-1)(N-n+1)(N-n+2)}|\chi_{n-2}\rangle] \\
L_y^2|\chi_n\rangle &= \frac{1}{4}[-\sqrt{(n+1)(n+2)(N-n)(N-n-1)}|\chi_{n+2}\rangle \\
&\quad +(n(N-n+1)+(n+1)(N-n))|\chi_n\rangle \\
&\quad -\sqrt{n(n-1)(N-n+1)(N-n+2)}|\chi_{n-2}\rangle] \\
L_z^2|\chi_n\rangle &= \frac{1}{4}[n^2 - 2n(N-n) + (N-n)^2]|\chi_n\rangle
\end{aligned} \tag{2.33}$$

Thus for the total angular momentum, $\mathbf{L}^2 (= {L_x}^2 + {L_y}^2 + {L_z}^2)$, one can write,

$$\mathbf{L}^2|\chi_n\rangle = \frac{N}{2}\left(\frac{N}{2}+1\right)|\chi_n\rangle \tag{2.34}$$

Comparing with the eigenvalue $l(l+1)$ for $\mathbf{L}^2$, we obtain $l = \frac{N}{2}$.

The dynamics of the system is obtained by computing the Heisenberg equation of motion (EOM) as,

$$\dot{\hat{L}}_k = \frac{1}{i}[\hat{L}_k, H] \tag{2.35}$$

In order to solve the EOMs for three components of the angular momentum operator, Eq.(2.35), the expectation values of the operators, $\hat{L}_i$ are required. However, the expectation values of the first-order operators, namely $\langle \hat{L}_i \rangle$ depend on the second-order correlations, such as, $\langle \hat{L}_i \hat{L}_j \rangle$ [118], which in turn would depend on higher order correlations, such as, $\langle \hat{L}_i \hat{L}_j \hat{L}_k \rangle$ and so on. Eventually, this provides the following Bogoliubov–Born–Green–Kirkwood–Yvon hierarchy (BBGKY hierarchy) of EOMs for the expectation values given as,

$$\begin{aligned} \frac{d}{dt}\langle \hat{L}_i \rangle &= f\big(\langle \hat{L}_{i'} \rangle, \langle \hat{L}_{i'} \hat{L}_{j'} \rangle\big) \\ \frac{d}{dt}\langle \hat{L}_i \hat{L}_j \rangle &= f\big(\langle \hat{L}_{i'} \hat{L}_{j'} \rangle, \langle \hat{L}_{i'} \hat{L}_{j'} \hat{L}_{k'} \rangle\big) \\ \frac{d}{dt}\langle \hat{L}_i \hat{L}_j \hat{L}_k \rangle &= f\big(\langle \hat{L}_{i'} \hat{L}_{j'} \hat{L}_{k'} \rangle, \langle \hat{L}_{i'} \hat{L}_{j'} \hat{L}_{k'} \hat{L}_{l'} \rangle\big) \\ &\vdots \end{aligned} \tag{2.36}$$

To have a tractable closed set of equations, the hierarchy must be terminated somewhere. For the lowest order truncation of Eqs.(2.36), only the first-order correlations, $\langle \hat{L}_i \rangle$ retains. This enables defining a Bloch vector $\mathbf{J} = (J_x, J_y, J_z)$ with the components,

$$J_i \equiv \frac{\langle \hat{L}_i \rangle}{N/2} \tag{2.37}$$

The EOMs hence become,

$$\begin{aligned} \frac{d}{dt}J_x &= -\gamma J_y + 2\alpha(J_y J_z) \\ \frac{d}{dt}J_y &= \gamma J_x - \epsilon J_z - 2\alpha(J_x J_z) \\ \frac{d}{dt}J_z &= \epsilon J_y \end{aligned} \tag{2.38}$$

where $\alpha = c\frac{N}{2}$ is the modified interaction strength.

Figs.(2.1) show the time evolution of the Bloch vector, $\mathbf{J}$ on the surface of a Bloch sphere of unit radius in a double well potential. Without any interaction, $\alpha = 0$, the usual Rabi oscillation is observed. Here the Bloch vector passes through the poles of the Bloch sphere as shown in Fig.2.1(a). It may be noted that the poles denote the maximum population difference between the wells, as the J_z values corresponding to the poles are $J_z = \pm 1$ [the third equation in Eqs.(2.30)]. Thus during the course of motion, the particles execute a back and forth (oscillatory) motion between the wells and hence signals the independent tunneling of particles between the wells.

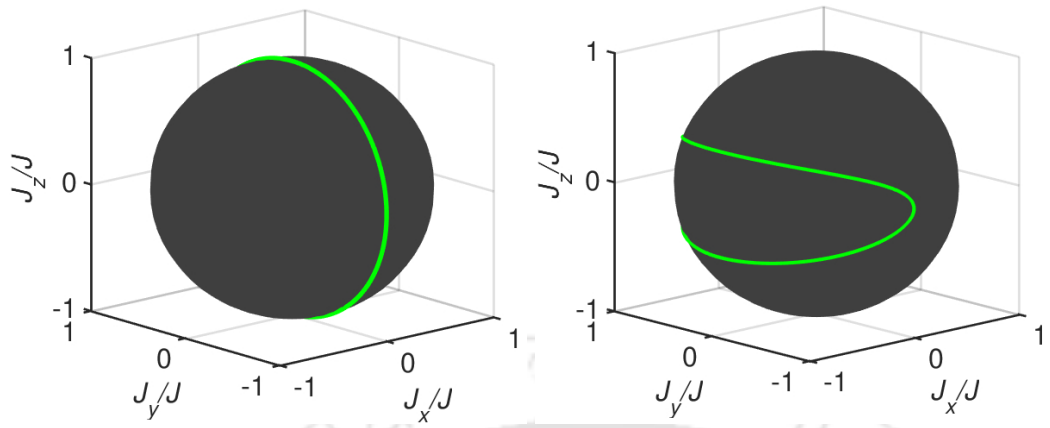

Figure 2.1: Dynamics of the components of the Bloch vectors, namely, J_x, J_y and J_z on the surface of a Bloch sphere of unit radius. (a) shows dynamics without any interaction, $\alpha = 0$ and (b) corresponds to the case of $\alpha \neq 0$.

As the amplitude of the interaction strength, α is enhanced further, the dynamics of the Bloch vector show very different features with the dynamics tracing out trajectories on the either sides of the equator of the sphere in the trapped regime [Fig.2.1(b)]. Also it is completely displaced from the poles of the Bloch sphere. This implies that all the bosons at no instant of time leave one of the wells and there is always a finite occupation density at each well. This scenario implies the onset of a trapping scenario at all instants of time.

2.2.3 Single-Site Mean Field Technique (MFT)

The site decoupling mean field technique in bosonic system is mainly based on the decoupling of the kinetic energy operator of the Hamiltonian. MFT transmutes the BHH into a effective single-site Hamiltonian and hence is expected to exclude the intersite correlations.

Here the decoupling of the kinetic energy is obtained as,

$$\hat{a}_i^\dagger \hat{a}_j \quad \rightarrow \quad \langle \hat{a}_i^\dagger \rangle \hat{a}_j + \hat{a}_i^\dagger \langle \hat{a}_j \rangle - \langle \hat{a}_i^\dagger \rangle \langle \hat{a}_j \rangle \quad = \quad \psi_i \hat{a}_j + \psi_j \hat{a}_i^\dagger - \psi_i \psi_j \tag{2.39}$$

$\psi_i = \langle \hat{a}_i^\dagger \rangle = \langle \hat{a}_i \rangle$ denotes the order parameter which for the number conserving case, is real. Now by employing single-site MFT, Eq.(2.18) can be written as a sum of single-site Hamiltonians, such as,

$$H \quad = \quad \sum_i H_i^{MF}(\psi_i, \phi_i) \tag{2.40}$$

here $\phi_i = \sum_{j=1}^{z} \psi_j$; where z is the coordination number of the lattice. Thus H_i^{MF} is given as,

$$H_i^{MF}(\psi_i, \phi_i) = \left[\frac{U}{2}\hat{n}_i(\hat{n}_i - 1) - \mu\hat{n}_i\right] - zJ\left[\phi_i(\hat{a}_i + \hat{a}_i^{\dagger}) + \psi_i\phi_i\right] \quad (2.41)$$

In case of a homogeneous system, the observables do not depend on the lattice site, thus $\phi_i = \psi_i = \psi$. Therefore, the site independent Hamiltonian is expressed as,

$$H^{MF}(\psi_i, \phi_i) = \left[\frac{U}{2}\hat{n}(\hat{n} - 1) - \mu\hat{n}\right] - \psi(\hat{a} + \hat{a}^{\dagger}) + \psi^2 \quad (2.42)$$

In Eq.(2.42) interaction parameter, U and the chemical potential, μ are scaled by the hopping term, zJ. In the occupation number basis, the matrix representation of the above Hamiltonian can be obtained as,

$$\langle n'|H^{MF}|n\rangle = \left[\psi^2 + \frac{U}{2}n(n-1) - \mu n\right]\delta_{nn'} - \left[\psi(\sqrt{n+1}\,\delta_{n+1n'} + \sqrt{n}\,\delta_{n-1n'})\right] \quad (2.43)$$

Now by diagonalizing the matrix in Eq.(2.43) in an occupation number basis [which will be truncated at some maximum value $n = n_{max}$], the eigenvalues and eigenstates for a homogeneous system can be obtained. Here by using the order parameter which is to be obtained self consistently, various ground state properties can be explored.

2.3 Multi-configurational Time-Dependent Hartree Approach for Bosons (MCTDHB)

A straightforward way to solve the time-dependent Schrödinger equation is by diagonalizing the Hamiltonian in some time-dependent basis sets and then obtain the solutions at a specific time from the eigenvectors and energy eigenvalues obtained thereby. This method is known as *direct diagonalization* or *configuration interaction*, however it is restricted to systems having small sizes in the weak interaction domain and is also crucially dependent on the choice of the basis sets. To overcome this problem, the key idea is to employ time-adaptive basis sets [119, 120]. A very efficient variant of this idea led to the development of the *multi-configurational time-dependent Hatree approach, MCTDH* and this method has successful application to multi-dimensional dynamical system comprised of distinguishable particles [57, 59]; whereas in order to deal with systems consisting of indistinguishable particles, it is important to exploit the symmetry of the

many-body wave function under particle exchange. First, this exploitation of symmetry was taken into account for identical fermions and that leads to the development of the fermionic version, MCTDHF, developed independently by various groups [121, 122]. In recent times, its bosonic version has been developed and is known as MCTDHB [60, 61]. This is a fully variational method and is very efficient in dealing with the properties of the interacting bosons.

2.3.1 The many-boson Hamiltonian

The general time-dependent Schrödinger equation for system of N indistinguishable bosons is given as,

$$\hat{H}\,\Psi(\mathbf{r}_1,...,\mathbf{r}_N;t) \;=\; i\hbar\,\frac{\partial}{\partial t}\,\Psi(\mathbf{r}_1,...,\mathbf{r}_N;t) \tag{2.44}$$

here both the Hamiltonian, $\hat{H}$ and the wave function, Ψ are dependent at the positions of all bosons $\{\mathbf{r}_i\}$. Generally, the Hamiltonian, $\hat{H}$ is a hermitian operator in N boson Hilbert space. In Eq.(2.44), both $\hat{H}$ and Ψ preserve translational symmetry for N indistinguishable bosons.

The Hamiltonian, $\hat{H}$ in Eq.(2.44) reads as,

$$\hat{H} \;=\; \sum_{i=1}^{N}\hat{h}(\mathbf{r}_i) \;+\; \sum_{i<j}^{N}\hat{W}(\mathbf{r}_i-\mathbf{r}_j) \tag{2.45}$$

here

$$\hat{h}(\mathbf{r}) \;=\; \hat{\mathbf{p}}(\mathbf{r})+\hat{V}(\mathbf{r}) = -\frac{1}{2}\frac{\partial^2}{\partial\mathbf{r}^2}+\hat{V}(\mathbf{r}) \tag{2.46}$$

is the single-particle Hamiltonian where the first term is the kinetic energy and the second one is the external trapping potential in Eq.(2.46). The second term, $\hat{W}(\mathbf{r}_i-\mathbf{r}_j)$ in Eq.(2.45) represents the two-body interactions of ultracold dilute bosonic gases. Here dimensionless units are employed with the choice $\hbar = m = 1$. The Hamiltonian, $\hat{H}$ in Eq.(2.45) can also have an explicit dependence on time via either a time-dependent single-particle external potential, $\hat{V}(\mathbf{r},t)$ or a two-body interaction term, $\hat{W}(\mathbf{r}_i,\mathbf{r}_j;t)$.

In second quantized notations, the many-body Hamiltonian, Eq,(2.45) is expressed as,

$$\hat{H} \;=\; \int d\mathbf{r}\;\hat{\Psi}^{\dagger}(\mathbf{r})\hat{h}(\mathbf{r})\hat{\Psi}(\mathbf{r}) \;+\; \frac{1}{2}\int d\mathbf{r}\int d\mathbf{r}'\;\hat{\Psi}^{\dagger}(\mathbf{r})\hat{\Psi}^{\dagger}(\mathbf{r}')\hat{W}(\mathbf{r}-\mathbf{r}')\hat{\Psi}(\mathbf{r})\hat{\Psi}(\mathbf{r}') \tag{2.47}$$

after substituting the representation for bosonic field operators [see Eq.(2.7)], the Eq.(2.47) reduces to,

$$\hat{H} = \sum_{i,j} h_{ij}(t)\,\hat{a}_i^\dagger(t)\,\hat{a}_j(t) + \frac{1}{2}\sum_{i,j,k,l} W_{ijkl}(t)\,\hat{a}_i^\dagger(t)\,\hat{a}_j^\dagger(t)\,\hat{a}_k(t)\,\hat{a}_l(t) \tag{2.48}$$

The matrix elements, $h_{ij}(t)$ and $W_{ijkl}(t)$ are read as,

$$\begin{aligned} h_{ij}(t) &= \int d\mathbf{r}\,\phi_i^*(\mathbf{r},t)\,\hat{h}(\mathbf{r})\,\phi_j(\mathbf{r},t), \\ W_{ijkl}(t) &= \int d\mathbf{r}\int d\mathbf{r}'\,\phi_i^*(\mathbf{r},t)\phi_j^*(\mathbf{r}',t)\,\hat{W}(\mathbf{r}-\mathbf{r}')\,\phi_k(\mathbf{r},t)\phi_l(\mathbf{r}',t) \end{aligned} \tag{2.49}$$

If the orbitals, ϕ_i is time-independent, the matrix elements of Eq.(2.49) reduces to time-independent case and have to calculate only once in a computation, whereas for time-dependent orbitals, the matrix elements of Eq.(2.49) have to be evaluated at every instant of time in the computation. Thus the evaluation of the matrix elements of Eq.(2.49) becomes the performance limiting factor especially for two and three dimensions [62].

2.3.2 Time-dependent variational principle

In general, all the physical laws can be derived from variational principle, though the time-dependent version is less popular. However, the MCTDHB method is completely based on the time-dependent variational principle (TDVP) [123] for quantum mechanics. Let us start with the form of the Lagrangian of a quantum mechanical (many-body) system with constant number of particles ,

$$\mathscr{L}[\Psi(t),\Psi^*(t)] = \left\langle \Psi(t)\middle|\hat{H} - i\frac{\partial}{\partial t}\middle|\Psi(t)\right\rangle \tag{2.50}$$

The wave function, $\Psi(t)$ is normalized at all times, that is, $\langle\Psi(t)|\Psi(t)\rangle = 1$. Here the equations of motion are determined by employing the principle of least action, that is, $\delta S = 0$. Here, the arbitrary variations of the action functional is given as,

$$S[\Psi,\Psi^*] = \int_0^{t'} dt'\,\mathscr{L}[\Psi(t'),\Psi^*(t')] \tag{2.51}$$

with respect to $\langle\Psi|$ and $|\Psi\rangle$ using $\langle\Psi|\dot{\Psi}\rangle = -\langle\dot{\Psi}|\Psi\rangle$ with $\dot{\Psi} = \frac{\partial}{\partial t}\Psi(t)$ render the Schrödinger equation and its hermitian conjugate as,

$$\begin{aligned} \hat{H}|\Psi\rangle &= i|\dot{\Psi}\rangle \\ \langle\Psi|\hat{H} &= -i\langle\dot{\Psi}| \end{aligned} \tag{2.52}$$

here the Hamiltonian is assumed to be hermitian in nature, that is, $\hat{H}^\dagger = \hat{H}$. Generally, in all practical computations, the variations are considered with respect to an *ansatz* corresponding to the wave function containing the parameters rather than the wave function itself. By considering several parameters into the *ansatz* of the wave function, the accuracy of the problem can be improved till the convergence of the system is reached.

2.3.3 The many-boson ansatz (The MCTDHB wave function)

The wave function corresponding to identical bosons can be expanded in a complete set of *permanents*. Using the bosonic creation operators, $\{\hat{a}_i^\dagger\}$ the time-dependent configurations (permanents) of a total of $\binom{N+M-1}{N}$ permanents corresponding to a set of M time-dependent orbitals $\{\phi_1,...,\phi_M\}$ and N bosons can be expressed

$$|n_1,n_2,...,n_M;t\rangle \quad = \quad \frac{[a_1^\dagger(t)]^{n_1}[a_2^\dagger(t)]^{n_2}...[a_M^\dagger(t)]^{n_M}}{\sqrt{n_1!n_2!n_3!...n_M!}}|0\rangle \tag{2.53}$$

by distributing N bosons over M number of accessible basis states (orbitals). $|0\rangle$ denotes the vacuum state. As a linear combination of these time dependent permanents, the general ansatz for the many-boson wave function of N identical bosons can be assumed as,

$$|\Psi(t)\rangle \quad = \quad \sum_{\mathbf{n}} C_{\mathbf{n}}(t)\,|\mathbf{n};t\rangle \tag{2.54}$$

Here the summation in Eq.(2.54) goes over all possible configurations $\{\mathbf{n}=(n_1,n_2,...,n_M)\}$ for which $n_1+n_2+...+n_M=N$. The MCTDHB method employs the general M-orbital ansatz (2.54) and hence is a many-body approach. As the permanents, $|\mathbf{n};t\rangle$ are a complete basis set of N-boson Hilbert space for $M\to\infty$, the variational principle [123] guarantees that the ansatz (2.54) for the wave function becomes exact rendering the solutions of the time-dependent many-body problem provided by the MCTDHB method gradually improve towards exactness when the number of considered creation operators M in the ansatz (2.54), is increased [63, 124].

For practical computations M is finite and therefore the finite size representations of the field operator, $\hat{\Psi}_M$ and the closure relation follow as,

$$\hat{\Psi}_M \quad = \quad \sum_{i=1}^{M} \hat{a}_i(t)\,\phi_i(\mathbf{r},t) \tag{2.55}$$

and

$$\sum_{i=1}^{M} \phi_i(\mathbf{r},t)\,\phi_i^*(\mathbf{r}',t) \quad = \quad \delta_M(\mathbf{r}-\mathbf{r}';t) \tag{2.56}$$

here both Eq.(2.55) and Eq.(2.56) are generally time-dependent and $\delta_M(\mathbf{r}-\mathbf{r}';t)$ corresponds to the finite size representation of a delta function. For any finite M representation, the many-body Hamiltonian can be achieved by substituting the respective field operator, Eq.(2.55) into Eq.(2.47).

The ansatz Eq.(2.54) is the most general M-orbital many-boson ansatz and here both the expansion coefficients, $C_{\mathbf{n}}(t)$ and the permanents, $|\vec{n};t\rangle$ are time-dependent. If $M=1$ is used in Eq.(2.54), the ansatz for many-boson wave function reduces to a single permanent, that is, all N bosons reside in only available single orbital. Thus it leads to the Gross-Pitaevskii theory. Hence MCTDHB is the generalization of the Gross-Pitaevskii method.

2.3.4 Reduced Density Matrices (RDM)

The p-particle reduced density matrix, $\rho^{(p)}$ (p-RDM) of a system with a given wave function, $\Psi(\mathbf{r}_1,...,\mathbf{r}_N)$ of N identical bosons is defined as,

$$\begin{aligned}\rho^{(p)}(\mathbf{r}_1,...,\mathbf{r}_p|\mathbf{r}'_1,...,\mathbf{r}'_p;t) &= \frac{N!}{(N-p)!}\int d\mathbf{r}_{p+1}...d\mathbf{r}_N\,\Psi(\mathbf{r}_1,...,\mathbf{r}_p,\mathbf{r}_{p+1},...,\mathbf{r}_N;t)\\ &\quad\times\Psi^*(\mathbf{r}'_1,...,\mathbf{r}'_p,\mathbf{r}_{p+1},...,\mathbf{r}_N;t)\end{aligned} \tag{2.57}$$

here the wave function is considered to be normalized at all times, $\langle\Psi(t)|\Psi(t)\rangle=1$. In terms of the kernel operator, the p-particle RDM of Eq.(2.57) can be expressed as,

$$\hat{\rho}^{(p)} = \frac{N!}{(N-p)!}\,\mathrm{Tr}_{(N-p)}\big[|\Psi(t)\rangle\langle\Psi(t)|\big] \tag{2.58}$$

here $\mathrm{Tr}_{(N-p)}$ signifies the partial trace over $N-p$ particles in the Fock space. The diagonal term of Eq.(2.57), $\rho^{(p)}(\mathbf{r}_1,...,\mathbf{r}_p|\mathbf{r}_1,...,\mathbf{r}_p;t)$, specifies the probability distribution of the p-particle at time t and is normalized to $N!/(N-p)!$. Similarly RDMs in momentum space can also be achieved as Eq.(2.57).

Now this p-particle RDM can also be expanded in terms of its eigenfunctions and this leads to the following representation,

$$\rho^{(p)}(\mathbf{r}_1,...,\mathbf{r}_p|\mathbf{r}'_1,...,\mathbf{r}'_p;t) = \sum_i n_i^{(p)}(t)\,\alpha_i^{(p)}(\mathbf{r}_1,...,\mathbf{r}_p;t)\,\alpha_i^{*(p)}(\mathbf{r}'_1,...,\mathbf{r}'_p;t) \tag{2.59}$$

where $n_i^{(p)}$ represents the i-th eigenvalue of the p-particle RDM and $\alpha_i^{(p)}$ is the corresponding eigenfunctions (symmetric) in real space. Here the eigenfunctions are termed as natural p-functions and the eigenvalues are known as natural occupations. In the case of

$p = 1$, the eigenfunctions are known as natural orbitals. For a specific number of orbitals, the eigenvalues are arranged in such a way that $n_1^{(p)}$ represents the largest eigenvalue of the p-particle RDM. With the normalization of the many-boson wave function, Eqs.(2.57) and (2.59) induce the following constraint

$$\sum_i n_i^{(p)}(t) = \frac{N!}{(N-p)!} \tag{2.60}$$

on the eigenvalues of the p-particle RDM. As a consequence of Eq.(2.60), the largest eigenvalue, $n_1^{(p)}(t)$ is bounded by [125, 126],

$$\sum_i n_1^{(p)}(t) \leqslant \frac{N!}{(N-p)!} \tag{2.61}$$

Again, the p-particle RDM in terms of bosonic field operators which is equivalent to Eq.(2.57) can be expressed as,

$$\rho^{(p)}(\mathbf{r}_1,...,\mathbf{r}_p|\mathbf{r'}_1,...,\mathbf{r'}_p;t) = \langle\Psi(t)|\hat{\mathbf{\Psi}}^\dagger(\mathbf{r'}_1)\hat{\mathbf{\Psi}}^\dagger(\mathbf{r'}_2)...\hat{\mathbf{\Psi}}^\dagger(\mathbf{r'}_p)\hat{\mathbf{\Psi}}(\mathbf{r}_p)...\hat{\mathbf{\Psi}}(\mathbf{r}_2)\hat{\mathbf{\Psi}}(\mathbf{r}_1)|\Psi(t)\rangle \tag{2.62}$$

here the field operators obey the usual bosonic commutation relations Eqs.(2.10). The presentation in Eq.(2.62) signifies that the p-particle RDM is equivalent to the p-th *order correlation function* at equal times [127–129]. However this conclusion holds true in the case of spatial correlations, that is correlation at equal times. We are going to elaborate about the p-th order correlation functions in the proceeding subsection.

The one-body RDM (that is $p = 1$ case) plays a crucial role to analyze various properties of bosonic systems, such as, to define phenomena like condensation and fragmentation and so on and is expressed as,

$$\begin{aligned}
\rho^{(1)}(\mathbf{r}_1|\mathbf{r'}_1;t) &= \frac{N!}{(N-1)!}\int d\mathbf{r}_2 d\mathbf{r}_3...d\mathbf{r}_N\ \Psi(\mathbf{r}_1,\mathbf{r}_2,...,\mathbf{r}_N;t)\Psi^*(\mathbf{r'}_1,\mathbf{r}_2,...,\mathbf{r}_N;t) \\
&= N\int d\mathbf{r}_2 d\mathbf{r}_3...d\mathbf{r}_N\ \Psi(\mathbf{r}_1,\mathbf{r}_2,...,\mathbf{r}_N;t)\Psi^*(\mathbf{r'}_1,\mathbf{r}_2,...,\mathbf{r}_N;t) \\
&= \langle\Psi(t)|\hat{\mathbf{\Psi}}^\dagger(\mathbf{r'}_1)\hat{\mathbf{\Psi}}(\mathbf{r}_1)|\Psi(t)\rangle \\
&= \sum_{i,j}\rho_{ij}(t)\ \phi_i^*(\mathbf{r'}_1,t)\ \phi_i(\mathbf{r}_1,t)
\end{aligned} \tag{2.63}$$

here the one-body density matrix for bosons is defined as, $\rho_{ij}(t) = \langle\Psi(t)|\hat{a}_i^\dagger\hat{a}_j|\Psi(t)\rangle$ [130].

In a similar way, the two-body RDM can be given as,

$$\begin{aligned}\rho^{(2)}(\mathbf{r}_1,\mathbf{r}_2|\mathbf{r'}_1,\mathbf{r'}_2;t) &= \frac{N!}{(N-2)!}\int d\mathbf{r}_3 d\mathbf{r}_4 ... d\mathbf{r}_N\ \Psi(\mathbf{r}_1,\mathbf{r}_2,...,\mathbf{r}_N;t)\Psi^*(\mathbf{r'}_1,\mathbf{r'}_2,...,\mathbf{r}_N;t)\\ &= N(N-1)\int d\mathbf{r}_3 d\mathbf{r}_4 ... d\mathbf{r}_N\ \Psi(\mathbf{r}_1,\mathbf{r}_2,...,\mathbf{r}_N;t)\Psi^*(\mathbf{r'}_1,\mathbf{r'}_2,...,\mathbf{r}_N;t)\\ &= \langle\Psi(t)|\hat{\Psi}^\dagger(\mathbf{r'}_1)\hat{\Psi}^\dagger(\mathbf{r'}_2)\hat{\Psi}(\mathbf{r}_1)\hat{\Psi}(\mathbf{r}_2)|\Psi(t)\rangle\\ &= \sum_{i,j,k,l}\rho_{ijkl}(t)\ \phi_i^*(\mathbf{r'}_1,t)\ \phi_j^*(\mathbf{r'}_2,t)\ \phi_k(\mathbf{r}_1,t)\ \phi_l(\mathbf{r}_2,t) \qquad (2.64)\end{aligned}$$

where the two-body density matrix for bosons is defined as, $\rho_{ijkl}(t) = \langle\Psi(t)|\hat{a}_i^\dagger\hat{a}_j^\dagger\hat{a}_k\hat{a}_l|\Psi(t)\rangle$ [130]. Moreover the upper bound of the largest eigenvalue of the RDM, Eq.(2.61) for $p=1$ and $p=2$ reduces to the following form respectively,

$$\begin{aligned}n_1^{(1)}(t) &\leqslant N\\ n_1^{(2)}(t) &\leqslant N(N-1) \qquad (2.65)\end{aligned}$$

The diagonal elements $\rho^{(1)}(\mathbf{r}|\mathbf{r};t)$ and $\rho^{(2)}(\mathbf{r},\mathbf{r}'|\mathbf{r},\mathbf{r}';t)$ are known as one-body and two-body densities respectively.

2.3.5 p-th order coherence

The normalized p-th order correlation function, $g^{(p)}$, for a system of N bosons can be evaluated by using the p-RDM, Eq.(2.57) as,

$$g^{(p)}(\mathbf{r'}_1,...,\mathbf{r'}_p|\mathbf{r}_1,...,\mathbf{r}_p;t) = \frac{\rho^{(p)}(\mathbf{r}_1,...,\mathbf{r}_p|\mathbf{r'}_1,...,\mathbf{r'}_p;t)}{\sqrt{\prod_{i=1}^{p}\rho^{(1)}(\mathbf{r}_i|\mathbf{r}_i;t)\rho^{(1)}(\mathbf{r'}_i|\mathbf{r'}_i;t)}} \qquad (2.66)$$

This specifies the definition of spatial coherence. In the case of $|g^{(p)}|=1$, one achieves a full spatial p-th order coherence. This condition valids only when p-RDM is a product of 1-RDMs [63, 131]. Also in this case, 1-RDM should be represented by a single complex-valued function, $\xi(\mathbf{r},t)$ as in the following,

$$\rho^{(1)}(\mathbf{r}|\mathbf{r}';t) = \xi^*(\mathbf{r}',t)\ \xi(\mathbf{r},t) \qquad (2.67)$$

and this signifies the fact that 1-RDM has only a single eigenvalue. Thus this 1-RDM represents a fully condensed state. When all N bosons reside in the same orbital, a maximally coherent particle state is achieved and also the correlation function reduces to

$$|g^{(p)}(\mathbf{r'}_1,...,\mathbf{r'}_p,\mathbf{r}_1,...,\mathbf{r}_p;t)| = \frac{N!}{(N-p)!N^p} \qquad (2.68)$$

The diagonal $g^{(p)}(\mathbf{r}'_1,...,\mathbf{r}'_p,\mathbf{r}_1,...,\mathbf{r}_p;t)$ of the normalized p-th order correlation function in real space measures the degree of p-th order coherence. $g^{(p)}$ also calculates the extent of statistical dependence of the simultaneous measurement of a set of p coordinates $\mathbf{r}_1,...,\mathbf{r}_p$ in a probabilistic sense. Consequently, when $g^{(p)}=1$, there is statistical independence of the measurement of the p coordinates and the positions of the particles are anti-correlated. Thus the system is said to be p-th order coherent. Therefore, a fully coherent state occurs only when $p=1$. Thus a maximally coherent N-boson state satisfies $|g^{(1)}(\mathbf{r}'_1,\mathbf{r}_1;t)|=1$. In experiments, the absolute value of $g^{(1)}$ can be realized by using Young double slit experiment [62]. The measurement of the p positions is correlated when $g^{(p)}>1$ and is anti-correlated if $g^{(p)}<1$. This leads to the fact that coherence corresponds to the condensation and correlation/anti-correlation correspond to the fragmentation phenomena. In a similar way, p-th order normalized correlation functions in momentum space can also be achieved from p-particle RDM in momentum space.

2.3.6 The building equations of MCTDHB

To derive the equations of motion of MCTDHB [60, 61, 132], the Lagrangian formulation of the time-dependent variational principle is employed [123]. Thus the many-boson ansatz Eq.(2.54) is substituted in Eq.(2.51), thereby imposing the constraint of orthonormality among the orbitals, $\phi_j(\mathbf{r},t)$ by Lagrange multipliers, $\mu_{jk}(t)$. Thus the functional action of the time-dependent Schrödinger equation becomes,

$$S[\{C_{\mathbf{n}}(t)\},\{\phi_j(\mathbf{r},t)\}] = \int dt\left\{\left\langle\Psi(t)\middle|\hat{H}-i\frac{\partial}{\partial t}\middle|\Psi(t)\right\rangle-\sum_{j,k}^{M}\mu_{jk}(t)[\langle\phi_j|\phi_k\rangle-\delta_{jk}]\right\} \quad (2.69)$$

In the next step, stationarity of the action with respect to its arguments, $\{\phi_j(\mathbf{r},t)\}$ and $\{C_{\mathbf{n}}(t)\}$ is required. As the orbitals, $\{\phi_j(\mathbf{r},t)\}$ and the coefficients, $\{C_{\mathbf{n}}(t)\}$ are independent variables or arguments of the action (2.69), this variation is performed separately for the orbitals and the coefficients as in the following.

(a) Variation with respect to the orbitals $\{\phi_j(\mathbf{r},t)\}$

To perform the variation of the function action (2.69) with respect to orbitals, $\{\phi_j(\mathbf{r},t)\}$, the expectation value of $\hat{H}-i\frac{\partial}{\partial t}$ of Eq.(2.69) is expressed in a form that explicitly depends on the orbitals with the help of one-body, $\rho^{(1)}(\mathbf{r}_1|\mathbf{r}'_1;t)$ and two-body $\rho^{(2)}(\mathbf{r}_1,\mathbf{r}_2|\mathbf{r}'_1,\mathbf{r}'_2;t)$

RDMs [see Eq.(2.63) and Eq.(2.64)] as,

$$\left\langle \Psi(t)\middle|\hat{H}-i\frac{\partial}{\partial t}\middle|\Psi(t)\right\rangle = \sum_{j,k=1}^{M}\rho_{jk}\left[h_{jk}-\left(i\frac{\partial}{\partial t}\right)_{jk}\right]+\frac{1}{2}\sum_{j,k,l,m}\rho_{jklm}\,W_{jklm}-i\sum_{\mathbf{n}}C_{\mathbf{n}}^{*}\frac{\partial C_{\mathbf{n}}}{\partial t} \tag{2.70}$$

here the time-derivative $\frac{\partial}{\partial t}$ is expressed as a one-body operator

$$i\frac{\partial}{\partial t} = \sum_{j,k}\hat{a}_j^{\dagger}\hat{a}_k\left(i\frac{\partial}{\partial t}\right)_{jk}, \qquad \left(i\frac{\partial}{\partial t}\right)_{jk} = i\int\phi_j^{*}(\mathbf{r},t)\,\frac{\partial\phi_k(\mathbf{r},t)}{\partial t}\,d\mathbf{r} \tag{2.71}$$

The time-argument is dropped everywhere for brevity. The matrix elements h_{jk} and W_{jklm} of Eq.(2.70) were defined in Eq.(2.49). Eq.(2.70) is very useful as the matrix elements h_{jk}, W_{jklm} and $(i\frac{\partial}{\partial t})_{jk}$ are only explicitly dependent on the orbitals, $\{\phi_j(\mathbf{r},t)\}$. While the elements ρ_{jk} and ρ_{jklm} of the one-body and two-body RDMs are independent of $\{\phi_j(\mathbf{r},t)\}$. Here the elements of ρ_{jk} are collected in a matrix $\boldsymbol{\rho}(t)=\{\rho_{jk}\}$ for convenience.

Now by considering the fact that the $\{\phi_j(\mathbf{r},t)\}$ are orthonormal functions, the Lagrange multipliers, $\mu_{jk}(t)$ can be eliminated. Finally the following set of equations of motion for time-dependent orbitals in which particles reside are obtained for $j=1,...,M$ as,

$$\begin{aligned}\hat{\mathbf{P}}\,i\left|\dot{\phi}_j\right\rangle &= \hat{\mathbf{P}}\left[\hat{h}|\phi_j\rangle+\sum_{j,k,l,m=1}^{M}\{\boldsymbol{\rho}(t)\}_{jk}^{-1}\,\rho_{jklm}\,\hat{W}_{kl}|\phi_k\rangle\right],\\ \hat{\mathbf{P}} &= 1-\sum_{j'=1}^{M}|\phi_{j'}\rangle\langle\phi_{j'}|\end{aligned} \tag{2.72}$$

Here

$$\hat{W}_{kl}=\int d\mathbf{r}'\phi_k^{*}(\mathbf{r}',t)\,\hat{W}(\mathbf{r}-\mathbf{r}')\,\phi_l(\mathbf{r}',t) \tag{2.73}$$

denote the time-dependent local interaction potentials. From Eq.(2.72) it is observed that the elimination of the Lagrange multipliers $\mu_{jk}(t)$ has emerged as a projection operator $\hat{\mathbf{P}}$ onto the subspace that is orthogonal to that spanned by the orbitals. In this picture, the MCTDHB equations are obtained by fixing the gauge freedom in the choice of the orbitals by the following condition,

$$\left\langle\frac{\partial\phi_j}{\partial t}\middle|\phi_k\right\rangle = 0, \quad \forall j,k\in[1,M] \tag{2.74}$$

If the conditions (2.74) are satisfied at any time, then the orbitals should remain orthonormal at any time and this simplifies the equations of motion for orbitals as, $j = 1, ..., M$,

$$\begin{aligned} i\left|\dot{\phi}_j\right\rangle &= \hat{\mathbf{P}}\left[\hat{h}|\phi_j\rangle + \sum_{j,k,l,m=1}^{M} \{\boldsymbol{\rho}(t)\}^{-1}_{jk}\ \rho_{jklm}\ \hat{W}_{kl}|\phi_k\rangle\right], \\ \hat{\mathbf{P}} &= 1 - \sum_{j'=1}^{M} |\phi_{j'}\rangle\langle\phi_{j'}| \end{aligned} \tag{2.75}$$

The presence of the projector $\hat{\mathbf{P}}$ on the right hand side of Eq.(2.75) implies that the conditions (2.74) are satisfied at any time throughout the propagation of the orbitals. This means that the temporal evolution of $\{\phi_j(\mathbf{r},t)\}$, that is, $\frac{\partial\phi_j}{\partial t}$ are always orthogonal to $\{\phi_j(\mathbf{r},t)\}$ themselves. This property utilized by the MCTDH developers [57, 58] usually renders the time propagation of Eq.(2.75) robust and stable and thus can be exploited to maintain accurate propagation results with lower computational costs.

(b) Variation with respect to the coefficients $\{C_{\mathbf{n}}(t)\}$

In this part, the variation of the function action (2.69) with respect to the coefficients, $\{C_{\mathbf{n}}(t)\}$ is discussed. This can be achieved by expressing the expectation value of $\hat{H} - i\frac{\partial}{\partial t}$ of Eq.(2.69) in a form that explicitly depends on $\{C_{\mathbf{n}}(t)\}$. This results into the following form,

$$\left\langle\Psi(t)\left|\hat{H} - i\frac{\partial}{\partial t}\right|\Psi(t)\right\rangle = \sum_{\mathbf{n}} C^*_{\mathbf{n}}\left[\sum_{\mathbf{n}'}\left\langle\mathbf{n};t\left|\hat{H} - i\frac{\partial}{\partial t}\right|\mathbf{n}';t\right\rangle C_{\mathbf{n}'} - i\frac{\partial C_{\mathbf{n}}}{\partial t}\right] \tag{2.76}$$

Now by employing the variation, we get

$$\frac{\partial S[\{C_{\mathbf{n}}(t)\},\{\phi_j(\mathbf{r},t)\}]}{\partial C^*_{\mathbf{n}}} = 0 \quad \Rightarrow \sum_{\mathbf{n}'}\left\langle\mathbf{n};t\left|\hat{H} - i\frac{\partial}{\partial t}\right|\mathbf{n}';t\right\rangle C_{\mathbf{n}'} = i\frac{\partial C_{\mathbf{n}}}{\partial t} \tag{2.77}$$

Now let us define a time-dependent matrix $\mathscr{H}(t)$ with matrix elements,

$$\mathscr{H}_{\mathbf{n}\mathbf{n}'}(t) = \left\langle n_1, n_2, ..., n_M;t\left|\hat{H} - i\frac{\partial}{\partial t}\right|n'_1, n'_2, ..., n'_M;t\right\rangle \tag{2.78}$$

and also a vector $\mathbf{C}(t)$ that collects the expansion coefficient, $\{C_{\mathbf{n}}(t)\}$. Thus Eq.(2.77) in a compact form can be written as,

$$\mathscr{H}(t)\,\mathbf{C}(t) = i\,\frac{\partial\mathbf{C}(t)}{\partial t} \tag{2.79}$$

By using the condition (2.74), finally Eq.(2.79) reduces to,

$$\mathbf{H}(t)\,\mathbf{C}(t) = i\,\frac{\partial\mathbf{C}(t)}{\partial t} \tag{2.80}$$

with the matrix elements

$$H_{\mathbf{n}\mathbf{n}'}(t) = \left\langle n_1, n_2, ..., n_M; t \middle| \hat{H} \middle| n_1', n_2', ..., n_M'; t \right\rangle \tag{2.81}$$

The equation of motion (2.80) for coefficients is a first-order differential equation in time. The right hand side of Eq.(2.80) is time-dependent as it is evaluated with time-dependent permanents, $|\mathbf{n};t\rangle$. The many-body wave function $\Psi(t)$ should preserve its normalized form in the course of evolution, as for the self adjoined Hamiltonian $\hat{H}$ the time evolution is unitary. To sustain the normalization of $\Psi(t)$, $\mathbf{C}(t)$ should remain normalized at all times throughout the propagation and to attain this the matrix $\mathbf{H}(t)$ should be Hermitian.

The coupled equations of motion (2.75) for orbitals, $\{\phi_j(\mathbf{r},t)\}$ and (2.80) for the expansion coefficients, $\{C_{\mathbf{n}}(t)\}$ are the building equations of MCTDHB [60, 61]. By propagating in imaginary time, the ground and excited states for interacting many-bosons systems can also be determined from the MCTDHB building equations [62]. The employment of time-dependent, variationally determined orbitals provide a greater advantage as the MCTDHB equations of motion become an exact representation of the time-dependent many-boson Schrödinger equation in the limit $M \to \infty$. Practically, M is finite. The number of permanents that are used in MCTDHB is given as $\binom{N+M-1}{N}$ as mentioned earlier and is an exponentially increasing function of the number of bosons and the number orbitals. Thus MCTDHB is a mathematically sound technique and optimally converges to the exact solution for the many-boson Schrödinger equation. MCTDHB can also be used for multidimensional systems and the fact that only a two-body interaction is required, it is possible to successfully and quantitatively simulate the dynamics as well as ground state properties for a large number of bosons using MCTDHB.

2.3.7 Condensation and Fragmentation

Penrose and Onsager provide [13] a new way to define Bose-Einstein condensation for interacting systems with the natural occupations, n_i which are the eigenvalues of the one-body RDM. For a system of identical bosons, when the largest eigenvalue of the one-body RDM, n_1 is of the order of total number of bosons, N in the system, that is,

$$n_1 \quad = \quad \mathcal{O}(N) \tag{2.82}$$

then it is said to be condensed. For the special case, a bosonic state with N bosons is said to maximally coherent (*fully condensed*) when $n_1 = N$ and $\left|g^{(1)}\right| = 1$, where $g^{(1)}$ is the

first-order correlation function. Here the system is in coherent state since all the bosons reside in the same orbital. The condensates in which natural occupation number is close to N, (to be specific $n_1/N > 86\%$ in the thesis) are known as depleted condensates.

When more than one natural occupation number is of the order of the number of bosons, N, that is, if $n_1, n_2 = \mathcal{O}(N)$ then one get a *two-fold fragmentation* of the condensate. Similarly, when $n_1, n_2, n_3 = \mathcal{O}(N)$, then a *three-fold fragmented* condensate emerges. Finally, *k-fold fragmented*, if k macroscopic eigenvalues of the one-body RDM is of the order of the total number bosons [133], such as, $n_1, n_2, n_3 ... n_k = \mathcal{O}(N)$.

Moreover, a useful quantity, fragmentation of the condensate, F which quantifies the fraction of bosons that does not occupy the eigenfunction of the one-body RDM or natural orbital corresponds to the macroscopic eigenvalues can be defined for M number of orbitals as,

$$F = \sum_{j=2}^{M} n_j = 1 - n_1 \tag{2.83}$$

Fig.(2.2) depicts the dynamics of fragmentation, F as function of time, t of a system

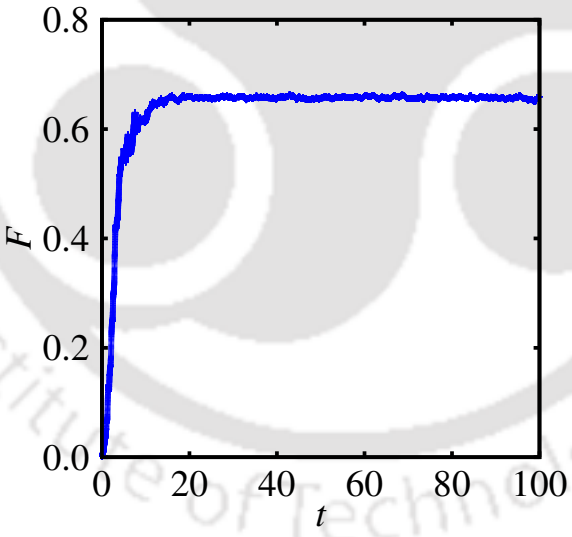

Figure 2.2: Fragmentation, F as a function of time, t in triple well optical potential. The plot saturating at ~ 0.67 indicates a threefold fragmentation of the condensate.

of bosons confined in a triple well potential with three natural orbitals, that is $M = 3$. Initially, it is observed that the rate of fragmentation, F increases rapidly till $t = 10$ and then it saturates at $F \sim 0.67$ with the passage of time (for large time period). Henceforth, the systems remains in a fully fragmented state (that is three-fold fragmented state) irrespective of the increase in t.

CHAPTER 3

STUDY OF TUNNELING DYNAMICS AND PHASES EMPLOYING BHM

In this chapter, we have employed variants of Bose-Hubbard model (BHM) to study the tunneling dynamics and various phases of correlated bosons under three different situations, such as, the tunneling dynamics of bosons in a double well potential, a periodically driven system and phases in presence of time-dependent synthetic gauge fields. We present them in the following.

3.1 Tunneling dynamics of correlated bosons in a double well potential

3.1.1 Introduction

The quantum tunneling of particles through a classically impenetrable barrier is a very famous problem of quantum physics community [65–70, 134–136]. Also the inclusion of interaction between these particles may help or hinder the tunneling phenomena. The time resolved tunneling probability may demonstrate interesting effects of the roles of the interaction parameters and the initial configuration of the particles. As an example, the phenomena of time evolved pair tunneling of bosons, as opposed to the individual tunneling across the barrier, can crucially rely upon the initial configuration of the

system.

In the weak interaction regime where the atoms are weakly interacting, the tunneling of individual particles dominate, as that is the case for normal Josephson junctions. However with increase in the (repulsive) interaction between the atoms, two of them located at one side of the barrier cannot tunnel independently and thus a pair tunneling becomes inevitable. There one can also observe a 'conditional tunneling regime' where tunneling of a single particle can happen only in the presence of a second particle that acts as switch [137].

In a simplified way, the tunneling dynamics of correlated particles in presence of confining potential can be investigated by considering a single particle or a few particles in a double well potential. Albeit straightforward, it has the potential to demonstrate a range of fundamental quantum phenomena with regard to the tunneling dynamics of the particles and abilities to manipulate them in terms of suppression of the tunneling probabilities, and thereby trapping them in one of the wells. These trapping phenomena are experimentally realized with a BEC [138]. These studies that involves a few bosons have turned out to be more significant in recent times with the experimental successes of 'Boson Sampling' [71, 139], where a smaller fraction of bosons were used for experimental demonstration of achieving unprecedented control of multiphoton interferences in large interferometers. These techniques offer huge prospects of simplifying the quantum computation problem and speeding it up further.

When the energy difference between the two lowest single particle eigenstates is far smaller than all other energy states, a two mode approximation is valid and can describe the tunneling between different Bloch bands in an optical lattice [140]. In this section, we are going to investigate a two-site Bose Hubbard model (BHM), which is the simplest candidate to investigate the dynamics of interacting bosonic atoms in a double well potential [79, 141–144] or a bosonic junction [145]. It is helpful to mention that we mainly focus on the physics of weak and strong interparticle repulsion limits and also the sensitivity of initial conditions on the tunneling dynamics.

The time evolution of the Fock space for a simple two-site Bose Hubbard model (BHM) (without the offsite density exchange term) with two bosons has been investigated and the tunneling probabilities are computed as a function of time [117, 146]. Whereas a detailed investigation of the tunneling dynamics in strong and weak coupling regimes and the sensitivity of the time evolved state to a variety of initial configurations were lacking. This is mainly significant in case of engineered waveguide lattices to achieve a

specific preferred final state. Hence, it is interesting to consider a few bosons (that is, $N \geq 2$ and $N = 3, 4$ etc) as the complexity of dynamics (compared to $N = 2$) is inevitable as the many boson effects will become very discernible in case of a larger number of particles. Moreover, an inter-site density exchange term in BHM, relevant in the case of a dipolar bosonic gas, can also be introduced in the present context. Therefore, the inclusion of this term in BHM is known to have density ordering effects and it enriches the various phases in a lattice [147].

Motivated by the above findings, we have considered a few bosons in a Bose Hubbard model (BHM) and investigate the quantum dynamics. Specifically, we have explored the dependencies of the tunneling probabilities in the strong and weak onsite interaction regimes, briefly the effect of the density ordering term therein and also the sensitivity of the dynamics to a variety of initial configurations. Here among the various results, the time resolved dynamics is seen to be crucially dependent on the initial state of the system in which it is prepared, especially when the initial population imbalance between the two wells is unity for an odd number of particles. Furthermore, we also include a brief discussion on the effect of using an admixture of initial configurations on the tunneling oscillations.

3.1.2 The BHM and EOMs for a few bosons

An extended density ordering term is included while deriving the equations of motion (EOM) with the motivation of investigating its competing effects with the onsite term on the tunneling dynamics even though we are going to restrict ourselves to the usual (short ranged) Bose Hubbard model [117, 148]. These extended range of interaction potentials are relevant to include for dipolar bosons, as the research of ultracold dipolar gases gained interest with the experimental realization of condensate of Cr atoms which hosts large long range interactions [103, 149, 150].

The BHH for a system of N interacting bosons occupying the weakly coupled low lying energy states of a symmetric double well potential is given as,

$$\begin{aligned} \hat{H}_{BHH} &= -J(\hat{a}_1^\dagger \hat{a}_2 + \hat{a}_2^\dagger \hat{a}_1) + \frac{U}{2}(\hat{a}_1^{\dagger 2}\hat{a}_1^2 + \hat{a}_2^{\dagger 2}\hat{a}_2^2) + V(\hat{a}_1^\dagger \hat{a}_1 \hat{a}_2^\dagger \hat{a}_2) \\ &= \hat{H}_J + \hat{H}_U + \hat{H}_V \end{aligned} \tag{3.1}$$

here $\hat{a}_1^\dagger(\hat{a}_2)$ are the creation (annihilation) operators of bosons in the left (right) wells, J being the tunneling parameter ($J > 0$) between the two modes, U is the strength of

the onsite interaction ($U > 0$) and V is the strength of the extended density interaction (or exchange interaction) that has, as mentioned earlier, significance in the formation of density order phases and are relevant in the context of dipolar bosons. All the energy scales including the time evolution in this work are expressed in units of tunneling frequency, J. Here the term, $\hat{H}_V$ includes $\hat{H}_U$ in the following way [151],

$$\hat{H}_V = V\left[N^2 - N - \frac{\hat{H}_U}{U}\right] \tag{3.2}$$

here $N = n_1 + n_2 = a_1^\dagger a_1 + a_2^\dagger a_2$ is the total number of bosons. In this context, the density exchange term ($\hat{H}_V$) has no role, apart from normalization of the interaction strength U as U' ($= U - V$). As a consequence of this, the noninteracting scenario is defined by $U = V$. Thus the role of interparticle interaction becomes relevant only for $U \neq V$. Also, the negative sign in the expression of U' denotes that it can either be negative (attractive) for $U < V$ [152] or positive (repulsive) for $U > V$, for which we have considered $V = 2.U$ and $V = 0.5U$ respectively as the representative values. Whereas due to the symmetric nature of the model, a sign change in interaction does not contribute in its dynamics. Albeit, we have used different values corresponding to attractive and repulsive region (as a pathological case) which effectively provides two different interaction strengths manifesting solely the role of interaction magnitude instead of its character. Moreover, the weak and strong coupling regimes are distinguished by assuming $U = 0.1$ and $U = 12$ (both in units of the tunneling frequency, J) respectively. Thus the *'strong'* and *'weak'* regimes will carry these values throughout this analysis. Finally, other representative values that assumed for the computation of the tunneling dynamics does not yield any new qualitative inference.

For the investigation of the tunneling dynamics, the state vector of the system is expanded in the basis of Fock states for a constant particle number N, as given by Eq.(2.24) in **Chapter 2**.

Finally, in terms of the coefficients $c_l(t)$, the EOM can be expressed as,

$$i\frac{dc_l(t)}{dt} = -k_l c_{l+1} - k_{l-1} c_{l-1} + a_l c_l + b_l c_l \tag{3.3}$$

where $k_l = J\sqrt{(l+1)(N-l)}$, $a_l = \frac{U}{2}[l^2 + (N-l)^2 - N]$, $b_l = V[l(N-l)]$

For two boson ($N = 2$) system, Eq.(3.3) reduces to the following three coupled EOMs,

$$i\frac{d}{dt}\begin{pmatrix} c_0 \\ c_1 \\ c_2 \end{pmatrix} = \begin{pmatrix} U & -\sqrt{2}J & 0 \\ -\sqrt{2}J & V & -\sqrt{2}J \\ 0 & -\sqrt{2}J & U \end{pmatrix}\begin{pmatrix} c_0 \\ c_1 \\ c_2 \end{pmatrix} \tag{3.4}$$

Thus the occupation probabilities of bosons can be obtained by solving these coupled equations. The various initial configurations in which the system can be prepared in are

$$\begin{aligned} c_0(0) &= 1,\ c_1(0) = c_2(0) = 0 \\ c_1(0) &= 1,\ c_0(0) = c_2(0) = 0 \\ c_2(0) &= 1,\ c_0(0) = c_1(0) = 0 \end{aligned} \tag{3.5}$$

In short we shall denote them as (100),(010) and (001) respectively, where (100) corresponds to the state where initially all the bosons are in the right well with the left one being empty. Similarly, (010) denotes one in each well, while (001) implies both in the left well with the right well being empty.

Similarly, in the case of three bosons, one obtains four coupled EOMs as in the following,

$$i\frac{d}{dt}\begin{pmatrix} c_0 \\ c_1 \\ c_2 \\ c_3 \end{pmatrix} = \begin{pmatrix} 3U & -\sqrt{3}J & 0 & 0 \\ -\sqrt{3}J & U+2V & -2J & 0 \\ 0 & -2J & U+2V & -\sqrt{3}J \\ 0 & 0 & -\sqrt{3}J & 3U \end{pmatrix}\begin{pmatrix} c_0 \\ c_1 \\ c_2 \\ c_3 \end{pmatrix} \tag{3.6}$$

Like earlier case, these equations can be solved for four different initial conditions, namely, (1000),(0100),(0010) and (0001), with implications as before. For example, (0100) defines a situation where two particles are in the right well, with the other in the left well and so on.

A straightforward extension provides similar set of EOMs (now a set of five) and the corresponding initial conditions for $N = 4$. This is procedure repeated till $N = 16$. For brevity, we skip them here.

By the method of induction, an extension of our results to the case of N bosons is possible. Thus a straightforward application of this method on Eqs.(3.4) and (3.6) renders,

$$i\frac{dc_0}{dt} = -\sqrt{N}Jc_1 + \frac{N(N-1)}{2}Uc_0 \tag{3.7}$$

where all the bosons are in the right well. Similarly the case corresponding to $(N-1)$ bosons in the right well and one in the left, can be expressed as,

$$i\frac{dc_1}{dt} = -\sqrt{N}Jc_0 - \sqrt{2(N-1)}Jc_2 + \frac{N^2-3N+2}{2}Uc_1 + (N-1)Vc_1 \tag{3.8}$$

For an equal distribution of the bosons with $N/2$ in each well (N: even) is

$$i\frac{dc_{N/2}}{dt} = -\frac{J}{2}\sqrt{N(N+2)}\,(c_{N/2+1}+c_{N/2-1})+\frac{U}{4}N(N-2)c_{N/2}+\frac{V}{4}N^2c_{N/2} \quad (3.9)$$

However we restrict ourselves to the case of a few bosons for analyzing the results in the following discussion.

3.1.3 Physical Observables and Results

We are interested in exploring the quantum tunneling dynamics of a few bosons in a double well potential as emphasized earlier. Thus the main focus relies on the effect of the interparticle repulsion and density exchange for two, three, four and five bosons and the variation of the tunneling dynamics corresponding to different initial configurations. In the following, we describe the cases associated with two, three and four bosons separately. With this regard, an useful (and experimentally measurable) observable to quantify the tunneling dynamics of bosons can be the population in one of the wells (say the right well), $P_R(t)$ as expressed in the following [148]. Thus, the right well population, $P_R(t)$ for a system of two bosons, can be defined as [117],

$$P_R(t) = |c_0(t)|^2+\frac{1}{2}|c_1(t)|^2 \quad (3.10)$$

which is a superposition of the probabilities of both the bosons in the right well, ($|c_0(t)|^2$) and half of that corresponding to one in each well, ($|c_1(t)|^2$).

Without any interaction that for $U'=0$ with $U=V$, the usual Rabi oscillations of the bosons between the wells is observed [Fig.3.1(a)]. Here the bosons tunnel independently back and forth between the wells. With the increase in interaction strength, for small values of U', the atoms can still tunnel independently, similar to that of the normal Josephson junction, albeit the time period for oscillations becomes enormously large that signals the onset of a trapping scenario. Similar scenario has been already reported by Zöllner *et al*. in [148], where they have found that for $g=1.3$ (g being the strength of the pairwise interaction potential), the time period of oscillations is as large as 2×10^3 s. In this situation, two or more atoms residing in one of the wells, form a 'repulsively bound pair' [153] and hence tunnel together. However these phenomena are difficult to contemplate in crystal lattices owing to relatively much shorter life times associated with the decay processes. In case of weak interaction regime, $U=0.1$, it is important to note that $P_R(t)$ collapses at a certain time as evident from Fig.3.1(b). Whereas there is again

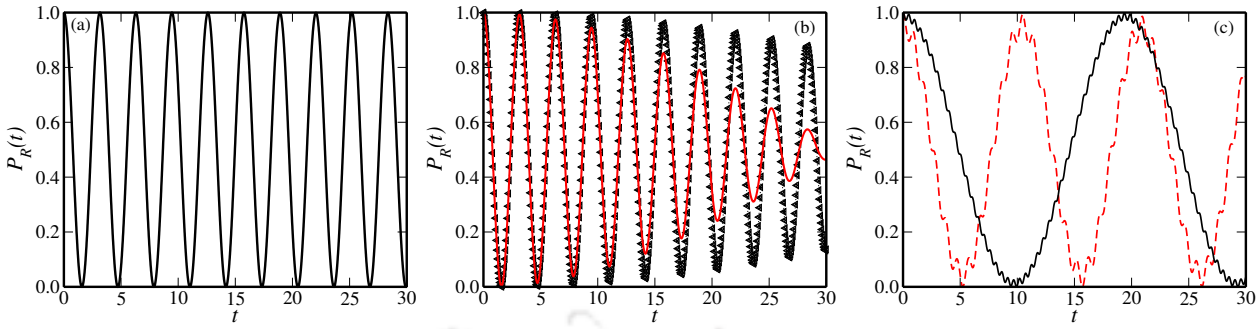

Figure 3.1: The right well population, $P_R(t)$ as a function of time for two bosons for non interacting case ($V = U$) in (a). In (b) left triangles with dots (black) denote $P_R(t)$ corresponding to $U' = 0.05$ and solid line (red) denotes $P_R(t)$ corresponding to $U' = -0.1$. Similarly in (c) dashed lines (red) denote $P_R(t)$ corresponding to $U' = 6$ and solid line (black) denotes $P_R(t)$ corresponding to $U' = -12$. The time t in the x-axis is measured in units of the tunneling frequency, J and is true for all plots.

a 'revival' of $P_R(t)$ as time progresses and this phenomenon is repeated with further increase in time. In this case, at time $t = 0$, the system is prepared in a definite state (as described by the initial configurations in the preceding subsection) and the two terms in Eq.(3.10) are correlated. However as time increases, the oscillations corresponding to different initial excitations pick up different frequencies and hence become uncorrelated, thereby leading to a collapse. With further increase in time, the correlation is partly (depending on the value of U) restored and revival occurs. This behavior repeats itself and thus an infinite sequence of collapse and revivals are obtained [154]. At large values of U, such as, $U = 12$, which is termed as the *fermionization limit* (where the bosons avoid each other and thus obey an *'exclusion principle'*), there are faster oscillations with smaller amplitudes, however $P_R(t)$ becomes zero eventually as evident from Fig.3.1(c), signaling a tunneling of the atoms at large time scales. Thus the time period of such 'eventual tunneling' phenomena, T_R (say) grows with the increase in the interparticle repulsion, U, thereby signaling the onset of intense trapping effects. The analytical expressions for T_R corresponding to the noninteracting ($U = V$), and interacting (considering two pathological cases $V = 2.U$ and $V = 0.5U$) are expressed as,

$$\begin{aligned} T_R &= \frac{\pi}{J} \quad \text{for } V = U \\ &= \left| \frac{8\pi}{U - \sqrt{64J^2 + U^2}} \right| \quad \text{for } V = 0.5U \\ &= \left| \frac{4\pi}{U - \sqrt{16J^2 + U^2}} \right| \quad \text{for } V = 2U \end{aligned} \tag{3.11}$$

Hence, T_R as a function of U scales linearly and the agreement between the analytic

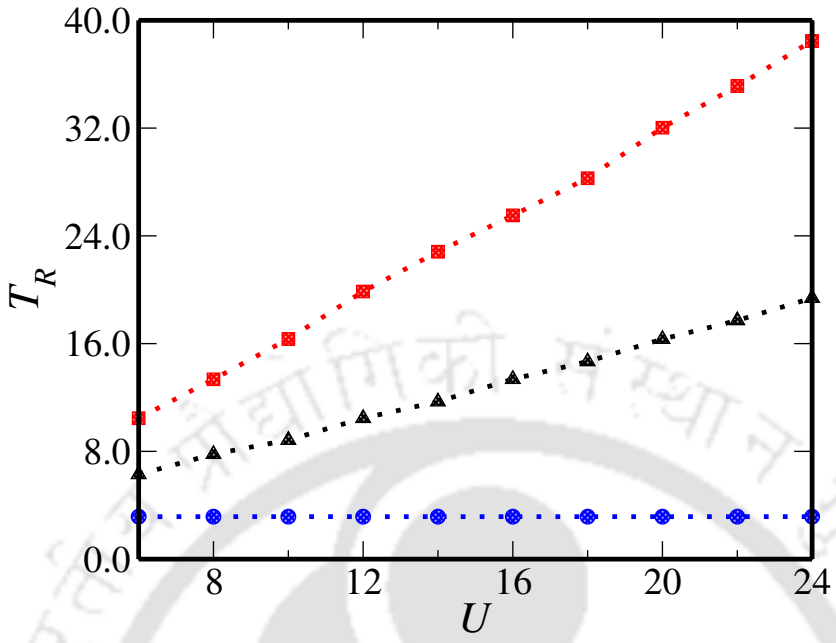

Figure 3.2: Time period T_R of two bosons as a function of U is shown in this figure. Here the circles with dotted line (blue), triangles with dotted line (black) and squares with dotted line (red) denote the analytical results for the non-interacting case ($V = U$), and interacting cases with $V = 0.5U$ and $V = 2U$ respectively. The associated open squares are the numerically obtained results.

expressions and the corresponding numeric estimates are evident from Fig.(3.2). Thus T_R is insensitive to the values of U for the non-interacting case, while it sharply increases with increase in U for the interacting cases.

Now let us investigate the impact of different initial configurations on the tunneling dynamics of two particles confined in a double well potential. Therefore, to prepare an initial state with a population imbalance, a tilt in the form of a linear potential $-\eta x$ ($\eta > 0$) can be introduced in the system [148, 155]. For relatively large η (magnitude of the tilt), all the particles can be made to reside in one well. The subsequent dynamics can be studied by allowing $\eta \to 0$ within some characteristic time scale. Motivated by these prospects of experimentally achieving different initial states [156], we analyze the tunneling dynamics subject to different initial configuration.

In the weak coupling regime ($U = 0.1$) and the attractive limit ($U' < 0$ or $V = 2.U$), $P_R(t)$ oscillates and slowly dampens for the initial conditions given by (100) and (001) [as evident from Fig.3.3(a)], while the damping is faster with further weakening of the interaction field ($U' > 0$ or $V = 0.5U$) [Fig.3.3(b)]. The situation in the strong coupling limit ($U = 12$) show Rabi oscillations with different frequencies corresponding to the

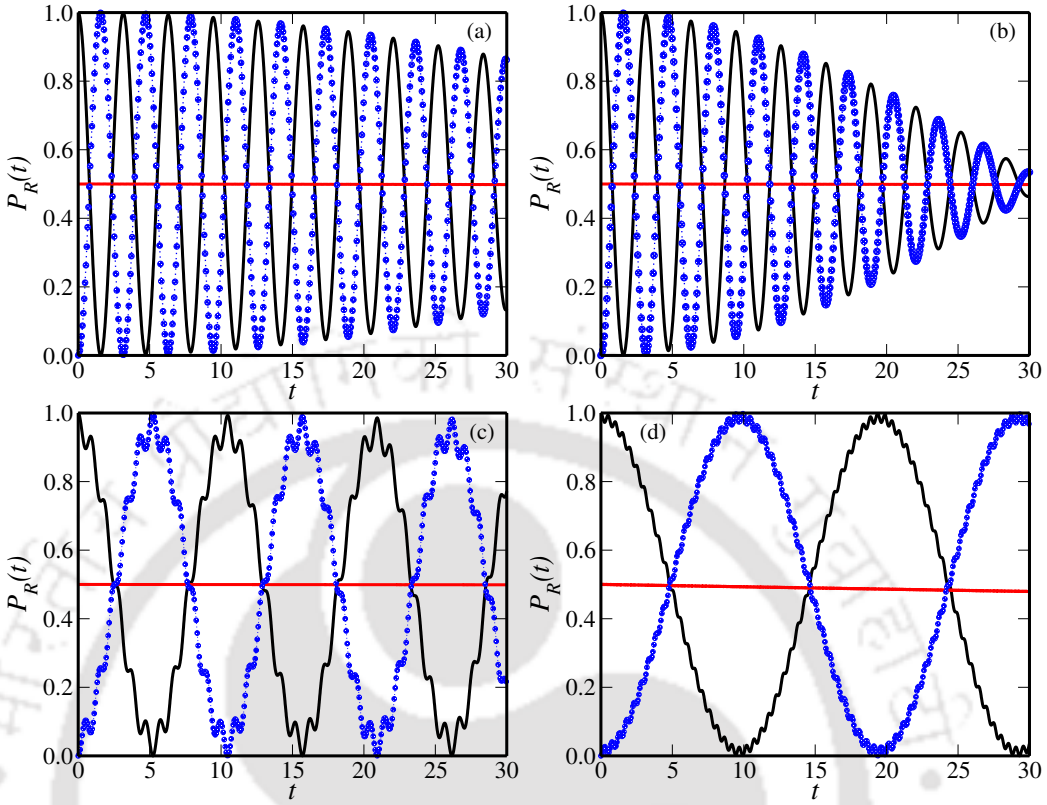

Figure 3.3: The right well population, $P_R(t)$ as a function of time corresponding to three different initial conditions is shown. In (a) $U' = 0.05$, and (b) $U' = -0.1$ solid line (black) denotes (100), dashed line (red) denotes (010) and diamonds with dots (blue) denote to(001). In (c) $U' = 6$ and (d) $U' = -12$ solid line (black) denotes (100), dashed-dotted line (red) denotes (010), and dashed lines (blue) denote (001).

$V = 2U$ [Fig.3.3(c)] and $V = 0.5U$ [Fig.3.3(d)] situations. It may also be noted that if we start with an initial condition (010) where one boson resides in each well, Eq.(2.24) reduces,

$$|\Psi(t)\rangle \quad = \quad c_1(t)\hat{a}_1^\dagger \hat{a}_2^\dagger |0\rangle \tag{3.12}$$

It can be shown that the above state is an eigenstate of the Hamiltonian in Eq.(3.1) and hence the dynamics is frozen which is seen from Fig.(3.3), where $P_R(t)$ stays at 0.5 irrespective of the values of parameters used. The frequency and time period of these oscillations depend upon the interaction parameters used in this work.

Let us now concentrate on the case of three bosons system ($N = 3$). The $P_R(t)$ in this case is defined as,

$$P_R(t) = |c_0(t)|^2 + \frac{2}{3}|c_1(t)|^2 + \frac{1}{3}|c_2(t)|^2 \tag{3.13}$$

Similar to the case of two bosons, here $P_R(t)$ is a combination of probabilities of all the bosons in the right well ($|c_0(t)|^2$), two in the right and one in the left with an amplitude $\frac{2}{3}$ and one in the right and two in the left with an amplitude $\frac{1}{3}$ respectively. While qualitatively the tunneling behavior remains unaltered as compared to two bosons, with regard to Rabi oscillations at $U' = 0$ (not shown here) and there is a temporary decay of the amplitude of oscillations [Fig.3.4(a)] due to the beating phenomena for $U' \neq 0$. It is also be observed that $V = 0.5U$ registers more significant decay of the amplitude owing to trapping effects. At large U, [Fig.3.4(b)], the time period of *'eventual'* oscillations becomes very large. This time period is about an order of magnitude larger compared to two bosons. In Fig.3.4(b), for $U' = 6$, one can observe tunneling phenomena at larger time scales, while at $U' = -12$ (large V), the tunneling of atoms take a very long time and we do not observe any tunneling until $t = 60$ and even to much large values of time (not shown here). This indicates emergence of trapping phenomena for large values of the exchange intercation V in the large U regime.

Next a close scrutiny of different initial conditions for three bosons in the small U regime reveals an interesting observation. $P_R(t)$, corresponding to the initial condition (0100) ((0010)), starts with $\frac{2}{3}$ ($\frac{1}{3}$), as expected. However, as time progresses, $P_R(t)$ modulates between values approximately 0.85 and 0.15 [Fig.3.4(c) and (d)]. Thus in the weak coupling regime ($U \simeq 0.1$), the fraction of the total number of bosons occupying the right well is becoming larger (smaller) than $\frac{2}{3}$ ($\frac{1}{3}$), thereby indicating a tendency of accumulation of particles in one of the wells. This seems like an interesting result as an accumulation of particles is not expected for $U < J$ ($U = 0.1$ in units of J here). $P_R(t)$ oscillating between values such as, $\frac{2}{3}$ and $\frac{1}{3}$ may have been more commonly expected. The other initial condition, namely, (1000) (or (0001)) does not exhibit any noteworthy feature and hence not included in the discussion.

Therefore, it indicates that in the case of odd number of particles, when both the wells contain unequal number of particles and the population difference between the wells differs by unity, then such a scenario of accumulation of particles may be observed. However in the noninteracting limit (with $V = U$), such accumulation of particles vanishes and $P_R(t)$ oscillates between $\frac{2}{3}$ and $\frac{1}{3}$. Similar result emerges for large U limit ($U = 12$) where the accumulation of particles ceases to be a possibility owing to trapping effects. We have skipped these plots for brevity.

As an extension of the ongoing discussion, we take a look at the case of four bosons.

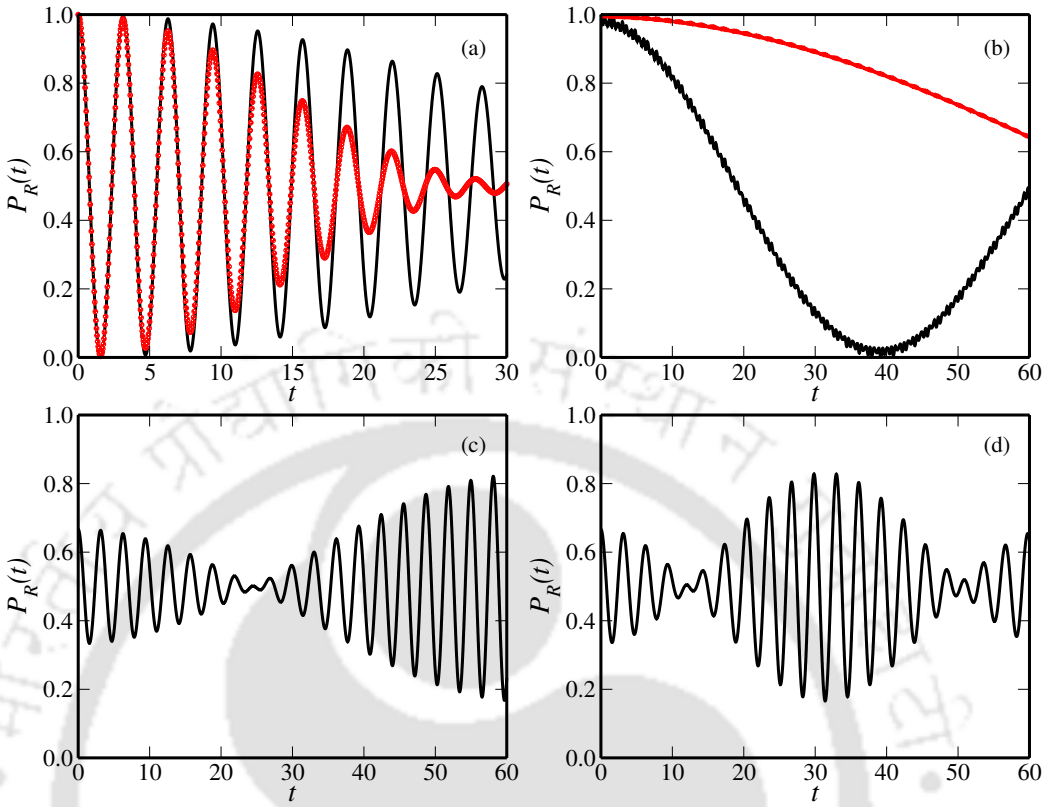

Figure 3.4: The time evolution of the right well population, $P_R(t)$ with the initial condition (1000) for three bosons. In (a) square with dots (black) denote $U' = 0.05$ and solid line (red) denotes $U' = -0.1$ and (b) solid line (black) denotes $U' = 6$ and dotted line (red) denotes $U' = -12$. $P_R(t)$ with (0100) initial condition is depicted in (c) with $U' = 0.05$ and (d) with $U' = -0.1$.

Here $P_R(t)$ is defined as,

$$P_R(t) = |c_0(t)|^2 + \frac{3}{4}|c_1(t)|^2 + \frac{1}{2}|c_2(t)|^2 + \frac{1}{4}|c_3(t)|^2 \tag{3.14}$$

There is no qualitative difference in the behavior for $P_R(t)$ both in $V = 2U$ and $V = 0.5U$ cases corresponding to the weak coupling regime for two or three bosons. In the strong coupling case as expected, the localization is strong, and a complete tunneling of all the particles is prohibited over a very large time scale. Thus the notion of (Rabi) oscillations at large U as inferred earlier, is no longer observed, at least for time scales $\sim 10^3$ (in limits of the tunneling frequency).

Again an inspection of $P_R(t)$ with different initial conditions such as (10000),(00001) and (00100) yield results similar to those corresponding to (100),(001) and (010), respectively, for two bosons with the last one in either case yields, $P_R(t) = 0.5$ for all t and this value is fairly insensitive to the values of U and V. For (01000) and (00010) as

possible initial conditions, that is, three particle in the right well and one in the left, $P_R(t)$ oscillate between values $\frac{3}{4}$ and $\frac{1}{4}$, and vice versa as expected.

Henceforth, the impact of initial conditions seem to be important for an odd number of bosons in a double well, specially when the population difference between the well is unity. The claim is substantiated by looking at the case of five bosons, for which, at small values of U, three particles in the right well and two in the left (or vice versa) produces probabilities nearly $\frac{4}{5}$ and $\frac{1}{5}$ as time progresses, which are greater than $\frac{3}{5}$ and $\frac{2}{5}$, thereby indicating a possibility of accumulation of particles. However, four particles in one well and one in the other demonstrates no such accumulation tendencies, where $P_R(t)$ values oscillate between $\frac{4}{5}$ and $\frac{1}{5}$ as expected. The plots are skipped here for brevity.

To see the effect of initial conditions, we have extended this work to triple well potential. The details are discussed in the Appendix A of the thesis.

3.1.3.1 Admixture of states

Further emphasis on the effect of initial conditions can be given as follows. Instead of choosing a particular initial state, one can consider an admixture of states. For example, for the case of two particles, instead of assigning an initial state (100), we may consider an admixture of the form,

$$\beta(100) + \gamma(010) + \delta(001)$$

with the restriction, $|\beta|^2 + |\gamma|^2 + |\delta|^2 = 1$. In this spirit, we have considered superposition of pure states by suitably choosing β, γ and δ and looked at the time evolved states via $P_R(t)$ for a comparison with those for the pure states. The corresponding plots for some specific choices of β, γ and δ are presented in Fig.(3.5). A slight deviation from a pure state, say (100) as an initial state, results in a slightly different [Fig.3.5(a) and (c)] or completely different dynamics [Fig.3.5(b) and (d)] where in the latter case, a small mixing of the probability amplitudes corresponding to (010) state yields an oscillatory dynamics. Thus the probability amplitudes of the initial states can slightly be modified to yield a desired oscillatory dynamics.

3.1.3.2 Time averaged dynamics - extrapolation to large N

In order to draw relevance of these results to the experiments done on cold atoms, we need to extend the studies for a large number of bosons. An exact computation of the quantum dynamics for such a large system is difficult. So we present a time averaged

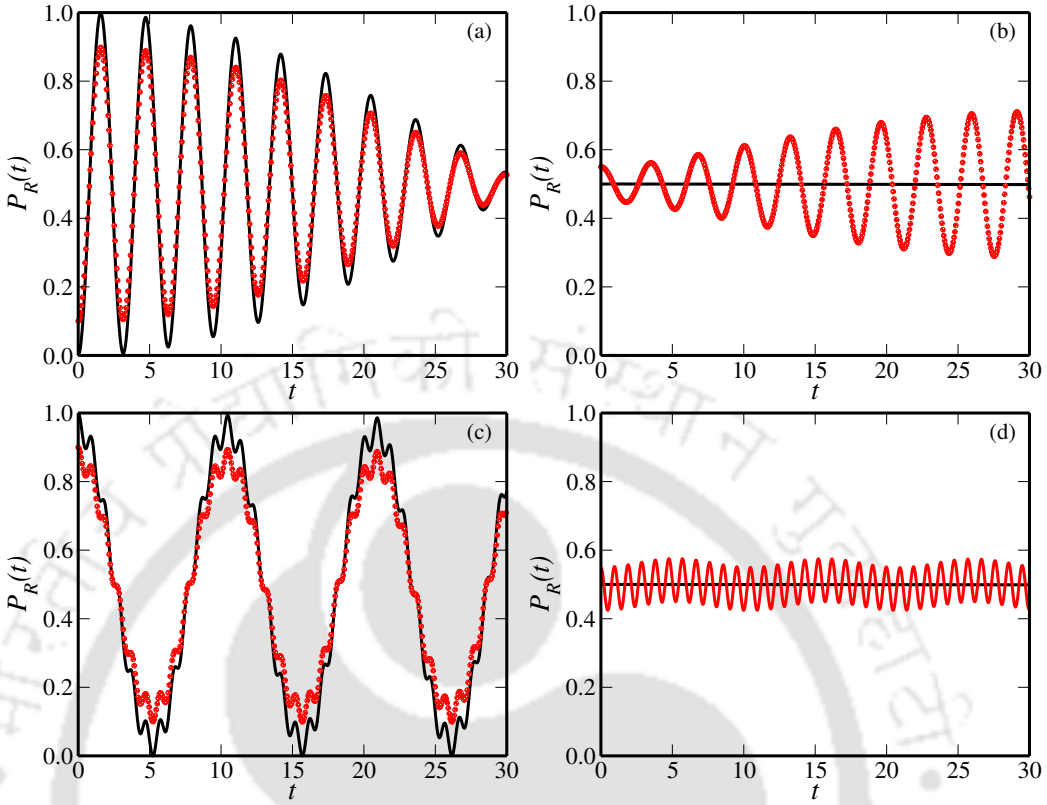

Figure 3.5: The time evolution of the right well population, $P_R(t)$ with different admixtures of initial conditions are shown for two bosons. In (a) $U' = -0.1$, squares with dashed lines (black) denote the initial condition (100) and solid line (red) denotes the initial condition $(\sqrt{0.9}, 0, \sqrt{0.1})$, (b) $U' = -0.1$, dashed lines (black) denote the initial condition (010) and solid line (red) denotes the initial condition $(\sqrt{0.1}, \sqrt{0.9}, 0)$, (c) $U' = 6$, squares with dashed lines (black) denote the initial condition (100) and solid line (red) denotes the initial condition $(\sqrt{0.9}, 0, \sqrt{0.1})$, (d) $U' = 6$ here dashed line (black) denotes the initial condition (010) and solid line (red) denotes the initial condition $(\sqrt{0.1}, \sqrt{0.9}, 0)$.

$P_R(t)$, denoted by α, which is defined as,

$$\alpha = \frac{1}{T}\int_0^T P_R(t) \tag{3.15}$$

by computing the EOM exactly for upto 16 bosons and plotted α as a function of $1/N$ (N being the number of bosons) and hence the results are extrapolated to $N \to \infty$ (or $1/N \to 0$). Here T is taken as 30 in units of $1/J$ (J being the tunneling amplitude). The results in the weak and strong coupling limits are presented in Fig.(3.6). In Fig.3.6(a) which corresponds to a small U regime, α does not depend on N and stays at an average value of 0.5, regardless of whether interaction effects have been included. In the large U regime [in fig. Fig.3.6(b)], α , although flat, yet different for different values of V corresponding to smaller number of particles, shows a linear fall off as N becomes large.

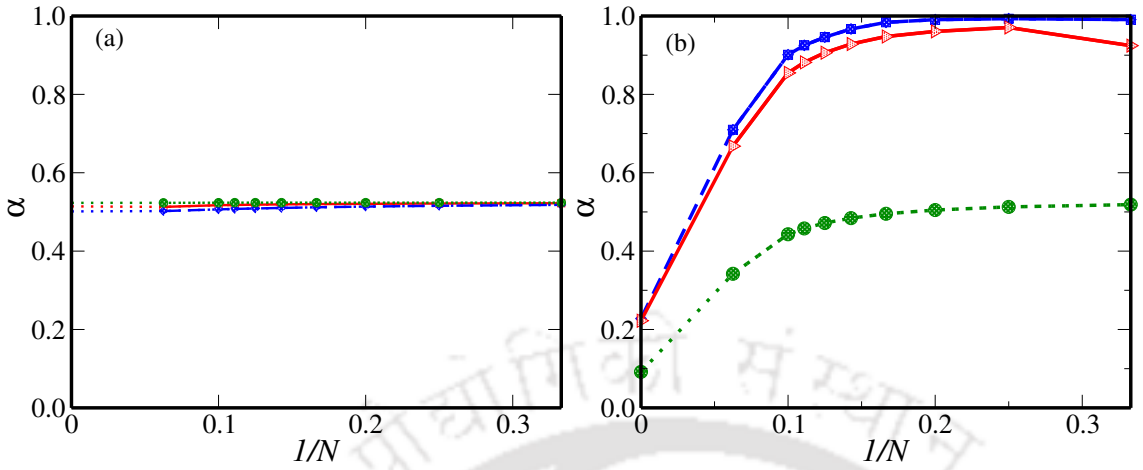

Figure 3.6: Time integrated value of the right well population i.e. α as a function of inverse of the number of bosons is shown for (a) weak and (b) strong coupling cases. In (a) circles with dotted line (green) denotes α for $V = U$ (non-interacting),solid line (red) denotes α for $V = 0.5U$ and diamonds with dashed line denotes α for $V = 2U$. In (b) circles with dotted line (green) denotes α for $V = U$ (non-interacting), right triangles with solid line (red) denotes α for $V = 0.5U$ and diamonds with dashed line (blue) denotes α for $V = 2U$.

In the limit $N \to \infty$, α becomes small $0.1 - 0.2$ (the extrapolated value), re emphasizing the onset of the trapping effects as the time averaged probability for the particles to spend in one of the wells (right well here) becomes small. Hence there is indeed a depreciation in the value of the time averaged right well population in presence of a large number of bosons in a double well potential, however qualitatively similar physics can be expected as that for a few bosons. To summarize the above discussions, we conclude by saying that the tunneling period not only increases with the particle number, but also depends on the interaction strength. Saturation behaviour of the time period (that is intense trapping) is expected in the limit of N for the strongly interacting regime as evident from Fig.(3.6).

3.1.4 Conclusions

We have carried out a detailed enumeration, though by no means exhaustive, of the effects of onsite interparticle repulsion on the tunneling dynamics of a few bosons in a double well potential. The strong and weak coupling limits are compared and contrasted with regard to the study of tunneling dynamics. Further, the sensitivity of the particle dynamics to different initial conditions is closely scrutinized. For an odd number of particles in the limit of weak repulsion, a population difference of one particle among the two wells seems to demonstrate accumulation tendencies. However, no such behavior

is observed for the population difference to be larger than one. Also the effect of an admixture of initial states on the tunneling oscillations has been studied. It is premature to comment on the implication of this result to more elegant phenomena, such as using it as an '*atom switch*' etc, however we feel that our results can motivate further experiments in the study of atomic dynamics in presence of correlation effects.

3.2 Dynamics of interacting bosons in a double well potential

3.2.1 Introduction

Following the realization of exotic behaviour of periodically driven systems, such as, ultracold atoms in a periodically shaken optical lattice, these systems have garnered unprecedented attention in recent years. One of the paradigmatic example of such a system is a kicked top or kicked rotor model where a particle moving on a ring is introduced to periodic kicks [157]. Hence the exhibition of transition from integrability to chaotic behaviour in specific limits [73, 74, 158, 159] and dynamical Anderson localization [73, 75, 158, 159], dynamical stabilization both in classical and quantum mechanics, coherent control of the phase transition from superfluid to Mott insulator [76], and parameter controlled the adiabatic transformation of a static Bose-Einstein condensate (BEC) into a dynamical Floquet condensate [77] are few conspicuous features of these systems. Therefore, they facilitate investigation of a particularly rich research area for the classical chaos and quantum chaos communities [160].

A substantial volume of literature exists in the field of driven BECs [117, 153]. Particularly, in the context of an optical lattice, a periodic driving can control the tunneling and interaction parameters, thereby providing the possibilities of manipulating the many-body states and quantum phases of the condensates [141, 142, 144, 161]. These periodically driven systems have been experimentally realized to induce many-body localization [78, 79, 162] and other exotic physical phenomena.

The double well trap is especially a paradigm model to study the fundamental tunneling properties of atoms. Here a system of bosons in a double well trap with driven interactions is identical to a two-site Bose Hubbard model (BHM) with time varying interaction potential [74, 144]. At zero or low values of the strength of the interaction

potential, the atoms execute usual Rabi oscillations. However, the scenario changes to a far from being Rabi-like, that is, a chaotic dynamics as the interaction strength is enhanced sufficiently. Depending on the system and forcing strength, there can be several routes to chaos, namely, quasiperiodicity [163, 164], period doubling [165], intermittency [166], crisis induced intermittency [167, 168], and Ruelle-Takens-Newhouse [169].

Motivated by such exciting possibilities, in this work, we consider a system of bosons in a double well trap interacting via a harmonically driven interaction between the bosons. We uncover distinct routes to chaotic dynamics using this setup. Furthermore, we show that an additional chirped frequency drive leads to a systematic control of the chaoticity of the system. A chirp is essentially a sinusoidal signal whose phase changes instantaneously at each time step and its correlation properties resemble an impulse function. In fact, adding chirp into the signal is an efficient tool in echolocation systems, such as radars and sonars etc. On the experimental front, the tunability of the rate of collisions in ultracold Rb atoms induced by near-resonant frequency chirp light, or the formation of these Rb molecules via photo-association technique have gathered momentum [170].

In this work, we use the harmonic and the chirp disturbances as agents that induce or suppress chaotic fluctuations in the dynamics. Further we present different routes to chaos arising in presence of different natures of the time varying interaction potential. In general we notice two kinds of route to chaos depending on the nature of the forcing: (1) quasiperiodic route to chaos in the situation where, frequency of the harmonic modulation (ω) is kept fixed at a particular value and the interparticle interaction strength is varied, and (2) the crisis induced intermittency route to chaos for the system where the interaction strength is kept fixed, while ω is varied within a certain range.

3.2.2 Equations of motion for the $SU(2)$ generators

We consider a system of interacting bosons in a double-well trap. In a two-mode approximation, the Bose-Hubbard Hamiltonian for a system of N interacting bosons occupying the weakly coupled lowest energy states (thereby enforcing the energies involved in system dynamics to be negligible corresponding to the excitation energies [47]) can be written as [74],

$$\hat{H} = \frac{\epsilon}{2}(\hat{a}_1^\dagger \hat{a}_2 + \hat{a}_2^\dagger \hat{a}_1) + \frac{\gamma}{2}(\hat{a}_1^\dagger \hat{a}_1 - \hat{a}_2^\dagger \hat{a}_2) - \frac{c(t)}{2}(\hat{a}_1^\dagger \hat{a}_1^\dagger \hat{a}_1 \hat{a}_1 + \hat{a}_2^\dagger \hat{a}_2^\dagger \hat{a}_2 \hat{a}_2) \quad (3.16)$$

where $\hat{a}_1^\dagger(\hat{a}_2)$ are the creation (annihilation) operators of bosons in the first (second) wells, ϵ is the coupling between the modes (i.e., the tunneling parameter and $\epsilon < 0$ here), γ is the energy difference between the quantum states and *c(t)* is the driving term that disturbs the system which is assumed to be time-dependent in our case (elaborated below). For $c(t) = c_0$, we recover the familiar BHM. The time-dependent interaction term has been studied earlier and periodic modulations for some or each of the terms in Eq. (3.16) have received some attention as well. In contrast to the above, we consider a chirp modulation in the driving term, in addition to a periodic component which we denote by,

$$c(t) \quad = \quad c_0 \cos(\omega t + \beta t^2) \tag{3.17}$$

where c_0 is the amplitude of the disturbance, ω and β denote harmonic and chirp modulations, respectively. Here, both the energy scales, namely γ and c_0 are measured in the units of ϵ.

It is observed that the Hamiltonian in Eq. (3.16) commutes with the total number of particles $N(=\hat{a}_1^\dagger\hat{a}_1 + \hat{a}_2^\dagger\hat{a}_2)$ and hence N is conserved. Further the Hamiltonian can be written in a symmetric fashion (upto a constant term depending on N) of the form,

$$\hat{H} \quad = \quad \frac{\epsilon}{2}(\hat{a}_1^\dagger\hat{a}_2 + \hat{a}_2^\dagger\hat{a}_1) + \frac{\gamma}{2}(\hat{a}_1^\dagger\hat{a}_1 - \hat{a}_2^\dagger\hat{a}_2) - \frac{c(t)}{4}(\hat{a}_1^\dagger\hat{a}_1 - \hat{a}_2^\dagger\hat{a}_2)^2. \tag{3.18}$$

To solve Eq. (3.18), it is convenient to introduce the SU(2) generators, namely the components of the angular momentum, [as discussed in **Chapter 2**] $\hat{L}_x$, $\hat{L}_y$ and $\hat{L}_z$ as, $\hat{L}_x = \frac{1}{2}(\hat{a}_1^\dagger\hat{a}_2 + \hat{a}_2^\dagger\hat{a}_1)$; $\hat{L}_y = \frac{1}{2i}(\hat{a}_1^\dagger\hat{a}_2 - \hat{a}_2^\dagger\hat{a}_1)$;$\hat{L}_z = \frac{1}{2}(\hat{a}_1^\dagger\hat{a}_1 - \hat{a}_2^\dagger\hat{a}_2)$ where the angular momentum operators, $\hat{L}_i$ obey the usual commutation relations, $[\hat{L}_i, \hat{L}_j] = i\hat{L}_k$ ($\hbar = 1$). With the above assumptions the Hamiltonian assumes the form,

$$\hat{H} \quad = \quad \epsilon\hat{L}_x + \gamma\hat{L}_z - c(t)\hat{L}_z^2 \tag{3.19}$$

The z-component, that is $\hat{L}_z$ denotes the difference in population density between the two wells.

The dynamics of the system is obtained by computing the equation of motion (EOM),

$$\frac{d}{dt}\hat{L}_i \quad = \quad \frac{1}{i}[\hat{L}_i, H] \tag{3.20}$$

In order to solve the EOMs it is necessary to take the expectation values of the operators, $\hat{L}_i$. However, even that has a difficulty as the expectation values of the first-order operators, namely $\langle\hat{L}_i\rangle$ depend on the second-order correlations, such as, $\langle\hat{L}_i\hat{L}_j\rangle$ [118],

which in turn would depend on higher order correlations, such as $\langle \hat{L}_i \hat{L}_j \hat{L}_k \rangle$ and so on. This will eventually render BBGKY hierarchy of EOMs for the expectation values. To have a tractable closed set of equations, the hierarchy must be terminated somewhere. The lowest order truncation retains only the first-order correlations, $\langle \hat{L}_i \rangle$. This enables defining a Bloch vector $\vec{J} = (J_x, J_y, J_z)$ with the components, $J_i \equiv \langle \hat{L}_i \rangle / N/2$. The EOMs hence read as,

$$\begin{aligned} \frac{d}{dt} J_x &= -\gamma J_y + 2\alpha (J_y J_z) \\ \frac{d}{dt} J_y &= \gamma J_x - \epsilon J_z - 2\alpha (J_x J_z) \\ \frac{d}{dt} J_z &= \epsilon J_y \end{aligned} \tag{3.21}$$

where the coupling $\alpha = c(t)\frac{N}{2} = c_0 \frac{N}{2} \cos(\omega t + \beta t^2) \equiv \kappa \cos(\omega t + \beta t^2)$. Here $\kappa = c_0 \frac{N}{2}$ is the modified interaction strength. Eq. (3.21) denote dynamics of the single-particle Bloch vector $\vec{J}$ whose length $|\vec{J}|$ is conserved and can be taken as unity. To solve Eq. (3.21) requires an initial condition, for which we can assume that at $t = 0$ the bosons populate both the wells equally, that is, half of them in each well, resulting in $J_z = 0$. Thus considering one of the possible initial condition as $\vec{J} = (0, 1, 0)$. Hence the tunneling dynamics can be obtained by solving Eq. (3.21).

To ascertain that the first-order truncation procedure outlined above is indeed sufficient, we have computed the exact dynamics by solving the time-dependent Schrödinger equation with the Hamiltonian in Eq. (3.16) in the Fock basis for a fixed (few) number of bosons. The exercise provides convincing evidence for similar tunneling characteristics, including the emergence of chaotic dynamics that are emphasized and carefully analyzed in the next section. Since computing the exact dynamics for larger number of particles is computationally expensive, it is sensible to resort to the solution of the truncated EOMs for our purpose.

3.2.3 Results

In order to have an intuitive idea about the dynamical behaviour of the system in a double well potential, we systematically investigate the time evolution of population imbalance between the wells, $J_z(t)$.

Next to get a deeper understanding of the trajectory of the system and the onset of chaotic behaviour therein, the power spectral density (PSD) is analyzed which is defined

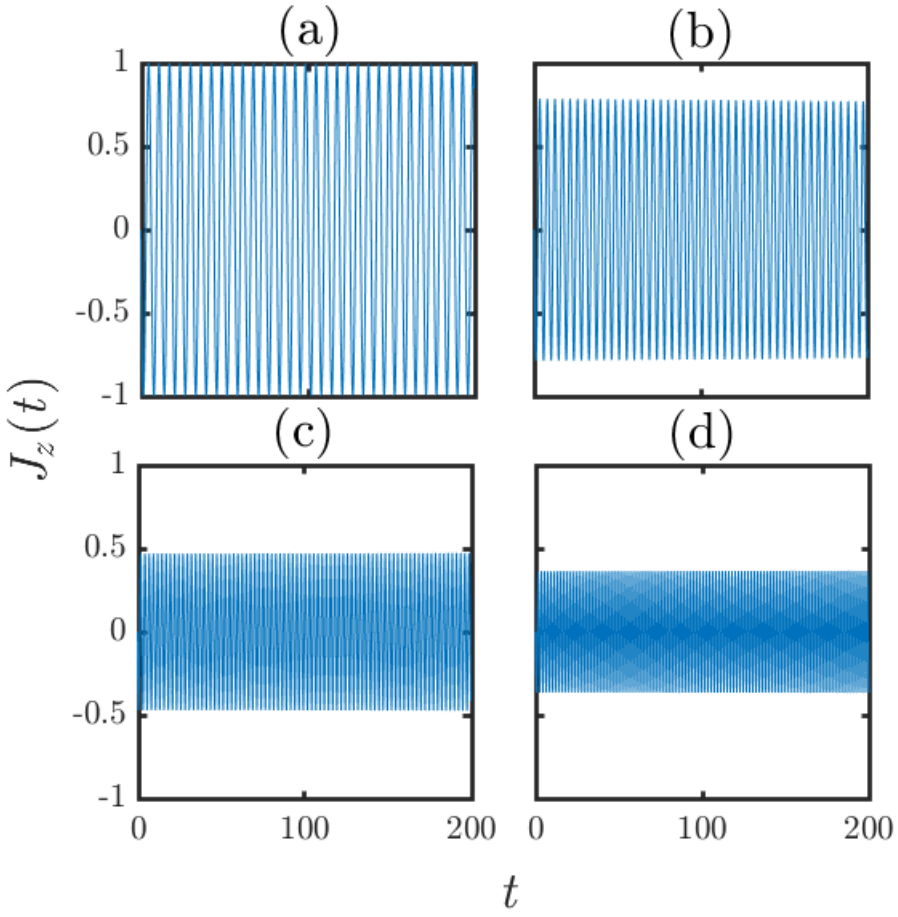

Figure 3.7: The dynamics of population imbalance, $J_z(t)$ for static interaction ($\omega = 0$, $\beta = 0$) with $|\epsilon| = 1$ and $\gamma = 0$. (a) $\kappa = 0$, (b) $\kappa = 1$, (c) $\kappa = 4$ and (d) $\kappa = 7$. t is in units of inverse of the energy scale, ϵ.

as,

$$PSD = \frac{1}{2\pi\mathcal{N}}|J_z(\mathcal{N}, f, \tau)|^2 \tag{3.22}$$

where $J_z(\mathcal{N}, f, \tau)$ is the discrete Fourier transform of the population imbalance, $J_z(t)$ evaluated at $t = k\tau$ ($k = 0, 1, ...\mathcal{N}$ and $\mathcal{N}$ is the length of the discrete time series). Finally, the corresponding phase space projection of $J_z(t+\tau)$ and $J_z(t)$ are plotted to distinguish different kinds of dynamics as the function of the driving term, α that emerge in a double well potential.

3.2.3.1 Static interaction, $\alpha = \kappa$

First we consider the case of static interaction, that is, without presence of any time variation in the coupling term, α. In absence of interaction, $\kappa = 0$, from the dynamics of

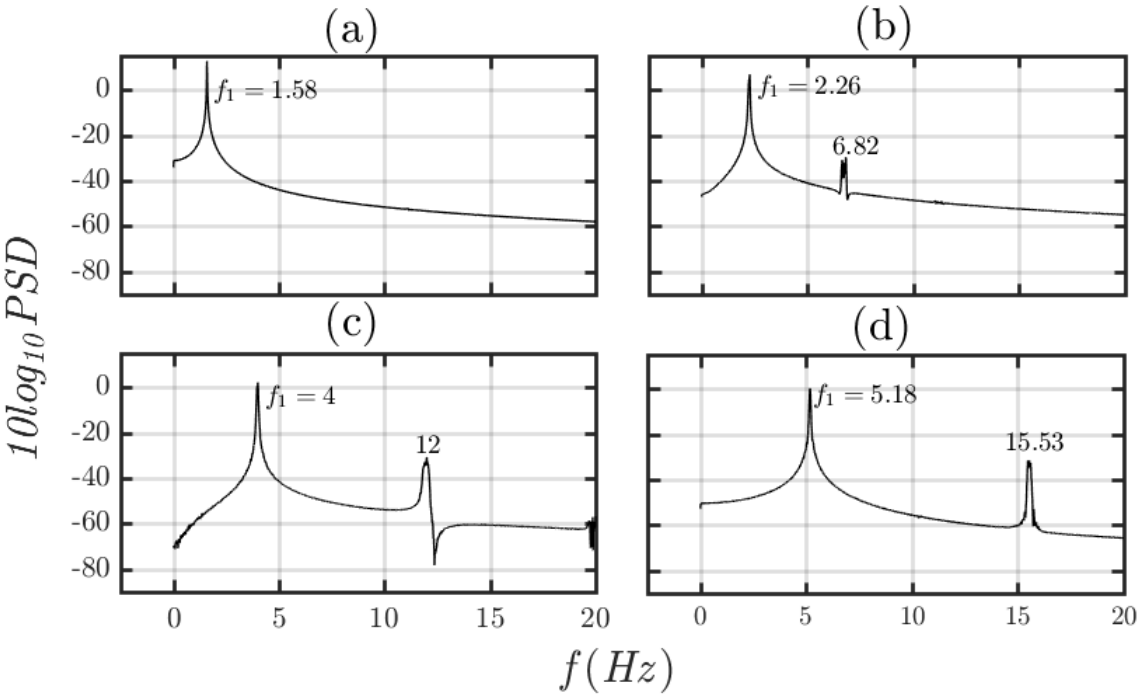

Figure 3.8: Power spectral density for static interaction ($\omega = 0$, $\beta = 0$) with $|\epsilon| = 1$, and $\gamma = 0$ with different values of κ, namely (a) $\kappa = 0$, (b) $\kappa = 1$, (c) $\kappa = 4$, and (d) $\kappa = 7$ respectively.

the population imbalance, $n(t)$ usual Rabi oscillation is observed (Fig.3.7(a)), where the particles periodically move back and forth among the two wells [117]. As the interaction strength, κ is gradually increased one observes damped Rabi oscillations, that is evident from Fig.3.7(b)-(d) where the amplitudes of $J_z(t)$ diminish indicating that only a fraction of the atoms move from one well to another [117].

In Fig.(3.8) we show the power spectral density, PSD of the temporal evolution of the population dynamics. We find that without any interaction, the fundamental frequency of the system appears at the frequency, $f_1 \simeq 1.6$, which is benchmarked as the frequency of Rabi oscillations.

Further, with the inclusion of the interaction term, the fundamental frequency gets shifted to larger values due to the change in the period of oscillations of the system (damped Rabi oscillations). For example, in Fig.3.8(b) f_1 gets shifted to 2.26 for $\kappa = 1$. In addition, we observe that for non-zero values of κ, PSD exhibits two peaks instead of one. However, a closer look reveals the fact that the second frequency present in the PSD at 6.82, which is simply a harmonic (or an overtone) of the fundamental frequency of the system, that is $f_2 \simeq 6.82 \simeq 3f_1$. Similarly in Figs.3.8(c) and 3.8(d), respectively for $\kappa = 4$ and $\kappa = 7$, two peaks are observed at $f_1 = 4$ and $f_2 = 12$ and $f_1 = 5.18$ and $f_2 = 15.53$.

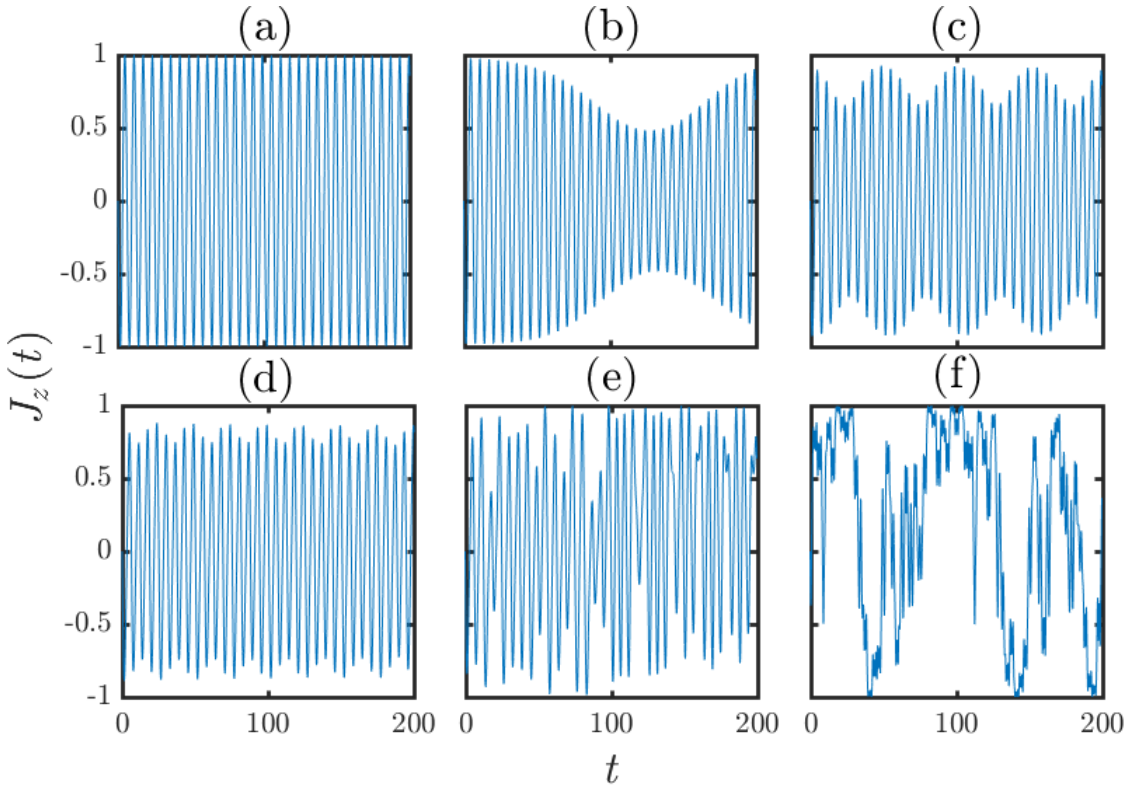

Figure 3.9: The dynamics of the population imbalance, $J_z(t)$ for $\omega = 1$, $\beta = 0$, $|\epsilon| = 1$ and $\gamma = 0$. (a) Presence of Rabi oscillations for $\kappa = 0$. (b) Appearance of two frequencies f_1 and f_2 at $\kappa = 0.3$. For (c) and (d), the observed dual periodicity becomes prominent for $\kappa = 0.6$ and $\kappa = 0.8$ respectively. Aperiodic nature is observed with further increase in κ in (e) and (f).

Again they satisfy $f_2 \simeq 3f_1$. Thus it is clear that upon increasing (only) the strength of the interaction potential (and no time variation yet), the dynamics of bosons in a double well involve only one frequency as it should be. This is also apparent from the dynamics presented in Fig.(3.7).

3.2.3.2 Harmonic modulation

Now we include the harmonically driven term in the interparticle interaction to see the effect on the dynamics of the system (that is, $\omega \neq 0$ and $\beta = 0$), such that $\alpha = \kappa\cos(\omega t)$. Let us further divide this scenario into two cases and explore the dynamics : first by keeping ω constant (say at $\omega = 1$) and by varying κ, and in the other, keeping κ fixed at a certain value and varying ω. We show that the two scenarios correspond to two different routes to chaos, namely,

(i) Fixed phase, varying amplitude: In the first case we keep the phase at $\omega = 1$

and vary the amplitude of the harmonic modulation, κ. With a gradual increase of the interaction strength, κ, it is observed that for $\kappa = 0.3$, the time evolved population imbalance, $J_z(t)$, shows appearance of a dual periodicity (Fig.3.9(b)), that is, both slow and fast oscillations are present, which is a hallmark signature of periodically driven systems. One of the periodicities corresponds to the natural dynamics with the other denoting the driving frequency. The slow oscillations become more frequent with increase in values for κ (see Fig.3.9(c)and 3.9(d)). However the observed dual periodicity in the behaviour of $J_z(t)$ gradually disappears at large values of κ. For very high values of κ ($\kappa = 7$), it is observed that the behaviour of $J_z(t)$ becomes completely aperiodic in nature (Fig.3.9(f)). There is an onset of chaotic dynamics in the system. Hence κ is fixed at this value, namely $\kappa = 7$ for subsequent discussion.

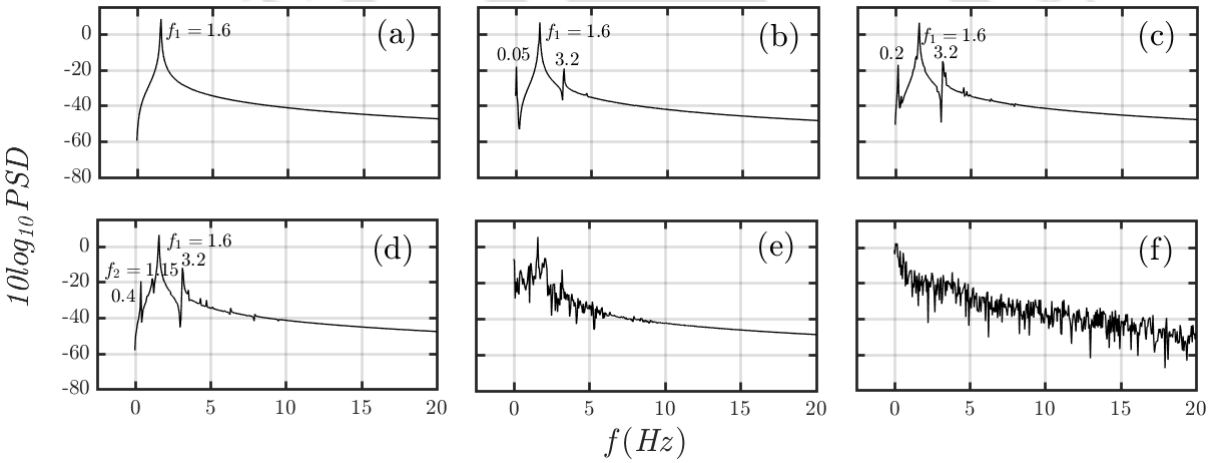

Figure 3.10: Power spectral density, PSD for $\omega = 1$, $\beta = 0$, $|\epsilon| = 1$, $\gamma = 0$ and for different values of κ, namely (a) $\kappa = 0$, (b) $\kappa = 0.3$, (c) $\kappa = 0.6$, (d) $\kappa = 0.8$, (e) $\kappa = 1$, and (f) $\kappa = 7$. Upto $\kappa = 0.6$, only frequency f_1 and it's harmonics are prsent. From $\kappa = 0.8$ onwards more frequencies start populating the spectrum. At $\kappa = 7$, it shows an exponential decay signaling to onset of chaos.

To probe deeper into the above scenario, we compute the power spectral density, PSD and systematically analyze the presence of different frequencies therein. In Fig.3.10 we show PSD for the case when the frequency is fixed ($\omega = 1$) and κ is varied in the range that is from $\kappa = 0$ to $\kappa = 7$. Without interaction, PSD peaks at the fundamental frequency $f_1 = 1.6$ (Fig.3.8(a) and 3.10(a)). For small and finite values of the interaction strength (for example, $\kappa = 0.3$), two peaks in PSD appears apart from f_1. One at $f \simeq 1.6$ and another at $f \simeq 0.05$ (marked in Fig.3.10(b)). These two frequencies are simply the harmonics of f_1. Upon further increase of κ, that is to $\kappa = 0.8$ results into the appearance of the peaks in PSD at frequencies $f_2 = 1.15$ and $f_1 = 1.6$. Since f_1 and f_2 are independent,

this indicates the involvement of two frequencies of oscillations in the time evolution of $J_z(t)$, which is a signature of the quasiperiodic nature of the system. With further increase in the interaction strength, we find that more frequencies near f_1 and f_2 start getting populated. Finally, for very large interaction strength, that is, $\kappa = 7$, PSD shows an exponential decay [164] with fully populated pattern over the entire frequency range (Fig.3.10(f)). This is the distinguishing feature of the onset of chaos. Thus for $\kappa = 7$, the observed aperiodic time evolution of $J_z(t)$ displays chaotic behaviour for the tunneling dynamics (see Fig.3.9(f)). Hence we obtain a series of transitions, namely, from periodic to quasiperiodic and finally to chaotic dynamics as the strength of the harmonic interaction is enhanced. Thus fixing ω and varying κ results in a *quasiperiodic route to chaos*.

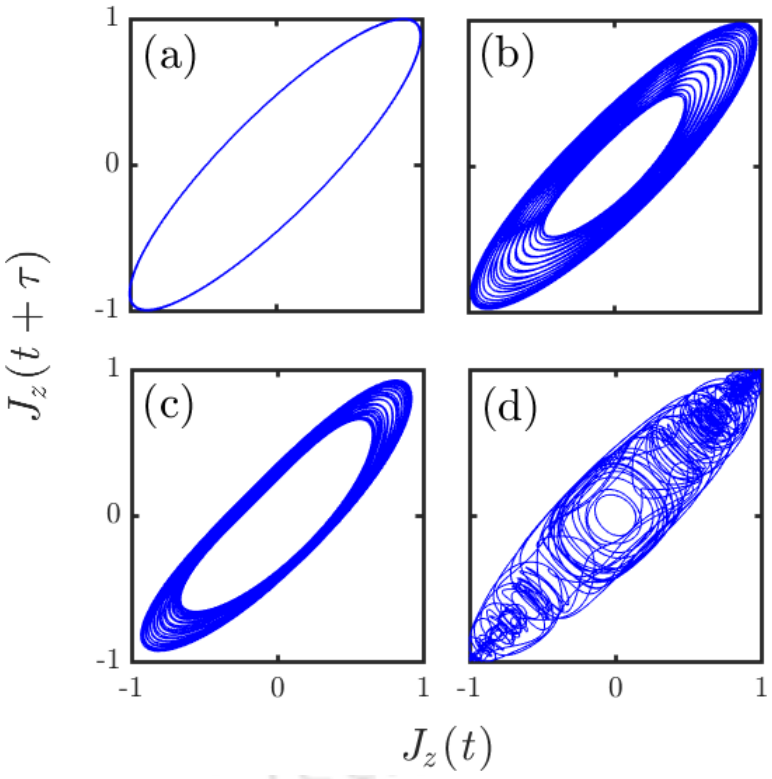

Figure 3.11: Phase space projection of the dynamics of population imbalance, $J_z(t)$ for constant ω, $\beta = 0$, $|\epsilon| = 1$, $\gamma = 0$ and varying κ). (a) periodic regime for $\kappa = 0$, (b)-(c) quasiperiodic regime for $\kappa = 0.3$ and $\kappa = 0.6$, and (d) chaotic regime for $\kappa = 7$.

Next we plot the phase space projection defined by $J_z(t+\tau)$ vs $J_z(t)$ to establish the observed chaotic behaviour in the system. Without any interaction ($\kappa = 0$), the phase space projection shows an usual elliptical trajectory (Rabi) depicting periodic behaviour of the system (Fig.3.11(a)). While for the quasiperiodic regime (small, but finite κ), the

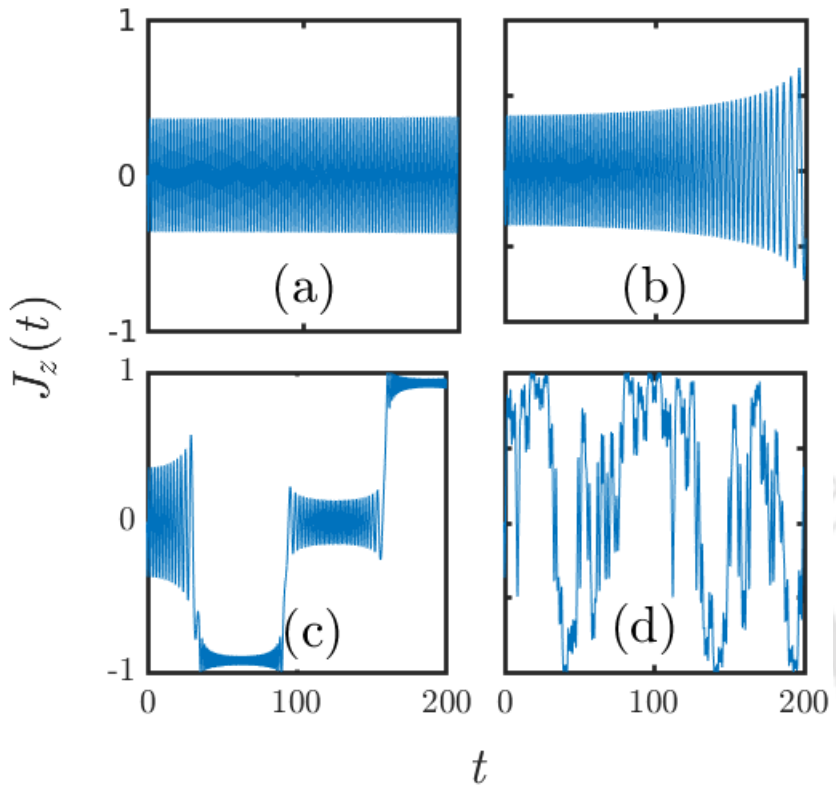

Figure 3.12: The dynamics of population imbalance, $J_z(t)$ for $\omega \neq 0$, $\beta = 0$, $|c| = 1$ and $\gamma = 0$ with constant κ, namely $\kappa = 7$. ω is varied, namely (a) $\omega = 0.002$, (b) $\omega = 0.008$, (c) $\omega = 0.05$, and (d) $\omega = 1$.

elliptical trajectory is observed with distinct width (see Fig.3.11(b)- 3.11(c)) denoting a quasiperiodic behaviour. Finally, for $\kappa = 7$, the phase space trajectory traces out path around multiple set of attractors that depict onset of a chaotic behaviour (Fig.3.11(d)). Thus the phase plots corroborate the information obtained from the spectral densities.

(ii) Fixed amplitude, varying phase:

In the second case, we fix $\kappa = 7$ and subsequently vary ω between 0 to 1. In Fig.3.12 we show the temporal evolution of the population imbalance, $J_z(t)$ in this case. For very small values of ω (say $\omega = 0.002$), we find that initially $J_z(t)$ exhibits damped Rabi oscillations with a single frequency (Fig.3.12(a)). On further increase in ω, say for $\omega = 0.008$ onwards, we observe appearance of multiple intermediate states in $J_z(t)$. The system fluctuates about the intermediate states for some time before making transition to another states. The switching between the states happens to be intermittently (Fig.3.12(b)). This feature becomes more distinct with further increase in ω and occurs for smaller time spans (see Fig.3.12(c)). Finally at $\omega = 1$, the dynamics of $J_z(t)$ become completely aperiodic (see

Fig.3.12(d)) as we have noted earlier. However the route to chaos appears to be different in this case. In what follows we will systematically analyze the appearance of the chaos in the system by analyzing PSD for this case.

The scenario of approaching to a chaotic trajectory on varying ω becomes clearer as we analyze PSD. In Fig.3.13 we show PSD for $\kappa = 7$ and varying the frequency in the range between $\omega = 0.002$ to $\omega = 1$. We find that PSD gets populated in a random fashion from $\omega = 0.002$ onwards (Fig.3.13(a)) and this random occurrence of a large number of new frequencies becomes more prominent with further increase in ω. Finally for $\omega = 1$ it leads to a chaotic behaviour which is quite evident from the exponential decay of PSD accompanied by the presence of large number of frequencies (Fig.3.13(d)). The transition in the dynamics from regular to a chaos happens due to the *crisis induced intermittency route to chaos*.

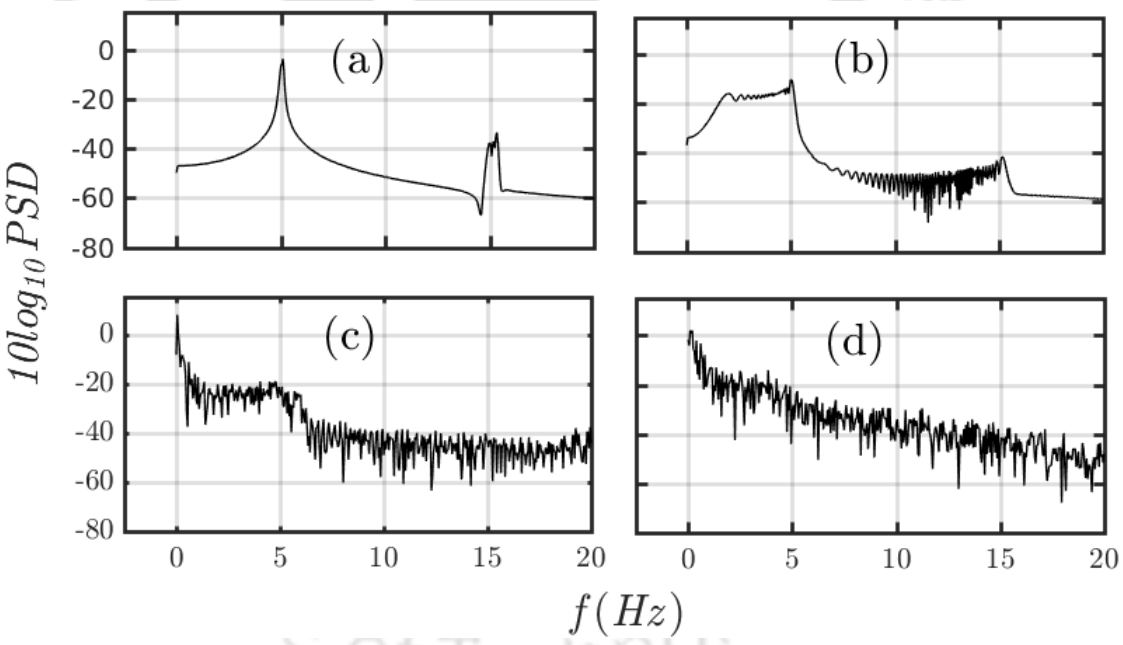

Figure 3.13: Power spectral density for a constant κ ($\kappa = 7$) and varying ω with $|\epsilon| = 1$ and $\gamma = 0$. (a) $\omega = 0.002$. (b)-(c) correspond to crisis induced intermittency at $\omega = 0.008$ and $\omega = 0.05$. (d) chaotic state at $\omega = 1$.

Hence with both the cases described above advocate chaotic scenario at $\kappa = 7$ and $\omega = 1$, however the routes to this transition to a chaotic regime are clearly different. To summarize, the first case suggests of a quasiperiodic route to chaos, while the latter bears fingerprints of an intermittency route to chaos. These are among the central results of our work, where a controlled variation of different parameters of a driven interaction

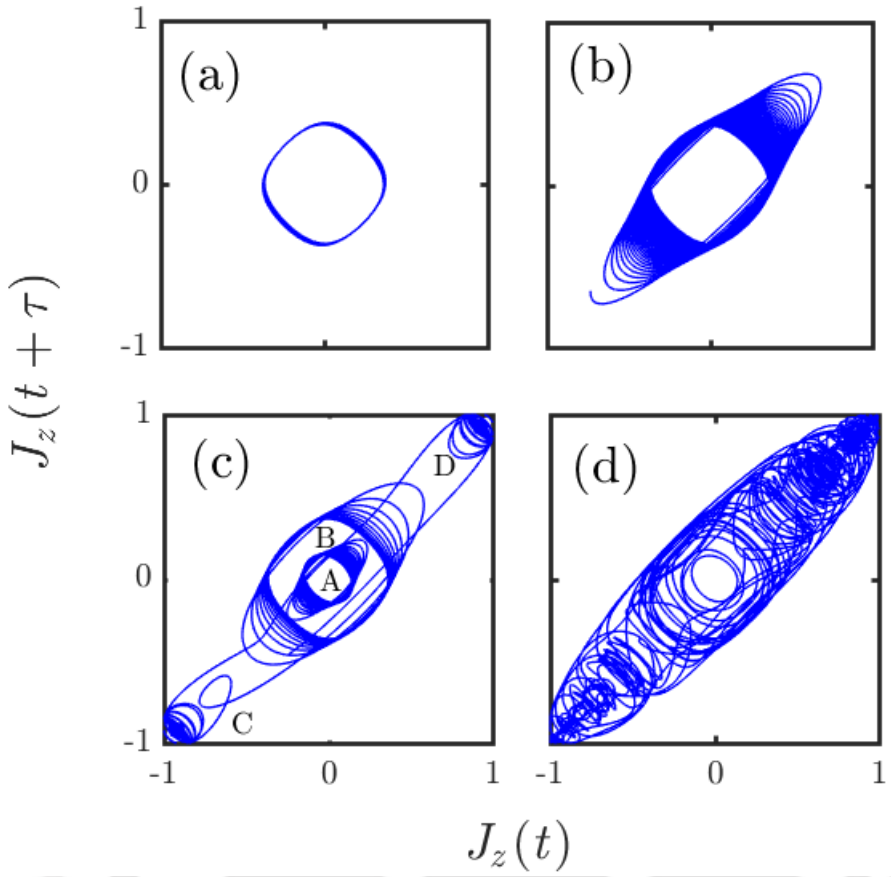

Figure 3.14: Phase space projection of $J_z(t)$ for $\kappa = 7$ and varying ω with $|\epsilon| = 1$ and $\gamma = 0$. (a) $\omega = 0.002$, (b) $\omega = 0.008$, (c) $\omega = 0.05$ and (d) $\omega = 1$. The orbit is regular for $\omega = 0.002$ which turns into torus (quasiperiodic) at $\omega = 0.008$. At $\omega = 0.05$ the system keeps on hopping intermittently between four attractors. At $\omega = 1$ orbit turns out to be completely chaotic.

renders different pathways leading to chaos.

A more lucid understanding of the above scenario can be offered in the following sense. Ramping up the amplitude (κ) of the driving term leaving the angular frequency (ω) all the while to have a constant value indicates a systematic way of perturbing the system. The dual, that is, slow and fast oscillations are preserved. Thus the chaos induced in this case is distinct from the one in which the amplitude is kept fixed and ω is varied. The later has different ramifications as the frequency associated with the driving term is constantly varied, however the natural frequency of the tunneling from one well to another remains the same. At large driving frequencies (here $\omega = 1$), a chaotic dynamics emerges which is distinct than the one noted in the previous case.

Finally, we study the phase space projection of the population imbalance, $J_z(t)$. For small value of ω ($\omega = 0.001$), it is observed that the phase space trajectory traces out

the usual elliptical orbit (Fig.3.14(a)) as the dynamics remain periodic at this value of ω. The regular orbits turns into torus (quasiperiodic) at $\omega = 0.008$ as shown in the Fig.3.14(b). In Fig.3.14(c) we find that for $\omega = 0.05$, the system intermittently keeps switching between the four torus (marked as A, B, C, D) which is also termed as crisis induced intermittency [167, 168]. At large frequency, namely, $\omega = 1$ the orbits turns out to be completely chaotic. Here it appears that the system remains around one of the orbit (torus) for sometime and further makes transitions to others in an intermittent way. This frequent visits to the different intermediate states lead to the chaotic behaviour in the system.

3.2.3.3 A chirp modulation ($\beta \neq 0$)

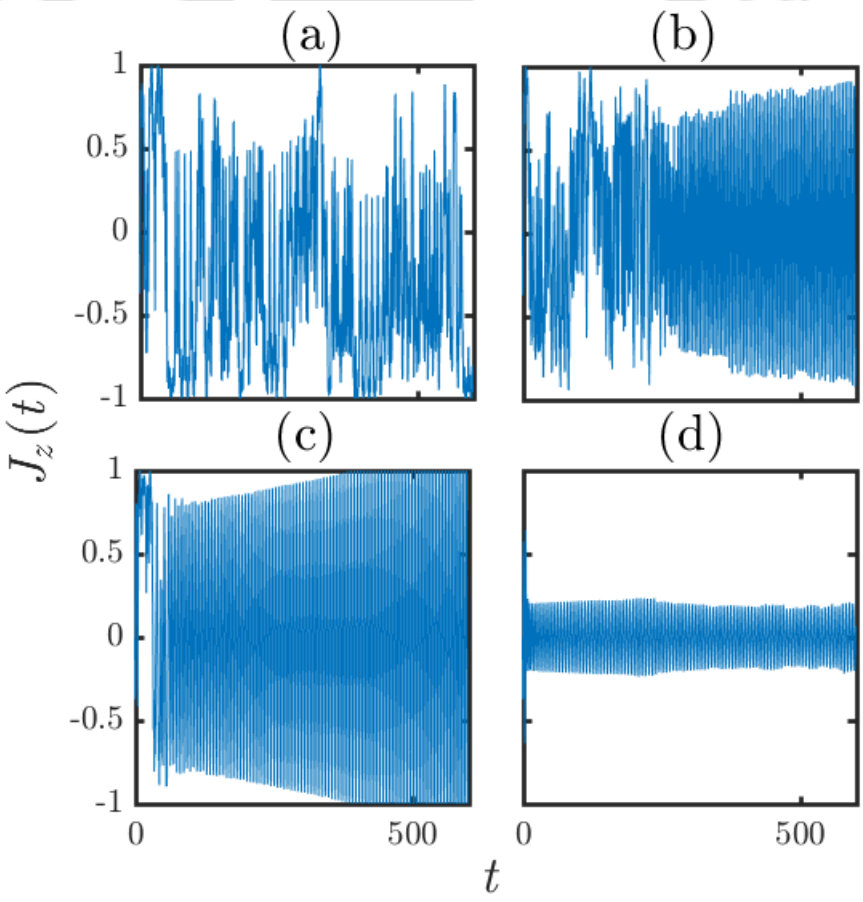

Figure 3.15: $J_z(t)$ for $\omega \neq 0$ and $\beta \neq 0$ with $|\epsilon| = 1$ and $\gamma = 0$. Here we keep $\omega = 1$ and varying β gradually for $\kappa = 7$. Transition from aperiodic to periodic trajectory is observed with gradual increase in β.

We now superpose a chirp signal on the harmonic interparticle interaction, that is,

$\omega \neq 0, \beta \neq 0$ (see Eq.(3.17)) and investigate what effects does it bring on the tunneling dynamics. We continue with $\kappa = 7$ and $\omega = 1$. Now we vary the frequency of the chirp modulation, β (in units of square of the energy scale) within a certain range. For very small value of β (namely, $\beta = 0.001$), the time evolution of the population imbalance, $J_z(t)$, shows aperiodic motion that is chaotic in nature (similar to Fig.3.9(f)). As we gradually increase β, periodicity in the evolution of $J_z(t)$ is restored partially as seen in Figs. 3.15(b) and 3.15(c) for $\beta = 0.009$ and 0.04, respectively. With further increase in β, for example, $\beta \sim 0.3$, the dynamics of Jz becomes periodic in nature (shows damped Rabi oscillation similar to the case shown in Fig.3.7(b)-(d)), which is clear from Fig.3.15(d).

The observed feature suggests that addition of a small amount of chirp signal in the forcing term suppresses the chaotic fluctuations in the tunneling dynamics where the latter was generated by the harmonic term in the driving.

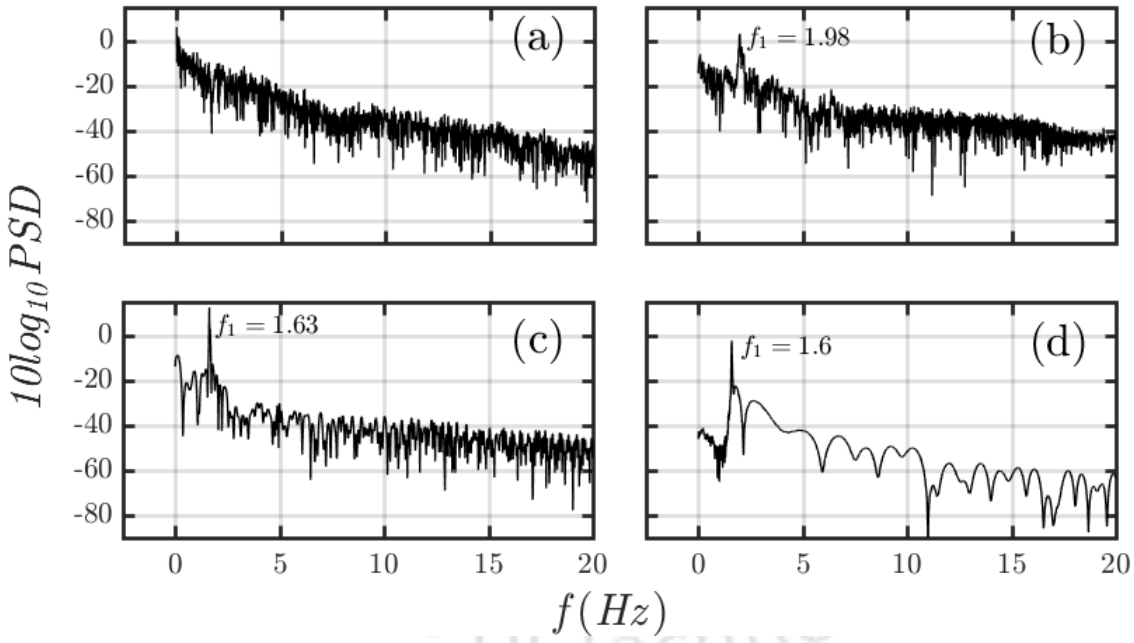

Figure 3.16: PSD for $\omega \neq 0$ ($\omega = 1$), $\beta \neq 0$ (varying β), $|\epsilon| = 1$ and $\gamma = 0$ with $\kappa = 7$. (a) $\beta = 0.001$, (b) $\beta = 0.009$, (c) $\beta = 0.04$, and (d) $\beta = 0.3$. With increase in β, the system restores its periodic behaviour. At $\beta = 0.3$ PSD is peaked at the frequency $f_1 = 1.6$ which is similar to the Rabi frequency.

The power spectral density, PSD yields deeper insights into the observed aperiodic–to–periodic transition of the dynamics in presence of a chirp modulation. For $\beta = 0.001$, PSD shows exponential decay with a large number of frequencies being present, which culminates into a chaotic behaviour (Fig.3.16(a)). With further increase in β, say for

$\beta = 0.009$, development of one prominent peak is observed at a frequency $f_1 = 1.98$, along with some fluctuations hinting towards the emergence of an orderly motion. At $\beta = 0.04$, the fluctuations gradually subside, and a prominent frequency shifts to a value $f_1 \sim 1.6$. It may be noted that this is the same frequency observed corresponding to the case of no interaction (similar to Fig.3.8(a)). Finally, for $\beta = 0.3$, PSD shows a distinct peak precisely at $f_1 = 1.6$ that indicates the dynamics to be orderly in nature that is the atoms execute (damped) Rabi-like oscillations. Thus the chirp modulation brings back periodic nature to the tunneling dynamics by suppressing the observed chaotic behaviour at large interaction strengths.

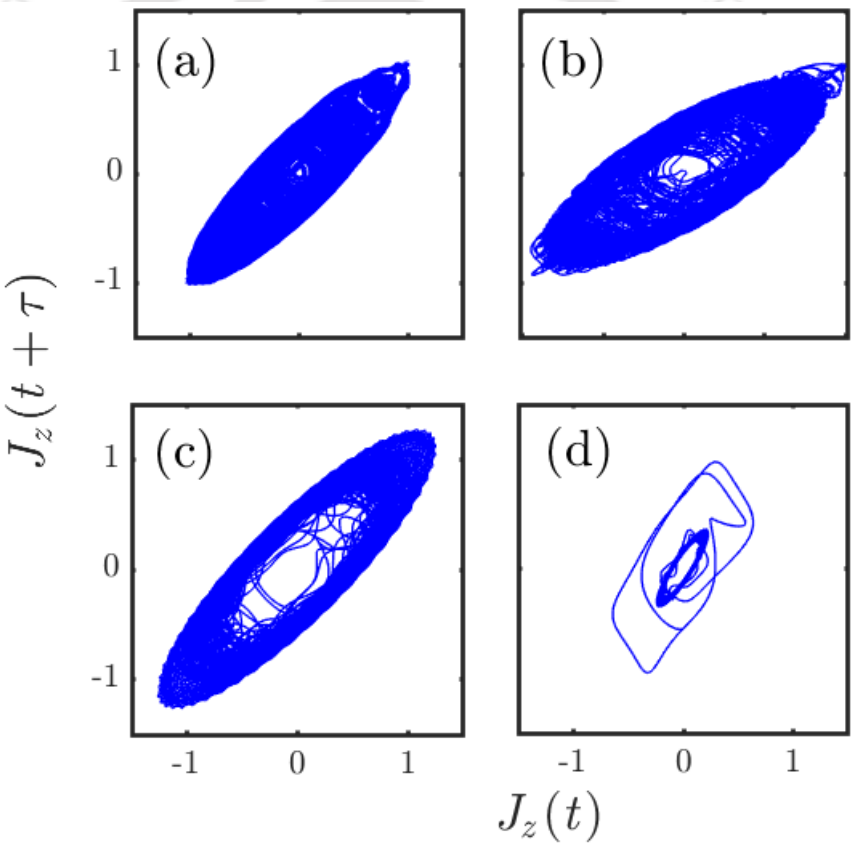

Figure 3.17: Phase space projection of $J_z(t)$ for $\omega \neq 0$ ($\omega = 1$), $\beta \neq 0$ (varying β), $|c| = 1$ and $\gamma = 0$ with $\kappa = 7$. (a) $\beta = 0.001$, (b) $\beta = 0.009$, (c) $\beta = 0.04$ and (d) $\beta = 0.3$. The orbit is completely chaotic for $\beta = 0.001$ which turns into a periodic one at $\beta = 0.3$.

A physical feel for the above result can be obtained in the following sense. Since the chirp term involves βt^2, it oscillates faster than the harmonic term and hence the system feels as if being subjected to a constant force owing to the fact that the chirp oscillations

are significantly faster than the natural frequency of the motion of the particles between the two wells.

To confirm the re-entrant of periodic behaviour, we also study the phase space projection of the population imbalance $J_z(t)$. It is observed that for small value of β ($\beta = 0.001$), the phase space orbit appears to be completely chaotic in nature as shown in Fig.3.17(a). However the orbit takes the shape of a toroid for $\beta = 0.04$ (Fig.3.17(c)). Finally, further increase in β ($\beta = 0.3$) leads to emergence of almost periodic orbit rendering to the onset of a orderly motion as shown in Fig.3.17(d). Similar effects of chirp modulation in frequency on the dynamics of collisions of Rb atoms has been reported in Ref. [170].

3.2.4 Conclusions

In this work, we have investigated the tunneling dynamics of a system of bosons in a double well potential in presence of a harmonic interaction potential. At large values of the interaction strength, the system makes a transition from a regular to a chaotic state. This feature is complemented very well by investigating the power spectral density and phase space projection. In particular, for the case of harmonic interaction potential, different routes to chaos emerge depending on whether the amplitude or the phase of the interaction term being tuned. In the former case, we observed that the route to chaos is quasiperiodic, while, for the latter case, the the route to chaos is through the crisis induced intermittency. Finally we demonstrated that superposition of a chirp modulation to the harmonic driving term restores the periodicity in the tunneling dynamics of bosons in a double well potential.

3.3 Ultracold gases in presence of time-dependent synthetic field

3.3.1 Introduction

The successful experimental realization of ultracold atoms render a defect free and powerful paradigm to explore various intriguing quantum many-body phenomena, for example, phase transition from superfluid (SF) to Mott insulating (MI) state for a system of neutral alkali atoms [3]. These quantum phase transitions in optical latices can be customarily achieved by tuning the shape of the trapping potential. Thus the tunability

of the lattice parameters and interaction between the trapped atoms via Feshbach resonance render an experimentally controlled environment. Here the employment of MI state leads to the detection of quantum entanglement in experiments [171–173].

In recent times, successful realization of synthetic gauge fields both in continuum [89] and in lattice systems [90, 91] have pioneered as well as elevated the way for studying the physics of charged particles with neutral atoms. Usually electrons in a periodic potential results into Bloch bands, however when a magnetic field is introduced in the system, the observed bands split into highly degenerate Landau levels. Thus the coupling between the periodic potential and the magnetic field for a two-dimensional electron gas results into the emanation of a self similar fractal energy spectrum, termed as Hofstadter's butterfly [174]. In case of a normalized magnetic flux, $\phi = p/q$ (where p, q are integers and ϕ is rational), each Bloch levels splits into q sub levels. When the fractal gap, that is the energy difference between the allowed and forbidden levels of the Hofstadter's spectrum vanishes, these self similar energy levels modify into the Bloch bands [175]. This result into a topological characterization of the system [176] and also emergence of topologically protected edge states. Ultimately the interaction of the particles with synthetic gauge field leads to the experimental investigation of various intriguing quantum phenomena, such as, topological properties [92–94], quantum Hall states [95], Hofstadter's fractal energy spectrum [90, 91], and supersolid like states in non-Abelian fields [96, 97]. The emergence of vortices in a Bose-Einstein condensate are also a hallmark signature of synthetic magnetic field [177] .

The charge neutrality of the ultacold atoms in optical lattices induces a restriction to study the behavior of these atoms in presence of a magnetic field. One way to overcome this constraint is by subjecting these neutral atoms to a rotational motion. Here the Coriolis force due to rotation of the ultracold atoms replace the role of Lorentz force on a charged particle induced by the magnetic field [177–180]. Hence the corresponding vector potential ($\mathbf{A} = \nabla \times \mathbf{B}$) is replaced by $\Omega \times \mathbf{r}$; Ω denotes the rotational frequency and $\mathbf{r}$ being the position vector. Thus the magnetic field $\mathbf{B}$ is mimicked by Ω. This effective magnetic field is termed as a synthetic or an artificial magnetic field and here the motion of cold atoms is analogous to that of the charged fluid in an external magnetic field. In experiments, the effects of synthetic magnetic fields are produced by utilizing a combination of light-atom interaction that induces a momentum space shift to form a spatially dependent vector potential [181]. Due to the coupling of momentum space technique to a real space manipulation, these experiments are highly sophisticated and achieved

mainly in lattices. Hence there are technical restrictions on the homogeneity, value of the synthetic magnetic field and the lifetime of these systems [91, 92]. The generation of synthetic field in continuous systems includes rotation [182] and laser illumination [89, 181] techniques. However, in lattice systems, it includes various microwave [183], optical [184–186] and cold-atom [91, 187, 188] techniques for generating a synthetic field.

We investigate the effect of a time-dependent synthetic field on the SF-MI phase transition in this work. The study of a time-dependent synthetic field is fascinating for the following reasons. Generally, a static synthetic field implemented in the current experiments mainly depend on imitating the effect of vector potential, $\mathbf{A}$ and do not produce the effect of the scalar potential, Φ. However, a time-dependent synthetic gauge field not only yields a time-dependent vector potential, $\mathbf{A}(t)$, but also creates the effect of a scalar potential, Φ [189]. Further for a static case, it is possible that two different forms of the vector potential have the same curl and hence correspond to an gauge field. The Hamiltonians are also equivalent upto a gauge transformation. However, in presence of time-dependencies, even if the curl of the vector potentials yield the same gauge field at all times, the Hamiltonians may not be connected by a gauge transformations owing to the value of the lack of of a scalar potential [190].

Moreover a time-dependent gauge field or a vector potential will result from time dependent current densities. Such a scenario can be mimicked by accelerating the lattice or applying a linearly varying potential as a function of time which would eventually result in movement of atoms with respect to the optical lattice, and hence results in a time dependent current. In experiments, such systems can be created by employing driven optical lattices. The driving is implemented by introducing a frequency difference between the counter-propagating laser beams (by employing acousto-optic modulators that control the power of the laser beams [191]), results into an inertial time-dependent force in the lattice frame. Thus on general grounds, time dependent gauge fields are interesting and its effects on the ground state phase diagram are worth exploring, apart from the fact that they have received scarce attention so far. Also, these time-dependent configurations are crucial for Floquet engineering, such as, Floquet topological insulators [93, 192–195] and also recently contemplate as probes for topological materials [196, 197].

3.3.2 Model

Consider a spin-0 ultracold bosonic gas in presence of a time dependent synthetic magnetic field $B_s(t)$ which is described by a vector potential $\mathbf{A}_s(t)$. In the chosen Landau gauge, $\mathbf{A}_s(t)$ is given as $\mathbf{A}_s(t) = B_s f(t) x\hat{y}$. The Bose Hubbard Hamiltonian for a system of scalar Bose gas in presence of a time dependent synthetic gauge field is written as [47, 178, 198, 199],

$$H = -\sum_{<ij>}(J_{ij}(t)a_i^\dagger a_j + h.c) - \mu\sum_i n_i + \frac{U}{2}\sum_i n_i(n_i - 1) \tag{3.23}$$

Here $J_{ij}(t)$ is the hopping matrix elements from site i to nearest neighbour site j which acquires a phase shift in presence of a gauge field as $J_{ij}(t) = Je^{-i\frac{2\pi}{\phi_0}\int_i^j \mathbf{A}_s(t).\mathbf{dl}}$. Thus $\mathbf{A}_s(t)$ (or the corresponding field) enters in the hopping term of the Hamiltonian through the phase factor via Peierls coupling. Here $f(t)$ takes care of the time dependence of $\mathbf{A}_s(t)$ and ϕ_0 is the magnetic flux quantum (= h/e). For this particular choice of the gauge field, the integral assumes the value as $\phi(t) = B_s f(t) l_0^2/\phi_0$, l_0 being the lattice spacing taken to be unity. $a_i^\dagger(a_i)$ is the boson creation (annihilation) operator at a site i and the particle number operator is $n_i = a_i^\dagger a_i$. U is the onsite interaction and μ is the chemical potential. Here we consider a two dimensional square lattice where every lattice site i can be expressed by two indices as $i = [l, m]$, l corresponds to lattice site along x direction and m along y direction of the lattice.

To decouple the hopping term, we use the mean field approximation where we can write the hopping term as [198–200],

$$a_{(l,m)}^\dagger a_{(l+1,m+1)} \simeq \langle a_{(l,m)}^\dagger\rangle a_{(l+1,m+1)} + a_{(l,m)}^\dagger\langle a_{(l+1,m+1)}\rangle \tag{3.24}$$

here $\langle\ \rangle$ denotes the equilibrium value of an operator. Defining the superfluid order parameter at a site (l, m) as, $\psi_{(l,m)} = \langle a_{(l,m)}\rangle$ and substituting this in Eq.(3.23), the BHM can be written as a sum of single site Hamiltonians as, $H = \sum_{l,m} H_{l,m}^{MF}$ where,

$$\begin{aligned} H_{l,m}^{MF} &= -[J_{l+1,m}\psi_{l+1,m}^* a_{l,m} + J_{l-1,m}\psi_{l-1,m}^* a_{l,m} \\ &+ J_{l,m+1}\psi_{l,m+1}^* a_{l,m} + J_{l,m-1}\psi_{l,m-1}^* a_{l,m} + h.c] \\ &+ \frac{U}{2}n_{l,m}(n_{l,m} - 1) - \mu n_{l,m}] \end{aligned} \tag{3.25}$$

Using the Bloch periodic boundary condition and calculating the hopping matrix element between site (l,m) to a nearest neighbour $(l\pm1,m\pm1)$ we can write,

$$J_{l\pm1,m\pm1}\psi_{l\pm1,m\pm1} = \begin{cases} J\psi_{l\pm1,m}; l, m = l\pm1, m \\ Je^{\mp i2\pi l\phi f(t)}\psi_{l,m}; l, m = n, m\pm1 \end{cases} \tag{3.26}$$

where the time dependent function, $f(t)$ is chosen as,

$$f(t) = \left(\frac{t}{\tau}\right)^{\alpha} \qquad \alpha = 0.5, 1, 2 \tag{3.27}$$

here τ is a constant in units of time and we fix it as $\tau = 1$ throughout the study. Now to compute the ground state energy of the system, we first evaluate the matrix elements of the mean field Hamiltonian, $H^{MF}_{l,m}$ in the occupation number basis, $|n_{(l,m)}\rangle$ as,

$$\langle n_{l,m}|H^{MF}_{l,m}|n'_{l,m}\rangle = h^{d}_{l,m} + h^{od}_{l,m} \tag{3.28}$$

where the $h^{od}_{l,m}$ correspond to the matrix elements coming from the off diagonal terms as,

$$h^{od}_{l,m} = -J\sqrt{n_{l,m}}[\psi^{*}_{l+1,m} + \psi^{*}_{l-1,m} + (e^{-i2\pi\phi l t^{\alpha}} + e^{i2\pi\phi l t^{\alpha}})\psi^{*}_{l,m}] \tag{3.29}$$

and the diagonal part, $h^{d}_{l,m}$ is calculated as,

$$h^{d}_{l,m} = \frac{U}{2}n_{l,m}(n_{l,m}-1) - \mu n_{l,m} + C_{l,m}(\psi^{2}_{l,m})] \tag{3.30}$$

Starting with some some guess value for $\psi_{l,m}$, we compute the ground state eigenfunctions, $\Psi_g(\psi_{l,m})$ after diagonalizing $\langle n_{l,m}|H^{MF}_{l,m}|n'_{l,m}\rangle$ with $n = 10$. Finally the equilibrium SF order parameter and the local densities are calculated using self consistency conditions and are given by,

$$\psi_{l,m} = \langle\Psi_g(\psi_{l,m})|a_{l,m}|\Psi_g(\psi_{l,m})\rangle \tag{3.31}$$

$$\rho_{l,m} = \langle\Psi_g(\psi_{l,m})|n_{l,m}|\Psi_g(\psi_{l,m})\rangle \tag{3.32}$$

3.3.3 Results

Let us consider that the bosons are subjected to a time dependent synthetic magnetic flux of the form, $\phi(t) = \phi f(t)$ where the time independent magnetic flux, ϕ can be expressed in the form of a rational fraction, that is, $\phi = p/q$, where p and q are integers. In our case, $\phi(t)$ can be thought of as a time-dependent magnetic flux. It may be noted that

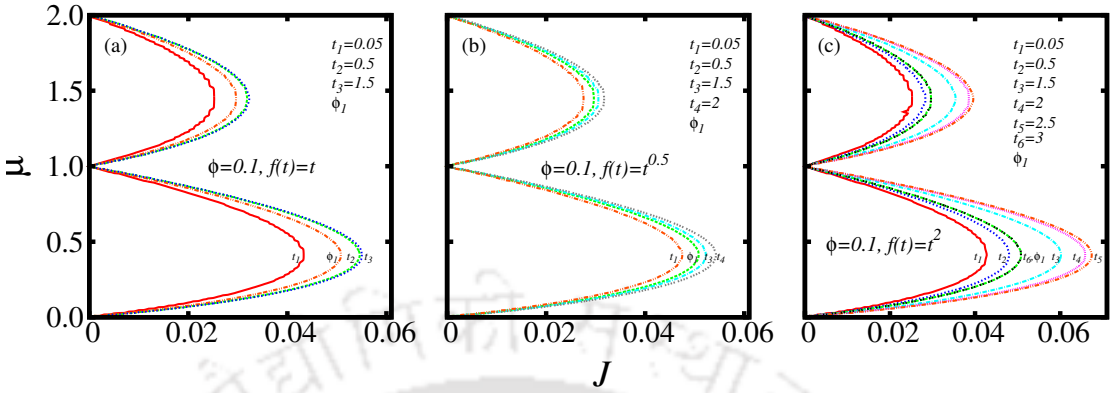

Figure 3.18: Phase diagram in presence of time dependent synthetic magnetic field in the $\mu - J$ plane with magnetic flux $\phi = 0.1$ at various times, t for (a) $f(t) = t$, (b) $f(t) = t^{0.5}$ and (c) $f(t) = t^2$.

the Hamiltonian is homogeneous and hence the SF order parameters are uniform over all the lattice sites in the absence of magnetic flux. While the presence of magnetic field introduces site dependence and thereby modifies the direct MI-SF phase transition scenario.

The mean field equation of Eq.(6) of Refs. [198, 199] shows that for a time independent synthetic flux, the system preserves its periodicity with period $l = q$ along the x-axis and hence we have $\Psi_l = \Psi_{l+q}$ and translationally invariant along the y-direction, $\Psi_{l,m} = \Psi_l$. The same periodicity also holds for the occupation density $\rho_l = \rho_{l+q}$ and hence $\rho_{l,m} = \rho_l$. However the inclusion of the time dependence in the synthetic magnetic flux raises a question whether the periodicity along the x-axis and invariance along the y-direction will remain intact or not. For the time being, we are assuming that such periodicity, as well as, the translational invariance remain unchanged even in presence of the time dependent gauge field.

Thus to calculate the ground state energy and eigenfunction of the system, we diagonalize the mean-field Hamiltonian over a magnetic supercell of dimension $1 \times q$ with periodic boundary conditions in the x-direction and finally the phase diagrams are calculated using the site averaged SF order parameter as, $\bar{\Psi} = \sum_q \frac{\Psi(q)}{q}$ for two different values of the magnetic flux, ϕ and different choices of $f(t)$.

In this study, the Bose- Hubbard model in presence of a magnetic field is studied using mean-field approach. This mean-field approximation is a self-consistent method which yields the order parameter and densities. Here we consider $U = 1$ throughout our study, and for $t = 1$, the time-dependent flux reduces to a constant flux and hence we

term it as ϕ_1.

The phase diagrams are shown in the $\mu - J$ plane for different form of time dependencies corresponding to two different values of magnetic flux, namely, $\phi = 0.1$ in Fig.3.18 and $\phi = 0.2$ in Fig.3.19.

For $f(t) = t$, it is observed that with increase in t, the MI-SF phase boundary for the first MI lobe shifts gradually towards larger values of hopping strength, J, thereby signaling a stabilization of the insulating phase [Fig.3.18(a)]. Inclusion of temporal variation in the magnetic flux, destroys the stability of the superfluid phase in the vicinity of the critical point and this is consistent with enhanced area of the MI lobe. This feature retains its nature for the second MI lobe, however the areas of these MI lobes decrease considerably in comparison to the first MI lobes. Whereas, for $f(t) = t^{0.5}$ [Fig.3.18(b)] and $f(t) = t^2$ [Fig.3.18(c)], we observe no particular pattern in the phase boundary demarcating the insulating and the superfluid phases. Thus, unlike the earlier case, as the time increases, the phase boundary may expand or contract. Importantly, the critical hopping strength, J_c that indicates the tip of the lobe remains unaffected with the passage of time for small time values ($t = 0.05$).

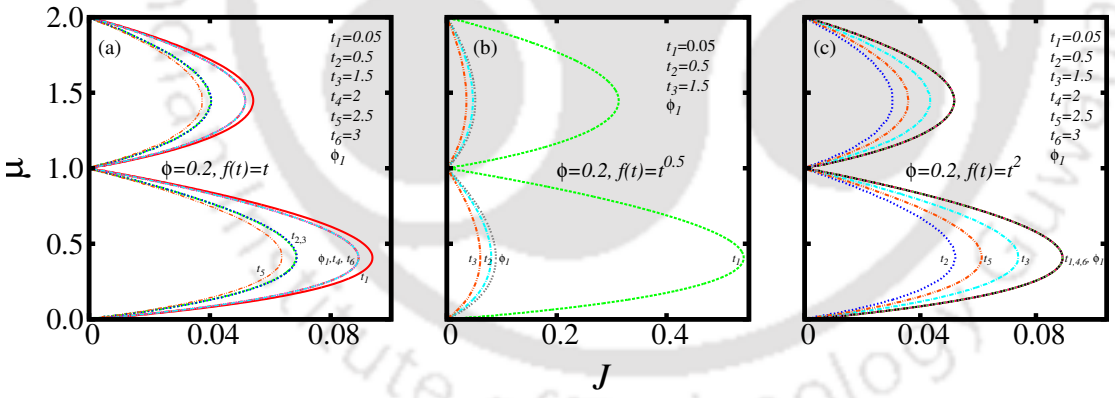

Figure 3.19: Phase diagram in presence of time dependent synthetic magnetic field in the $\mu - J$ plane with magnetic flux $\phi = 0.2$ at various times, t for (a) $f(t) = t$, (b) $f(t) = t^{0.5}$ and (c) $f(t) = t^2$.

Now we increase the flux, $\phi = 0.2$ and study the above scenario. Here the common feature is that the insulating phase is stable in case of $t = 0.05$ for all the three time dependencies [Figs.3.19(a),(b),(c)]. From Fig.1.2(b), it is observed that the most stable insulating phase is obtained corresponding to $f(t) = t^{0.5}$ and at small t, namely $t = 0.05$.

Finally, in order to get a complete picture about the impact of the time dependent magnetic field on BHM, we have presented how the critical hopping strength, J_c for

MI-SF phase transition is changing as a function of the time dependent magnetic flux in Table 3.1.

ϕ	t	$J_c[f(t) = t]$	$J_c[f(t) = t^2]$	$J_c[f(t) = t^{1/2}]$
0.1	0.05	0.044	0.043	0.048
	0.5	0.055	0.048	0.059
	1.0	0.052	0.052	0.052
	1.5	0.057	0.061	0.053
	2.0	0.059	0.066	0.055
	2.5	0.062	0.068	0.057
	3.0	0.065	0.052	0.059
0.2	0.05	0.096	0.091	0.550
	0.5	0.069	0.052	0.082
	1.0	0.091	0.091	0.091
	1.5	0.069	0.074	0.061
	2.0	0.091	0.091	0.068
	2.5	0.064	0.062	0.068
	3.0	0.091	0.091	0.068

Table 3.1: The critical hopping strength, J_c for the MI-SF phase transition for different form of the time dependent magnetic flux.

Now let us study the effect of time-dependent magnetic flux on the energy spectrum of BHM. Fig.3.20 represents the discrete energy spectrum for a full range of flux, $\phi = [0, 1]$ as a function J, that is, the phase diagram in the $J - \phi$ plane for $\mu = 0.4$. Fig.3.20(a) corresponds to the energy spectrum for constant flux, ϕ_1 $[t = 1]$. A periodicity of $\phi = \phi + N$ is observed without any time dependency, where N being an integer. Also the energy spectrum is symmetric about $\phi = \frac{\phi}{2} = 0.5$ in this case. Here the insulating phase gradually increases with ϕ till about $\phi/2$, and hence the MI phase falls off gradually. Thus the energy spectrum shows symmetry about $\phi = \phi/2 = 0.5$.

Now let us consider the time dependent case, $f(t) = t$ in Fig.3.20(b). For $t = 0.05$, it is observed that the energy spectrum remains almost flat about $J \sim 0.04$ and it doesn't vary for the entire range of ϕ. With further increase in t, for $t = 0.5$ the insulating phase increases with ϕ, till $\phi = 0.8$. While for $t = 3$, it shows an increment till $\phi = 0.1$. Thus for both the values of t, the energy spectrum is not symmetric about $\phi = \phi/2$. This observed asymmetry in the energy spectrum retains also for $f(t) = t^{0.5}$ and $f(t) = t^2$ and for all t values. Hence, asymmetry appears in the energy spectrum with the inclusion of time dependent synthetic field which is expected.

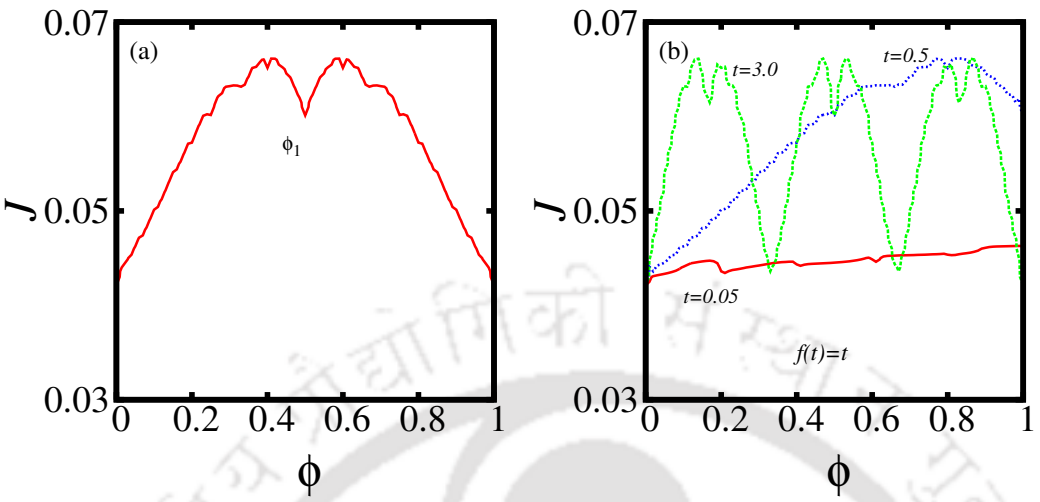

Figure 3.20: The energy spectrum for a complete range of ϕ for first MI lobe. (a) corresponds to constant flux, $\phi = \phi_0$. (b) corresponds to time-dependent flux, $\phi(t)$.

Now we study the behavior of a one-dimensional SF order parameter, Ψ_l as a function of J corresponding to the first MI lobe ($\mu = 0.4$). It is observed that the MI-SF phase transition occurs at the same value of the critical strength J_c for all the lattice sites for constant magnetic flux, $\phi_1 = 0.1$ [Fig.3.21(a)] and obeys periodicity condition, $\Psi_l = \Psi_{l+q}$. Let us first consider the case of $f(t) = t$. For $t = 0.05$, all Ψ_ls coincide with each other signifying the fact that the SF order parameter become site independent in this case [Fig.3.21(b)]. With further increase in t, the SF order parameters become site dependent, however does not obey the usual periodic condition, that is, $\Psi_l = \Psi_{l+q}$, where l is the number of lattice sites of the magnetic supercell of dimension $1 \times q$ [Fig.3.21(c)] unlike the case of constant synthetic field [Fig.3.21(a)]. This feature is preserved till $t = 2.5$. Whereas for $t = 3$, the SF order parameters obey the periodic condition, that is, $\Psi_l = \Psi_{l+q}$ [Fig.3.21(d)] similar to that of a constant gauge field [Fig.3.21(a)].

Again for $f(t) = t^{0.5}$ and $t = 0.05$ [Fig.(3.22)], we have found that the site independent scenario of SF order parameter as observed for $f(t) = t$ [see Fig.3.21(b)] is destroyed completely. Here the SF order parameter become completely site dependent. Also it does not obey the usual periodicity, that is, $\Psi_l = \Psi_{l+q}$ unlike constant flux. The lattice periodicity can not be revived for any value of t in this case.

Corresponding to $f(t) = t^2$ and $t = 0.05$, the SF order parameters become site independent similar to what presented in Fig.3.21(b). With further increase in t, the SF order parameters become site dependent and does not obey the lattice periodicity. Again for

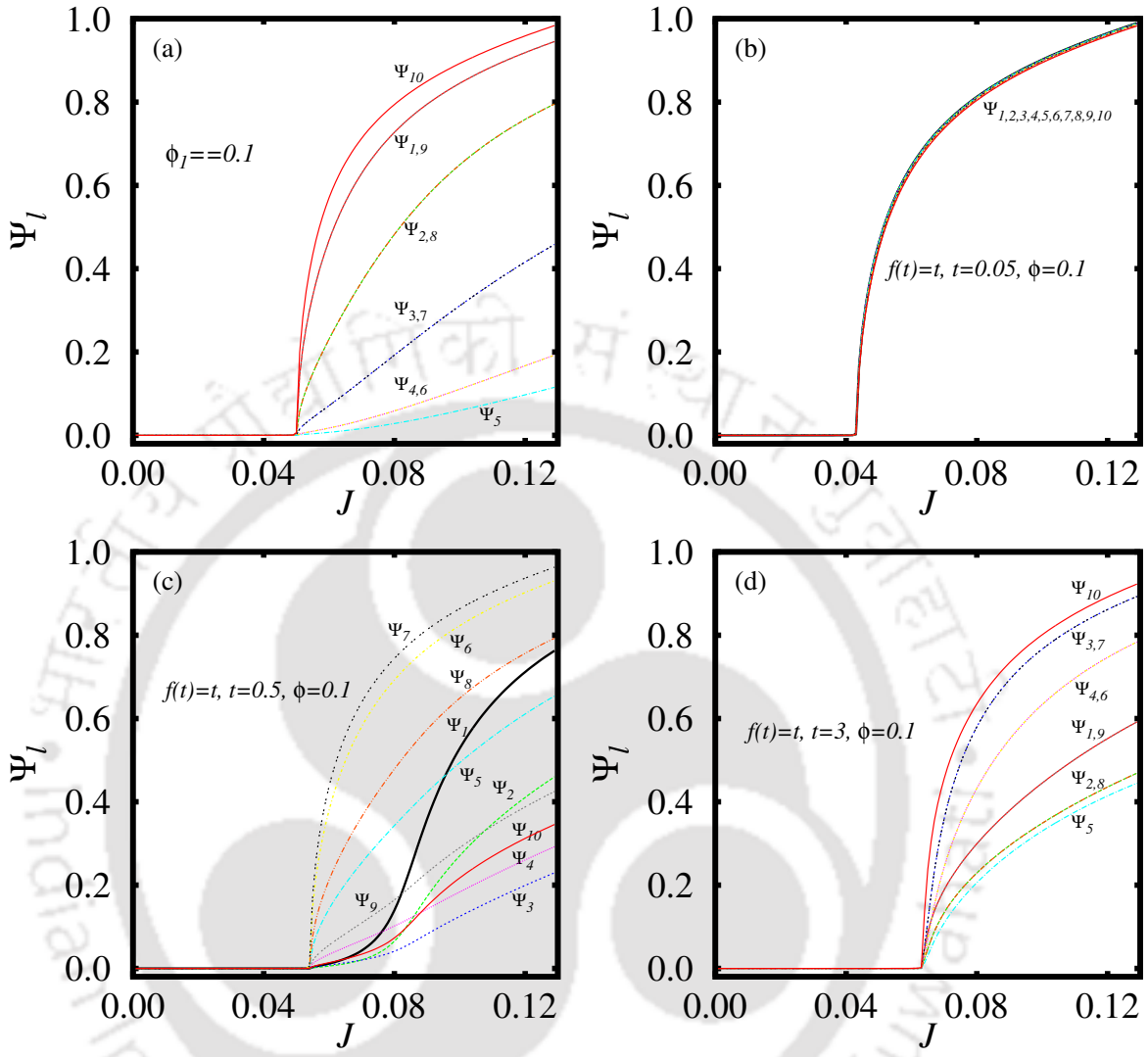

Figure 3.21: The 1D behaviours of Ψ_l for $\mu = 0.4$, $\phi = 0.1$ and $f(t) = t$ with various values of t.

$t = 3$, the lattice periodicity $\Psi_l = \Psi_{l+q}$ is restored back and the variation is similar to [Fig.3.21(d)]. Hence $f(t) = t^2$ shows similar behaviour of SF order parameter to that for $f(t) = t$.

For these all cases, the SF order parameters Ψ_l exhibit the disappearance of insulating phase at the same critical value, $J = J_c$, however the rate of increase of Ψ_l for $J > J_c$ varies across the sites of the lattices.

Figs.(3.23) show the evolution of the single particle energy as determined by the eigenvalues of the matrix in Eq.(3.28) at various times. For a constant flux, that is, without any time dependency [Fig.3.23(a) for $t = 1$], the energy spectrum shows the usual self similar structure, that is, the celebrated Hofstadter butterfly effect [174].

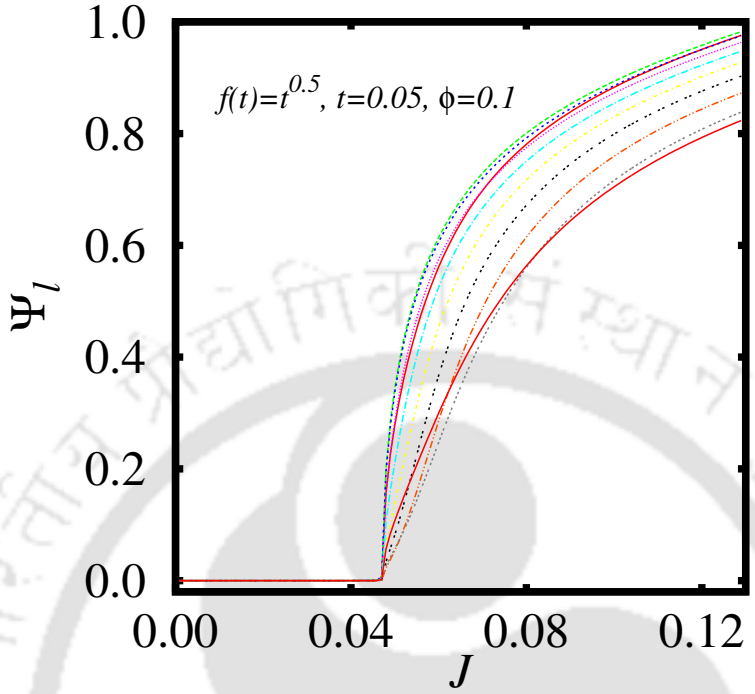

Figure 3.22: The 1D behaviours of Ψ_l corresponds to $\phi = 0.1$ and $\mu = 0.4$ for $f(t) = t^{0.05}$ and $t = 0.05$.

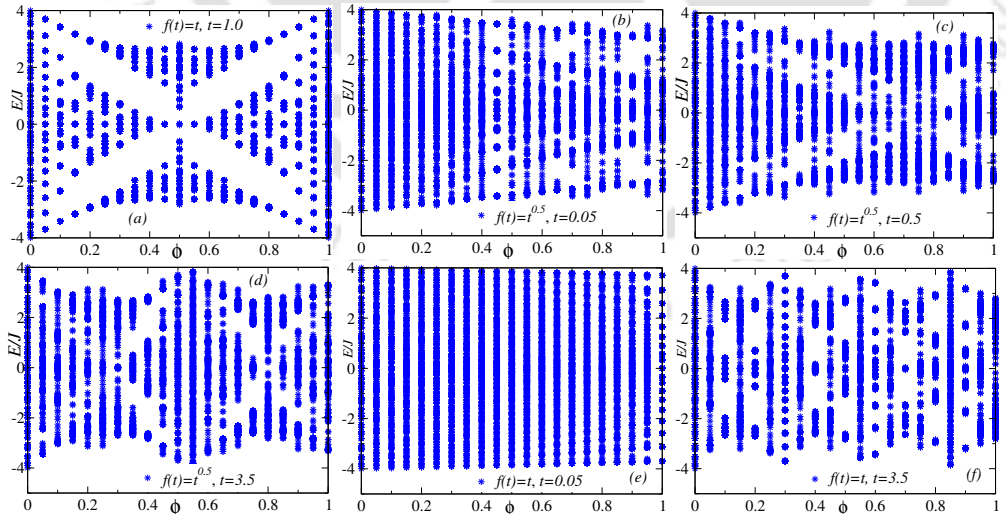

Figure 3.23: Hofstadter's butterfly effect in the non interacting limit ($U = 0$) corresponding to $f(t) = t^{0.5}$ in Figs.(b)-(d) and $f(t) = t$ in Figs.(e)-(f) respectively. Fig.(a) corresponds to the time independent magnetic field, that is $t = 1$.

Further with the inclusion of time dependency in the magnetic flux, the Hofstadter butterfly pattern completely vanishes [see Figs.3.23(b)-(f)]. This re-emphasizes the lack of symmetry in the dispersion induced by the time-dependent gauge field.

3.3.4 Conclusions

We have investigated the effect of time-dependent synthetic magnetic fields on the Mott-Insulating (MI) to superfluid (SF) phase transition and also on the energy spectrum of a BHM. It is observed that the behaviour of critical hopping strength, J_c, that is, the value of the hopping strength at which phase transition occurs, vary differently for different time variation of the time-dependent synthetic field. Whether the Mott insulating lobe stabilizes or contracts depends on the nature of the tuning of the time-dependent synthetic field, that is, on the form of $f(t)$ of Eq.(3.27). It is also observed that the inclusion of time in the synthetic field destroys the lattice periodicity, however with proper tuning of the time dependency, the periodicity can be restored back. Hence the periodicity of the one-dimensional superfluid (SF) order parameter sensitively depends on the nature of the time-dependent gauge field. Also in presence of such time-dependent fields, the order parameter becomes either site independent or dependent based on the tuning of the these fields. Finally, these time-dependent fields also induce an asymmetry in the discrete energy spectrum of the system which is evident from the vanishing of the symmetric 'butterfly' structure corresponding to the time independent case. It is good to remind that the asymmetry originates from the emergence of a scalar potential, ϕ which alongwith the variation of the vector potential, $\mathbf{A}(t)$ yields a loss in symmetry. We have also presented an experimental scenario that could possibly give rise to a time dependent synthetic gauge field.

CHAPTER 4

EXPLORATION OF PHASES AND DYNAMICS USING MCTDHB APPROACH

In this chapter, we employ our second formalism and study the phases and dynamics of correlated bosons via multiconfigurational time-dependent Hartree approach for bosons (MCTDHB) to tackle three different problems, for example, management of the Correlations of Ultracold Bosons in Triple Wells, dynamics of interacting bosons in a quantum seesaw potential, and dynamics bosons in presence of a synthetic gauge field as elaborated in the subsequent sections.

4.1 Management of the Correlations of Ultracold Bosons in Triple Wells

4.1.1 Introduction

The impressive degree of experimental controllability of ultracold atoms confined in optical lattices incorporated that it can be used to emulate the condensed matter systems and allow to simulate and probe the quantum phase transitions [47, 48, 83, 97, 201]. In addition, a direct imaging of quantum many-body correlations is achievable, for example, one-, two-, and even many-body correlations have already been reported in Refs. [80–82, 202].

In order to estimate and understand the many-body physics of interacting ultracold atoms in mesoscopic systems, it is a viable approach to first study and investigate their (few-body) building blocks [83–86, 203]. In this work, we employ a mesoscopic system of ultracold bosons confined in a triple-well potential as a candidate system to analyze the possibility for the control and manipulation of correlations in many-body systems. Although some of their many-body aspects have been previously reported in [87, 88], however a scheme to control the emergent correlations still needs to be devised.

In this work, we formulate such a protocol for the management of correlations by including the tilt in the optical lattice as a tuning parameter. In the laboratory, a *tilted lattice* can routinely be formed by superimposing a magnetic bias field to the optical potential. Thus the inclusion of the tilt in the system broaden up the spectrum of controllable parameters and also it enriches the emergent physics. For example, Ising density wave order and the emergence of superfluidity in transverse directions of a system of ultracold charged bosons confined in a lattice with a tilt were described in Ref. [155]. Also Ref. [204] establishes that some eigenstates in the spectrum of neutral bosons confined in a tilted one-dimensional lattice exhibit localization and are robust against the external perturbations. Furthermore, Ref. [156] demonstrates that the tilt is a source of quantum decoherence for macroscopic quantum superpositions in ultracold atoms in confined a tilted well.

Motivated by the above findings, in this work, the many-body correlations in the ground state of interacting ultracold bosonic atoms confined in a tilted triple well potential is investigated by solving the corresponding Schrödinger equation via the multiconfigurational time-dependent Hartree approach for bosons (MCTDHB).

Here the reduced density matrix (RDM) of the many-body state is employed to quantify the correlations. Hence the system is said to be coherent and condensed if only one eigenvalue of the RDM is macroscopic [13] and is said to be correlated and fragmented if multiple eigenvalues of the RDM are macroscopic [133, 205]. To get a spatially resolved insight of the emergent correlations, the Glauber first-order correlation function is also computed from the RDM [128]. Henceforth, the emergence of correlations and fragmentation in the many-body system is investigated as a function of the interaction strength and the tilt of the triple well. Our results unravel a fascinating interplay between the tilt of the lattice potential and the strength of the interparticle interactions. We further demonstrate that how this interplay can be exploited to manage the correlations and fragmentation of the many-boson system in the tilted optical lattices to a larger extent.

4.1.2 Hamiltonian

As we already know that the N-boson state $|\Psi\rangle$ is governed by the time-dependent Schrödinger equation given as,

$$i\partial_t|\Psi\rangle = \hat{H}|\Psi\rangle \tag{4.1}$$

with the Hamiltonian in our case is written as,

$$\hat{H}(x_1,x_2,...,x_N) = \sum_{j=1}^{N}\hat{h}(x_j)+\sum_{k>j=1}^{N}\hat{W}(|x_j-x_k|) \tag{4.2}$$

In this work, the ground state of the Hamiltonian in Eq. (4.2) is computed by propagating Eq. (4.1) in imaginary time to damp out any excitation in the one-dimensional many-body system. Here x_j represents the position of the j^{th} boson. The single-boson Hamiltonian, $\hat{h}$ is defined as,

$$\hat{h}(x) = \hat{T}(x)+\hat{V}_{trap}(x) \tag{4.3}$$

with $\hat{T}(x)(=-\frac{\hbar^2}{2m}\frac{\partial^2}{\partial x^2})$ and $\hat{V}_{trap}(x)$ are the usual kinetic and external potential energy respectively. Here the interactions of the ultracold dilute bosonic gases are considered as contact interaction which is modeled by using a Dirac-delta distribution of the form,

$$\hat{W}(x_j-x_k) = \lambda_0\delta(x_j-x_k) \tag{4.4}$$

where λ_0 denotes the strength of interaction. We scale λ_0 with the particle number as $\lambda=\lambda_0(N-1)$. In Eqs. (4.1),(4.2) and the remainder of this work dimensionless units are employed. To define dimensionless units, the Hamiltonian is divided by $\hbar^2/(mL^2)$, where m is the mass of the considered boson and L is a convenient length scale. We first choose a length scale of $L=1\mu$m. The scale of energy for the mass of ^{87}Rb is $\hbar^2/(mL^2)=2\pi\hbar\times 116$Hz and the scale of time is $mL^2/\hbar=1.37$ms. The one-dimensional scattering parameter λ is related to the three-dimensional scattering length a_{3D} by $\lambda=2Lm\omega_\perp a_{3D}/\hbar$, where $\omega_\perp$ is the frequency of the transversal confinement [206]. Using $a_3D=100.4a_0$, where a_0 is the Bohr radius, and $\lambda=6$ ($\lambda=20$), one obtains $\omega_\perp=41.3$kHz ($\omega_\perp=1376$kHz).

Now we consider the following form of the trapping potential with $N=90$ interacting bosons,

$$V_{trap}(x) = -\alpha x+V_0\sin^4(kx)+f_w(x) \tag{4.5}$$

Here α is the tilt and V_0 is the barrier height of the trapping potential. We also fix $k = 2$ for the lattice spacing. The term $f_w(x)$ introduces quasi-hard-wall boundary conditions to the system. The tilt αx renders the trapping potential similar to that of charged particles in a constant electric field and can be realized by applying a magnetic field gradient to ultracold neutral bosons in a lattice. It is important to note that the possibility of achieving of this system, virtually, any periodic lattice in the experiment [207]. In this study α varies from 0 to 16. In Fig.4.1(a), the potential is plotted in for $\alpha \in [0, 16]$.

4.1.2.1 Quantities of interest

The one-body reduced density matrix, RDM of the N-boson state $|\Psi(t)\rangle$ can be defined as,

$$\rho^{(1)}(x,x') = \langle\Psi|\hat{\Psi}^\dagger(x')\hat{\Psi}(x)|\Psi\rangle = \sum_i n_i \phi_i^*(x')\phi_i(x) \tag{4.6}$$

in the eigenbasis $\{\phi_i(x)\}$ [62, 127]. Here n_i is the i^{th} eigenvalue and $\phi_i(x)$ the corresponding eigenfunction, also known as natural occupation and natural orbital, respectively. The diagonal of $\rho^{(1)}$ corresponds to the single-particle probability distribution $\rho(x)$. Therefore, a system of interacting bosons is said to be in a condensed state if its RDM has only a single macroscopic eigenvalue [13] and k-fold fragmented, if its RDM has k macroscopic eigenvalues. Here the first-order coherence of a condensed state is maintained everywhere in space. Therefore, the value of the first occupation $\frac{n_1}{N} \approx 1$ ($\frac{n_1}{N} < 1$) is also indicative of the (loss of) coherence of the state (as evident from Eq. (4.7) below).

To obtain a spatially resolved picture of the correlations between the atoms in the many-body state that are triggered by a specific trap geometry, we also analyze the behaviour of the first-order correlation function defined as,

$$|g^{(1)}(x,x')|^2 = \left| \frac{\rho^{(1)}(x,x')}{\sqrt{\rho^{(1)}(x,x)\rho^{(1)}(x',x')}} \right|^2 \tag{4.7}$$

The value of $|g^{(1)}(x,x')|^2$ marks the first-order coherence between the points x and x' ($|g^{(1)}(x,x')|^2 \approx 1$) or its absence ($|g^{(1)}(x,x')|^2 \approx 0$) in the state $|\Psi\rangle$ [128]. Here the system of bosons is said to be in a coherent state if $|g^{(1)}(x,x')|^2 \approx 1$, similarly it is said to be in an incoherent state when $|g^{(1)}(x,x')|^2 \approx 0$. In the following discussion, for first-order correlation (see Sec. 4.1.3.3), the term *inter-well coherence* is used if x is in the vicinity of a different minimum of V_{trap} than x' and the condition $|g^{(1)}(x,x')|^2 \approx 1$ holds. Moreover, we use the term *intra-well coherence* if $|g^{(1)}(x,x')|^2 \approx 1$ holds for coordinates x and x' that are both in the vicinity of the same minimum of V_{trap}.

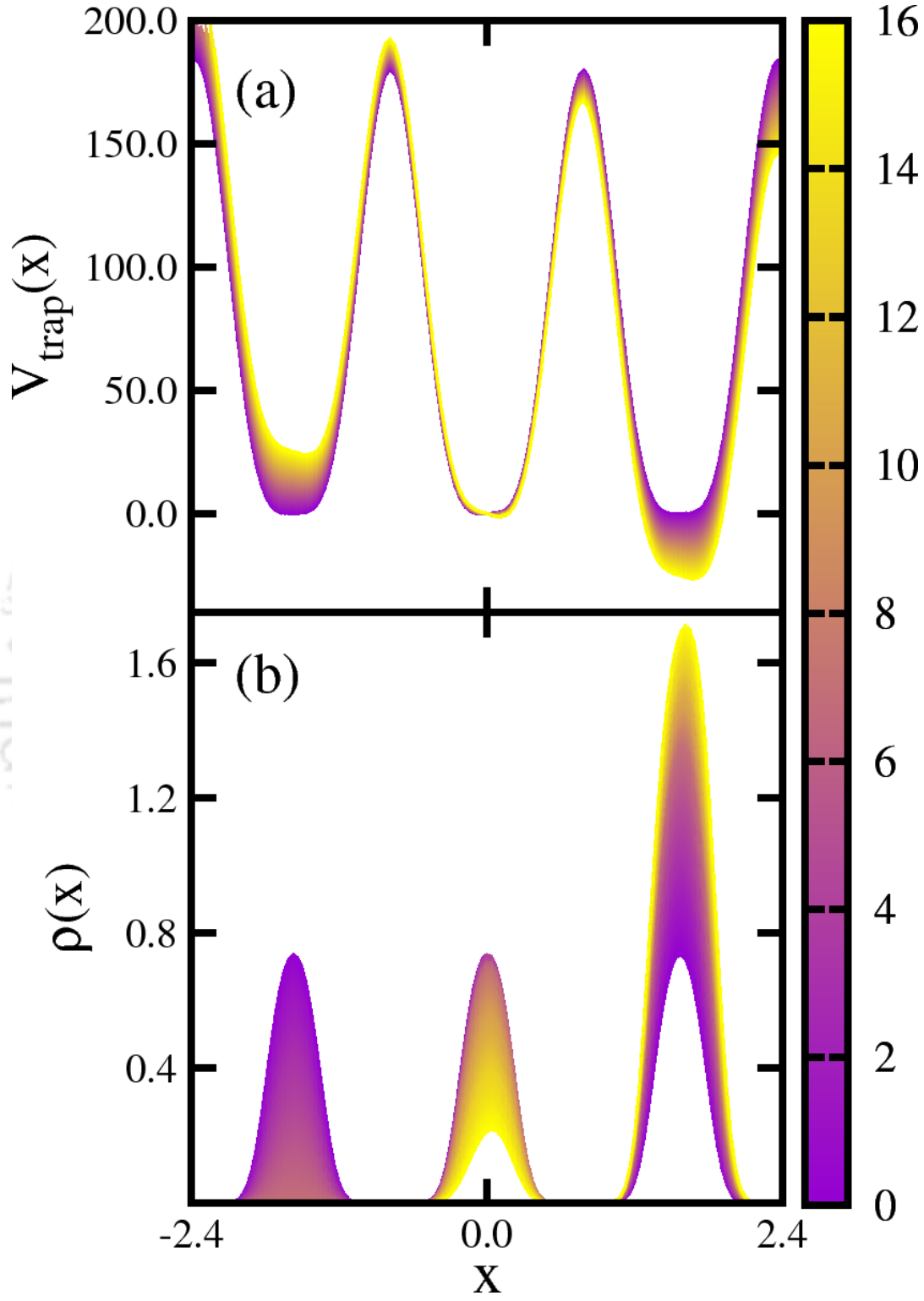

Figure 4.1: Potential and density as a function of the tilt is shown. (a) represents the shape of the triple well $V_{trap}(x)$ for $V_0 = 180$, $\lambda = 6$ and various tilts α and (b) is the corresponding density $\rho(x)$ for the same α, ranging from $\alpha = 0$ to $\alpha = 16$ (see color code/gray-scale).

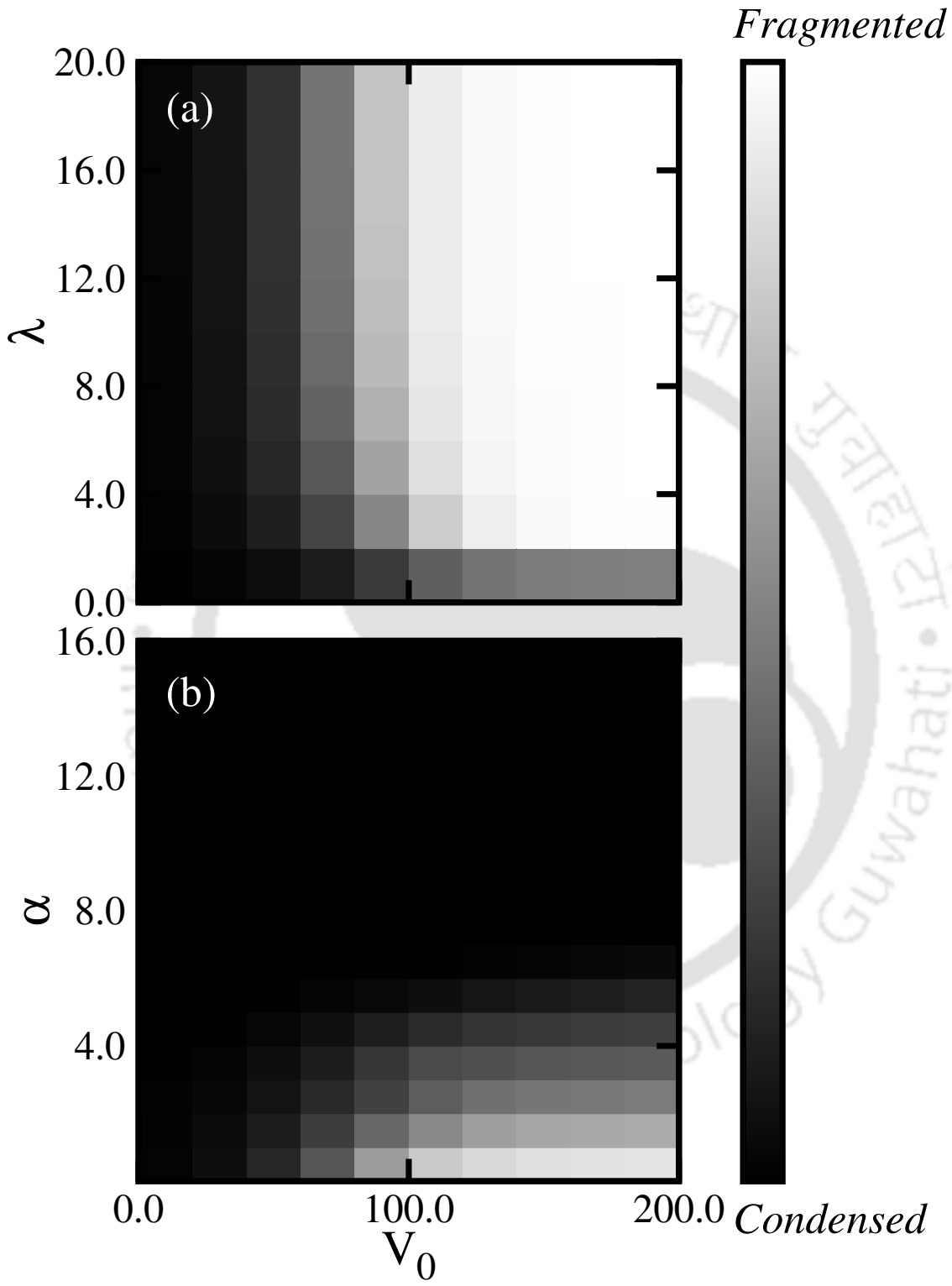

Figure 4.2: The phase diagrams show the variation of fragmentation, F as function of (a) the interaction strength, λ without inclusion of tilt, α and (b) with respect to tilt, α for a specific value of interaction strength, $\lambda = 6$ for contact interaction.

4.1.3 Results

For our numerical calculations, we use $M = 3$ one-dimensional single-particle basis functions and consider $N = 90$ bosons which yields a total of $\binom{N+2}{N} = 4186$ variationally optimized permanents. We have also tested $M > 3$ for convergence and checked the consistency of our results with a potential where we replace the $\sin^4 kx$ term in Eq. (4.5) by $\sin^2 kx$; see Appendix B. In the present computations, we use the MCTDH-X implementation of the MCTDHB theory [208–210]. For the following simulations, we set the quasi-hard-wall boundaries as $f_w(x) = \left(\frac{x}{x_c}\right)^{60}$ and $x_c = \frac{3\pi}{2k} - \frac{1}{k}$ to define the effective extension of the triple well, such that, the density at the boundaries of the trapping potential remains minimum for the entire parameter space. Our numerical grid runs from $x_{min} = -x_c - 1.09/k$ to $x_{max} = x_c + 1.09/k$ and we use 256 grid points.

We start our investigation by plotting the one-body density $\rho(x)$ in Fig.4.1(b) as a function of the tilt α. The effect of the tilt on the density $\rho(x)$ is intuitive, where as α increases the density of the atoms is gradually forced downhill and $\rho(x)$ is localized mostly at the rightmost well where the potential energy is minimal for $\alpha > 0$.

To define the parameter field, we scan the phase diagrams as shown in Figs.(4.2). These plots depicts the variation of the fragmentation, F, [as given in Eq.(2.83)] for the contact interaction of the type given in Eq.(4.4). Fig.4.2(a) depicts the variation of F as a function of the interaction strength, λ in absence of the tilt, that is, $\alpha = 0$. It is evident that for the smaller values of the barrier height, V_0 and the interaction strength, λ, the fragmentation of the condensate is negligible (~ 0), thereby indicating that the system remains in a fully condensed state with macroscopic population in the first natural orbital, ϕ_1 only. With increase in V_0, it is observed that the condensate gradually transits from a fully condensed state to a depleted state. Again increase in λ results into the transition from a condensed to a fragmented state, which is accompanied by the increase in the population of the second, ϕ_2 as well as the third natural orbitals, ϕ_3 alongwith corresponding decrease in the population of ϕ_1 Finally, for large λ, a fully fragmented state is observed even for moderate barrier heights due to the presence of two-body interaction to minimize the energy of the condensate. At the maximum value of F, that is, a fully fragmented phase of the condensate (here it is a three-fold fragmentation as $M = 3$), all the orbitals populate equivalent densities of boson.

Similarly, Fig.4.2(b) depicts the behaviour of fragmentation, F in presence of the tilt, α. It is observed that the fragmentation vanishes gradually with increase in α. The rate

of disappearance of fragmentation is more in moderate barrier heights than that for large barrier heights. Here, in the competition between α and λ, α has a dominant effect for contact interaction between the bosons as given Eq.(4.4). Therefore, with increase in α, the condensate experiences a downhill motion and localized itself in a single orbital, that is the orbital where the potential energy is minimum.

Henceforth, we chose the values of the interaction strength ($\lambda = 6$) and barrier height ($V_0 = 180$) such that the ground state is threefold fragmented in the absence of tilt ($\alpha = 0$). To assess the impact of the barrier height and the interaction strength on the properties of the many-body state, we additionally consider a larger interaction strength, namely $\lambda = 20$, and a moderate barrier height, namely $V_0 = 80$.

4.1.3.1 Convergence of results with respect to the number of orbitals

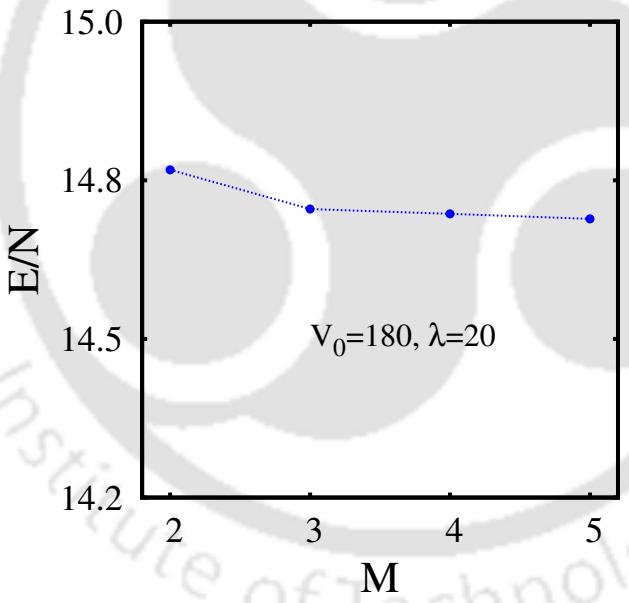

Figure 4.3: Ground state energy per particle, E/N as a function of the number of orbitals, M for barrier height $V_0 = 180$ and $\lambda = 20$ for contact interactions. The energy converges for increasing M (from $M = 3$ onwards).

To check the convergence of the system, in Fig.(4.3) the behaviour of the ground state energy per particle E/N is shown. It is observed that for a fixed barrier height and interaction strength as the number of orbitals M increases, E/N drops at a decreasing rate demonstrating the convergence of the system. The same behaviour is observed for E/N for different values of the barrier height and interaction strengths. Hence, we

conclude that the convergence of our results with respect to the number of orbitals is satisfactory.

4.1.3.2 Natural occupations

To quantify the fragmentation, coherence, and correlation properties of the many-boson system we discuss the behaviour of the natural occupations, $\frac{n_i}{N}$, as a function of the tilt α [see. Eq. (4.5)] as shown in Figs.(4.4).

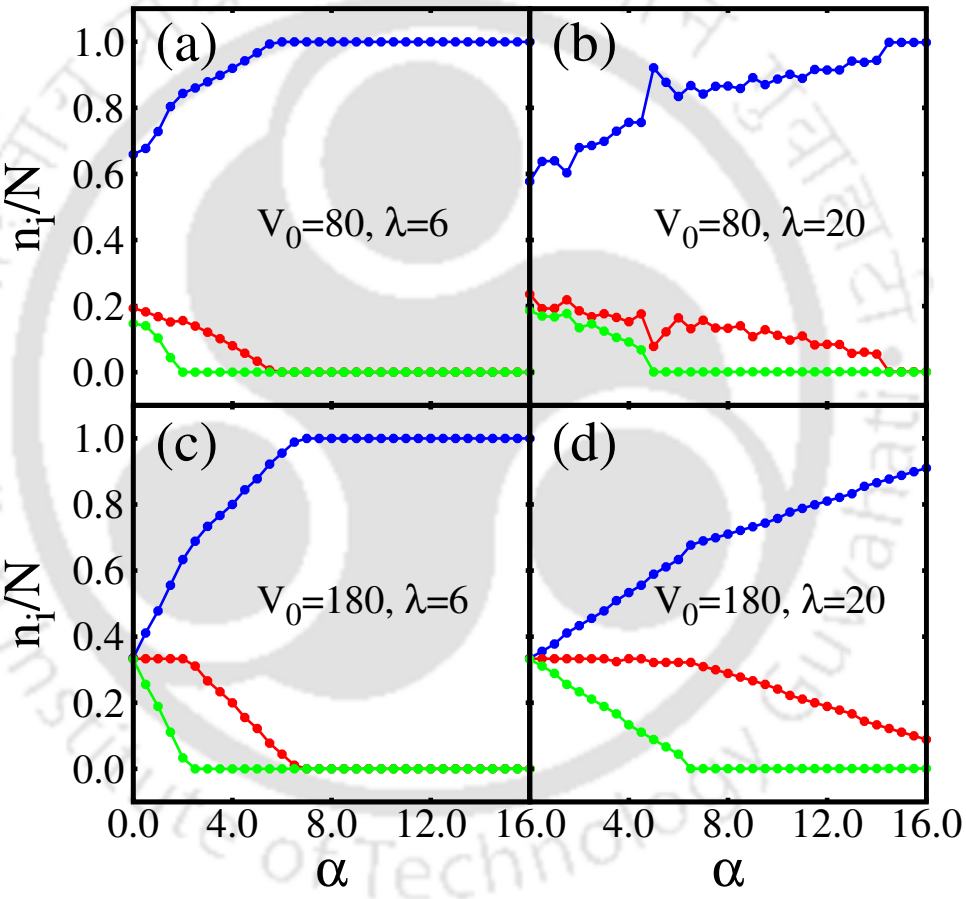

Figure 4.4: The natural occupations, $\frac{n_i}{N}$ are shown as a function of the tilt α for barrier heights $V_0 = 80$ [$V_0 = 180$] in (a),(b) [(c),(d)]. Panels (a),(c) [(b),(d)] correspond to interaction strength $\lambda = 6$ [$\lambda = 20$]. In all panels, the blue line with circles represents $\frac{n_1}{N}$, the red line with circles represents $\frac{n_2}{N}$, and the green line with circles represents $\frac{n_3}{N}$. For all depicted parameters, fragmentation gradually diminishes with increasing tilt α; for large tilts, the state hence becomes coherent and the occupation numbers obtained are $\frac{n_1}{N} \approx 1; \frac{n_2}{N} \approx \frac{n_3}{N} \approx 0$. All quantities shown are dimensionless, see text for further discussion.

It is observed that for moderate barrier height, $V_0 = 80$, and zero tilt, $\alpha = 0$, the bosons

are not completely fragmented, that is, the first natural occupation $\frac{n_1}{N} > 60\%$ and the second and the third natural occupations $\frac{n_{2,3}}{N} < 20\%$, for both small and large interaction strengths ($\lambda = 6$ and $\lambda = 20$). This is in contrast to the entirely threefold fragmented state found for $V_0 = 180$ with $\frac{n_1}{N} \approx \frac{n_2}{N} \approx \frac{n_3}{N} \approx 33.33\%$ [see. Fig.(4.4), panels (a),(b) and Fig.(4.4), panels (c),(d)]. Therefore, we conclude that, at zero tilt, fragmentation can be tuned by the barrier height alone. As α grows larger so does the first natural occupation as $\frac{n_1}{N} \to 1$, while the other two natural occupations decrease, that is $\frac{n_{2,3}}{N} \to 0$, see Figs. 4.4(a) and (b).

At large values of the barrier heights, namely, $V_0 = 180$, and moderate interaction strengths, such as, $\lambda = 6$, the condensate exhibits a fully threefold fragmentation with $\frac{n_1}{N} \approx \frac{n_2}{N} \approx \frac{n_3}{N} \approx 33.33\%$ in absence of the tilt, $\alpha = 0$. As α increases past a threshold value of $\alpha \approx 7.5$, the state becomes coherent with the first natural occupation $\frac{n_1}{N} \approx 1$ and correspondingly the second and the third natural occupations $\frac{n_2}{N} \approx \frac{n_3}{N} \approx 0$ as evident from Fig.4.4(c). Interestingly, the second natural occupation $\frac{n_2}{N}$ remains constant up to tilts as large as $\alpha \approx 2$, while $\frac{n_3}{N}$ starts to drop from $\frac{1}{3}$ to 0 already at small values of α. For $\alpha > 2$, n_2 falls off gradually and vanishes at $\alpha \approx 7.5$ [see Fig.4.4(c)]. Beyond this tilt, the density is almost exclusively localized in the rightmost well. For larger barriers, $V_0 = 180$, and moderate interactions, $\lambda = 6$, an increasing tilt α thus triggers a transition from a fully threefold fragmented to a fully condensed state thereby, the tilt can be used to control the fragmentation.

For larger interactions, $\lambda = 20$, and a large barrier height, $V_0 = 180$, the transition between a fragmented and a depleted state is still found, however, at larger tilts α [compare Figs. 4.4(c) and (d)].

We have verified that the above findings for the natural occupations and the fragmentation of the state also hold for the case of long range interactions which is discussed elaborately in **Chapter 5**. The natural occupations follow the same pattern as their contact interaction counterparts, but the restoration of coherence seems to happen at even larger values α as compared to the case of contact interactions. This demonstrates the sharper effect of long range interactions on the fragmentation, see **Chapter 5**. We thus conclude that the tilt of the triple well can be used to tune the many-body state from fragmented to condensed phase.

4.1.3.3 First-order correlation

To get a spatially resolved picture of the correlations between the atoms, we plot the first-order correlation function, $|g^{(1)}|^2$ [as defined in Eq. (4.7)] for various tilts (α = 0, 2.5, 6.5, 16), barrier heights (V_0 = 80, 180) and interaction strengths (λ = 6, 20) in Figs.(4.5).

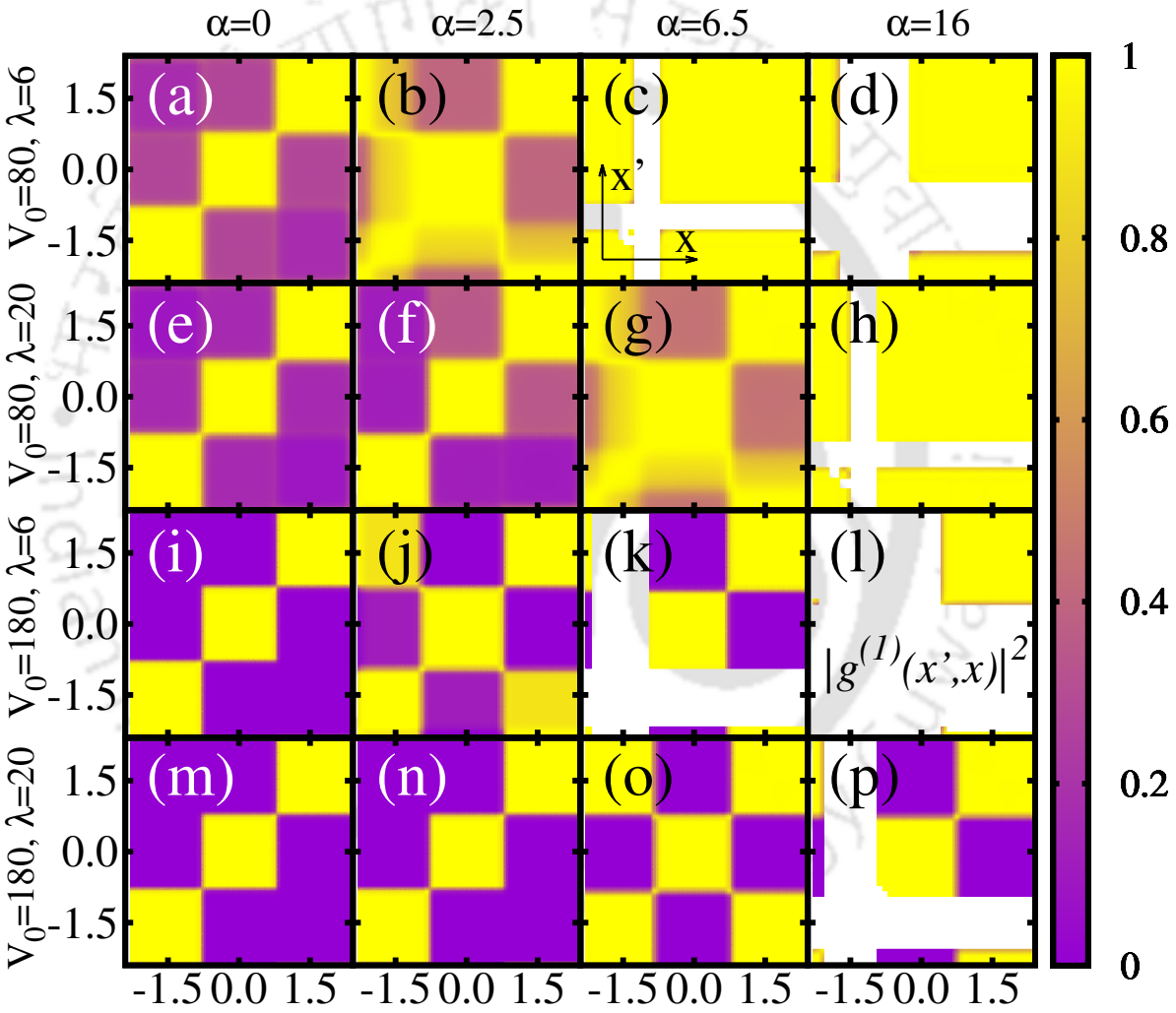

Figure 4.5: Spatially tracing correlations between the bosons in the triple well as a function of the tilt and barrier height is shown. The first-order normalized correlation function $|g^{(1)}(x',x)|^2$ is visualized as a function of α wherever the density is larger than a threshold value, that is, where $\rho^{(1)}(x,x) > 0.01$ and $\rho^{(1)}(x',x') > 0.01$. See labels for the respective values of the barrier height V_0 and the tilt α. We infer that an increased repulsion between the bosons, postpones changes in the coherence to larger tilts; see the similarity of panels (b) and (g), (c) and (h) for $V_0 = 80$ and of panels (j) and (o), (k) and (p) for $V_0 = 180$.

We first discuss the correlation function for a moderate barrier height, $V_0 = 80$, in Fig.4.5(a)–(h). At a small interaction strength ($\lambda = 6$), coherence between different wells persists since $|g^{(1)}(x,x')|^2$ is significantly larger than zero at off-diagonal values $x \neq x'$ for all tilts, Fig.4.5(a)–(d). For larger interaction strengths ($\lambda = 20$), inter-well coherence is absent for no tilt ($\alpha = 0$), Fig.4.5(e). As the tilt increases, inter-well coherence between populated neighbouring wells is gradually restored, see Fig.4.5(a)–(d) for $\lambda = 6$ and Fig.4.5(f)–(h) for $\lambda = 20$, here $|g^{(1)}(x,x')|$ gradually grows towards unity for values $x \neq x'$. We note that a tilt-driven localization takes place for larger tilts: for tilts $\alpha \gtrsim 10$, the left well contains almost no particles [see. Fig.4.1(b)].

The effect of interactions is to merely diminish the inter-well coherence, see. Fig.4.5 (a)–(d) and (e)–(h), here the value of $|g^{(1)}(x,x')|^2$ is generally closer to unity on the off-diagonal $x \neq x'$ for small interactions [Fig.4.5 (a)–(d)] as compared to larger interactions [Fig.4.5 (e)–(h)].

We now turn to an analysis of the details of the spreading of the coherence. Two competing tendencies are observed in the evolution of coherence as a function of the tilt α that can be illustrated with panels (a),(b),(e),(f),(g) of Fig.(4.5); where Tendency **I.** is an increase of the coherence between the center and the right well with the tilt see Fig.4.5(a) to (b), and Fig.4.5(e) to (f), respectively. Tendency **II.** is the restoration of coherence between the central and the left well. Both, tendency **I.** and **II.** can be understood by the following consideration about the behaviour of the interaction and interaction energy as a function of increasing tilt α; where naturally, an increase of α forces the particles downhill and the density gradually accumulates more in the right well, depleting the central and the left well (see also Fig.(4.1)). This leads to an interaction induced broadening of the density in the right well, because the presence of more particles implies a larger local portion of interaction energy; thus, due to the tilt, the density in the right well penetrates more into the potential barrier between the central and the right well and, thereby, increases the tunneling between these wells; hence the partial revival of coherence between the central and right well seen going from Fig.4.5(a) to (b) and going from Fig.4.5 (e) to Fig.(f). Tendency **II.**, the restoration of coherence between the left and central wells going from Fig.4.5(a) to Fig.4.5(b) or, equivalently, from Fig.4.5(f) to Fig.4.5(g), can also be understood as a consequence of the tilt-driven migration of interaction energy towards the right well; since the central and the left wells are gradually depleted, the local contribution to the interaction energy is decreasing there. The coherence between the left and the central well is restored [Fig.4.5(b) and

(g)], when the sub-system remaining in these wells is effectively non-interacting and its "local" state is well described by a product of a single complex-valued function.

It is important to note here that we have verified that the above tendency **I.** starts affecting the correlation patterns at smaller tilts than the tendency **II.** not only for $\lambda = 20, V_0 = 80$ [see change from Fig.4.5(e) to 4.5(f)], but also for $\lambda = 6, V_0 = 80$; for tilts $\alpha \lesssim 1.5$ with $V_0 = 80$ and $\lambda = 6$, here the correlation pattern (not shown) closely resembles the one depicted in panel (f) of Fig.(4.5) for $\lambda = 20$ and $V_0 = 80$.

We thus demonstrate that an increase of the tilt, at a fixed interaction strength, assists inter-well coherence of bosons in neighbouring wells, while an increase of the interaction strength, for fixed moderate barrier heights, diminishes inter-well coherence [Sec. 4.1.3.4].

We now analyze the correlations for larger barrier heights ($V_0 = 180$), Fig.4.5(i)–(p). For zero tilt and in comparison to moderate barrier heights, inter-well coherence is completely lost at large barrier heights, $|g^{(1)}(x,x') \approx 0|^2$ for $x \neq x'$ in Fig.4.5(i),(m).

By comparing the correlations at moderate barrier heights to the correlations at larger barrier heights, as expected, we find that a larger value of V_0 increases the degree of localization of the system. This is true, independently of the interparticle interaction strength; compare first and third as well as second and fourth row of Fig.(4.5).

Similarly to moderate barrier heights, a restoration of the coherence is also seen as the tilt α is increased as that for larger barriers V_0. This restoration of coherence is followed by a revival of next-to-nearest-neighbour coherence to a smaller degree [see Fig.4.5(b) and Fig.4.5(g)] in the case of moderate barriers. For large barriers, however, the revival of the next-to-nearest-neighbour coherence is much more prominent, while the nearest neighbours remain incoherent, see Fig.4.5(j) for weak interactions and Fig.4.5(o) for strong interactions.

It is important to mention that we have checked the persistence of the revival of next-to-nearest-neighbour coherence at a larger accuracy, that is, for $M = 4$ orbitals. We found that the effect appears at larger tilts ($\alpha = 7.1$) for the case of $M = 4$. We therefore speculate that the next-to-nearest neighbour coherence results from a resonance condition involving two- or many-particle correlated tunneling processes [63, 148, 211]; the lowered energy at the $M = 4$-level of MCTDHB seems to cause the resonance condition to be fulfilled at a different tilt.

The effect of stronger interactions is, one, to defer the restoration of coherence to larger tilts (from $\alpha = 2.5$ for $\lambda = 6$ to $\alpha = 6.5$ for $\lambda = 20$) and, two, to shift the tilt-driven

localization of the bosons to larger tilts. For strong interactions, $\lambda = 20$, at $\alpha = 16$ two wells are populated and at $\alpha = 6.5$ three wells are populated. For weak interactions, $\lambda = 6$, in contrast, only one well is populated at $\alpha = 16$ and two wells are populated at $\alpha = 6.5$.

We assess the generality of our findings for the coherence properties for long range interactions as discussed in the **Chapter 5**. The inclusion of long range interactions favours the fragmentation of the BEC for a larger barrier height. We find that our main conclusions for short ranged interactions hold also for the case of long ranged interactions.

4.1.3.4 Inter-well correlation

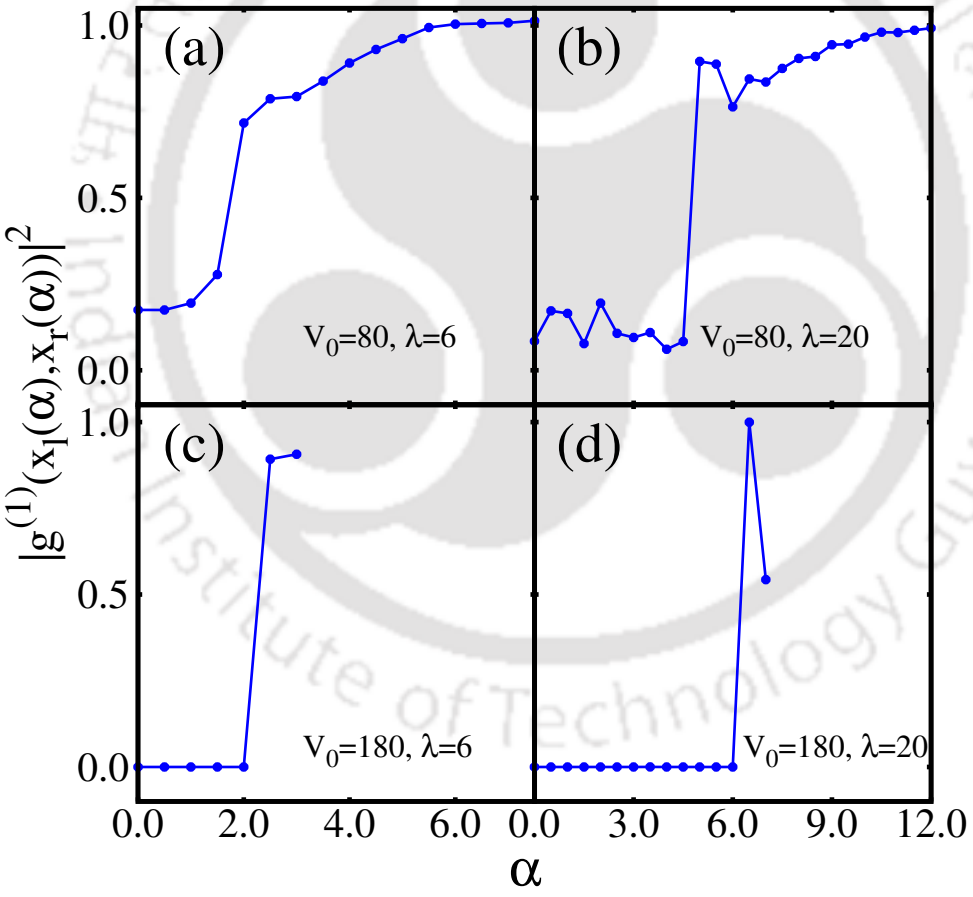

Figure 4.6: Behaviour of the first-order inter-well correlation function, $|g^{(1)}(x_l(\alpha), x_r(\alpha))|^2$, with varying barrier heights, V_0 and interaction strengths, λ for various values of the tilt, α. (a) and (b) correspond to $\lambda = 6$ and $\lambda = 20$ for $V_0 = 80$. We plot the correlations for values of α where the one-body density $\rho(x_{l,r})$ is larger than 0.01. Similarly (c) and (d) correspond to $\lambda = 6$ and $\lambda = 20$ for $V_0 = 180$.

The left-right inter-well correlation can be defined as,

$$|g^{(1)}(x_l,x_r)|^2 = \left|\frac{\rho^{(1)}(x_r,x_l)}{\sqrt{\rho^{(1)}(x_r,x_r)\rho^{(1)}(x_l,x_l)}}\right|^2 \tag{4.8}$$

The quantity $|g^{(1)}(x_l(\alpha),x_r(\alpha))|^2$ gives the degree of the first-order correlation between the points $x = x_r(\alpha)$ and $x' = x_l(\alpha)$. For our potential in Eq. (4.5), the position $x_r(\alpha)$ ($x_l(\alpha)$) of the right (left) well minimum is weakly dependent on the tilt, α. The right (left) well extends from about 1.5 to 2.1 (-1.5 to -2.1) for the considered tilts α. We plot the inter-well correlations as a function of the tilt, α for various barrier heights, V_0 and interaction strengths, λ in Fig.(4.6).

For moderate barrier height (and smaller interaction strength), significant inter-well correlations persists for a smaller α window (it is important to note the different ranges of the panels in Fig.(4.6)). However, it disappears with a further increase of α at $\lambda = 6$ [see Fig.4.6(a)]. Further increasing the interaction strength ($\lambda = 20$) leads to left-right correlations that persist out to larger tilts α [Fig.4.6(b)]; this behaviour is a consequence of the delay of the tilt-driven localization by the increased repulsion.

In the case of larger barrier height, the left-right correlation is observed only for certain values of the tilting parameter [Fig.4.6(c) and (d)]. Hence, by tuning the barrier height, interaction strength and tilt of the well, the left-right coherence can be adjusted.

4.1.3.5 Natural orbitals: variation as a function of the tilt

The behaviour of the natural orbitals $\phi_i(x)$ is shown in Fig.(4.7) as a function of the tilt, α for a fixed barrier height, V_0 and a fixed interaction strength, λ for contact interactions. Without a tilt ($\alpha = 0$), the first natural orbital, $\phi_1(x)$ has three maxima which are centered at positions of the wells. The second natural orbital, $\phi_2(x)$ has two maxima that are localized in the left and the right wells and the third natural orbital, $\phi_3(x)$ has three maxima which are localized at the positions of the minima of the triple well similar to $\phi_1(x)$ [see Fig.4.7(a)]. The behaviour of the natural orbitals complement the nearly equal population in the three natural orbitals, that is, the threefold fragmentation of the condensate [see Fig.4.4(d) and Fig.4.5(m)].

For $\alpha > 0$, the natural orbitals, $\phi_i(x)$ adapt their shape to fit the new form of the external trapping potential. The orbitals, $\phi_i(x)$ now have a single maximum and are localized independently in the three different wells [Fig.4.7(b)]. With a further increase

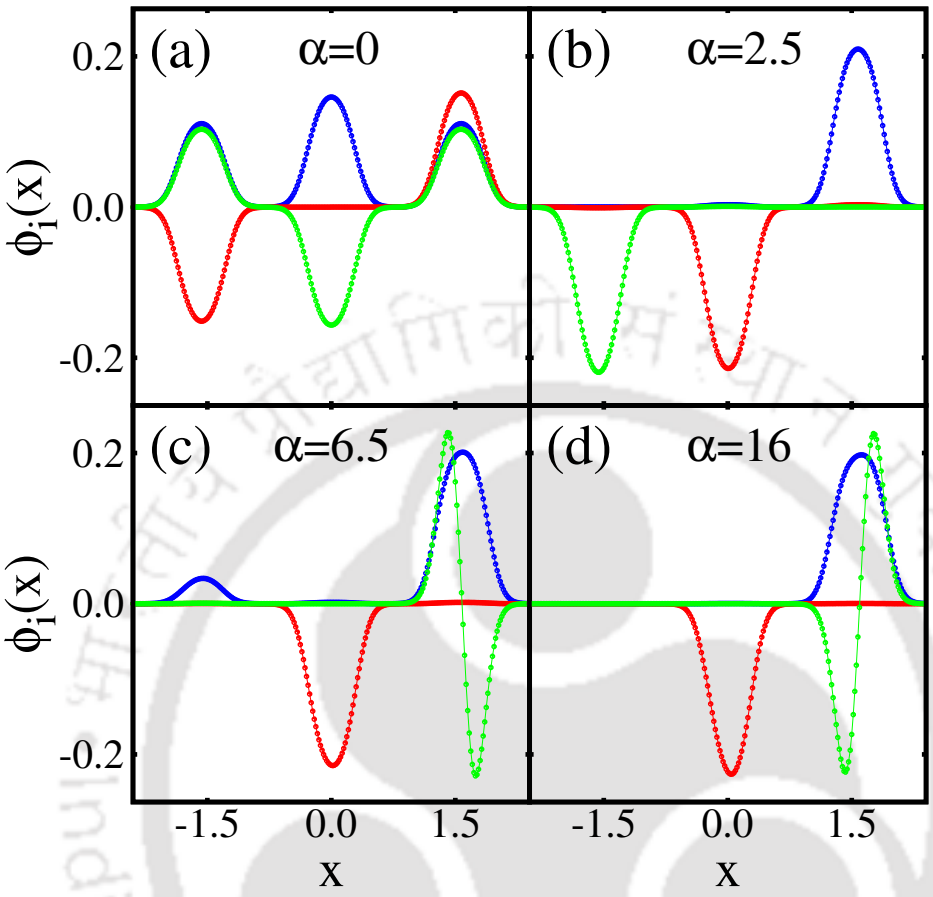

Figure 4.7: This figure shows the variation of natural orbitals, $\phi_i(x)$ as a function of the tilt α for $V_0 = 180$ and $\lambda = 20$ for contact interactions. (a) corresponds to $\alpha = 0$, (b) corresponds to $\alpha = 2.5$, (c) corresponds $\alpha = 6.5$ and (d) corresponds $\alpha = 16$. In all panels, blue lines with circles represents ϕ_1, red lines with circles represents ϕ_2 and green lines with circles represents ϕ_3. We note that, in order to assess their contribution to the one-body density $\rho^{(1)}(x,x)$, the orbitals $\phi_i(x)$ in this Figure would have to be scaled by their respective occupation number n_i given in Fig.(4.4).

in α [Fig.4.7(c)], two maxima emerge in $\phi_1(x)$ that are localized in the left and the right wells with different amplitudes. This structure of ϕ_1 is responsible for the next-to-nearest-neighbour correlations, that is, correlations between the left and the right wells [see Fig.4.5(o)]. The third orbital, $\phi_3(x)$, shows a node at the center of the right well leading to a higher kinetic energy. The occupation of the third natural orbital becomes therefore the least energetically favourable. To have a closer look, we plot Fig.(4.8) that shows the distribution of all the three natural orbitals in the left well in the next-to-nearest-neighbour correlations ($V_0 = 180, \lambda = 6, \alpha = 2.5$). Though all orbitals have significant densities in the right well, it is evident from Fig.(4.8) that ϕ_1 dominantly contributes to

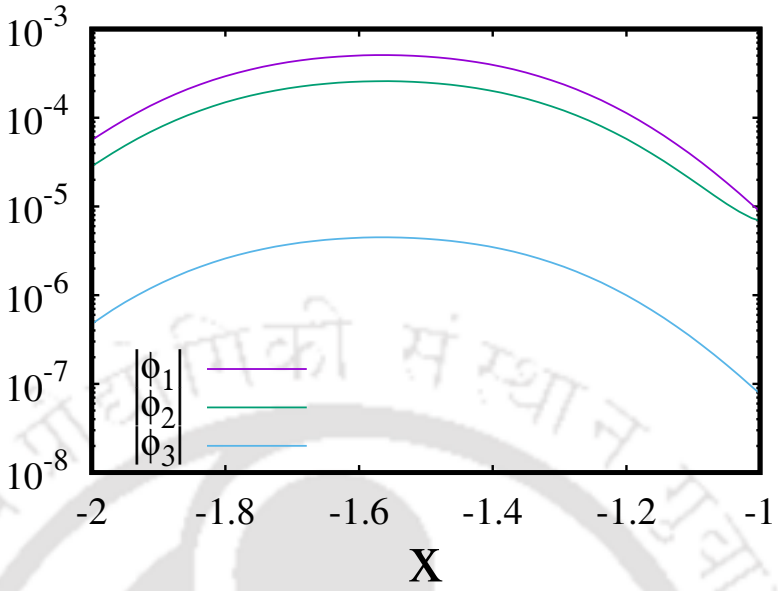

Figure 4.8: Natural orbitals in the left well for $V_0 = 180, \lambda = 6, \alpha = 2.5$. ϕ_1 dominantly contributes to the left well, ϕ_2 has a somewhat smaller (negative) contribution, while ϕ_3's density is practically negligible.

the left well in comparison to ϕ_2.

For large values of the tilt α, the natural orbitals are mainly localized in the central and the right wells [Fig.4.7(d)].

Here it is important to note that similar to Fig.4.5(o), we also found the origin of the next-to-nearest-neighbour correlations in Fig.4.5(j) for $V_0 = 180, \lambda = 6, \alpha = 2.5$ to be the delocalization of the first natural orbital between the left and right wells.

4.1.4 Conclusions

This investigation has shown some intriguing features of the first-order correlation and the coherence of a system of bosons confined in a tilted triple well [212, 213]. Given the ease in defining the system parameters in experimental setups with ultracold bosons, our work provides a protocol to manage the coherence of the many-body state, that is, a variety of correlation patterns is accessible simply by appropriately controlling the interaction strength, potential depth and tilt of the potential. The superfluid states which are associated with condensation can be created either localized in one well or delocalized across all the wells. Similarly, the Mott-insulating states those are associated with fragmented systems with a customized particle number imbalance between distinct

wells can also be prepared. The superfluid state, that is, the fully coherent state and the Mott-insulating that corresponds to fully incoherent phase represent extreme cases. Fig.(4.5) illustrates how the intermediate degrees of correlation can also be achieved with this system. The counter-intuitive revivals of coherence between next-to-nearest neighbouring sites seen in panels (j) and (o) of Fig.(4.5) hint that even a management of non-local correlations is possible, if the tuning of the tilt and the interaction strength is sufficiently accurate. A natural extension of our work and in the light of recent technical developments [214] would cover bosons with internal structure and/or embedded in an optical cavity.

Further we remark that, owing to its long decoherence time, the many-body state of ultracold atoms can provide a means to cache correlations and entanglement arising in the quantum information processing [215]. For this purpose protocols to control and quantify correlations in the many-body state of ultracold atoms, like the one that we have outlined in this work, are necessary [216]. As a further continuation of our work, we therefore also consider to quantify entanglement entropy and other quantities of relevance for quantum information processing for tilted multi-well systems in future.

4.2 Dynamics of interacting bosons in a quantum seesaw potential

4.2.1 Introduction

The experimental realization of ultracold atoms confined in an optical lattice subjected to a time-periodic external force [143, 172, 217, 218] has garnered significant attention in the quantum physics community. One prototype of these systems is a shaken optical lattice. The exceptional temporal control of the system parameters leads to the investigation of coherent dynamics of the many-body system [219, 220]. In recent times, this area has grown widely that addressed the coherent control of the single-particle tunneling amplitude in shaken lattices [143], that has applications in shifting of phase boundaries [76, 221] and transport phenomena [222, 223], topological band structures [93], observation of tunable occupation-dependent tunneling in a Bose-Hubbard system via periodically driven particle interactions [224]. Also a periodically driving potential assisted to the observation of photon-assisted tunneling [225], dynamical localization

[226, 227], coherent destruction of tunneling [144, 228], creation of the particle pair in the driven lattice that have potential applications in quantum computing and engineering [229] etc. Thus a significant amount of literature exists in the field of driven optical lattices. In particular, a periodic drive can be used to control the tunneling and interaction parameters and, thereby, provide the possibility to bias the many-body states and quantum phases of Bose-Einstein condensates [141, 142, 144] in the context of optical lattices. Recently, the experimental realization of such systems led to the realization of many-body localization [78, 79] and other exotic physical phenomena. Hence, such systems exhibit potential applications of quantum control and more lucid understanding of the solid-state physics, that surround various intriguing phenomena.

Motivated by the above findings, in this work, we use the MCTDHB method to simulate the tunneling dynamics of correlated bosons that interacts via contact interaction which are confined in a temporally driven tilted double-well potential with a periodically oscillating spatial bias that imitates a *quantum seesaw*. In this study, the main observables are the temporal evolution of the natural occupations, the first-order correlation and the population imbalance of the number of atoms in the left and the right well. To complement the features observed in the temporal evolution of the population imbalance, we further analyze the power spectral density of the population imbalance both in absence and in presence of the temporally driven tilt.

4.2.2 Quantities of interest

The details of the MCTDHB formalism is already elaborated in the **Chapter 2** and partly in Sec. 4.1 of the ongoing chapter. In this subsection, we are going to briefly discuss the quantities that are employed to study the interacting bosons in a temporally driven tilted double well potential. Here the one-body reduced density matrix, RDM of the N-boson state $|\Psi(t)\rangle$ is defined as,

$$\rho^{(1)}(x,x';t) = \langle\Psi|\hat{\Psi}^{\dagger}(x',t)\hat{\Psi}(x,t)|\Psi\rangle = \sum_{i} n_i \phi_i^*(x',t)\phi_i(x,t) \tag{4.9}$$

in its eigenbasis $\{\phi_i(x,t)\}$ [62, 127]. Here n_i is the i^{th} eigenvalue and $\phi_i(x,t)$ the corresponding eigenfunction, also known as natural occupation and natural orbital, respectively. The diagonal of $\rho^{(1)}$ corresponds to the single-particle probability distribution $\rho(x,t)$. A bosonic system is said to be in a fully condensed state if the largest eigenalue

of RDM is of the order of total number of bosons, N and k-fold fragmented state if the RDM has k eigenvalues of the order of N.

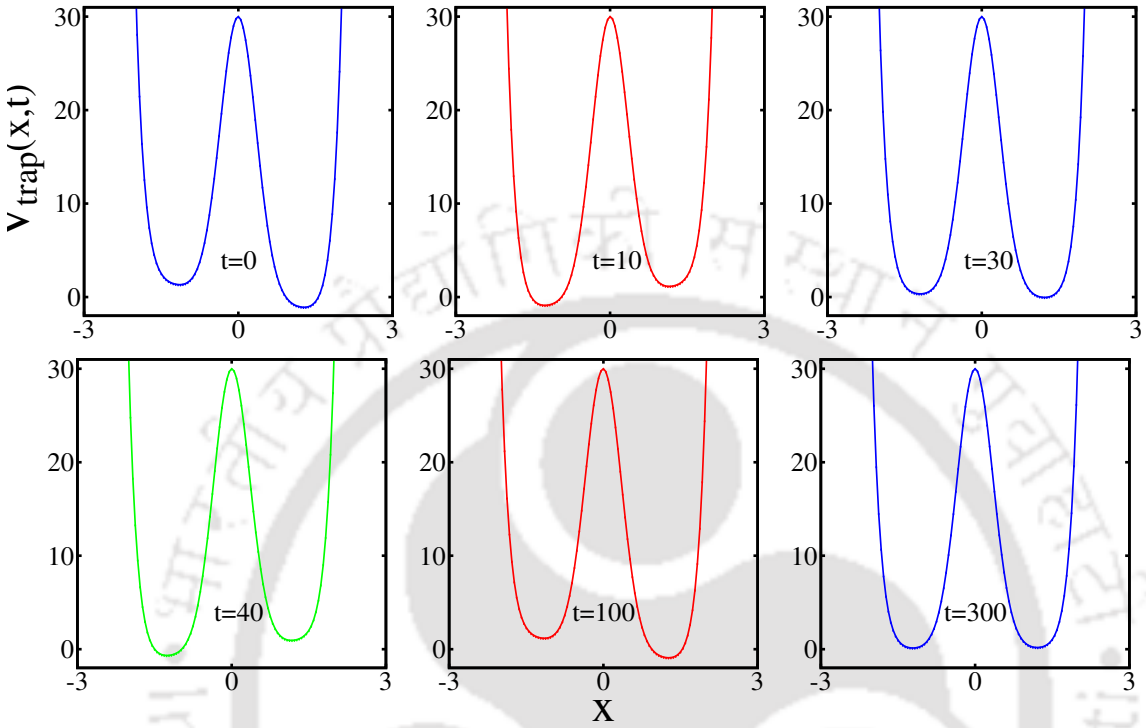

Figure 4.9: Quantum seesaw potential as a function of time. This figure shows snapshots of the temporally driven tilted double well potential as defined in Eq.(4.14) at various times, t for driving amplitude $\alpha = 1$, frequency $\omega = 1$, and barrier height $V_0 = 30$.

To get a deeper insight into the spatially resolved picture of the correlations between the bosons in the many-body state, we explore an important quantity, that is, the behaviour of the first-order correlation function which is defined as,

$$|g^{(1)}(x,x';t)|^2 = \left| \frac{\rho^{(1)}(x,x';t)}{\sqrt{\rho^{(1)}(x,x;t)\rho^{(1)}(x',x';t)}} \right|^2 \tag{4.10}$$

The value of $|g^{(1)}(x,x';t)|^2$ depicts the first-order coherence between the points x and x' in the state $|\Psi(t)\rangle$ [128]. The bosonic system is said to be in a coherent state if $|g^{(1)}(x,x';t)|^2 \approx 1$, similarly it is said to be in an incoherent state when $|g^{(1)}(x,x';t)|^2 \approx 0$.

To get an intuitive idea about the dynamical behaviour of the system, there is another important quantity which is the nonescape probability, P_{not}. During quantum tunneling, the particles are not localized at a particular position of the trap unlike the initial state, where the system is localized at a particular position with unit probability. Therefore,

one way to calculate the particular state in concern is by integrating the one-body density corresponding to the space, $\mathcal{V}$ where initially the state of the system is localized [63]. Hence, the nonescape probability corresponding to the one-body density is given as,

$$P_{not,\rho}(t) = \int_{\mathcal{V}} \rho(x,t)dx \tag{4.11}$$

Here $\rho(x,t) = \langle\Psi|\hat{\Psi}^{\dagger}(x,t)\hat{\Psi}(x,t)|\Psi\rangle$ is the one-body density. $P_{not,\rho}$ measures the nonescape probability for single particle state.

In the other way, by taking the integration of the full wave function, Ψ in the space, $\mathcal{V}$ that corresponds to the initially localized state of system. Thus the nonescape probability that related to the wave function is defined as,

$$P_{not,\Psi}(t) = \int_{\mathcal{V}} \Psi^*(x_1,..x_N)\Psi(x_1,..x_N)dx_1...dx_N \tag{4.12}$$

Now by employing density involved nonsecape probability, $P_{not,\rho}$, the population imbalance between the double wells can be evaluated as,

$$n = N - P_{not,\rho} \tag{4.13}$$

where N denotes the total number of bosons in the system.

4.2.3 Results

In this work, we consider $N = 90$ bosons in one spatial dimension interacting via a contact interaction of the form $\hat{W}(x-x') = \lambda_0\delta(x-x')$; $\hat{W}(x-x')$ and λ_0 being the two-body interaction and the interaction strength, which trapped in a temporally driven tilted double well potential, $V_{trap}(x,t)$ that imitates a quantum seesaw. Thus the potential can be defined as,

$$V_{trap}(x,t) = V_0\, e^{-\frac{x^2}{2d^2}} - \alpha x\cos(\omega t) + f_w(x) \tag{4.14}$$

Here V_0 is the barrier height of the trapping potential, $d = 0.35$ is the displacement and αx is the relative tilt between the two wells. Thus, the parameter α defines the strength of the drive of the quantum seesaw. By tuning the frequency ω, we drive the tilt of the seesaw temporally. In the following analysis, we choose the barrier height $V_0 = 30$, the interaction strengths of the bosons, λ_0 ranging from 0 to 5.6 and the amplitude of the driving force, α between 0 to 20. For the following simulations the quasi-hard-wall

boundaries are set as $f_w(x) = \left(\frac{x}{1.5}\right)^{10}$, while the numerical grid extends from $x_{min} = -2\pi$ to $x_{max} = +2\pi$, so that the one body density at the boundaries remain minimum for the entire parameter range. Note that we keep the driving frequency $\omega = 1$ for the entire simulation.

It is important to note that the features corresponding to larger barrier heights, such as, $V_0 = 120$ remain similar to that for smaller barrier heights, for example $V_0 = 30$. Therefore, we skip the analysis that corresponds to large V_0 for brevity.

We simulate the dynamics from time $t = 0$ to $t = 1000$ with MCTDH-X software package [208–210] using $M = 3$ orbitals for all calculations owing to the convergence of the system, that provides $\binom{N+2}{N} = 4186$ variationally optimized permanents. However we have shown the plots only till relevant time to capture the interesting features in more details. Fig.(4.9) shows snapshots of the temporally driven tilted double well potential at various instants of time that emulates a quantum seesaw.

As an initial state for the computation, we use the ground state of the interacting bosons in a potential given as,

$$V_{relax}(x) = \frac{\omega^2}{2}(x - x_0)^2 \tag{4.15}$$

with the potential parameters $\omega = 3$ and $x_0 = 0$.

It is important to note that in this computation, all the parameters are defined in dimensionless units and to do so we divide the MCTDHB Hamiltonian by $\hbar/mL^2$ with $\hbar = m = 1$ where L is the convenient length scale of the system. We first choose a length scale of $L = 1\mu$m. The scale of energy for the mass of ^{87}Rb is $\hbar^2/(mL^2) = 2\pi\hbar \times 116$Hz and the scale of time is $mL^2/\hbar = 1.37$ms.

4.2.3.1 Natural occupations

Let us analyze the temporal evolution of the natural occupations, $\frac{n_i}{N}$ for different values of the amplitude of the drive, α as shown in [Fig.(4.10)].

For no interaction, that is, at $\lambda_0 = 0$, the bosons are remained in a completely condensed state at all the time following the values of the first natural occupation as $\frac{n_1}{N} \sim 1$ while the second and the third occupations $\frac{n_{2,3}}{N} \sim 0$ as evident from Fig.4.10(a). With increase in interaction, λ_0, we observe a gradual decrease in the value of the temporal evolution of $\frac{n_1}{N}$ and corresponding increment in the values of the temporal evolution of $\frac{n_2}{N}$ and $\frac{n_3}{N}$ which is the effect of two-body interaction between the bosons.

Now, for large interaction strength, namely $\lambda_0 = 5.6$ with no drive ($\alpha = 0$), it is observed that initially for $t = 0$, the bosons are in a depleted state (that is with first natural occupation $\frac{n_1}{N} \leq 96\%$). However, with increase in time, t, the system gradually transits from depleted to a fully fragmented phase. At time $t \sim 10$, the state exhibits a threefold fragmentation with $\frac{n_1}{N} \approx \frac{n_2}{N} \approx \frac{n_3}{N} \approx 33\%$. Here the system remains in this threefold fragmented state as time, t progresses [as clear from Fig.4.10(b)]. Hence, a

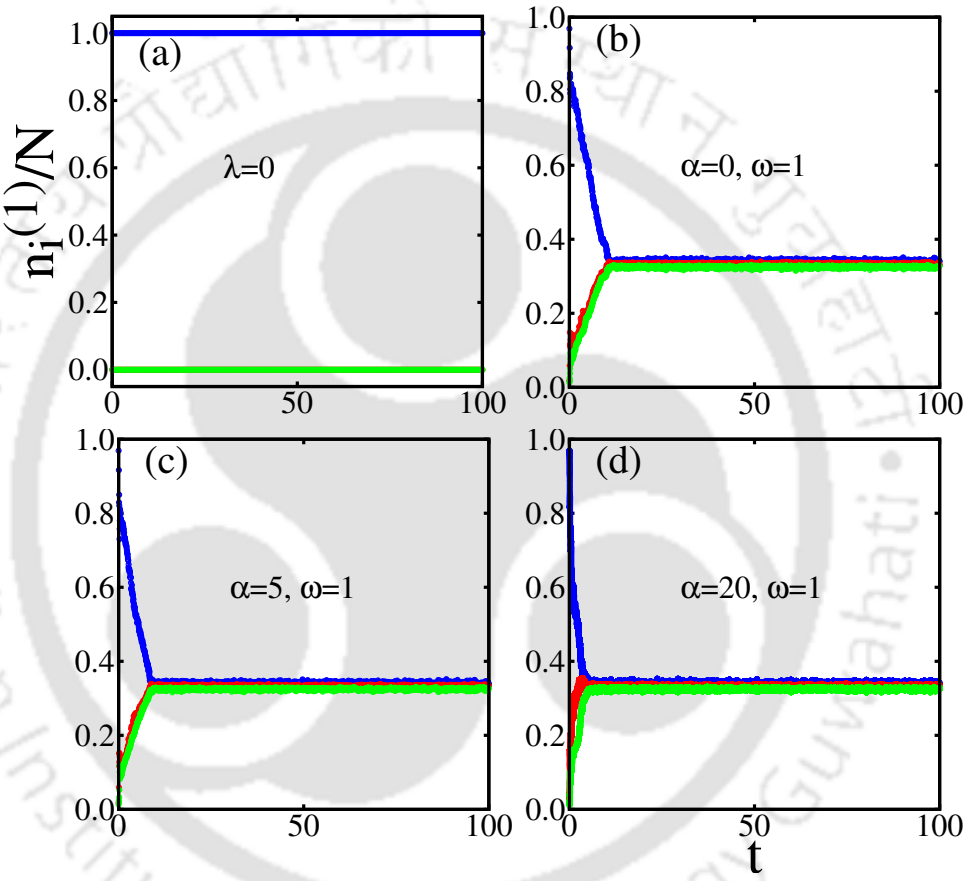

Figure 4.10: The time evolution of the natural occupations $\frac{n_i}{N}$ are shown for barrier height $V_0 = 30$. (a) corresponds to the case of no interaction, that is, $\lambda_0 = 0$, (b) corresponds to $\lambda_0 = 5.6, \alpha = 0$, (c) corresponds to $\lambda_0 = 5.6, \alpha = 5$ and (d) corresponds to $\lambda_0 = 5.6, \alpha = 20$. In all panels, the blue line represents $\frac{n_1}{N}$, the red line represents $\frac{n_2}{N}$, and the green line represents $\frac{n_3}{N}$.

series of transition takes place in the dynamic of natural occupations, $\frac{n_i}{N}$, namely, from fully condensed to depleted and finally to a threefold fragmented state of the condensate with the manipulation of interaction strength only.

Now let us explore the dynamics with the inclusion of the temporally driven tilt in the potential. It is observed that with the increment of the driving amplitude, α, there is a gradual growth in the rate of fragmentation of the condensate. For example, for $\alpha = 5$,

it is evident that threefold fragmentation appears earlier [see Fig.4.10(c)] in comparison to that for $\alpha = 0$ [see Fig.4.10(b)]. This rate of transition from depleted to threefold fragmented state is enhanced with further increase in α, see Fig.4.10(d). Therefore, the temporally driven tilted double well potential favours the fragmentation scenario.

4.2.3.2 First-order correlation

To get a spatially resolved picture of the correlations between the atoms, let us study the first-order correlation function, $|g^{(1)}(x,x';t)|$ [as defined in Eq.(4.10)] as a function of time, t [shown in Figs.(4.11) and (4.12)] for $V_0 = 30$.

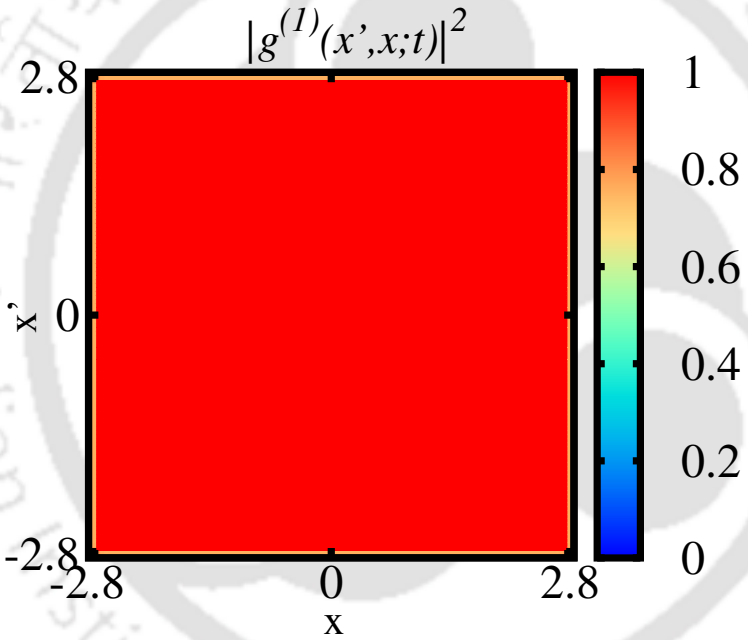

Figure 4.11: The normalized first-order correlation function $|g^{(1)}(x,x';t)|^2$ is depicted for no interaction $\lambda_0 = 0$. The plot indicates that both the wells being completely correlated.

Fig.(4.11) shows the behaviour of the first-order correlation function, $|g^{(1)}(x,x';t)|^2$ without any interaction, that is, for $\lambda_0 = 0$. In this case, it is observed that the two wells become fully coherent with $|g^{(1)}(x,x';t)|^2 = 1$ for the entire space in the coherent plot as evident from Fig.(4.11).

With increase in the interaction strength, λ_0, the fully coherent state gradual disappears. Now let us consider the case of large interaction, namely, $\lambda_0 = 5.6$ and explore the time evolution of $|g^{(1)}(x,x';t)|^2$ at various time. At small time, $t = 2$, it observed that coherence is restricted to a certain area of the space as $|g^{(1)}(x,x';t)|^2 \sim 1$ within a

specific area [see Fig.4.12(a)] that corresponds to a depleted state of the condensate. As t progresses, the depleted region gradually disappears [as clear from Fig.4.12(b)-(c)]. Here the region with maximum coherence, that is, $|g^{(1)}(x,x';t)|^2 \sim 1$, is gradually centered around the diagonal region. With the passage of time, for $t = 100$, it is observed that region with $|g^{(1)}(x,x';t)|^2 \sim 1$ completely align along the diagonal, which is evident from the non-zero diagonal strip which is represented by a red line in the Fig.4.12(d). This region corresponds to the threefold fragmentation of the condensate as obtained in the behaviour of the natural occupations.

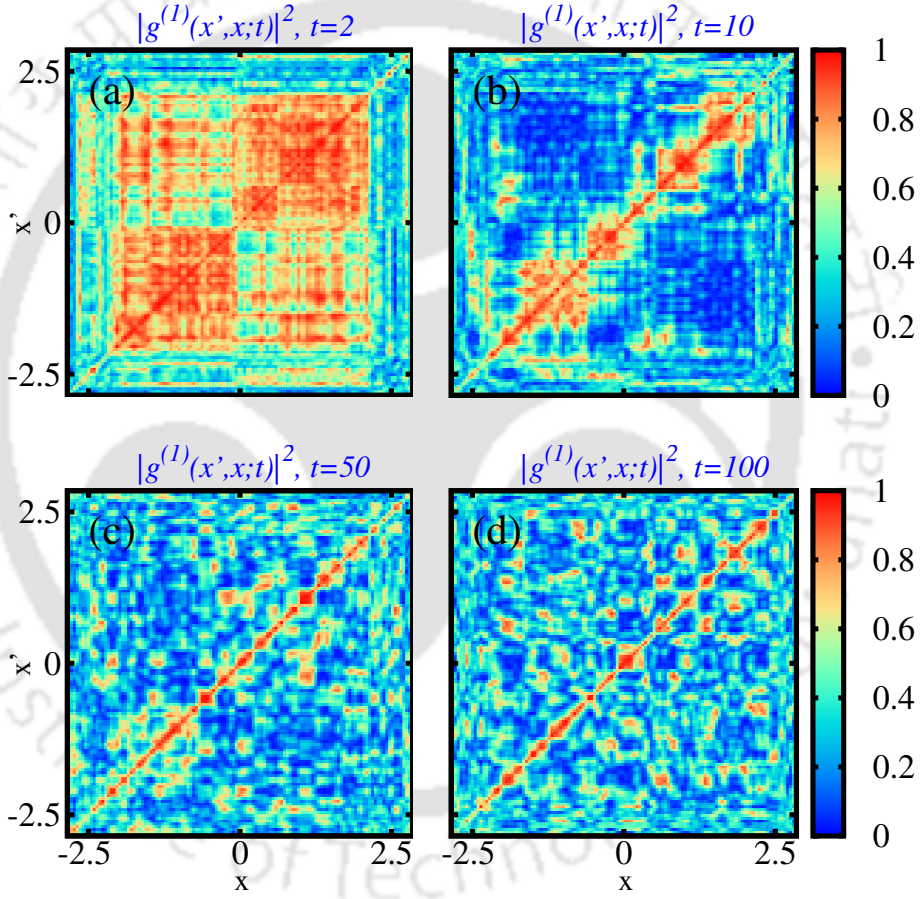

Figure 4.12: The normalized first-order correlation function $|g^{(1)}(x,x';t)|^2$ is visualized for various times, t for barrier height $V_0 = 30$, interaction strength $\lambda_0 = 5.6$ and driving amplitude $\alpha = 0$. (a) corresponds to $t = 2$, (b) corresponds to $t = 10$, (c) corresponds to $t = 50$ and (d) corresponds to $t = 100$.

Similar features for the time evolution of $|g^{(1)}(x,x';t)|^2$ is observed with the inclusion of the driving force, α. However, features correspond to Fig.4.12(c) and (d) appear at earlier times, such as, at $t = 10$ in this case. Therefore, we skip the plots of $|g^{(1)}(x,x';t)|^2$

that corresponds to $\alpha \neq 0$ case for brevity.

4.2.3.3 Population imbalance and Power spectral density

To get an intuitive idea about the dynamical behaviour of the interacting bosons confined in the driven seesaw potential, let us further investigate the time evolution of the population imbalance between the wells, $n(t)$, that can be obtained from Eq.(4.13) as shown in Fig.(4.13). Without any interaction, that is, $\lambda_0 = 0$, the dynamics of population

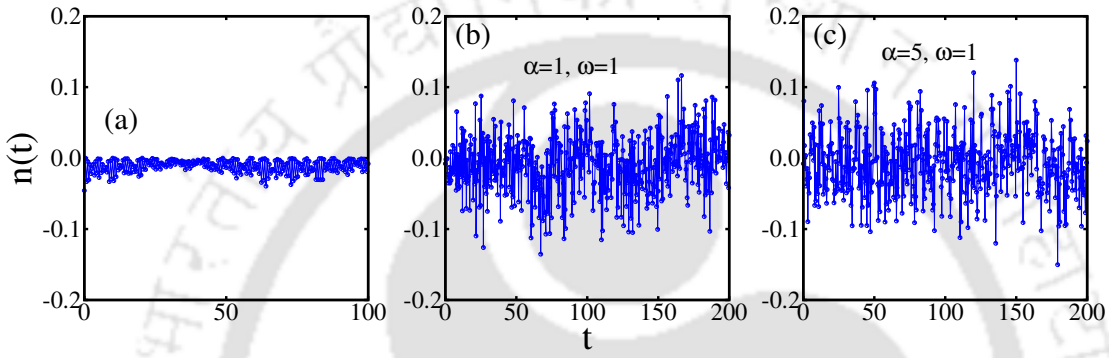

Figure 4.13: The variation of population imbalance $n(t)$ as a function of time, t for $V_0 = 30$. (a) corresponds to the case of no interaction, that is, $\lambda_0 = 0$, (b) and (c) correspond to $\lambda_0 = 5.6$ for $\alpha = 1$ and $\alpha = 5$ respectively.

imbalance between the two wells, $n(t)$ is frozen, that is, centered almost around zero and this indicates an equal population densities in each well [see Fig.4.13(a)] and it remains unaltered with the passage of time.

With the inclusion of the driving, α and interaction strength, λ_0, for small values of α, the dynamics of the population imbalance $n(t)$ feature oscillatory behaviour with faster oscillations and damping amplitude as shown in Fig.4.13(b). With further increase in α, the fluctuations in the dynamics reduce a bit [Fig.4.13(d)].

In order to have a deeper understanding of the above observed dynamical features of the population imbalance, $n(t)$ of interacting bosons in the seesaw potential, let us analyze the power spectral density, PSD of $n(t)$ which is defined as,

$$PSD = \frac{1}{2\pi\mathcal{N}}|n(\mathcal{N}, f, \tau)|^2 \tag{4.16}$$

where $n(\mathcal{N}, f, \tau)$ is the discrete Fourier transform of the population imbalance, $n(t)$ evaluated at $t = k\tau$ ($k = 0, 1, ...\mathcal{N}$ and $\mathcal{N}$ is the length of the discrete time series).

Fig.4.14(a) corresponds to the power spectral density for no interaction case, that is, $\lambda = 0$. In this case, the PSD shows that the fundamental frequency of the system

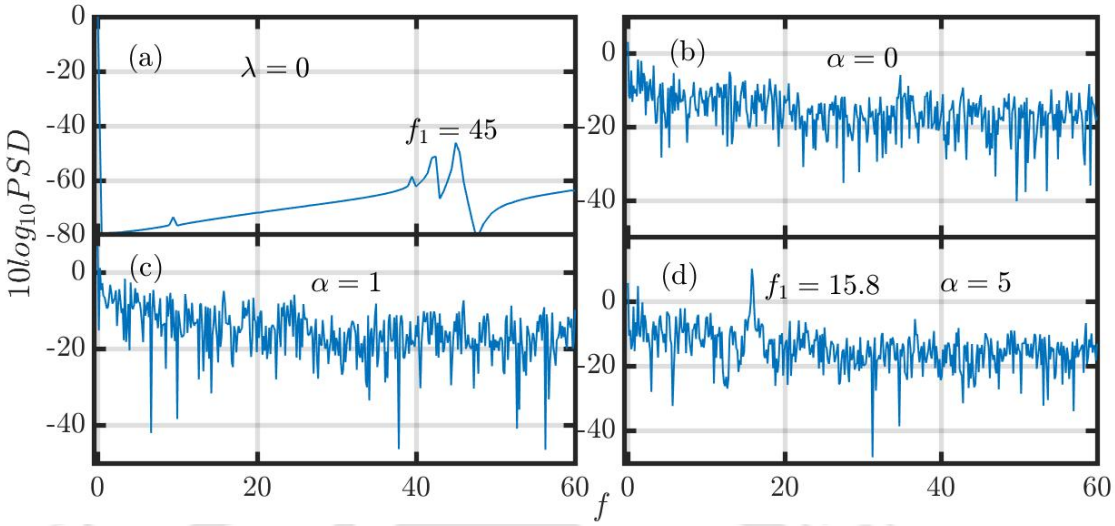

Figure 4.14: The power spectral density, PSD for $V_0 = 30$. (a) corresponds to the case of no interaction, that is, $\lambda = 0$, (b) corresponds to $\alpha = 0, \lambda = 5.6$, (c) corresponds to $\alpha = 1, \lambda = 5.6$ and (d) corresponds to $\alpha = 5, \lambda = 5.6$.

appears at $f_1 = 45$. With the inclusion of the interaction, for large values of λ ($\lambda = 5.6$), the PSD shows fully populated pattern over the entire frequency range that establishes the presence of white noise in the particle dynamics as seen in Fig.4.14(b).

Now to probe deeper, let us fix the interaction strength at $\lambda = 5.6$ and investigate the effect of the amplitude of the driving term, α in PSD. For small amplitude, that is, $\alpha = 1$, the observed white noise in the dynamics of the bosons prevails [see Fig.4.14(c)] as that for $\alpha = 0$. With further increase in α, for moderate α ($\alpha = 5$), the development of one prominent peak is observed at a frequency $f_1 = 15.8$ along with some smaller fluctuations, thereby hinting towards the reduction of the white noise present in the dynamics as clear from Fig.4.14(d). Further increase in the driving amplitude results into a visible reduction of the white noise which is present in the dynamics in absence of the driving force. Therefore, the dynamics of the system of interacting bosons in a temporally driven tilted well undergo a series of transitions from a regular to a noise induced and finally to a orderly system.

4.2.4 Conclusions

We have investigated the tunneling dynamics of the quantum seesaw; where a system of interacting bosons trapped in a temporally driven tilted double well potential. We studied a periodic drive of the seesaw with a constant frequency. Without any interaction,

the time evolution of the natural occupations depict that the system of interacting bosons remain in a fully condensed state irrespective of time which is verified from the fully coherent correlation plot. For a finite interaction strength, the system transits from a depleted condensate to a threefold fragmented state with the passage of time. With the inclusion of the periodic drive, the dynamics of the transition from depleted to fully fragmented state becomes faster. Furthermore, for large driving amplitude, the rate of appearance of fragmentation is enhanced. To probe deeper into the particle dynamics, we have also investigated the time evolution of the population imbalance along with the power spectral density, PSD. For no interaction, the dynamics of population imbalance almost frozen around zero and remains so irrespective of time, thereby indicating a scenario where both the wells consist of equal number of boson population. With increase in interaction and the periodic drive, it is observed that the initially frozen dynamics show features with fast oscillations and damped amplitude. Further from PSD, it is observed that for finite interaction strength without any drive, the PSD shows presence of white noise in the trajectory of the particle dynamics. For gradual increase in the periodic drive, PSD shows reduction of the noisy signal. Finally, for strong driving amplitudes, it is observed that the white noise is reduced significantly with the appearance of a distinct peak at a certain frequency. Since this temporally driven tilted potential that imitates a quantum seesaw are experimentally achievable, hence it may be used as a '*noise filter*', that is, as a passive noise controller where the noise reduction is achieve by using some noise insulating material.

4.3 Simulation of rotating condensates confined in a 2D harmonic trap

4.3.1 Introduction

The successful experimental realization of artificial magnetic field in the domain of ultracold atoms confined in optical potentials [89–91] have paved the path to explore the physics of charged particles with neutral atoms. The charge neutrality inherent to the ultacold atoms in an optical potential introduces a constraint to explore the behviour of the many-body physics in presence of an external magnetic field. Thus to overcome this restriction, one can can set the neutral atoms into a rotational motion. Basically, the

Coriolis force corresponding to the rotational motion of these atoms emulates the role of Lorentz force on a charged particle induced by an external magnetic field [177–180].

In this work, we introduce a mechanical rotation into the condensate confined in a two dimensional harmonic trap, with a rotational frequency $\boldsymbol{\omega}$. This rotational motion introduces a synthetic gauge field into the system, where the symmetric gauge potential may be given by $\mathbf{A}_s = \boldsymbol{\omega} m(-y,x)$ with m as the mass of the constituent bosons of the condensate. This gauge is known as the mixed gauge which is extensively used to study two dimensional quantum Hall physics [230].

In order to proceed with the formalism, one needs to take account of the proper boundary conditions. Hence we introduce the magnetic Fourier transform and compose the continuous MCTDHB equations that build the MCTDHB wave functions with the proper periodic structure. As the magnetic Fourier transform naturally incorporates the twisted boundary conditions (explained later) that applies to the case of rotating bosons, hence we shall apply it in our work as well [231].

In this section, we simulate the dynamics of interacting bosons in a synthetic gauge field confined in a harmonic trap via MCTDHB. It is important to mention that in this section, we are going discuss a few preliminary results on the effect of the gauge field on the temporal evolution of the natural occupation and the natural orbitals. In future, we are going to probe deeper into this problem.

4.3.2 Magnetic translational group and magnetic Fourier transform

In this simulation, the vector potential in the symmetric gauge can be expressed as,

$$\mathbf{A} = \boldsymbol{\omega} m\left(-y\hat{x} + x\hat{y}\right) \tag{4.17}$$

Hence, the effective magnetic field, B in the chosen gauge is given by,

$$\mathbf{B} = 2\,\boldsymbol{\omega}\, m\, \hat{z} \tag{4.18}$$

The kinetic momentum operator given in Eq.(2.46) is modified in presence of the effective magnetic field as,

$$\mathbf{P} \equiv \mathbf{p} - \mathbf{A} \tag{4.19}$$

here $\mathbf{p} = -i\hbar\nabla$. In addition, gradient of any arbitrary function, λ which depends on the position coordinates can be added to the vector potential. For example, $\mathbf{A}_s = \mathbf{A}_s + \nabla\lambda$,

where one can choose $\lambda = -\omega mxy$. This of course leaves the magnetic field unchanged. It is convenient to introduce a new set of quantum mechanical operators [231] as defined below,

$$\begin{aligned} \prod_x &= p_x - By - \partial_x \lambda \\ \prod_y &= p_y + Bx - \partial_y \lambda \end{aligned} \tag{4.20}$$

These operators commute with the kinetic momentum operator, $\left[\prod_i, P_j\right] = 0$. Henceforth, the magnetic translational operators (MTOs) can be defined in terms of these quantum mechanical canonical operators as,

$$T(\mathbf{R}) = e^{\frac{i}{\hbar}\boldsymbol{\Pi}.\mathbf{R}} \tag{4.21}$$

Let us consider a rectangular computational magnetic supercell of dimensions $D_x \times D_y$. In analogy with a particle in a periodic potential (without any magnetic field), it induces the boundary conditions on Ψ as in the following,

$$\begin{aligned} \Psi(x,y) &= T(D_x\hat{x})\Psi(x,y) = e^{-\frac{i}{\hbar}ByD_x} e^{-\frac{i}{\hbar}[\lambda(x+D_x,y)-\lambda(x,y)]}\Psi(x+D_x,y) \\ \Psi(x,y) &= T(D_y\hat{y})\Psi(x,y) = e^{\frac{i}{\hbar}BxD_y} e^{-\frac{i}{\hbar}[\lambda(x,y+D_y)-\lambda(x,y)]}\Psi(x,y+D_y) \end{aligned} \tag{4.22}$$

These boundary conditions reveal that the presence of a gauge field induces a phase 'twist' over the conventional periodic boundary conditions [231, 232] . Therefore, the boundary conditions in Eqs.(4.22) are termed as the twisted boundary conditions (TBC) [233].

Now by employing the Fourier transform, Ψ can be expanded in a basis of functions that are eigenstates of the canonical momentum operators, $\prod$ and they obey periodic boundary conditions. Here instead we expand Ψ in terms of the eigenfunctions of the magnetic translational operators and hence they satisfy the TBCs. Thus we arrive at the expressions those define the magnetic Fourier transform as,

$$\begin{aligned} \tilde{\Psi}(k_x,y) &= \frac{1}{\sqrt{D_x}} \int_0^{D_x} dx\, e^{-i\left[k_x x + \frac{B}{\hbar}xy - \frac{1}{\hbar}\lambda(x,y)\right]}\Psi(x,y) \\ \tilde{\Psi}(x,k_y) &= \frac{1}{\sqrt{D_y}} \int_0^{D_y} dy\, e^{-i\left[k_y y - \frac{B}{\hbar}xy - \frac{1}{\hbar}\lambda(x,y)\right]}\Psi(x,y) \end{aligned} \tag{4.23}$$

and its inverse as,

$$\begin{aligned} \Psi(x,y) &= \frac{1}{\sqrt{D_x}} \sum_{k_x} e^{i\left[k_x x + \frac{B}{\hbar}xy - \frac{1}{\hbar}\lambda(x,y)\right]}\tilde{\Psi}(x,k_y) \\ \Psi(x,y) &= \frac{1}{\sqrt{D_y}} \sum_{k_y} e^{i\left[k_y y - \frac{B}{\hbar}xy - \frac{1}{\hbar}\lambda(x,y)\right]}\tilde{\Psi}(x,k_y) \end{aligned} \tag{4.24}$$

here $k_x = \sum_n \frac{2\pi n}{D_x}$ and $k_x = \sum_n \frac{2\pi n}{D_x}$ and n is an integer (D_x and D_y are the dimensions of the supercell). The above equations satisfy the TBCs given in Eqs.(4.22).

4.3.2.1 Quantities of interest

The details of the MCTDHB formalism is already elaborated in **Chapter 2**. In this subsection, we are going to briefly discuss an important quantity which is employed to simulate the dynamics of interacting bosons in presence of a synthetic gauge field, that is, the one-body reduced density matrix, RDM of the N-boson state $|\Psi(t)\rangle$ and which is defined as,

$$\rho^{(1)}(x,y;t) = \langle\Psi|\hat{\Psi}^{\dagger}(x',y';t)\hat{\Psi}(x,y;t)|\Psi\rangle = \sum_i n_i \phi_i^*(x',y';t)\phi_i(x,y;t) \tag{4.25}$$

in its eigenbasis $\{\phi_i(x,y;t)\}$ [62, 127]. Here n_i is the i^{th} eigenvalue and $\phi_i(x,y;t)$ the corresponding eigenfunction, also known as natural occupation and natural orbital, respectively. The diagonal of $\rho^{(1)}$ corresponds to the single-particle probability distribution $\rho(x,y;t)$. A bosonic system is said to be condensed if the RDM has only a single macroscopic eigenvalue and k-fold fragmented if the RDM has k macroscopic eigenvalues.

4.3.3 Results

In this work, we consider the rotating condensate of $N = 40$ number of bosons which interact via contact interaction, $\hat{W}(\mathbf{r}_i - \mathbf{r}_j) = \lambda_0(N-1)$ with $\mathbf{r} = x, y$, trapped in a two dimensional harmonic trap of the form given below

$$V_{trap}(x,y) = \frac{1}{2}\left(\omega_x^2 x^2 + \omega_y^2 y^2\right) \tag{4.26}$$

For the following simulation, we consider the values of the frequencies of the harmonic trap as $\omega_x = \omega_y = 1$, the interaction strength, $\lambda_0 = 0.05$. Here the numerical grid in the x-direction extends from $x_{min} = -14$ to $x_{max} = 14$, similarly in the y-direction it extends from $y_{min} = -14$ to $y_{max} = 14$, where one body density vanishes at the boundaries.

We simulate the dynamics of the rotating condensate with MCTDH-X software package [208–210] using $M = 4$ orbitals that provides 12341 variationally optimized permanents for the complete computation [as the convergence of energy achieved with four orbitals in this system]. Fig(4.15) depicts the schematic view of the trapping potential, V_{trap} as given in Eq.(4.26).

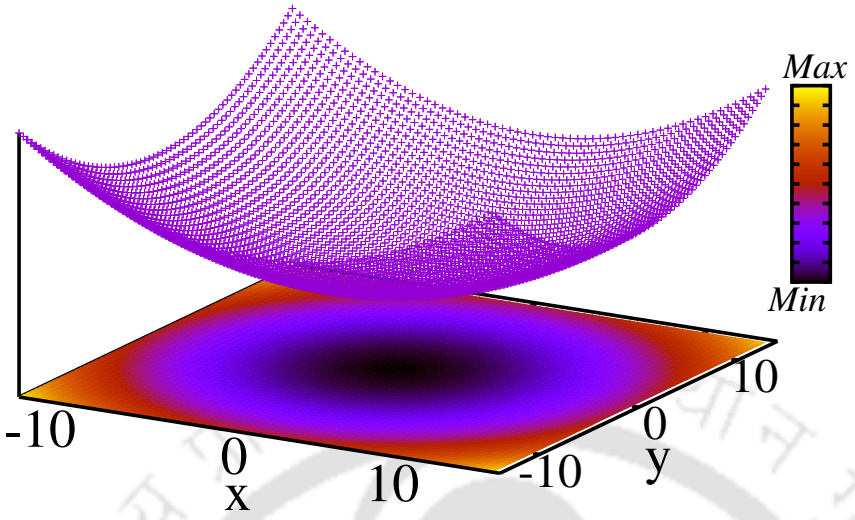

Figure 4.15: The schematic diagram of the trapping potential given in Eq.(4.26).

As an initial state for the computations, we use the ground state of the interacting bosons confined in the potential mentioned in Eq.(4.26) with angular frequency of the condensate as $\omega = 0.01$. To simulate the dynamics, we vary ω from 0 to 0.7 which represents that the magnetic field is varied in this range. In the following we present the results that correspond to the parameter field $(\lambda, \omega) = (0.05, 0.1)$ owing to the observed distinct features in the system.

In this simulation, to define dimensionless units, the MCTDHB Hamiltonian is divided by $\hbar/mD^2$ with $\hbar = m = 1$ and D is the convenient scale of the system.

4.3.3.1 Natural occupations

Let us explore the effect of the synthetic gauge field on the time evolution of the natural occupations, $\frac{n_i}{N}$ as depicted in Fig.(4.16). At a initial time, that is, at $t = 0$, the condensate remains in a depleted state with the value of the first natural occupation, $\frac{n_1}{N} \sim 86\%$, the second natural occupation, $\frac{n_2}{N} \sim 14\%$, with the third and fourth natural occupations being zero, that is, $\frac{n_3}{N} = \frac{n_4}{N} = 0$. As time, t progresses, within a specific range of time, namely, from $t = 6$ to $t = 50$, we observe some features in the pattern of $\frac{n_1}{N}$ and $\frac{n_2}{N}$ along with a gradual increase in the values. After $t = 50$, the fluctuations observed in the pattern of the natural occupations completely vanish and this prevails with further increase in time. Finally, the system transits to a fully condensed state with $\frac{n_1}{N} = 100\%$, $\frac{n_2}{N} = \frac{n_3}{N} = \frac{n_4}{N} = 0$ and remains so irrespective with the passage of time.

It is also important to mention that, in the absence of the synthetic field ($\omega = 0$), we

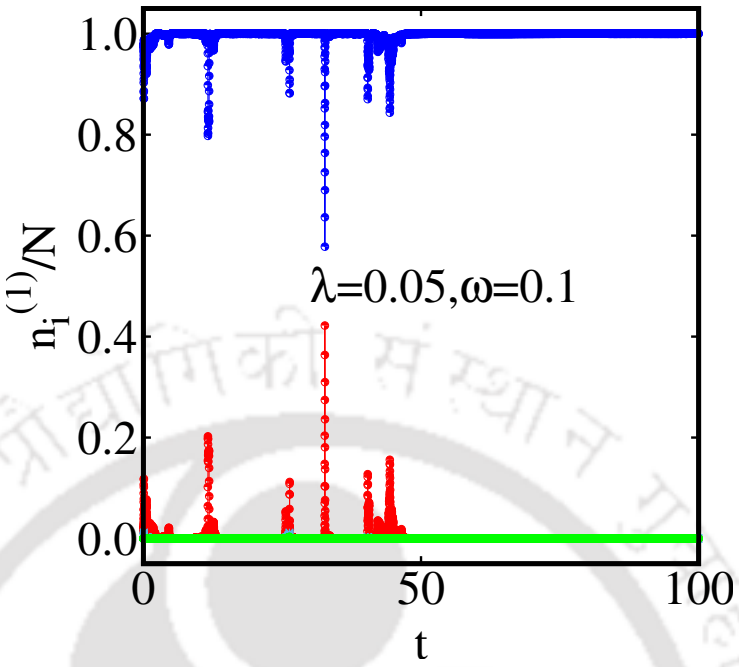

Figure 4.16: The time evolution of the natural occupations $\frac{n_i}{N}$ for angular frequency, $\omega = 0.1$ and interaction strength, $\lambda_0 = 0.05$. In this figure the blue line with circles represents $\frac{n_1}{N}$, the red line with circles represents $\frac{n_2}{N}$, turquoise blue line with circles represents $\frac{n_3}{N}$ and the green line with circles represents $\frac{n_4}{N}$.

have noticed a fully condensed state at $t = 0$ and the situation prevails as time progresses. Henceforth, the occurrence of depleted condensate at $t = 0$ is observed in presence of a gauge field.

4.3.3.2 One-body density and natural orbitals

Now we are going to discuss the impact of the synthetic gauge field on the temporal evolution of the one-body density, ρ and the natural orbitals, ϕ_i at various times, t as shown in Figs.(4.17). Fig.4.17(a)-(e) correspond to ρ and ϕ_i respectively at small time, that is, $t = 10$. It is observed that one-body density, ρ shows maximum which is centered at the origin of the harmonic trap Fig.4.17(a). Here the first natural orbital, ϕ_1 shows a maximum and some fragmented amplitude around the origin of the harmonic trap, see Fig.4.17(b). The second natural orbital, ϕ_2 also renders a similar pattern as evident from Fig.4.17(c). However, the third natural orbital, ϕ_3 is distinctively fragmented into four maxima around the origin [see Fig.4.17(d)]. Finally, the fourth natural orbital, ϕ_4 shows only one distinct maximum centered at the origin along with a few fragmented amplitudes as evident from Fig.4.17(e).

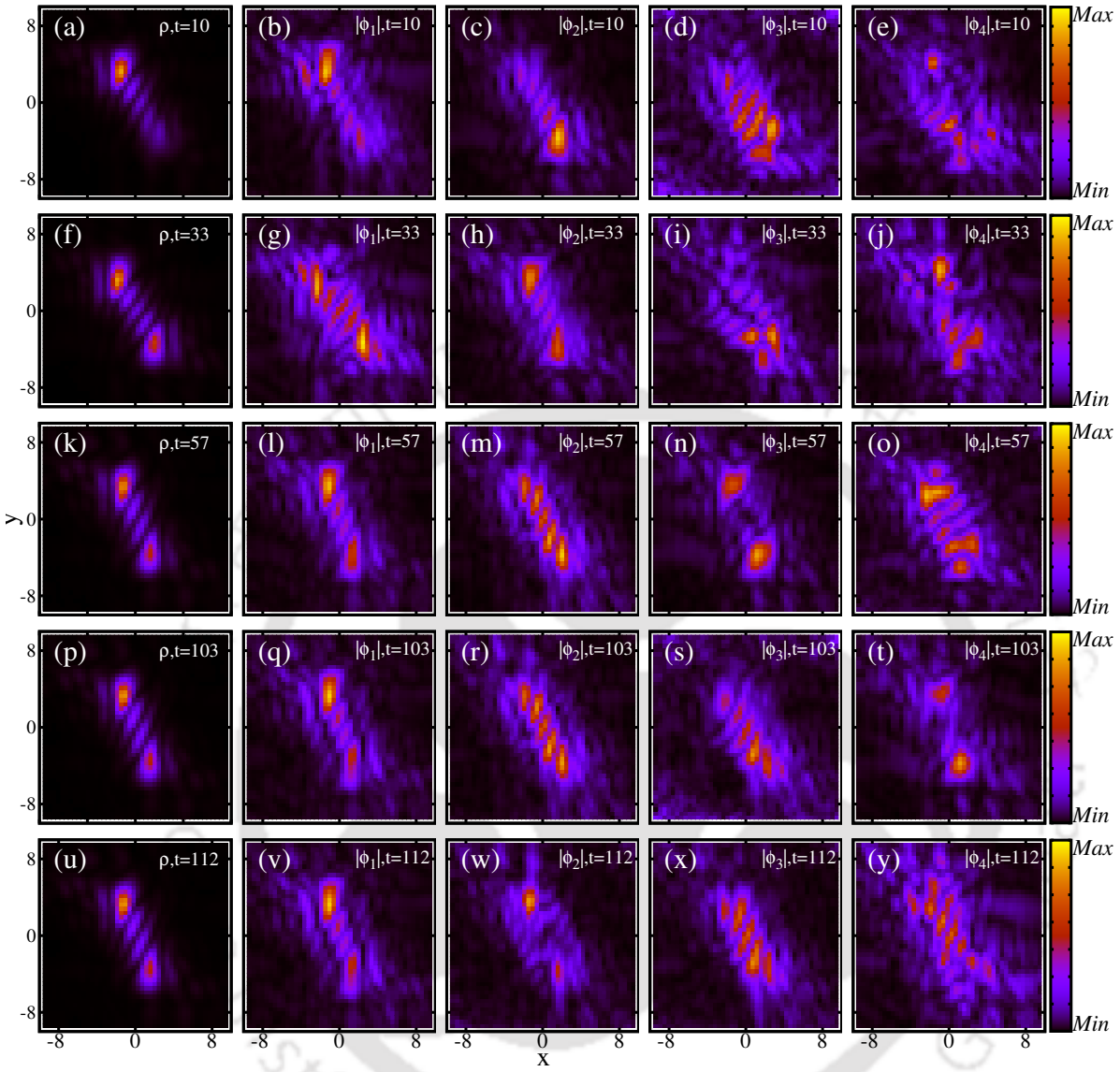

Figure 4.17: These figures depict the snapshots of one-body density, ρ and natural orbitals, ϕ_i at various instants of time, t. (a), (f), (k), (p), (u) correspond to ρ for $t = 10$, 33, 57, 103 and 112 respectively. (b)-(e) denote ϕ_1, ϕ_2, ϕ_3 and ϕ_4 for $t = 10$. (g)-(j) represent ϕ_1, ϕ_2, ϕ_3 and ϕ_4 for $t = 33$. (l)-(o) correspond to ϕ_1, ϕ_2, ϕ_3 and ϕ_4 for $t = 57$, similarly (q)-(t) represent ϕ_1, ϕ_2, ϕ_3 and ϕ_4 for $t = 103$. Finally, (v)-(y) denote ϕ_1, ϕ_2, ϕ_3 and ϕ_4 for $t = 112$ respectively.

As time progresses, for $t = 33$, it is observed that ρ is fragmented into two maxima around the center of the harmonic trap [Fig.4.17(f)]. Also ϕ_1, ϕ_2, ϕ_3 and ϕ_4 show more than one maximum around the origin of the trap [see Figs.4.17(g), (h), (i) and (j) respectively]. With further increase in t, the density profile, ρ yields similar feature as that for $t = 33$ as evident from Figs.4.17(k), (p) and (u). Also the profile of the natural orbitals, ϕ_i show features with more than one maximum with increase in t.

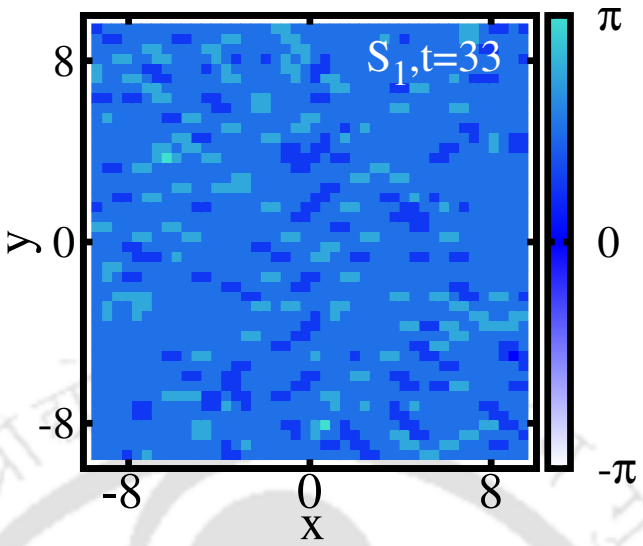

Figure 4.18: The orbital phase, S_1 corresponding to the first natural orbital, ϕ_1 as obtained from Eq.(4.27) for time $t = 33$.

To check whether the observed features in the one-body density, ρ and the natural orbitals, ϕ_i have indeed the characters of vortices, we further calculate another useful quantity, namely, the orbital phase and is expressed as,

$$S_i(x,y;t) \quad = \quad \arg[\phi_i(x,y;t)] \tag{4.27}$$

It is already known that in presence of vortices, the orbital phase depicts a feature in which it shows patterns which replicates when the phase has varied by 2π [234]. Whereas the orbital phase plot in our case does not show any of these features for any of the orbitals as evident from Fig.(4.18). Similar feature is obtained for all other orbital phases that is evaluated for parameter values corresponding to that for Figs.(4.17). We must admit that these are preliminary results and need more close investigation.

We have repeated our analysis for different values of the magnetic field which enters into our calculation through $\boldsymbol{\omega}$, however the results do not show any important features as that are presented earlier.

4.3.4 Conclusions

We have simulated a scenario where a rotating condensate confined in a two-dimensional harmonic trap that induces an effective magnetic field into the system. Thereafter we have investigated the temporal evolution of the natural occupations as well as the natural orbitals of the system for a specific set of field parameters owing to the distinctive features

of the dynamics. It is observed that the temporal evolution of the natural occupation features a transition from depleted to fully condensed state along with some distinct features within a certain range of time, that is from $t = 6$ till $t = 50$. Moreover, from the temporal evolution of the one-body density and the natural orbitals, it is observed that for certain values of time, the one-body density and all the four natural orbitals show a feature that comprise of more than one maximum around the center of the harmonic trap. To verify whether the observed features in the one-body density and all the four natural orbitals, we have also computed the orbital phases and it appears that there are no vortices present in the system. It is important to note that the results explored in this section are very preliminary and in future we aim to investigate deeper in this field.

CHAPTER 5

IMPORTANCE OF THE MCTDHB FORMALISM: A STUDY FOR CONTACT AND NON-CONTACT INTERACTIONS

5.1 Introduction

In this chapter, we discuss and enumerate the importance of the Multiconfigurational time-dependent Hartree approach for bosons, MCTDHB that have been employed to study various problems in the thesis. The motive is to emphasize the superiority of the simulation techniques over the Bose Hubbard model, BHM. However, by no means this is an exhaustive study and we wish to restrict the comparison in some specific cases as described below.

In recent times, it is observed that, apart from the interaction strength, the geometry of the trapping potential is also have a strong impact on the behaviour of the condensate for interacting bosons. Hence, to capture the true physics, the model should not have a limitation on the choice of the form of the trap. Here, the MCTDHB simulation technique is a generalized (continuum) model where one is not restricted by the form of the trapping potential. A more detailed note on the applications and usefulness of the MCTDHB technique is included later.

On the other hand, the BHM assumes presence of a lattice (an optical lattice) very similar to a crystal lattice where the ultracold atoms are loaded and they are coupled by density-density interaction potential. The bosons are allowed to move by means of a

hopping energy from one lattice site to its neighbour and in the same site, they interact via an onsite Hubbard potential. Also we can explore the physics of long-range interaction between the bosons with the help of a nearest neighbour density exchange term. The latter case exhibits a significant rich physics.

It is known that generalizations within the BH model depends on the multi-band or Wannier-Stark single-particle basis states. However with MCTDHB, we can go beyond the BH models and employ the optimized single particle basis given by MCTDHB. The optimized MCTDHB basis has been demonstrated to be far more accurate than the non-optimized basis states [124]. The MCTDHB theory optimizes variationally both the basis set *and* the expansion coefficients in that basis set (see [60, 61] and references therein); its solutions thus assume no predetermined symmetry or shape of the many-body state employed there. Therefore, we use MCTDHB to obtain an optimized problem-adapted basis to investigate various properties of bosons in optical lattice potentials.

It may be noted that we are not going to do an exhaustive comparison of the MCTDHB and the BHM with regard to each of the topics dealt with in the thesis. It may also be noted that a direct comparison has been done in [63, 235–237]. All these studies [63, 235–237] as well as, for instance, the reference [124], demonstrate that MCTDHB represents a generalization beyond the exact diagonalization approaches with static basis sets like that of the Bose-Hubbard approach, where the latter uses only site localized Wannier functions. Necessarily, the self-consistent basis of MCTDHB is superior to a fixed static basis as shown directly in [63, 124, 235–237].

In this chapter, we consider the case of tilted triple wells as a prototype example (as mentioned in Eq.(4.5)) to emphasize upon with the importance of the MCTDHB formalism as discussed in the following. It is important to mention that in this simulation, all the parameters are defined in dimensionless units and to do so we divide the MCTDHB Hamiltonian by $\hbar/mL^2$ with $\hbar = m = 1$ where L is the convenient length scale of the system.

5.2 Variation of natural orbitals with interaction strength

In this section, we are going to discuss about the behaviour of the natural orbitals, $\phi_i(x)$ for a fixed tilt $\alpha = 2.5$ (α being the tilt parameter) and the barrier height of the

trapping potential, $V_0 = 180$ as a function of the interaction strength, λ for the case of contact interactions as shown in Fig.(5.1). The motivation and background of the study has been discussed in the **Chapter 4**. We do not intend to repeat the same. Fig.(5.1)

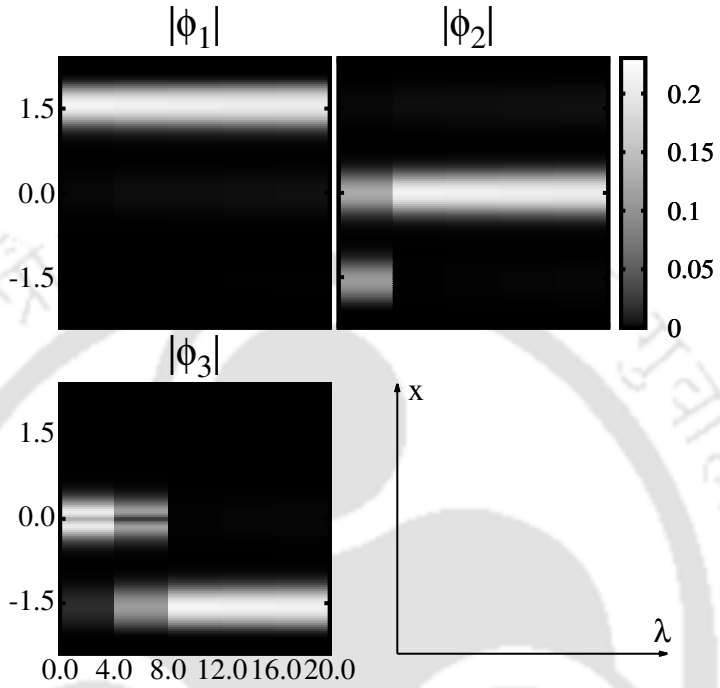

Figure 5.1: The figure shows the natural orbitals, $|\phi_i(x)|$, as a function of the interaction strength λ for $V_0 = 180$ and non-zero tilt $\alpha = 2.5$. It is clearly seen that the optimal MCTDHB basis does *not* correspond to site-localized Wannier or Wannier-Stark states, that is, the Hubbard model is not applicable.

depicts how the basis functions obtained from MCTDHB, that is, the natural orbitals, ϕ_i, are adapted to optimally represent the many-body state. Up to a tilt value given by $\alpha = 2.5$ and at large interaction strengths ($\lambda \gtrsim 8$), it is observed that the localized, Wannier-like single-particle basis states are optimal choices. Hence, a Bose-Hubbard description can be expected to provide accurate results for the parameter values, $\alpha = 2.5$ and $\lambda \gtrsim 8$. However, for a range of small to moderate interaction strengths ($\lambda \lesssim 8$) with a tilt of value, $\alpha = 2.5$, the optimal single-particle basis states obtained from MCTDHB drastically depend on the values of the interaction strength. Thus the second, $|\phi_2(x)|$ and third, $|\phi_3(x)|$ natural orbitals change their degree of delocalization/localization and even their intra-well structure as made clear through Fig.(5.1). In this regime, described by $\alpha = 2.5$ and $\lambda \lesssim 8$, the optimized single-particle basis states are not of the Wannier type and hence the Bose-Hubbard model ceases to be a valid description corresponding to this case.

5.3 Long range interaction

The many-body physics of interacting bosons can be characteristically defined by a "diluteness parameter" that incorporates the importance of interactions [238] between bosons. Therefore, the samples produced in experiments which are characterized by such diluteness parameter, intrinsically renders true physics as the mean interparticle distance is much smaller in comparison to the range of the interparticle interactions. In particular, a gas is more dilute for short-range interactions, however in the case of long-range interactions, for example, Coulomb interactions, the gas cannot be considered as dilute because of the decrease in density for three dimension [239]. This fact results into the formation of Wigner crystals at very low densities [240]. Whereas, in one dimension, with high densities, the presence of Coulomb interaction leads to the formation of a strongly correlated Tonks-Girardeau gas [241]. In recent times, the experimental realization of Cr atoms with no nuclear spin, but only hyperfine spin-3 [103] have paved the way to explore the area of long range interactions with ultracold atoms confined in optical lattices. In Ref. [242], with the help of single mode approximation (SMA), the ground state properties of spin-1 dipolar condensate has been studied in the regime of smaller dipole interaction strengths. Also the investigation of polar vortices with various spin textures, chiral spin vortex in ferromagnetic case has been reported in [243, 244].

In the BHM, the long range interactions between the bosons are included via nearest neighbour density-density interaction. Thus to include longer range interaction, the best one can do is to include a term $n_i n_j$, where i and j are nearest neighbours. Although this extended interaction yields rich quantum features, such as, different density ordered superfluid phases etc, but it mostly defeats the essence of longer range (coulomb like) interaction potential which should vanish only at infinite distances which is beyond the ambit of BHM.

Thus to retain the spirit of long range term, that is, $V_{int}(r) \propto 1/r^n$, let us discuss the effect of long range interactions on the ground state properties of interacting bosons in tilted triple wells [for visual clarity of the potential, see Fig.(4.1)] by employing MCTDHB formalism. The long-range interaction of two bosons at x_j and x_k, respectively, [that is the two-boson interaction term in the Hamiltonian in Eq.(4.2)] is written as [239, 245, 246]

$$\hat{W}(x_j - x_k) = \frac{\lambda_0}{|x_j - x_k|^3 + \Delta^3} \tag{5.1}$$

where Δ^3 denotes the threshold of the long-range interaction and is taken to be 0.07

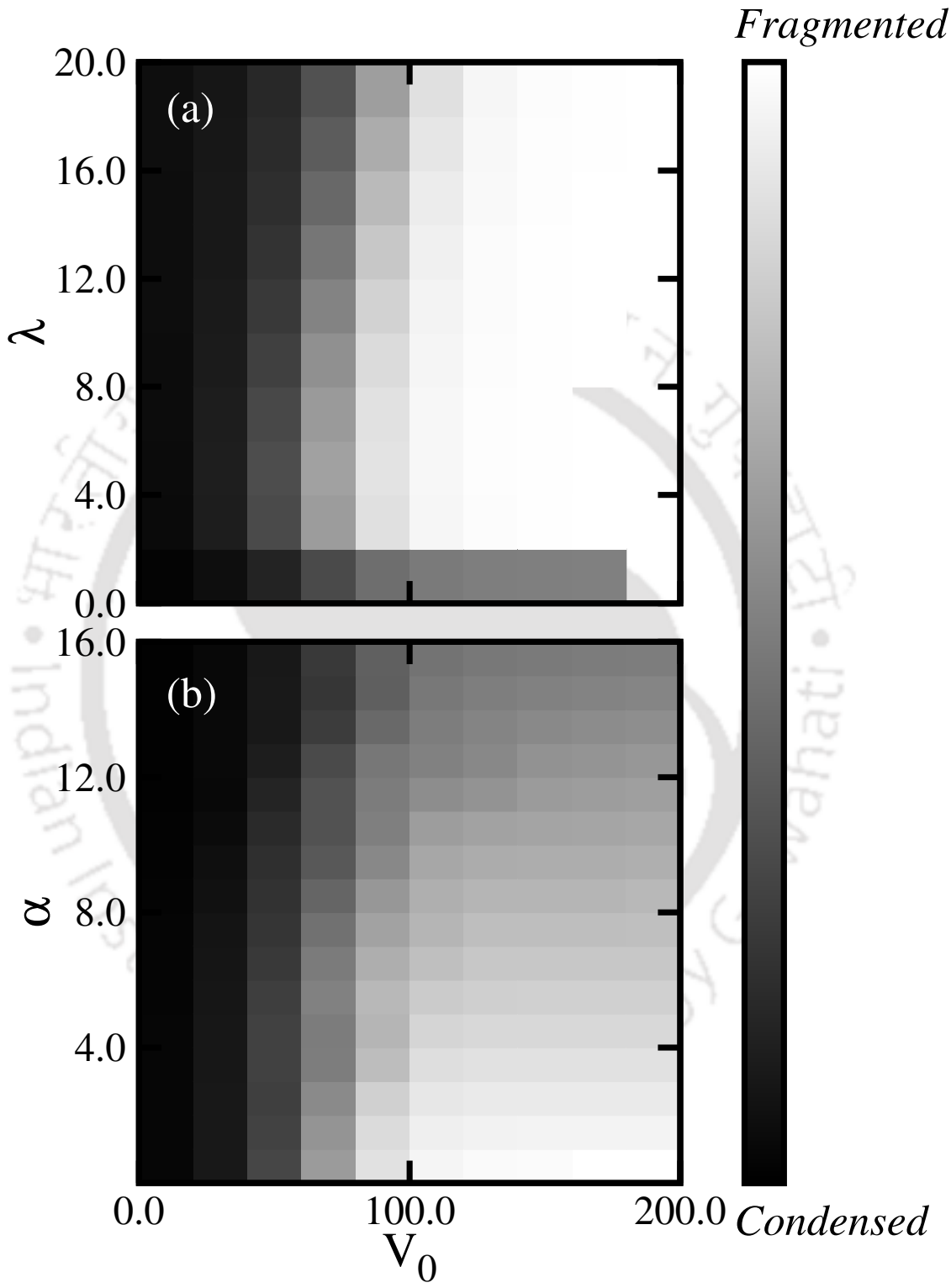

Figure 5.2: The phase diagrams show variation of fragmentation, F (a) as a function of the interaction strength, λ without inclusion of tilt, α and (b) with respect to tilt, α for a specific value of interaction strength, $\lambda = 6$ in the case of long range interaction.

for this study [61, 62]. λ_0 is the interaction strength. Such long-range interactions are relevant for atomic clouds made of Cr [103], Dy [247] or Er [248].

Figs.(5.2) show the phase diagrams in the parameter space that depict the variation of fragmentation, F [Eq.(2.83)] for long range interaction of the type of Eq.(5.1). Let us first analyze the situation in absence of tilt, that is, $\alpha = 0$ [see Fig.5.2(a)]. It is observed that for the smaller values of the barrier height, V_0 and the interaction strength, λ, there is negligible fragmentation of the condensate. This signifies that the system remains in a fully condensed state with macroscopic population in the first natural orbital, ϕ_1 only. The fragmentation, F of the condensate, starts appearing for moderate values of both V_0 and λ. However for large V_0, even for small values of λ, the system transits to a fully fragmented state. Now with the increment in V_0 and small λ, the condensate slowly transits to fragmented phase. However for moderate V_0 and large λ, a peculiar behaviour is observed, where the observed fragmentation gradually disappears and the condensate transits to a depleted state with population in the first natural orbital $\sim 70\%$. This feature will be clear from the discussion of natural occupation, presented in the subsequent subsection. With further increase in V_0 and for very large V_0 three is an increase in the population of the second, ϕ_2 as well as the third natural orbitals, ϕ_3 with corresponding decrease in population of ϕ_1. Hence, at the maximum value of F which is a three-fold fragmented phase of the condensate (as we have $M = 3$ orbitals), all the orbitals populate equivalent boson densities. Finally, for large λ, the fragmentation starts appearing even in moderate barrier height due to the presence of two-body interaction to minimize the energy of the condensate.

Fig.5.2(b) depicts the behaviour of fragmentation, F with the inclusion of tilt, α. It is observed that the fully fragmented state gradually disappears with increase in α and the barrier height, V_0. Here the system transits from a fully fragmented state to a state with certain degree of fragmentation unlike the case for contact interactions. In the competition between α and λ, λ has a dominant effect due to the presence of longer range interaction between the bosons. Hence, the rate of reduction of F in this case is slower in comparison to that for contact interactions [Fig.4.2(b)] and also it is appeared that the system does not transit to a fully condensed state atleast for the range of the tilt that we have considered for this study. Therefore, the fragmented state is energetically favourable for large barrier heights in presence of both tilt and long-range interaction.

Now we are going to discuss about the other ground state properties, such as, natural occupations and first-order correlations in the following subsections to get a clearer

picture pertaining to the presence of long range interaction between the bosons.

5.3.1 Natural Occupations

To explore the fragmentation, coherence, and correlation properties of a many-boson system, let us discuss the behaviour of the natural occupations, $\frac{n_i}{N}$. Fig.(5.3) shows the behaviour of the natural occupations, $\frac{n_i}{N}$ as a function of the tilt parameter, α for fixed barrier height, V_0 and interaction strength, λ, in the case of long-range interactions as given by Eq.(5.1). For the following choices of parameters, namely $V_0 = 80$, $\lambda = 6$ and zero

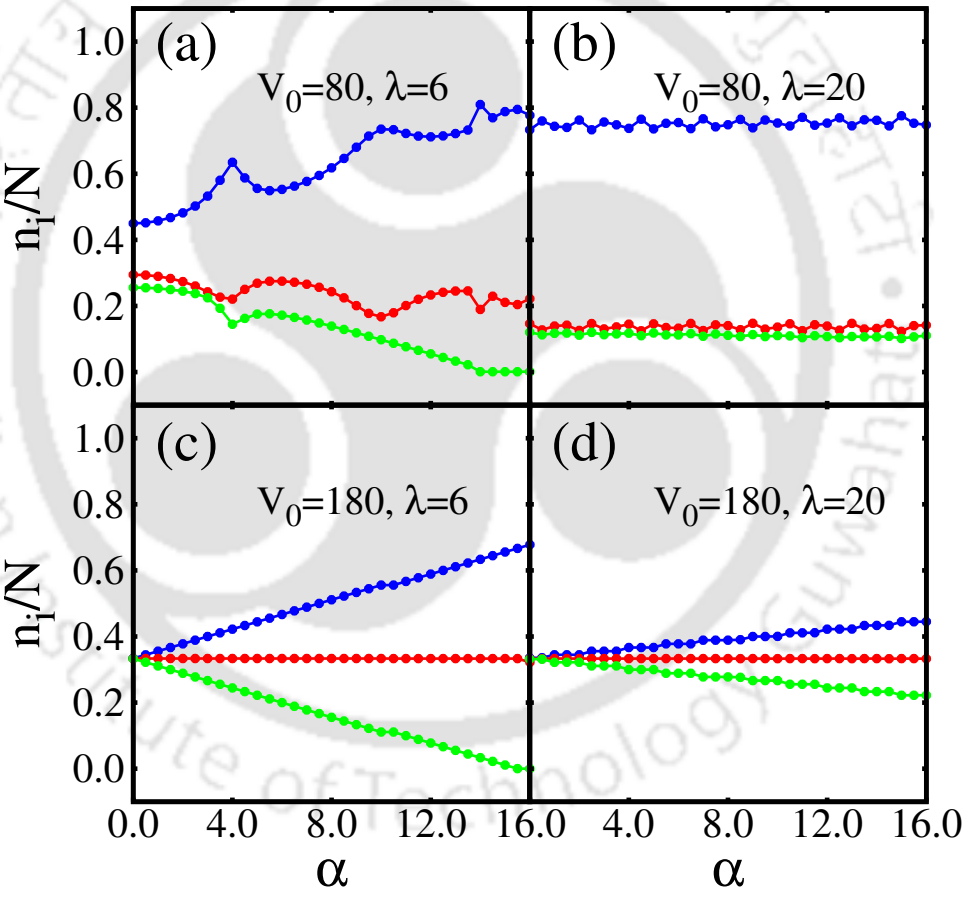

Figure 5.3: Figures depict the variation of natural occupations, n_i/N as a function of the tilt α for long-range interactions. (a) corresponds to $V_0 = 80$ and $\lambda = 6$, (b) corresponds to $V_0 = 80$ and $\lambda = 20$, (c) corresponds $V_0 = 180$ and $\lambda = 6$ and (d) corresponds $V_0 = 180$ and $\lambda = 20$. In all panels, blue lines with circles represent n_1, red lines with circles represent n_2 and green lines with circles represent n_3.

tilt, $\alpha = 0$, the bosons have certain degree of fragmentation with the value of first natural

occupation, $\frac{n_1}{N} \sim 45\%$, the second and the third natural occupations, $\frac{n_2}{N} \sim 30\%$, $\frac{n_3}{N} \sim 25\%$ respectively [Fig.5.3(a)]. With the inclusion of the tilt, $\alpha > 0$, there is a gradual increase in the value of the first natural occupation, n_1/N, and the corresponding decrease in the second and the third natural occupations, n_2/N and n_3/N. However, for a larger interaction strength, $\lambda = 20$, the occupations are unaffected by the presence of the tilt in the trapping potential. This is due to the (surprising) fact that the zero-tilt strongly-interacting system exhibits very little fragmentation; increasing values of α do not alter this behaviour [Fig.5.3(b)].

For larger barrier height, namely $V_0 = 180$ and a moderate interaction strength, $\lambda = 6$, a completely threefold fragmented state is observed with $\frac{n_1}{N} \approx \frac{n_2}{N} \approx \frac{n_3}{N} \approx 33.33\%$ for no tilt, that is, $\alpha = 0$, as clear from Fig.5.3(c). For $\alpha > 0$, a gradual increase of the first natural occupation, n_1/N, and a corresponding decrease of the third natural occupation, n_3/N are observed. However, the second natural occupation, n_2/N remains constant irrespective of the increase in α (unlike in the case of contact interaction, see Fig.4.4(c) in the **Chapter 4**). The unaltered nature of $\frac{n_2}{N}$ signifies that the population in the second natural orbital, ϕ_2 remains unaltered. That means inclusion of the tilt in the potential renders ϕ_2 unaffected since that way it remains energetically favourable. Finally, even for large α, there is a certain degree of fragmentation in the system due to the dominating effect of longer range two body interaction.

For larger interaction strength, $\lambda = 20$, the system remains threefold fragmented up to a moderate value of α near $\alpha \sim 4$. With a further increase of α, a very slow increase in n_1/N and a corresponding slow decrease in n_3/N are observed, while n_2/N remains constant irrespective of the increase in α. However, the state of the system is not settling back to fully condensed not even to depleted state as α increases further [Fig.5.3(d)] at least for the tilt values corresponding to $\alpha \leq 16$ which we have considered here.

Thus, we observe that, generally, inclusion of long range interactions favours the fragmentation of the condensate for a larger barrier height, and is clear by comparing Fig.(5.3) with Fig.(4.4) of **Chapter 4**. At this point, in the competition between α and λ, λ has a dominating effect due to long-range nature.

5.3.2 First-order correlation function

To gain a spatially resolved picture of the fragmentation and coherence properties of the many-body state for the case of long-range interactions, we discuss the behaviour of

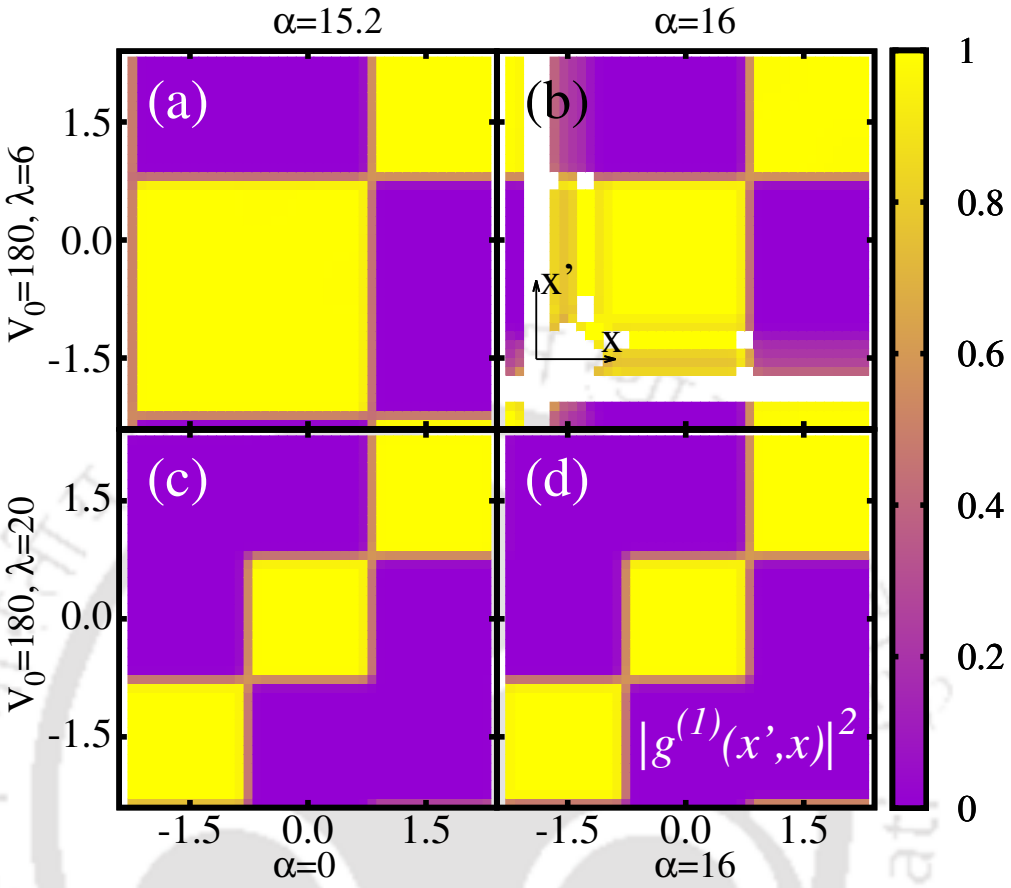

Figure 5.4: The first-order correlation $|g^{(1)}(x_1^{'},x_1)|^2$ is visualized as a function of the tilt and barrier height for $V_0 = 180$ in the case of long-range interaction. (a) and (b) correspond to $\alpha = 15.2$ and $\alpha = 16$ respectively for $\lambda = 6$. Similarly (c) and (d) correspond to $\alpha = 0$ and $\alpha = 16$ for $\lambda = 20$.

the first-order correlation function $|g^{(1)}(x_1',x_1)|^2$. The latter is plotted for $\alpha = 15.2, 16$ and interaction strengths $\lambda = 6, 20$ for a large barrier height, $V_0 = 180$, in Fig.(5.4).

For $\lambda = 6$, an increase in the barrier height leads to the localization of the system. Similarly to the case of contact interactions studied in **Chapter 4** [see Fig.(4.5) and its discussion], a decrease in the coherence between bosons in distinct wells is observed as α grow larger. However, for some values of the tilt, that is, $\alpha = 15.2$, the inter-well coherence between the bosons re-emerges, that is, the coherence between the left and central well is restored where the value of $|g^{(1)}(x_1^{'},x_1)|^2$ is usually closer to unity on the off-diagonal $x \neq x'$ for moderate interaction strength $\lambda = 6$ as shown in Fig.5.4(a). The inter-well coherence is merely diminished with further increase in α ($\alpha = 16$) [Fig.5.4(b)].

For large interaction strength, $\lambda = 20$, the coherence among bosons in distinct wells is lost, that is, $|g^{(1)}(x_1^{'},x_1)|^2 \approx 0$ for $x \neq x'$ irrespective of the increase in the values of α

[panels (c)-(d) of Fig.(5.4)]. As in the case of contact interactions in **Chapter 4**, the barrier height can be used to quench the inter-well coherence also for long-ranged interactions. Further the system remains fully fragmented event at large α, as evident from Fig.5.4(d). This feature again proves the dominant effect of λ. Moreover, the tilt can be used to tune the coherence between neighboring wells for long-ranged interactions, too. Thus a rich set of information is obtained for the case of long range potential as relevant for ultracold atomic gases, such as, Cr, Er, Dy etc.

5.4 Conclusions

We have demonstrated and established the significance of the Multiconfigurational time-dependent Hartree approach for bosons, MCTDHB with the correlated bosons confined in a tilted triple well potential as a paradigm in presence of both contact and long range interactions for the study. In the first part, we have emphasized on how the optimized MCTDHB basis has a greater efficiency to describe the system with accuracy than the Wannier type BH basis. Henceforth, the Bose-Hubbard model fails to describe the system at certain extent.

In the second part, we have also analyzed different ground state properties of the system, for example, fragmentation, coherence etc with the inclusion of long range interaction of the interacting bosons in a true sense with the help of MCTDHB. It is observed that in the competition between the tilt induced in the trapping potential and the long range interaction between the bosons, the long range interaction has a dominant effect on the ground state feature, namely, fragmentation of the condensate.

CHAPTER 6

CONCLUSIONS

This thesis deals with the exploration of various fascinating properties and phases of correlated bosons in different optical potentials. It primarily focused on the investigation of the tunneling dynamics and ground state properties of these interacting bosons and the manipulation of their exotic quantum features by tuning the fundamental properties of the systems, for example, type of the interaction along with its interaction strengths, depth and geometry of the trapping potential etc. We have segmented the thesis mainly into two parts depending on the methodologies, namely, the Bose-Hubbard model (BHM) and the Multiconfigurational time-dependent Hartree approach for bosons (MCTDHB) used therein to investigate various intriguing quantum features. Henceforth, we proceed with a brief conclusion on the content of each of the chapters as summarized in the following.

Chapter 1 contains an overview of the field of interacting bosons, their properties, methodologies and an account of work done. **Chapter 2** includes an elaborate description of the formalisms used and the relevant formulae etc.

In **Chapter 3**, we have employed the BHM to study the tunneling dynamics and various phases of the correlated bosons under three different scenarios, such as, the tunneling dynamics of bosons in a double well potential, a periodically driven system and a time-dependent synthetic gauge field. We have studied them in the following sections.

In the Sec.**3.1**, we have investigated a detailed enumeration, which is by no means exhaustive, of the effects of onsite interparticle interaction on the tunneling dynamics of

a system of few bosons confined in a double well potential. Here the strong and weak coupling regimes are compared and contrasted with regard to the study of tunneling dynamics. Further, we closely scrutinized the sensitivity of the tunneling dynamics to different initial configurations of the system prepared in. It is observed that for an odd number of particles in the limit of weak coupling regime with an initial condition of a population difference of one particle among the two wells is observed to demonstrate accumulation tendencies. However, this behavior is not observed in the case where the population difference is larger than one. Also the effect of an admixture of initial configurations on the tunneling dynamics has been studied further. Though it is premature to comment on the significance of these results to more elegant phenomena, such as using it as an 'atomic switch' etc, however our results can motivate further experiments in the study of atomic dynamics in presence of correlation effects.

Sec.**3.2** dealt with the investigation of the tunneling dynamics of a system of correlated bosons that interacts via a harmonic interaction potential confined in a double well potential. From the time evolution of the population imbalance between the wells, we have observed that at large values of the interaction strength, the system makes a transition from regular to a chaotic state. Further this feature is complemented by investigating the power spectral density, PSD and phase space projection of the population imbalance. Particularly, in the presence of harmonic interaction potential, different routes to chaos have emerged depending on the condition whether the amplitude or the phase of the interaction term being manipulated. We have observed that route to chaos is quasiperiodic in the former case, while, for the latter case, the route to chaos is through the crisis induced intermittency. Furthermore, we have established that the superposition of a chirp modulation to the harmonic driving term reinstates the periodicity in the tunneling dynamics of bosons in a double well potential.

In the Sec.**3.3**, we have explored the effect of time-dependent synthetic gauge fields on the quantum phase transition from the Mott-Insulating (MI) to superfluid (SF) phase and also studied the effect on the discrete energy spectrum of a system of interacting bosons. The behaviour of critical hopping strength, J_c, that is, the value of the hopping strength at which the phase transition occurs is observed to vary differently for various time variation of the time-dependent gauge field. In particular, the Mott insulating lobe whether stabilizes or contracts is dependent on the nature of manipulation of the time- dependent synthetic field, that is, on the form of the time variation which is given by the function $f(t)$ as $f(t) = t^{\alpha}$ with $\alpha = 0.5, 1, 2$ has been considered. Further,

the inclusion of time in the synthetic gauge field destroys the lattice periodicity of the system, however it is observed that with proper tuning of the time dependency, the periodicity can be restored back. Thus the periodicity of the one-dimensional superfluid (SF) order parameter sensitively depends on the nature of the time-dependent synthetic field. Moreover, it is observed that in presence of such time-dependent fields, the order parameter becomes either site independent or dependent based on the tuning of these fields. Furthermore, the time-dependent gauge fields also impose an asymmetry in the discrete energy spectrum of the system that is perceptible from the ceasing effect of the symmetric 'butterfly' structure corresponding to the time independent case. Finally, it is important to remind that the observed asymmetry in energy originates from the emergence of a scalar potential which together with the variation of the vector potential has induced a loss in symmetry.

Further, **Chapter 4** dealt with the implementation of the second formalism, that is, MCTDHB to investigate the ground state and the quantum dynamics of the problems, such as, the ground state properties of correlated bosons confined in a tilted triple well, tunneling dynamics of bosons confined in a quantum seesaw potential and finally dynamics of bosons in presence of a synthetic gauge field, as discussed in the following three sections.

Sec.**4.1** reports an investigation of correlated bosons trapped in a tilted triple well potential. This analysis has shown some fascinating features of the first-order correlation and coherence of bosons confined in the tilted triple well potential. This work yields a protocol to manage the coherence of the many-body state, that is, a variety of correlation patterns is obtainable simply by appropriately tuning the interaction strength, potential depth and tilt of the system. Therefore, superfluid state which is associated with condensation can be formed either localized in one well or delocalized across all the wells. In similar way, Mott-insulating state which is associated with fragmented systems with a customized population difference between distinct wells can also be prepared. Thus the fully coherent superfluid state and the fully incoherent Mott-insulating phase represent the extreme situations. Further, how the intermediate degrees of correlation can also be achieved with the system is explored here . The observed counter-intuitive revivals of coherence between next-to-nearest neighboring sites in the system implies the fact that even a management of non-local correlations is possible with sufficiently accurate tuning of the tilt and the interaction strengths. In the light of recent advanced techniques, a natural extension of this work would cover the field of bosons with internal structure

and/or embedded in an optical cavity. Owing to the long decoherence time, it is also remarked that the many-body state of ultracold atoms can also provide a means to cover correlations and entanglement arising in quantum information processing. Therefore, it is necessary to control and quantify correlations in the many-body state of ultracold atoms, like the one that we have outlined in this work. As a continuation of this work, in future, we will also consider to quantify entanglement entropy and other quantities of relevance for quantum information processing for tilted multi-well systems.

In the Sec.**4.2**, we have explored the tunneling dynamics of the quantum seesaw where a system of correlated bosons are confined in a temporally driven tilted double-well potential. It is observed that for no interaction, the temporal evolution of the natural occupations shows that the system of interacting bosons remains in a fully condensed state at all time which is further confirmed from the fully coherent first-order correlation. With the increase in the interaction strength, for a certain value of the interaction, it is observed that the system transits from being a depleted condensate to a threefold fragmented state with the passage of time. Further, the inclusion of the periodic drive leads that the rate of transition from a depleted to a fully fragmented state becomes rapid. Henceforth, for large amplitude of the driving, the rate of fragmentation is enhanced further. To get a better insight into the quantum dynamics, we have further investigated the time evolution of the population imbalance along with power spectral density, PSD. Without any interaction, the frozen dynamics of population imbalance is observed and it remains so irrespective of the growth in time, thereby indicating a scenario where both the wells consist of equal number of boson population. Further increase in interaction and the periodic drive, it is observed that the initially frozen dynamics of the population imbalance depict some features with fast oscillations. With further investigation of PSD, it appears that for finite interaction strength in absence of the drive, the PSD shows presence of white noise in the dynamics. The gradual increase in the periodic drive, PSD shows a reduction in noise present in the system. Finally, for strong driving amplitudes, a complete disappearance of the white noise is observed with a distinct finite peak at a certain frequency in the PSD. As the temporally driven tilted potential that emulates a quantum seesaw are experimentally achievable, thus it may be used as a '*noise filter*'.

In the Sec.**4.3**, a scenario is simulated, by using MCTDH-X package, where a rotating condensate confined in a two-dimensional harmonic trap that induces an effective magnetic field into the system. Henceforth, we have investigated the temporal evolution of the natural occupations and the natural orbitals of the system for a specific set of

field parameters owing to the distinctive features of the dynamics. It is observed that the temporal evolution of the natural occupation features a transition from depleted to fully condensed state along with some distinct features within a certain range of time. Moreover, from the temporal evolution of natural orbitals, it is observed that for certain values of time, the one-body density and all the four natural orbitals show a feature that comprise of more than one maxima around the center of the harmonic trap. To verify whether the observed features persist in the one-body density and all the four natural orbitals, we have also computed the orbital phases and it appears that there are no vortices present in the system. It is important to mention that the dynamics studied in this section are very preliminary and in future we aim to investigate deeper in this field.

Finally, in **Chapter 5**, we have discussed and specified the importance of the Multi-configurational time-dependent Hartree approach for bosons, MCTDHB by considering the case of correlated bosons confined in tilted triple wells as a prototype example. Here we have demonstrated how the optimized MCTDHB basis has been far more accurate to describe the system than the Wannier type BH basis. Therefore, the Bose-Hubbard model fails to describe the system at this point. In the second part, we have investigated various ground state properties of the system, such as, fragmentation, coherence etc with the inclusion of long range interaction between the bosons in a true sense by employing MCTDHB. Finally, it is observed that the inclusion of long range interaction favours the fragmentation of the condensate at large barrier height and interaction strength, irrespective of the growth in the tilt of the confining potential.

APPENDIX A

EQUATION OF MOTION FOR TRIPLE WELL: EFFECT OF INITIAL CONDITIONS

Here we derive the equations of motion for a few bosons confined in a triple well. The BH Hamiltonian for a system of N interacting bosons in a triple well potential is written as,

$$\begin{aligned}\hat{H}_{BHH} &= -J(\hat{a}_1^\dagger\hat{a}_2+\hat{a}_2^\dagger\hat{a}_1+\hat{a}_1^\dagger\hat{a}_3+\hat{a}_3^\dagger\hat{a}_1+\hat{a}_2^\dagger\hat{a}_3+\hat{a}_3^\dagger\hat{a}_2)+\frac{U}{2}(\hat{a}_1^{\dagger 2}\hat{a}_1^2+\hat{a}_2^{\dagger 2}\hat{a}_2^2+\hat{a}_3^{\dagger 2}\hat{a}_3^2) \\ &+ V(\hat{a}_1^\dagger\hat{a}_1\hat{a}_2^\dagger\hat{a}_2\hat{a}_3^\dagger\hat{a}_3) \end{aligned} \tag{A.1}$$

$\hat{a}_i^\dagger(\hat{a}_i)$ $(i=1,2,3)$ are the creation (annihilation) operators of bosons in the left, central and right wells respectively, J being the tunneling parameter $(J>0)$ between the two modes, U is the strength of the on-site interaction $(U>0)$ and V is the strength of the extended density interaction.

To obtain the tunneling dynamics, the state vector of the system is expanded in the basis of Fock states for a constant particle number N, as in the following,

$$|\Psi(t)\rangle = \sum_{l,k=0}^{N}\frac{c_{lkm}(t)}{\sqrt{l!k!m!}}\hat{a}_1^{\dagger l}\hat{a}_2^{\dagger k}\hat{a}_3^{\dagger m}|0\rangle \tag{A.2}$$

where out of N particles, l are in the left well, k are in the central well and $m=N-(l+k)$ are in the right well. $c_{lkm}(t)$s being the complex coefficients.

In terms of the coefficients $c_{lkm}(t)$, EOM is expressed as,

$$\begin{aligned} i\frac{dc_{lkm}(t)}{dt} &= -J[\sqrt{k(l+1)}c_{l+1k-1m} + \sqrt{l(k+1)}c_{l-1k+1m}] + \sqrt{m(k+1)}c_{lk+1m-1} \\ &+ \sqrt{k(m+1)}c_{lk-1m+1} + \sqrt{m(l+1)}c_{l+1km-1} + \sqrt{l(m+1)}c_{l-1km+1}] \\ &+ \frac{U}{2}[l^2+k^2+m^2]c_{lkm} + V[lkm]c_{lkm} \end{aligned} \tag{A.3}$$

Now we consider the case of three boson system, that is, $N = 3$, then Eq.(A.3) reduces to ten coupled equations as in the following,

$$i\begin{pmatrix} \dot{p}_1 \\ \dot{p}_2 \\ \dot{p}_3 \\ \dot{p}_4 \\ \dot{p}_5 \\ \dot{p}_6 \\ \dot{p}_7 \\ \dot{p}_8 \\ \dot{p}_9 \\ \dot{p}_{10} \end{pmatrix} = \begin{pmatrix} \frac{9}{2}U & -\alpha J & 0 & 0 & 0 & 0 & 0 & 0 & 0 & 0 \\ -\alpha J & \frac{5}{2}U & -2J & 0 & -J & 0 & 0 & 0 & 0 & 0 \\ 0 & -2J & \frac{5}{2}U & -\alpha J & 0 & -\beta J & 0 & 0 & 0 & 0 \\ 0 & 0 & -\alpha J & \frac{9}{2}U & 0 & 0 & -\alpha J & 0 & 0 & 0 \\ 0 & -J & 0 & 0 & \frac{5}{2}U & -\beta J & 0 & 0 & 0 & 0 \\ 0 & 0 & -\beta J & 0 & -\beta J & \frac{3}{2}U+V & -\beta J & -\beta J & 0 & 0 \\ 0 & 0 & 0 & -\alpha J & 0 & -\beta J & \frac{5}{2}U & 0 & -2J & 0 \\ 0 & 0 & 0 & 0 & 0 & -\beta J & 0 & \frac{5}{2}U & -J & 0 \\ 0 & 0 & 0 & 0 & 0 & 0 & -2J & -J & \frac{5}{2}U & -\alpha J \\ 0 & 0 & 0 & 0 & 0 & 0 & 0 & 0 & -\alpha J & \frac{9}{2}U \end{pmatrix} \begin{pmatrix} p_1 \\ p_2 \\ p_3 \\ p_4 \\ p_5 \\ p_6 \\ p_7 \\ p_8 \\ p_9 \\ p_{10} \end{pmatrix} \tag{A.4}$$

here $\alpha = \sqrt{3}$, $\beta = \sqrt{2}$ and finally p_i correspond the possible initial configurations of the system given in Table(A.1).

p_i	c_{lkm}	Initial configuration
p_1	c_{003}	All bosons in right well
p_2	c_{012}	Two bosons in right and one in central wells
p_3	c_{021}	One boson in right and two in central wells
p_4	c_{030}	All bosons in central well
p_5	c_{102}	Two bosons in right and one in left wells
p_6	c_{111}	One boson in each well
p_7	c_{120}	Two bosons in central and one in left wells
p_8	c_{201}	One boson in right and two in left wells
p_9	c_{210}	One boson in central and two in left wells
p_{10}	c_{300}	All bosons in left well

Table A.1: This table presents various possible initial configurations for $N = 3$ bosons in triple well potential.

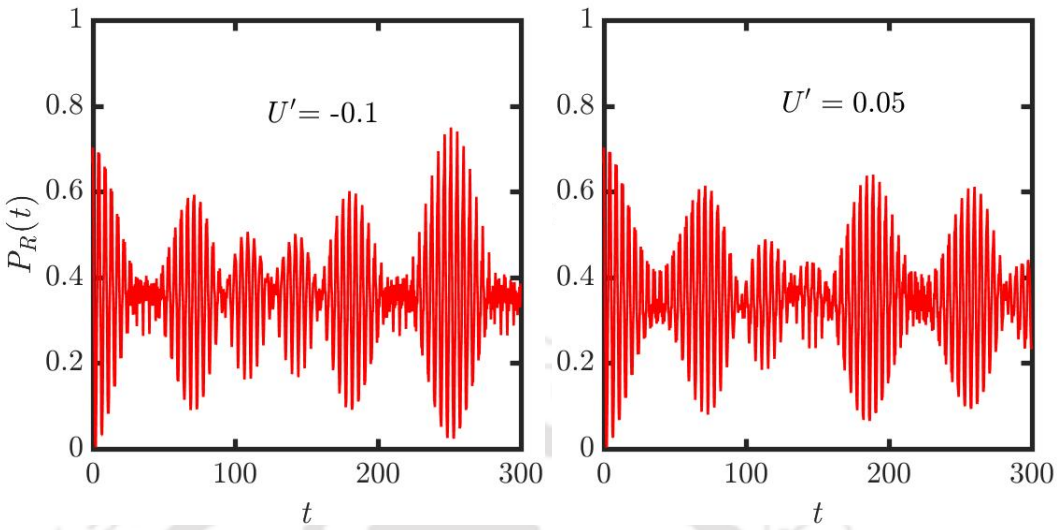

Figure A.1: The right well population, $P_R(t)$ as a function of time is shown for a system of $N = 3$ bosons confined in a triple well potential with the initial condition $(0,1,0,0,0,0,0,0,0,0)$. (a) corresponds to the attractive interaction limit with $U' = -0.1$ and (b) represents $P_R(t)$ for repulsive interaction limit with $U' = 0.05$. Both the figures depict the time evolution in the weak coupling regime.

The right well population, $P_R(t)$ of three bosons confined in a triple well potential is defined as[117],

$$P_R(t) = |p_1(t)|^2 + \frac{2}{3}\left(|p_2(t)|^2 + |p_3(t)|^2\right) + \frac{1}{3}\left(|p_4(t)|^2 + |p_5(t)|^2 + |p_6(t)|^2\right) \quad \text{(A.5)}$$

The different initial conditions, p_i of the bosons in the triple well potential is represented by the various possible combinations of p_i as given in Table(A.1). Figs.(A.1) depict the time evolution of the right well population, $P_R(t)$ in the weak coupling regime for both attractive as well as repulsive interactions with an initial configuration in which the system is prepared is considered as $(0,1,0,0,0,0,0,0,0,0)$. In this case we consider the population difference to be unity that is the left well contain no bosons, while there is one in the central and two in the right well. It is observed that there is no accumulation of bosons in any one of the wells, for odd number of bosons (say $N = 3$) with population imbalance of unity unlike the case of the three boson system confined in a double well potential as evident from Fig.3.4(c) and (d).

APPENDIX B

COMPARISON BETWEEN $\sin^2 kx$ AND $\sin^4 kx$ TRAPPING POTENTIAL

A comparison between the $\sin^4 kx$ and a more familiar $\sin^2 kx$ is carried out for tilted triple well as paradigm to asses the generality of results presented in Sec.4.1. of **Chapter 4**. It may be noted that a $\sin^4 kx$ potential considered in our work (**Chapter 4**) has flatter minima and sharper boundaries in comparison to $\sin^2 kx$ term.

Here, we assess the generality of our results in the **Chapter 4** for a trapping potential of the form given as,

$$V_{trap}(x) = -\alpha x + V_0 \sin^2(kx) + f_w(x) \tag{B.1}$$

Here Eq. (4.5) of **Chapter 4** with $\sin^4 kx$ is replaced by $\sin^2 kx$. α is the tilt parameter, V_0 is the barrier height and $f_w(x)$ is the hard-wall boundary as similar to Eq. (4.5). $k = 2$ is fixed for the lattice spacing.

We re-investigate the first-order correlation function given as,

$$|g^{(1)}(x,x')|^2 = \left| \frac{\rho^{(1)}(x,x')}{\sqrt{\rho^{(1)}(x,x)\rho^{(1)}(x',x')}} \right|^2 \tag{B.2}$$

and inter-well (left-right well correlation) given as,

$$|g^{(1)}(x_l,x_r)|^2 = \left| \frac{\rho^{(1)}(x_r,x_l)}{\sqrt{\rho^{(1)}(x_r,x_r)\rho^{(1)}(x_l,x_l)}} \right|^2 \tag{B.3}$$

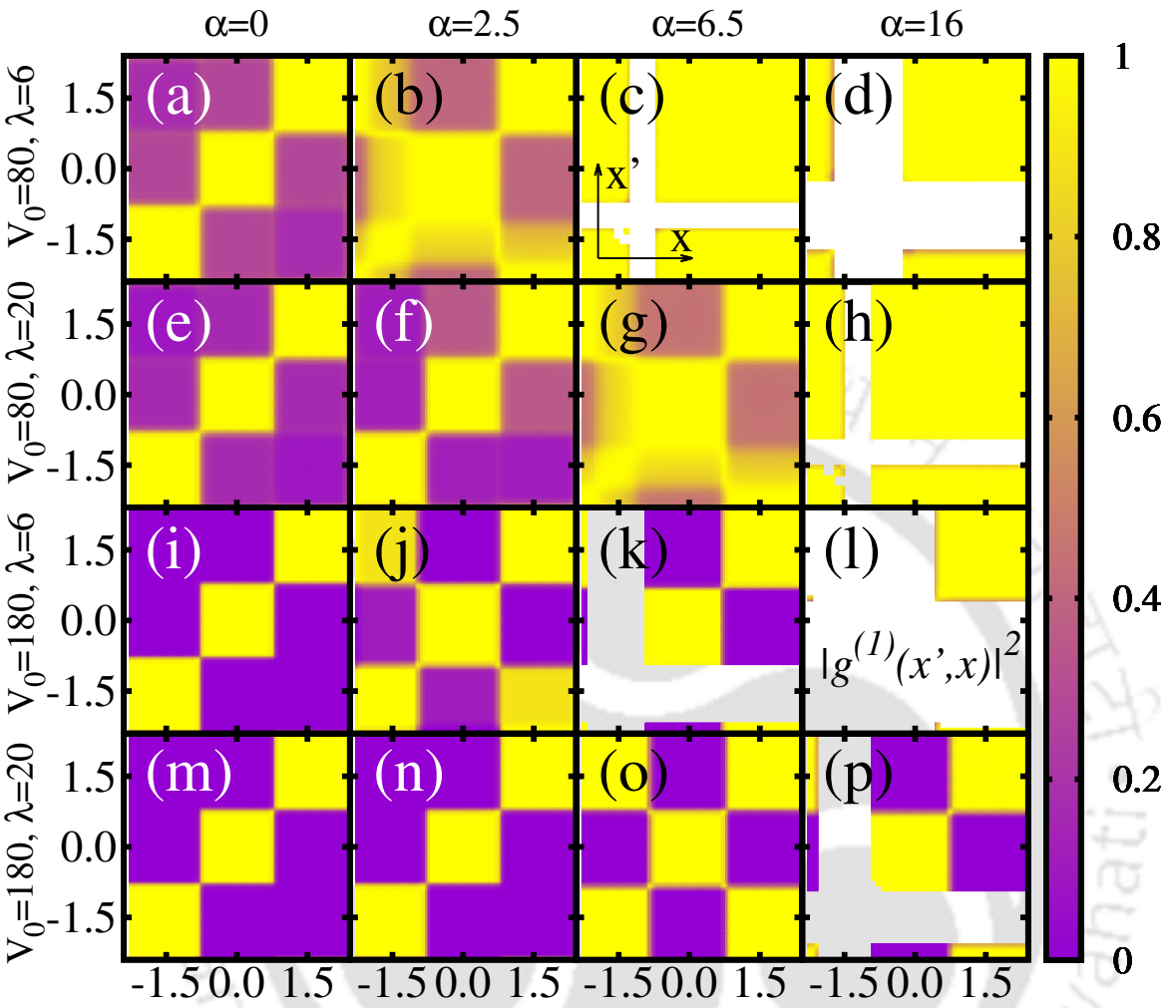

Figure B.1: First-order Glauber correlation function for $\sin^2(kx)$-potential as given in Eq.(B.1). All the other parameters are identical to Fig.(4.5) of the **Chapter 4**. There is no qualitative changes with respect to the $\sin^4(kx)$-potential given in Eq. (4.5) of **Chapter 4**.

as depicted in Figs.(4.5),(4.6) of **Chapter 4** with the $\sin^2(kx)$ potential, see Figs.(B.1) and (B.2). In Eq.(B.2) $\rho^{(1)}(x,x')$ is one-body reduced density matrix as defined in Eq.(4.6). Similarly in Eq.(B.3), $\rho^{(1)}(x_r,x_l)$ is the one-body reduced density matrix evaluated at points $x = x_r(\alpha)$ and $x' = x_l(\alpha)$. For this potential, the position $x_r(\alpha)(x_l(\alpha))$ of the right(left) well minimum is weakly dependent on the tilt parameter α.

Figs.(B.1) and (B.2) depicts the behaviour of first-order correlation function, $|g^{(1)}(x,x')|^2$ and first-order inter-well (left-right) correlation function, $|g^{(1)}(x_l(\alpha),x_r(\alpha))|^2$ for $\sin^2 kx$ potential as a function of α for various barrier heights, V_0 and interaction strengths, λ. It is observed that the similar qualitative features of correlation prevails for $\sin^2 kx$

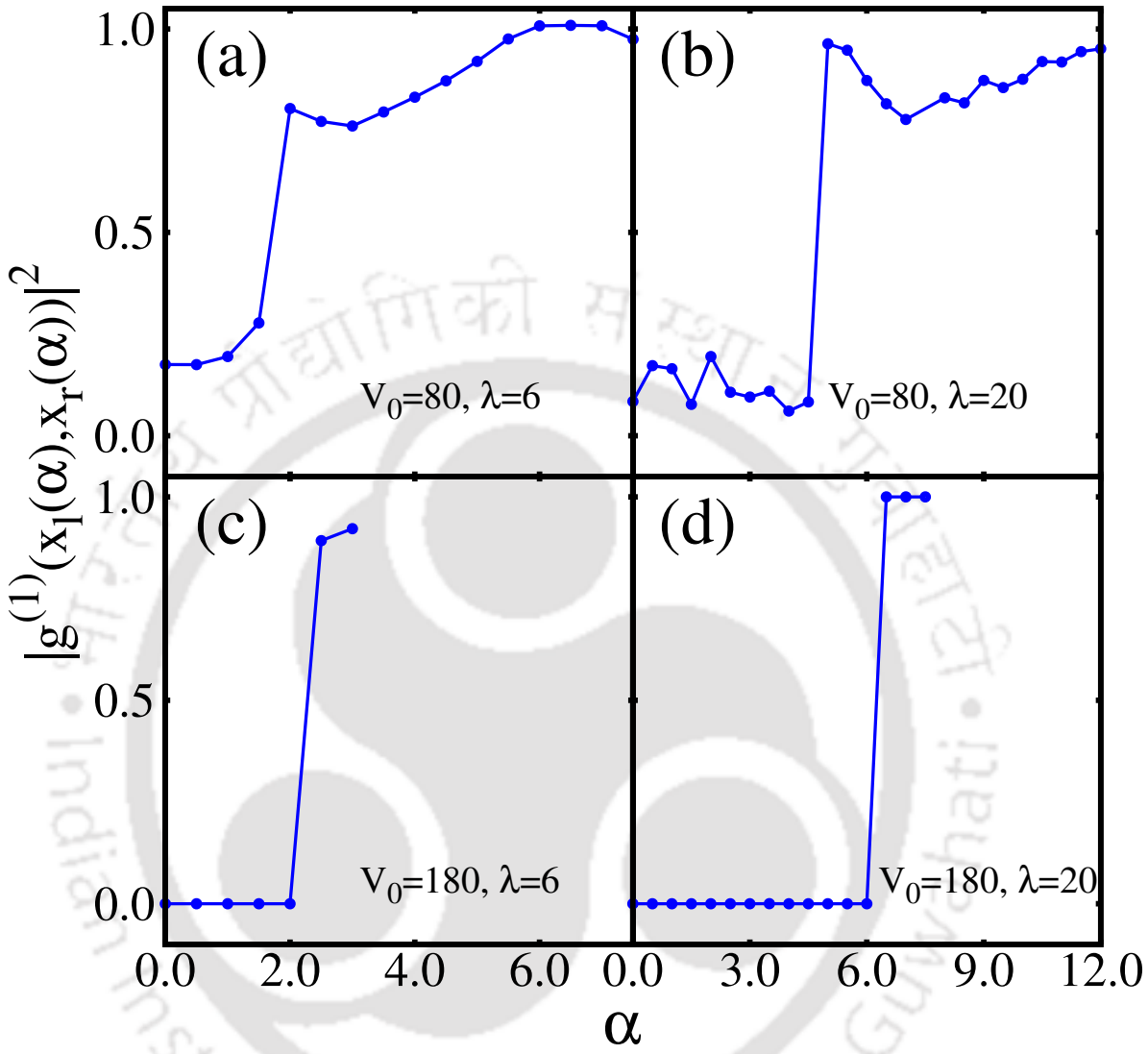

Figure B.2: Left-right correlation function, $|g^{(1)}(x_l(\alpha),x_r(\alpha))|^2$ for $\sin^2 kx$-potential as given in Eq.(B.1). All other parameters are identical to Fig. (4.6) of $\sin^4 kx$-potential. There is no qualitative changes with respect to the $\sin^4 kx$-potential given in Eq. (4.5) of **Chapter 4**.

potential. For example, we observe prominent next–to–nearest coherence (inter-well correlation, that is, $|g^{(1)}(x,x')|^2 \approx 1$ at $x \neq x'$) as evident from Fig.B.1(j) for $V_0 = 180$ and $\lambda = 6$ as similar to $\sin^4 kx$ potential.

We further extend the computation even for $M = 4$ orbitals and no qualitative changes in the results for the correlations are observed.

BIBLIOGRAPHY

[1] M H Anderson, J R Ensher, M R Matthews, C E Wieman, and E A Cornell. *Science*, 269.

[2] K B Davis, M-O Mewes, M R Andrews, N J van Druten, D S Durfee, D M Kurn, and W Ketterle. *Physical Review Letters*, 75(22):3969, 1995.

[3] M Greiner, O Mandel, T Esslinger, T W Hänsch, and I Bloch. *Nature*, 419:51, 2002.

[4] I Bloch. *Nature Physics*, 1(1):23, 2005.

[5] D Jaksch and P Zoller. *Annals of Physics*, 315(1):52–79, 2005.

[6] Y Zhou, H Zhai, R Lü, Z Xu, and L Chang. *Physical Review A*, 67(4):043606, 2003.

[7] M R Andrews, C G Townsend, H-J Miesner, D S Durfee, D M Kurn, and W Ketterle. *Science*, 275(5300):637–641, 1997.

[8] M R Matthews, B P Anderson, PC Haljan, DS Hall, CE Wieman, and E A Cornell. *Physical Review Letters*, 83(13):2498, 1999.

[9] I Bloch, T W Hänsch, and T Esslinger. *Nature*, 403(6766):166, 2000.

[10] S N Bose. *Z. Phys*, 26(1):178, 1924.

[11] F London. *Nature*, 141(3571):643, 1938.

[12] F London. *Physical Review*, 54(11):947, 1938.

[13] O Penrose and L Onsager. *Physical Review*, 104(3):576, 1956.

[14] T R Sosnick, W M Snow, and P E Sokol. *Physical Review B*, 41(16):11185, 1990.

[15] D M Ceperley. *Reviews of Modern Physics*, 67(2):279, 1995.

[16] S Chu. *Reviews of Modern Physics*, 70(3):685, 1998.

[17] C N Cohen-Tannoudji. *Reviews of Modern Physics*, 70(3):707, 1998.

[18] W D Phillips. *Reviews of Modern Physics*, 70(3):721, 1998.

[19] C Monroe, W Swann, H Robinson, and C Wieman. *Physical Review Letters*, 65(13):1571, 1990.

[20] C C Bradley, C A Sackett, J J Tollett, and R G Hulet. *Physical Review Letters*, 75(9):1687, 1995.

[21] D G Fried, T C Killian, L Willmann, D Landhuis, Stephen C Moss, D Kleppner, and T J Greytak. *Physical Review Letters*, 81(18):3811, 1998.

[22] F P Dos Santos, J Léonard, J Wang, C J Barrelet, F Perales, E Rasel, C S Unnikrishnan, M Leduc, and C Cohen-Tannoudji. *Physical Review Letters*, 86(16):3459, 2001.

[23] G Modugno, G Ferrari, G Roati, R J Brecha, A Simoni, and M Inguscio. *Science*, 294(5545):1320–1322, 2001.

[24] *The Nobel Prize in Physics 2001, Information for the Public*. *The Royal Swedish Academy of Sciences*, 2001.

[25] T W Hänsch and A L Schawlow. *Optics Communications*, 13(1):68–69, 1975.

[26] W Ketterle and N J Van Druten. In *Advances in Atomic, Molecular and Optical Physics*, volume 37, pages 181–236. Elsevier, 1996.

[27] D J Wineland, J Dalibard, and C Cohen-Tannoudji. *JOSA B*, 9(1):32–42, 1992.

[28] E Cornell. *Journal of Research of the National Institute of Standards and Technology*, 101(4):419, 1996.

[29] P Courteille, R S Freeland, D J Heinzen, F A Van Abeelen, and B J Verhaar. *Physical Review Letters*, 81(1):69, 1998.

[30] S Inouye, M R Andrews, J Stenger, H-J Miesner, D M Stamper-Kurn, and W Ketterle. *Nature*, 392(6672):151, 1998.

[31] F Dalfovo, S Giorgini, L P Pitaevskii, and S Stringari. *Reviews of Modern Physics*, 71(3):463, 1999.

[32] A J Leggett. *Reviews of Modern Physics*, 73(2):307, 2001.

[33] P W Anderson. *Reviews of Modern Physics*, 38(2):298, 1966.

[34] A J Leggett and F Sols. *Foundations of Physics*, 21(3):353–364, 1991.

[35] A J Leggett. Broken gauge symmetry in a bose condensate. *Bose-Einstein Condensation*, page 452, 1995.

[36] P S Julienne, F H Mies, E Tiesinga, and C J Williams. *Physical Review Letters*, 78(10):1880, 1997.

[37] N N Bogolyubov. On the theory of superfluidity. *Izv. Akad. Nauk Ser. Fiz.*, 11:23–32, 1947.

[38] E P Gross. Structure of a quantized vortex in boson systems. *Il Nuovo Cimento (1955-1965)*, 20(3):454–477, 1961.

[39] L P Pitaevskii. Vortex lines in an imperfect bose gas. *Sov. Phys. JETP*, 13(2):451–454, 1961.

[40] K W Madison, F Chevy, W Wohlleben, and J Dalibard. *Physical Review Letters*, 84(5):806, 2000.

[41] W Zwerger. *Journal of Optics B: Quantum and Semiclassical Optics*, 5(2):S9, 2003.

[42] S L Cornish, N R Claussen, J L Roberts, E A Cornell, and C E Wieman. *Physical Review Letters*, 85(9):1795, 2000.

[43] E A Donley, N R Claussen, S L Cornish, J L Roberts, E A Cornell, and C E Wieman. *Nature*, 412(6844):295, 2001.

[44] P O Fedichev, M W Reynolds, and G V Shlyapnikov. *Physical Review Letters*, 77(14):2921, 1996.

[45] M Greiner. *Ultracold quantum gases in three-dimensional optical lattice potentials*. PhD thesis, lmu, 2003.

[46] M P A Fisher, P B Weichman, G Grinstein, and D S Fisher. *Physical Review B*, 40(1):546, 1989.

[47] D Jaksch, C Bruder, J I Cirac, C W Gardiner, and P Zoller. *Physical Review Letters*, 81(15):3108, 1998.

[48] M Greiner, O Mandel, T Esslinger, T W Hänsch, and I Bloch. *Nature*, 415(6867):39, 2002.

[49] R Grimm, M Weidemüller, and Y B Ovchinnikov. Optical dipole traps for neutral atoms. In *Advances in Atomic, Molecular and Optical Physics*, volume 42, pages 95–170. Elsevier, 2000.

[50] P S Jessen and I H Deutsch. Optical lattices. In *Advances in Atomic, Molecular and Optical Physics*, volume 37, pages 95–138. Elsevier, 1996.

[51] P B Blakie and C W Clark. *Journal of Physics B: Atomic, Molecular and Optical Physics*, 37(7):1391, 2004.

[52] I Bloch, J Dalibard, and W Zwerger. *Reviews of Modern Physics*, 80(3):885, 2008.

[53] C Chin, R Grimm, P Julienne, and E Tiesinga. *Reviews of Modern Physics*, 82(2):1225, 2010.

[54] H A Gersch and G C Knollman. *Physical Review*, 129(2):959, 1963.

[55] G J Milburn, J Corney, E M Wright, and D F Walls. *Physical Review A*, 55(6):4318, 1997.

[56] J Hubbard. *Proceedings of the Royal Society of London. Series A. Mathematical and Physical Sciences*, 276(1365):238–257, 1963.

[57] H-D Meyer, U Manthe, and L S Cederbaum. *Chemical Physics Letters*, 165(1):73–78, 1990.

[58] U Manthe, H-D Meyer, and L S Cederbaum. *The Journal of Chemical Physics*, 97(5):3199–3213, 1992.

[59] H-D Meyer, F Gatti, and G A Worth. *Multidimensional quantum dynamics: MCTDH theory and applications*. John Wiley & Sons, 2009.

[60] A I Streltsov, O E Alon, and L S Cederbaum. *Physical Review Letters*, 99(3):030402, 2007.

[61] O E Alon, A I Streltsov, and L S Cederbaum. *Physical Review A*, 77(3):033613, 2008.

[62] K Sakmann. *Many-Body Schrödinger Dynamics of Bose-Einstein Condensates*. Springer Science & Business Media, 2011.

[63] A UJ Lode. *Tunneling Dynamics in Open Ultracold Bosonic Systems: Numerically Exact Dynamics–Analytical Models–Control Schemes*. Springer, 2014.

[64] K Byczuk and D Vollhardt. *Physical Review B*, 77(23):235106, 2008.

[65] A N Salgueiro, A F R de Toledo Piza, G B Lemos, R Drumond, M C Nemes, and M Weidemüller. *The European Physical Journal D*, 44(3):537–540, 2007.

[66] B Juliá-Díaz, D Dagnino, M Lewenstein, J Martorell, and A Polls. *Physical Review A*, 81(2):023615, 2010.

[67] M Melé-Messeguer, B Juliá-Díaz, M Guilleumas, A Polls, and A Sanpera. *New Journal of Physics*, 13(3):033012, 2011.

[68] Q Zhu, Q Zhang, and B Wu. *Journal of Physics B: Atomic, Molecular and Optical Physics*, 48(4):045301, 2015.

[69] B Juliá-Díaz, J Martorell, and A Polls. *Physical Review A*, 81(6):063625, 2010.

[70] M A Cazalilla, R Citro, T Giamarchi, E Orignac, and M Rigol. *Reviews of Modern Physics*, 83(4):1405, 2011.

[71] J B Spring, B J Metcalf, P C Humphreys, W S Kolthammer, X-M Jin, M Barbieri, A Datta, N Thomas-Peter, N K Langford, D Kundys, et al. *Science*, 339(6121):798–801, 2013.

[72] M A Broome, A Fedrizzi, S Rahimi-Keshari, J Dove, S Aaronson, T C Ralph, and A G White. *Science*, 339(6121):794–798, 2013.

[73] F Haake, M Kuś, and R Scharf. *Zeitschrift für Physik B Condensed Matter*, 65(3):381–395, 1987.

[74] M P Strzys, E M Graefe, and H J Korsch. *New Journal of Physics*, 10(1):013024, 2008.

[75] L Reichl. *The transition to chaos: conservative classical systems and quantum manifestations*. Springer Science & Business Media, 2013.

[76] A Eckardt, C Weiss, and M Holthaus. *Physical Review Letters*, 95(26):260404, 2005.

[77] C Heinisch and M Holthaus. *Journal of Modern Optics*, 63(18):1768–1776, 2016.

[78] P Ponte, Z Papić, F Huveneers, and D A Abanin. *Physical Review Letters*, 114(14):140401, 2015.

[79] A Eckardt, M Holthaus, H Lignier, A Zenesini, D Ciampini, O Morsch, and E Arimondo. *Physical*

Review A, 79(1):013611, 2009.

[80] T Betz, S Manz, R Bücker, T Berrada, C Koller, G Kazakov, I E Mazets, H-P Stimming, A Perrin, T Schumm, et al. *Physical Review Letters*, 106(2):020407, 2011.

[81] A Perrin, R Bücker, S Manz, T Betz, C Koller, T Plisson, T Schumm, and J Schmiedmayer. *Nature Physics*, 8(3):195, 2012.

[82] T Langen, R Geiger, M Kuhnert, B Rauer, and J Schmiedmayer. *Nature Physics*, 9(10):640, 2013.

[83] A UJ Lode and C Bruder. *Physical Review Letters*, 118(1):013603, 2017.

[84] B Chatterjee, M C Tsatsos, and A UJ Lode. *New Journal of Physics*, 2018.

[85] R Roy, A Gammal, M C Tsatsos, B Chatterjee, B Chakrabarti, and A UJ Lode. *Physical Review A*, 97(4):043625, 2018.

[86] A N Wenz, G Zürn, S Murmann, I Brouzos, T Lompe, and S Jochim. *Science*, 342(6157):457–460, 2013.

[87] A I Streltsov, K Sakmann, O E Alon, and L S Cederbaum. *Physical Review A*, 83(4):043604, 2011.

[88] B Chatterjee, I Brouzos, L Cao, and P Schmelcher. *Journal of Physics B: Atomic, Molecular and Optical Physics*, 46(8):085304, 2013.

[89] Y-J Lin, R L Compton, K Jimenez-Garcia, J V Porto, and I B Spielman. *Nature*, 462(7273):628, 2009.

[90] M Aidelsburger, M Atala, M Lohse, J T Barreiro, B Paredes, and I Bloch. *Physical Review Letters*, 111(18):185301, 2013.

[91] H Miyake, G A Siviloglou, C J Kennedy, W Cody Burton, and W Ketterle. *Physical Review Letters*, 111(18):185302, 2013.

[92] M Aidelsburger, M Lohse, C Schweizer, M Atala, J T Barreiro, S Nascimbène, N R Cooper, I Bloch, and N Goldman. *Nature Physics*, 11(2):162, 2015.

[93] G Jotzu, M Messer, R Desbuquois, M Lebrat, T Uehlinger, D Greif, and T Esslinger. *Nature*, 515(7526):237, 2014.

[94] N Goldman, J C Budich, and P Zoller. *Nature Physics*, 12(7):639, 2016.

[95] L J LeBlanc, K Jiménez-García, Ross A Williams, M C Beeler, A R Perry, W D Phillips, and I B Spielman. *Proceedings of the National Academy of Sciences*, 109(27):10811–10814, 2012.

[96] J-Ru Li, J Lee, W Huang, S Burchesky, B Shteynas, F Ç Top, A O Jamison, and W Ketterle. *Nature*, 543(7643):91, 2017.

[97] J Léonard, A Morales, P Zupancic, T Esslinger, and T Donner. *Nature*, 543(7643):87, 2017.

[98] M Fierz. "U about the relativistic theory of kr ä free particles with arbitrary spin. *Helvetica Physica Acta*, 12:3–37, 1939.

[99] W Pauli. *Physical Review*, 58(8):716, 1940.

[100] G H Wannier. *Reviews of Modern Physics*, 34(4):645, 1962.

[101] T Stöferle, H Moritz, C Schori, M Köhl, and T Esslinger. *Physical Review Letters*, 92(13):130403, 2004.

[102] I B Spielman, W D Phillips, and J V Porto. *Physical Review Letters*, 98(8):080404, 2007.

[103] A Griesmaier, J Werner, S Hensler, J Stuhler, and T Pfau. *Physical Review Letters*, 94(16):160401, 2005.

[104] R V Pai and R Pandit. *Physical Review B*, 71(10):104508, 2005.

[105] M Iskin and J K Freericks. *Physical Review A*, 79(5):053634, 2009.

[106] H Q Lin. *Physical Review B*, 42(10):6561, 1990.

[107] J M Zhang and R X Dong. *European Journal of Physics*, 31(3):591, 2010.

[108] K Sheshadri, H R Krishnamurthy, R Pandit, and T V Ramakrishnan. *EuroPhysics Letters*, 22(4):257, 1993.

[109] D Van O, P van der Straten, and H T C Stoof. *Physical Review A*, 63(5):053601, 2001.

[110] W Krauth, M Caffarel, and J-P Bouchaud. *Physical Review B*, 45(6):3137, 1992.

[111] C Schroll, F Marquardt, and C Bruder. *Physical Review A*, 70(5):053609, 2004.

[112] J Zakrzewski. *Physical Review A*, 71(4):043601, 2005.

[113] R V Pai, J M Kurdestany, K Sheshadri, and R Pandit. *Physical Review B*, 85(21):214524, 2012.

[114] P Sengupta, M Rigol, G G Batrouni, P J H Denteneer, and R T Scalettar. *Physical Review Letters*, 95(22):220402, 2005.

[115] B Capogrosso-Sansone, Ş Söyler, N Prokof'ev, and B Svistunov. *Physical Review A*, 77(1):015602, 2008.

[116] J M Kurdestany, R V Pai, and R Pandit. *Annalen der Physik*, 524(3-4):234–244, 2012.

[117] S Longhi. *Journal of Physics B: Atomic, Molecular and Optical Physics*, 44(5):051001, 2011.

[118] J R Anglin and A Vardi. *Physical Review A*, 64(1):013605, 2001.

[119] N Makri and W H Miller. *The Journal of Chemical Physics*, 87(10):5781–5787, 1987.

[120] A D Hammerich, R Kosloff, and M A Ratner. *Chemical Physics Letters*, 171(1-2):97–108, 1990.

[121] J Zanghellini, M Kitzler, C Fabian, T Brabec, and A Scrinzi. *Laser Physics*, 13(8):1064–1068, 2003.

[122] M Nest, T Klamroth, and P Saalfrank. *The Journal of Chemical Physics*, 122(12):124102, 2005.

[123] P H Kramer and M Saraceno. *Geometry of the time-dependent variational principle in quantum mechanics*. Springer, 1981.

[124] A UJ Lode, K Sakmann, O E Alon, L S Cederbaum, and A I Streltsov. *Physical Review A*, 86(6):063606, 2012.

[125] A J Coleman and V I Yukalov. *Reduced density matrices: Coulson's challenge*, volume 72. Springer Science & Business Media, 2000.

[126] D A Mazziotti. *Reduced-density-matrix mechanics: with applications to many-electron atoms and molecules*, volume 134. Wiley Online Library, 2007.

[127] K Sakmann, A I Streltsov, O E Alon, and L S Cederbaum. *Physical Review A*, 78(2):023615, 2008.

[128] R J Glauber. *Physical Review*, 130(6):2529, 1963.

[129] M Naraschewski and R J Glauber. *Physical Review A*, 59(6):4595, 1999.

[130] A I Streltsov, O E Alon, and L S Cederbaum. *Physical Review A*, 73(6):063626, 2006.

[131] U M Titulaer and R J Glauber. *Physical Review*, 140(3B):B676, 1965.

[132] O E Alon, A I Streltsov, and L S Cederbaum. *The Journal of Chemical Physics*, 127(15):154103, 2007.

[133] P Nozieres and D Saint James. *Journal de Physique*, 43(7):1133–1148, 1982.

[134] B Chatterjee, I Brouzos, L Cao, and P Schmelcher. *Physical Review A*, 85(1):013611, 2012.

[135] L Cao, I Brouzos, S Zöllner, and P Schmelcher. *New Journal of Physics*, 13(3):033032, 2011.

[136] L Cao, I Brouzos, B Chatterjee, and P Schmelcher. *New Journal of Physics*, 14(9):093011, 2012.

[137] S Fölling, S Trotzky, P Cheinet, M Feld, R Saers, A Widera, T Müller, and I Bloch. *Nature*, 448(7157):1029, 2007.

[138] S Levy, E Lahoud, I Shomroni, and J Steinhauer. *Nature*, 449(7162):579, 2007.

[139] A Crespi, R Osellame, R Ramponi, D J Brod, E F G, N Spagnolo, C Vitelli, E Maiorino, P Mataloni, and F Sciarrino. *Nature Photonics*, 7(7):545, 2013.

[140] B Wu and Q Niu. *Physical Review A*, 61(2):023402, 2000.

[141] X Luo, Q Xie, B Wu, et al. *Physical Review A*, 77(5):053601, 2008.

[142] H L Haroutyunyan and G Nienhuis. *Physical Review A*, 70(6):063603, 2004.

[143] H Lignier, C Sias, D Ciampini, Y Singh, A Zenesini, O Morsch, and E Arimondo. *Physical Review Letters*, 99(22):220403, 2007.

[144] J Gong, L Morales-Molina, and P Hänggi. *Physical Review Letters*, 103(13):133002, 2009.

[145] R Gati and M K Oberthaler. *Journal of Physics B: Atomic, Molecular and Optical Physics*, 40(10):R61, 2007.

[146] A Smerzi, S Fantoni, S Giovanazzi, and S R Shenoy. *Physical Review Letters*, 79(25):4950, 1997.

[147] M Iskin. *Physical Review A*, 83(5):051606, 2011.

[148] S Zöllner, H D Meyer, and P Schmelcher. *Physical Review Letters*, 100(4):040401, 2008.

[149] J Stuhler, A Griesmaier, J Werner, T Koch, M Fattori, and T Pfau. *Journal of Modern Optics*, 54(5):647–660, 2007.

[150] A Greiner, J Sebastian, P Rehme, A Aghajani-Talesh, A Griesmaier, and T Pfau. *Journal of Physics B: Atomic, Molecular and Optical Physics*, 40(5):F77, 2007.

[151] P Buonsante, R Burioni, E Vescovi, and A Vezzani. *Physical Review A*, 85(4):043625, 2012.

[152] A R Kolovsky, J Link, and S Wimberger. *New Journal of Physics*, 14(7):075002, 2012.

[153] K Winkler, G Thalhammer, F Lang, R Grimm, J H Denschlag, A J Daley, A Kantian, H P Büchler, and P Zoller. *Nature*, 441(7095):853, 2006.

[154] M O Scully and M S Zubairy. Quantum optics cambridge university press. *Cambridge, CB2 2RU, UK*, 1997.

[155] S Sachdev, K Sengupta, and S M Girvin. *Physical Review B*, 66(7):075128, 2002.

[156] D R Dounas-Frazer, A M Hermundstad, and L D Carr. *Physical Review Letters*, 99(20):200402, 2007.

[157] G Casati, B Chirikov, F M Izraelev, and J Ford. Stochastic behavior of a quantum pendulum under a periodic perturbation. In *Stochastic behavior in classical and quantum Hamiltonian systems*, pages 334–352. Springer, 1979.

[158] S Fishman, D R Grempel, and R E Prange. *Physical Review Letters*, 49(8):509, 1982.

[159] F Haake. Quantum signatures of chaos. In *Quantum Coherence in Mesoscopic Systems*, pages 583–595. Springer, 1991.

[160] A Frisch, M Mark, K Aikawa, F Ferlaino, J L Bohn, C Makrides, A Petrov, and S Kotochigova. Quantum chaos in ultracold collisions of gas-phase erbium atoms. *Nature*, 507(7493):475, 2014.

[161] W Hai, C Lee, G Chong, and L Shi. *Physical Review E*, 66(2):026202, 2002.

[162] P Bordia, H Lüschen, U Schneider, M Knap, and I Bloch. *Nature Physics*, 13(5):460, 2017.

[163] A R Bishop, M Forest, D W McLaughlin, and Edward A Overman I I. *Physica D: Nonlinear Phenomena*, 23(1-3):293–328, 1986.

[164] P K Mishra, J Herault, S Fauve, and M K Verma. *Physical Review E*, 91(5):053005, 2015.

[165] M V Jakobson. *Communications in Mathematical Physics*, 81(1):39–88, 1981.

[166] A Prasad, V Mehra, and R Ramaswamy. *Physical Review Letters*, 79(21):4127, 1997.

[167] C Grebogi, E Ott, and J A Yorke. *Physica D: Nonlinear Phenomena*, 7(1-3):181–200, 1983.

[168] G Tanaka, M A F Sanjuan, and K Aihara. *Physical Review E*, 71(1):016219, 2005.

[169] G J De Valcárcel, E Roldán, and R Vilaseca. *Physical Review A*, 45(5):R2674, 1992.

[170] M J Wright, J A Pechkis, J L Carini, and P L Gould. *Physical Review A*, 74(6):063402, 2006.

[171] O Mandel, M Greiner, A Widera, T Rom, T W Hänsch, and I Bloch. *Nature*, 425(6961):937, 2003.

[172] W K Hensinger, H Häffner, A Browaeys, N R Heckenberg, K Helmerson, C McKenzie, G J Milburn, W D Phillips, S L Rolston, H Rubinsztein-Dunlop, et al. *Nature*, 412(6842):52, 2001.

[173] D Alves, C Mand Jaksch. *Physical Review Letters*, 93(11):110501, 2004.

[174] D R Hofstadter. *Physical review B*, 14(6):2239, 1976.

[175] R Banerjee, Timothy C H Liew, and O Kyriienko. *Physical Review B*, 98(7):075412, 2018.

[176] D J Thouless, M Kohmoto, M P Nightingale, and M den Nijs. *Physical Review Letters*, 49(6):405, 1982.

[177] I Coddington, P C Haljan, P Engels, V Schweikhard, S Tung, and E A Cornell. *Physical Review A*, 70(6):063607, 2004.

[178] D Jaksch and P Zoller. *New Journal of Physics*, 5(1):56, 2003.

[179] S Tung, V Schweikhard, and E A Cornell. *Physical Review Letters*, 97(24):240402, 2006.

[180] T A Zaleski and T P Polak. *Physical Review A*, 83(2):023607, 2011.

[181] J Dalibard, F Gerbier, G Juzeliūnas, and P Öhberg. *Reviews of Modern Physics*, 83(4):1523, 2011.

[182] A L Fetter. *Reviews of Modern Physics*, 81(2):647, 2009.

[183] S Raghu and F D M Haldane. *Physical Review A*, 78(3):033834, 2008.

[184] M Hafezi, E A Demler, M D Lukin, and J M Taylor. *Nature Physics*, 7(11):907, 2011.

[185] K Fang, ZŸu, and S Fan. *Nature Photonics*, 6(11):782, 2012.

[186] S Mittal, J Fan, S Faez, A Migdall, J M Taylor, and M Hafezi. *Physical Review Letters*, 113(8):087403, 2014.

[187] C Chin and E J Mueller. *Physics*, 6:118, 2013.

[188] R Umucalılar, H Zhai, and M Ö Oktel. *Physical Review Letters*, 100(7):070402, 2008.

[189] M Aidelsburger, S Nascimbene, and N Goldman. *Comptes Rendus Physique*, 19(6):394–432, 2018.

[190] F Yılmaz and M Ö Oktel. *Physical Review A*, 97(2):023612, 2018.

[191] D Ciampini, O Morsch, and E Arimondo. *International Journal of Quantum Information*, 9(supp01):139–144, 2011.

[192] T Oka and H Aoki. *Physical Review B*, 79(8):081406, 2009.

[193] T Kitagawa, T Oka, A Brataas, L Fu, and E Demler. *Physical Review B*, 84(23):235108, 2011.

[194] J Cayssol, Bal Dóra, F Simon, and R Moessner. *Rapid Research Letters*, 7(1-2):101–108, 2013.

[195] M C Rechtsman, Julia M Zeuner, Y Plotnik, Y Lumer, D Podolsky, F Dreisow, S Nolte, M Segev, and A Szameit. Photonic floquet topological insulators. *Nature*, 496(7444):196, 2013.

[196] F de Juan, A G Grushin, T Morimoto, and J E Moore. *Nature Communications*, 8:15995, 2017.

[197] D T Tran, A Dauphin, A G Grushin, P Zoller, and N Goldman. *Science Advances*, 3(8):e1701207,

2017.

[198] M Ö Oktel, M Niţă, and B Tanatar. *Physical Review B*, 75(4):045133, 2007.

[199] Sk N Nabi and S Basu. *EuroPhysics Letters*, 116(4):46001, 2016.

[200] R V Pai, K Sheshadri, and R Pandit. *Physical Review B*, 77(1):014503, 2008.

[201] K Baumann, C Guerlin, F Brennecke, and T Esslinger. *Nature*, 464(7293):1301, 2010.

[202] T Schweigler, V Kasper, S Erne, I Mazets, B Rauer, F Cataldini, T Langen, T Gasenzer, J Berges, and J Schmiedmayer. *Nature*, 545(7654):323, 2017.

[203] S Murmann, A Bergschneider, V M Klinkhamer, G Zürn, T Lompe, and S Jochim. *Physical Review Letters*, 114(8):080402, 2015.

[204] M Hiller, H Venzl, T Zech, B Oleś, F Mintert, and A Buchleitner. *Journal of Physics B: Atomic, Molecular and Optical Physics*, 45(9):095301, 2012.

[205] R W Spekkens and J E Sipe. *Physical Review A*, 59(5):3868, 1999.

[206] M Olshanii. *Physical Review Letters*, 81(5):938, 1998.

[207] Y Wang, S Subhankar, P Bienias, M Łącki, T-C Tsui, M A Baranov, A V Gorshkov, P Zoller, J V Porto, S L Rolston, et al. *Physical Review Letters*, 120(8):083601, 2018.

[208] A UJ Lode. *Physical Review A*, 93(6):063601, 2016.

[209] E Fasshauer and A UJ Lode. *Physical Review A*, 93(3):033635, 2016.

[210] A UJ Lode, M C Tsatsos, E Fasshauer, R Lin, L Papariello, P Molignini, and C Lévêque. Mctdh-x: The time-dependent multiconfigurational hartree for indistinguishable particles software, 2018.

[211] A UJ Lode, A I Streltsov, K Sakmann, O E Alon, and L S Cederbaum. *Proceedings of the National Academy of Sciences*, 109(34):13521–13525, 2012.

[212] S Pielawa, T Kitagawa, E Berg, and S Sachdev. *Physical Review B*, 83(20):205135, 2011.

[213] F Meinert, M J Mark, E Kirilov, K Lauber, P Weinmann, A J Daley, and H-C Nägerl. *Physical Review Letters*, 111(5):053003, 2013.

[214] A UJ Lode, F S Diorico, R Wu, P Molignini, L Papariello, R Lin, C Lévêque, L Exl, M C Tsatsos, R Chitra, et al. *New Journal of Physics*, 20(5):055006, 2018.

[215] I Bloch. *Nature*, 453(7198):1016, 2008.

[216] M Cramer, A Bernard, N Fabbri, L Fallani, C Fort, S Rosi, F Caruso, M Inguscio, and Martin B Plenio. *Nature Communications*, 4:2161, 2013.

[217] N Gemelke, E Sarajlic, Y Bidel, S Hong, and S Chu. *Physical Review Letters*, 95(17):170404, 2005.

[218] V V Ivanov, A Alberti, M Schioppo, G Ferrari, MLCM Artoni, M L Chiofalo, and GM Tino. *Physical Review Letters*, 100(4):043602, 2008.

[219] A Polkovnikov, K Sengupta, A Silva, and M Vengalattore. *Reviews of Modern Physics*, 83(3):863, 2011.

[220] J Eisert, Mathis F, and C Gogolin. *Nature Physics*, 11(2):124, 2015.

[221] A Zenesini, H Lignier, D Ciampini, O Morsch, and E Arimondo. *Physical Review Letters*, 102(10):100403, 2009.

[222] A Alberti, VV Ivanov, GM Tino, and G Ferrari. *Nature Physics*, 5(8):547, 2009.

[223] E Haller, R Hart, M J Mark, J G Danzl, L Reichsöllner, and H-C Nägerl. *Physical Review Letters*, 104(20):200403, 2010.

[224] F Meinert, M J Mark, K Lauber, A J Daley, and H-C Nägerl. *Physical Review Letters*, 116(20):205301, 2016.

[225] C Sias, H Lignier, YP Singh, A Zenesini, D Ciampini, O Morsch, and E Arimondo. *Physical Review Letters*, 100(4):040404, 2008.

[226] D H Dunlap and V M Kenkre. *Physical Review B*, 34(6):3625, 1986.

[227] S Longhi. *Journal of Physics: Condensed Matter*, 24(43):435601, 2012.

[228] F Grossmann, T Dittrich, P Jung, and P Hänggi. *Physical Review Letters*, 67(4):516, 1991.

[229] Y Zheng and S-J Yang. *Physical Review A*, 93(6):063609, 2016.

[230] A H MacDonald, editor. *Quantum Hall effect: a perspective*. Springer, Netherlands, 1989.

[231] L Mingarelli, E E Keaveny, and R Barnett. *Journal of Physics: Condensed Matter*, 28(28):285201, 2016.

[232] N Byers and C N Yang. *Physical Review Letters*, 7(2):46, 1961.

[233] G tt Hooft. *Nuclear Physics: B*, 153:141–160, 1979.

[234] S E Weiner, M C Tsatsos, L S Cederbaum, and A UJ Lode. *Scientific Reports*, 7:40122, 2017.

[235] S I Mistakidis, L Cao, and P Schmelcher. *Physical Review A*, 91(3):033611, 2015.

[236] S I Mistakidis and P Schmelcher. *Physical Review A*, 95(1):013625, 2017.

[237] J Neuhaus-Steinmetz, S I Mistakidis, and P Schmelcher. *Physical Review A*, 95(5):053610, 2017.

[238] C J Pethick and H Smith. *Bose–Einstein condensation in dilute gases*. Cambridge university press, 2008.

[239] U R Fischer, A UJ Lode, and B Chatterjee. *Physical Review A*, 91(6):063621, 2015.

[240] E Wigner. *Physical Review*, 46(11):1002, 1934.

[241] G E Astrakharchik and M D Girardeau. *Physical Review B*, 83(15):153303, 2011.

[242] S Yi, L You, and H Pu. *Physical Review Letters*, 93(4):040403, 2004.

[243] S Yi and H Pu. *Physical Review Letters*, 97(2):020401, 2006.

[244] Y Kawaguchi, H Saito, and M Ueda. *Physical Review Letters*, 97(13):130404, 2006.

[245] S Zöllner, G M Bruun, C J Pethick, and S M Reimann. *Physical Review Letters*, 107(3):035301, 2011.

[246] S Zöllner. *Physical Review A*, 84(6):063619, 2011.

[247] M Lu, N Q Burdick, S H Youn, and B L Lev. *Physical Review Letters*, 107(19):190401, 2011.

[248] K Aikawa, A Frisch, M Mark, S Baier, A Rietzler, R Grimm, and F Ferlaino. *Physical Review Letters*, 108(21):210401, 2012.

VITA

Sunayana Dutta was born on 16th January, 1988 in Assam, India. She did her B.Sc. with Physics Honours in 2009 from Debraj Roy College under Dibrugarh University and M.Sc. in Physics from Dibrugarh University in 2011. She had enrolled into the Ph.D programme at Indian Institute of Technology Guwahati in 2014. She had qualified Graduate Aptitude Test in Engineering (GATE) in 2014. She has earned the Senior Research Fellowship in 2016 by Indian Institute of Technology Guwahati.